Injection and Autoignition of Methane

in Diesel Engines: A Numerical Study

by

Jianfang Zhang

A thesis

presented to the University of Waterloo

in fulfilment of the

thesis requirement for the degree of

Doctor of Philosophy

in

Mechanical Engineering

Waterloo, Ontario, Canada 1997

The author has granted a non-exclusive licence allowing the National Library of Canada to reproduce, loan, distribute or sell copies of this thesis in microform, paper or electronic formats.

The author retains ownership of the copyright in this thesis. Neither the thesis nor substantial extracts from it may be printed or otherwise reproduced without the author's permission.

L'auteur a accordé une licence non exclusive permettant à la Bibliothèque nationale du Canada de reproduire, prêter, distribuer ou vendre des copies de cette thèse sous la forme de microfiche/film, de reproduction sur papier ou sur format électronique.

L'auteur conserve la propriété du droit d'auteur qui protège cette thèse. Ni la thèse ni des extraits substantiels de celle-ci ne doivent être imprimés ou autrement reproduits sans son autorisation.

0-612-22254-3

Canadä

The University of Waterloo requires the signatures of all persons using or photocopying this thesis. Please sign below, and give address and date.

Abstract

This thesis presents a numerical study on the autoignition process of methane in diesel engines. Traditionally, the method used by similar studies is based on numerical studies in shock tube geometries. This work represents the first computational work on the autoignition of natural gas in geometric environments which closely mimic those encountered in diesel engines.

In the present work, a numerical study that models the injection process up to the time of autoignition uses an in-house code developed by the author which solves the Reynolds averaged Navier-Stokes equations coupled with a simplified reaction (ignition) model. The equations are implicitly solved in fully coupled format. Turbulence viscosity is obtained by solving a specialized $k - \varepsilon$ turbulence model which has been specially modified for application to the engine flow. The transient flow computation stops as soon as local ignition occurs.

As part of this research, a specialized conjugate gradient algorithm with block correction algorithm, B-CGSTAB, has been developed. The scheme greatly improves upon the inherent disadvantage of standard conjugate gradient methods, i.e., it improved convergence rate for solving large numbers of grids and improved capabilities for handling large aspect ratio grids.

This work establishes that the injector/cylinder orifice velocity and temperature profiles are characterised by a double-hump shape, significantly different from the conventional box-hat or parabolic profile usually assumed for unsteady high speed injection processes. The double-hump profile results from supersonic injection causing radical expansion when the flow is transient.

The present study formulates a new kinetic model for modelling natural gas autoignition. Numerical regression is used to modify Arrhenius constants and activation

iv

energies so as to make the computational results conform to the experimental data. In addition, this analysis has lead to a better understanding of how to determine possible ignition locations. Ignition generally occurs at locations where the fuel-air mixture is near: stoichiometric and the fluid velocities are low. This latter condition is interpreted to coincide with regions where the convective heat losses are minimal.

Acknowledgments

I would like to thank Professor R.A. Fraser and Professor A.B. Strong for their supervision and guidance throughout this work. Dr. Fraser was invaluable in his efforts concerning perspective of the work, while Dr. Strong encouraged me to develop initiatives and provided insightful advice and constructive criticisms.

I also wish to thank Dr. G. Stubley, Dr. J.G.H. Howard, Dr. G.D. Raithby, Dr. H.F. Sullivan, Dr. G. Naterer, and Dr. H. Karimian for many valuable discussions.

The financial support of the Natural Sciences and Engineering Research Council of Canada and the Manufacturing Research Corporation of Ontario is gratefully acknowledged.

The work is dedicated to Professor Chengyi Peng, ex-supervisor, and Mrs. Jing (Gina) Xie. Dr. Peng provided strong encouragement by letters. The selflessness of my wife Jing has helped this work come to a successful completion. Her support will not be forgotten.

Contents

List of Figures

xviii

List of Tables

Nomenclature

a	speed of sound	m/sec
A	Arrhenius constant	$(\text{mole/m}^3)^{1-m}$ /sec
c_p	specific heat at constant pressure	J/(kg K)
c_p^a, c_T^a	buffering coefficients	
D_k	diffusion coefficient of kth component	m^2/sec
E_0	molar activation energy	J/kgmole
E	Arrhenius activation energy	J/kg
h	specific enthalpy, including chemical contribution	J/kg
K	heat conductivity	W/(m K)
k	specific reaction rate or turbulent kinetic energy	$(\text{mole/m}^3)^{1-m}$ /sec or m^2 /sec^2
M	molar mass	kg/kgmole
m	mass or molar mass	kg/m^3 or kg/kgmole
N	total number of components in a mixture or the size of matrix	
n	molar number	

p	hydrostatic pressure	Pa
P_r	Prandtl number	
$\mathfrak{R}$	universal gas constant	J/(kgmole K)
R_t	turbulent Reynolds number based on Taylor micro scale	
r	coordinate at radial direction	m
s	specific entropy	J/(kg K)
S_c	Schmidt number	
T	temperature	K
t	time	sec
U_i	macroscopic velocity vector	m/sec
u_i'	turbulent fluctuation velocity	m/sec
$u_{d,k}$	diffusion velocity vector of kth component	m/sec
w	shock velocity	m/sec
w_k	volumetric reaction rate of kth component	mole/(m^3 sec)
X	mole fraction	
x_1, x_2, x_3	cartesian coordinates	m
Y	mass fraction	

Greek

ξ_1, ξ_2, ξ_3	computational domain coordinates	m
$\alpha, \beta, \alpha_1, \alpha_2$	weight functions	
γ	ratio of specific heat	
ε	turbulent dissipation energy	m^2/sec^3
σ_t	Prandtl number	
μ	shear viscosity coefficient	kg/(m sec)
ν	kinematic viscosity coefficient	m^2/sec
ρ	mass density	kg/m^3
$\wp$	entropy production rate	$J/(m^3 K sec)$
s_{ij}	stress tensor	Pa
τ	time in computational space	sec
τ_{ij}	viscous-stress tensor	Pa
ω	reaction rate	kg/sec

Superscripts

i	ith nonlinear iteration
n	nth time iteration
~	Favre averaging
-	Reynolds averaging

`"`   fluctuation of mass-averaged mean

`'`   fluctuating quantity

Subscripts

0 initial condition

d mass diffusion

inj injection condition

k kth component

w wall condition

Chapter 1

Introduction

1.1 Background

Natural gas[1] (NG) has been suggested to be the best near term solution to clean air requirements [Jeske and Jennings, 1992] because it offers an attractive combination of reduced emissions, low cost, and domestic availability [Beck, 1990]. In addition, natural gas has a low propensity to soot, hence, it is known as a clean burning fuel. Reduced sooting is a very attractive feature for diesel engines in particular [Jeske and Jennings, 1992]. Consider, for example, emissions from a *TecoDrive 7000* compressed natural gas engine test [SAE Detroit, 1993] where nitric oxides (NO_x)[2], carbon monoxide (CO), and hydrocarbon (HC) emission levels of *1.4 gm/bhp-hr, 14.5 gm/bhp-hr*, and *0.3 gm/bhp-hr* were measured, respectively. These are extremely low levels in comparison to the

---

[1]   Natural gas is a mixture of hydrocarbon fuels. The largest fraction, often 90 % or more, is methane, followed by ethane (2 to 10 %), propane (1 to 4 %) and trace elements [Fraser, 1991].

[2]   Nitric Oxide (NO) and nitric dioxide (NO_2) emission levels are commonly grouped together and are referred to collectively as NO_x. This practice is pragmatic in origin as the reactive NO readily becomes the more stable NO_2 during the typical gas sampling process. Consequently, reliable NO or NO_2 emission measurements are much more difficult to obtain than a total NO_x measurement.

California Air Resources Board (CARB) requirements for 1994 which are *5 gm/bhp-hr, 37.1 gm/bhp-hr,* and *1.7 gm/bhp-hr,* for NO_x, *CO*, and non-methane hydrocarbon *(NMHC)* emissions levels, respectively. It is estimated that over one million vehicles in North America will be on the road by the year *2000* [Naber *et al.*, 1994], and the use of natural gas *(NG)* as a fuel for internal combustion engines *(ICEs)* has been growing in recent years.

There are several technological issues specific to the application of natural gas in internal combustion engines that have been identified through discussions with engine manufacturers [Hall, 1988]. The three major needs identified were: the reliable spark ignition of lean mixtures, the compression-ignition of natural gas in diesel-cycle engines, and the control of knock. **This thesis is directed at addressing the second item, compression-ignition of natural gas.**

Much of the work on *NG* engines to date has focused on premixed spark-ignited engines [Naber *et al.*, 1994]. Recently, however, engine manufactures have begun exploring the use of *NG* in medium- to heavy-duty direct-injection *(DI)* diesel engines. Examples of *DI* operation with *NG* are a modified two-stroke *6V-92 (205 kw)* by *Detroit Diesel Corporation (DDC),* a modified four-stroke *3516* locomotive engine (*1550 kw*) by Caterpillar, and the Wartsila *GD32 (5900 kw)* [Naber *et al.*, 1994] . Such engines offer the potential for higher efficiency and power density than other *NG* engine options because conventional liquid-fuelled, *DI,* diesel engines benefit from an ability to operate at higher compression ratios than premixed spark ignition engines. A higher compression ratio improves engine efficiency and power density [Heywood, 1988]. The easiest method to convert diesel engines to natural gas operation is by using a premixed charge.

Unfortunately, diesel engines using natural gas premixed with the intake air are limited by the same uncontrollable knock problems that limit the compression ratios of premixed spark ignition engine. Throttling losses may also exist in premixed charge natural gas engines. Thus, premixed charge, natural gas, diesel engines suffer from lower efficiencies than conventional diesels. A *DI*, natural gas, diesel engine such as those mentioned above eliminates throttling losses, and the uncontrolled autoignition problem of knock is less severe (to non-existent).

The development of a *DI*, gaseous-fuelled, diesel engine, however, is a non-trivial extension of *DI*, liquid-fuelled, diesel engine technology. Liquid injection is a well developed technology whereas high pressure (e.g., 20 Mpa), supersonic transient (process completed in about 3 ms), gas injection is not. In fact, suitable high pressure gas injectors are still in the development stage and, as yet, are not commercially available. In addition, the conversion of liquid-fuelled *DI* diesel engines to natural gas *DI* diesel operation results in a number of other unique design problems. For example, there are differences between liquid and gaseous fuel-air mixing; differences in fuel autoignition delay times; and differences in flame propagation (e.g., flame speed). There are also uncertainties of the sensitivity of natural gas ignition to engine operating conditions and to the large variations in composition[3] that occur across the U.S. and Canada [Liss, 1992].

With few exceptions, attempts at natural gas *DI* engines have relied on forced ignition, (i.e., spark-plugs and glow-plugs) or dual fuelling [Wakenell, 1987] rather than natural gas compression-ignition because of the poor compression ignitability of natural gas

---

[3]   Commercial grade natural gas reported by Liss, et al [1991] has a composition by weight of 99.6 % methane, while natural gas from U.S. has a composition of 75-98 % methane, 0.5-13 % ethane, and 0-2.6 % propane.

(octane number = 120 [Kubesh, 1992]). The recently modified two-stroke 6V-92 Detroit Diesel natural gas engine under development is an exception. Reduced scavenging (i.e., in-cylinder exhaust gas recirculation) and high compression ratio (23:1) were used to achieve autoignition conditions in the 6V-92. The advantages of compression-ignition over ignition assisted and dual fuelling *DI* options are simplicity and cost [Naber *et al.*, 1994].

Understanding the processes controlling the ignitability (autoignition) of natural gas in diesel engines is critical to the development of a compression ignition, DI, natural gas, diesel engine. Determination of the autoignition delay time of a diesel fuel as a function of environment (e.g., pressure, temperature) and system (e.g., combustion chamber geometry) variables permits quantification of a fuel's ignitability.

With the success of multidimensional computations, which can provide improved understanding of the ignition process and prediction of in-cylinder flow fields, it is of no surprise that modelling efforts are being pursued to assist natural gas *DI* diesel engine development efforts. With respect to modelling natural gas *DI* diesel engines there are two basic approaches being pursued.

First, a detailed kinetic code has been used [Westbrook, 1979 and 1987; Naber *et al.*, 1994], however, this code calculates detailed kinetics (for example, several hundred reaction equations) and is hence computationally intensive. Consequently, the effects of in-cylinder turbulence, mixing, and geometry are neglected. These omissions severely limit these works' ability to reproduce experimental results [Fraser *et al.*, 1991; Naber *et al.*, 1994] beyond identifying gross trends.

Second, using simplified kinetic relations for natural gas, many researchers [Hill, 1993, Papageorgakis, 1996] are modelling in detail the turbulent mixing environment into

which the DI natural gas is injected. Engine geometries and operating conditions are realistic. These computations generally follow a complete engine cycle. Unfortunately, just as it is computationally prohibitive for this approach to model the detailed kinetics, it is also computationally prohibitive for them to model in detail the injection process.

The work reported in this thesis models the details of the injection process [Zhang *et al*, 1994]. To reduce the computational expense the use of a simplified kinetics scheme and a simplified but realistic geometry are assumed. The calculation follows the injection process only up to the time of autoignition. Modelling the details of natural gas DI diesel engine injection is the major contribution of this thesis. This work represents the first, and currently only known, detailed analysis of the high pressure, supersonic, transient injection of natural gas into a turbulent diesel engine type environment.

The overall goal of this work is to develop an improved understanding of the processes governing the autoignition of natural gas in a diesel engine environment. Specific objectives are given in Section 1.3 which focus this thesis' work on the task of understanding the details of the natural gas injection process through modelling. In 1991 when this work began the only data on the autoignition characteristics of natural gas injected into diesel engine type environments was that of Fraser *et al* [1991]. The only supporting computational work is that provided indirectly by detailed kinetic calculations [Westbrook, 1979]. This thesis directly complements the experimental work of Fraser *et al*. [1991], and more recently, Naber *et al*. [1994] who extended the work of Fraser *et al*.

1.2. Objectives

Works modelling the autoignition details of natural gas injected at high pressures directly into diesel engines in a fashion similar to liquid-injected diesel fuel are quite limited. Most of these works that model natural gas autoignition in diesel engine environments focus on the chemical kinetic mechanisms through detailed kinetic calculations from which it is currently impossible to determine autoignition site location, its cycle-to-cycle variability, and the important role played by turbulence mixing. As a result, further study and development into modelling natural gas autoignition in diesel engines is justified.

The two primary objectives of the present study are as follows:

(1)   to improve our understanding of the autoignition characteristics of natural gas injected directly, at high pressure (e.g. 3000 psi), into diesel engines. Specifically the influence of various factors such as rate of injection, injector shape, cylinder and fuel temperature and pressure, are to be considered. Autoignition delay times, autoignition site location variability, and fuel-air mixing are also of interest. This objective will be achieved upon

(2)   development/selection of a computational model and solution algorithm for turbulent, unsteady, compressible reacting flows suitable for predicting the autoignition characteristics of natural gas in a diesel engine geometry.

This work is an extension of earlier research by Fraser *et al* [1991]. Fraser *et al.*'s and Naber *et al's* [1994] studies represent the available experimental data on the autoignition characteristics of natural gas over a range of typical diesel engine condition temperatures (*1000 K* to *1800 K*) and pressures (*5 atm* to *55 atm*). In addition, these

experiments simulate diesel engine geometry and characteristic times of injection. This work focuses on modelling the compression-ignition properties of natural gas injected into a combustion chamber similar to that used by Fraser *et al.* and Naber *et al.* This work complements and extends the work of Fraser *et al.* and Naber *et al.* by providing insight into the role of mixing on autoignition delay times; on the cycle-to-cycle variation in location of autoignition in the combustion chamber; and on the sensitivity of parameters. These results can hopefully be used to provide a basis for future high-pressure natural gas injector design and assist in the selection of operation procedures for natural gas fueled diesel engines.

1.2.1 Direction and Scope

This research focuses on studying the autoignition characteristics of natural gas in diesel engines with particular contributing emphasis on three aspects of this problem. First, to identify a global reaction model that, when coupled with a detailed injection flow model, provides ignition delay times consistent with the experiments of Fraser *et al.* [1991][4]. Second, to ascertain the role of temperature, pressure, boundary conditions, and turbulent mixing, on natural gas autoignition delay times. Third, to determine the location(s) of the first autoignition event(s). Note, the combustion process following autoignition is not

---

[4]   The experimental data of Naber et al. [1994] was not available during the global reaction selection phase of this work. Regardless, the work of Naber et al. [1994] simply extends the work of Fraser et al. and hence represents data that can be used in the future to refine the global model selected in this work [Section 3.5].

investigated. The associated complexities of following the combustion process/flame put such an investigation beyond the scope of this work.

As implied in the objectives identified in section 1.2, this study of natural gas autoignition in diesel engines seeks to enhance the engine community literature. Hence, a detailed analysis of numerical procedures, such as the order of discretization, the error of numerical methods, the details of algebraic solver principles, the universality of turbulence and chemical kinetic models, etc., are for the most part beyond the scope of this work. The rationale for the numerical methods, the models, and the solvers selected for solving the specific problem of diesel engine natural gas autoignition, however, is provided.

1.3. Outline

The structure of this thesis is as follows. This chapter identified the motivation behind this work to model natural gas autoignition in DI natural gas diesel engines. Chapter 2 provides a more detailed history with respect to natural gas autoignition studies, both experimental and computational. As background, section 2.1 describes some of the more important features with respect to this work of diesel engine operation. The equations, which involve the conservation of mass, momentum, energy, and species under Cartesian and axisymmetric frames, as well as the turbulence model and reaction mechanism, are discussed in Chapter 3. Chapter 4 follows with a discussion of the selected numerical approach. Some aspects of matrix solver behavior are covered in chapter 5. While Chapters 3 to 5 are concerned with code selection, i.e., primary objective (2), Chapter 6

addresses objective (1). Chapter 6 presents the modelling results showing the effects of injection pressure, initial temperature, and turbulence mixing. The analysis of the characteristics of pressure-wave propagation in two-dimensional or axisymmetric geometrical cases is also presented. In the final chapter, Chapter 7, the major contributions and conclusions of this work, and recommendations for further work, are summarized.

Chapter 2

Literature Review

2.1. Overview

In this chapter three topics directly related to the direct, high pressure, injection of natural gas into a diesel engine are reviewed: basic diesel engine operation, background experimental work, and background modelling work. The first part, diesel engine operation, discusses major characteristics of diesel engine operation and identifies why autoignition delay time and ignition location are important design parameters. The second part, experimental work, reviews the experimental work of Fraser *et al.* [1991] and Naber *et al.* [1994] and its relevance to the present study. These are the only two publicly available works to detail the autoignition characteristics of natural gas under diesel engine type pressure and temperature operating conditions. The final part, modelling work, reviews previous autoignition modelling work and then critically assesses this work against the experimental work of Fraser *et al.* and Naber *et al.* This being a first attempt at a detailed modelling of the events leading to NG autoignition in

diesel engine environments it was necessary to restrict the scope of this work to a manageable level, e.g., flame propagation is not pursued. One development, (writing the code), and three technical problems were identified for study (injector boundary conditions, reaction kinetics, and autoignition site location).

2.2. Diesel Engine Operation

Figure 2.1 shows a schematic of the combustion chamber of a typical direct injection (DI) diesel engine. When the piston is at top-dead-center (TDC) (i.e., a minimum volume for
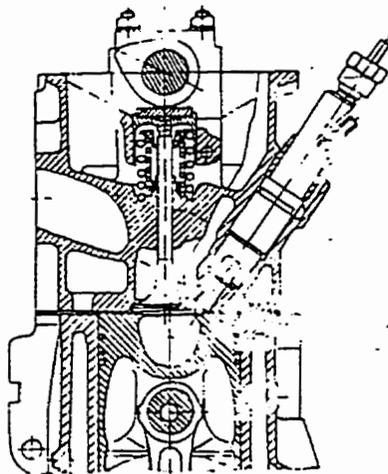
Figure 2.1: A typical direct-injection diesel-fueled engine [Benson, 1979].

the combustion chamber), this corresponds to the zero (and 360^0) crankshaft angle degree location. Remaining piston positions are then referred to as so many degrees before, or after, TDC, e.g., -10^0 is equivalent to 350^0, with the angle determined with respect to the location of the rotating crankshaft (see Figure 2.2).

TC ---- top center
BC ---- bottom center
B ---- diameter of cylinder
L ---- distance between top center and bottom center
V_c ---- a volume when piston is on top center
V_d ---- a volume when piston is on bottom center
l ---- length of connecting rod
a ---- radius of crankshaft
θ ---- angle of crankshaft
s ---- distance between piston center and crankshaft
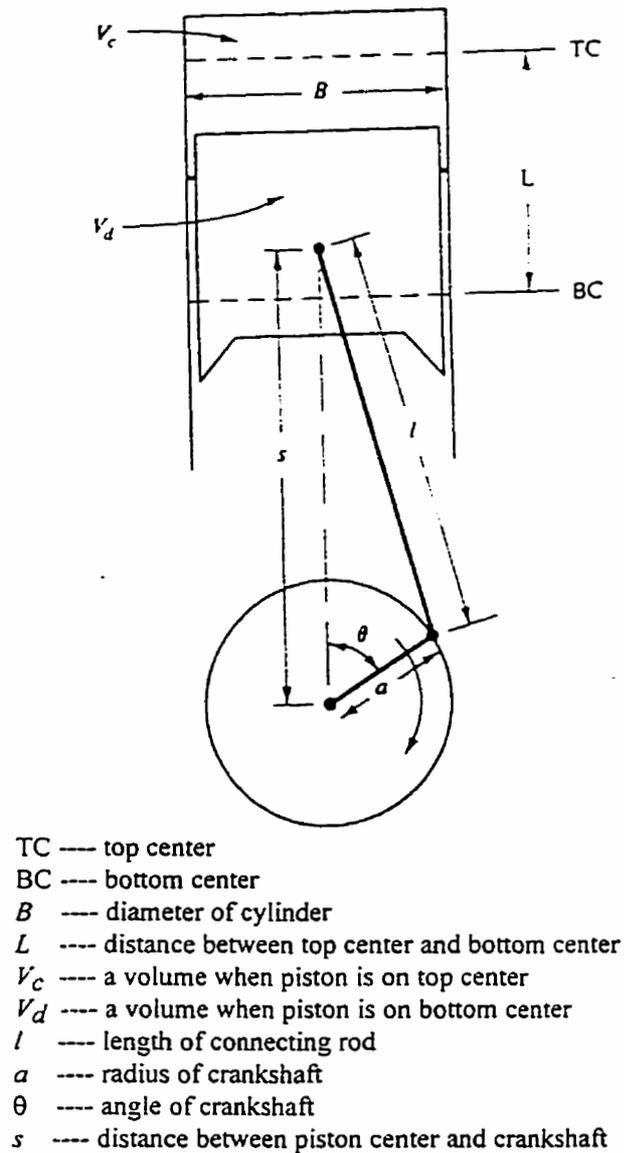
Figure 2.2: Geometry of cylinder, piston and crankshaft,

In production diesel engines, fuel is injected in advance of TDC (e.g., -10^0) to accommodate the autoignition delay time of diesel fuel while attempting to realize an ideal diesel cycle (see Figure 2.3). Knowledge of the autoignition delay time is therefore an important factor in DI engine operation.
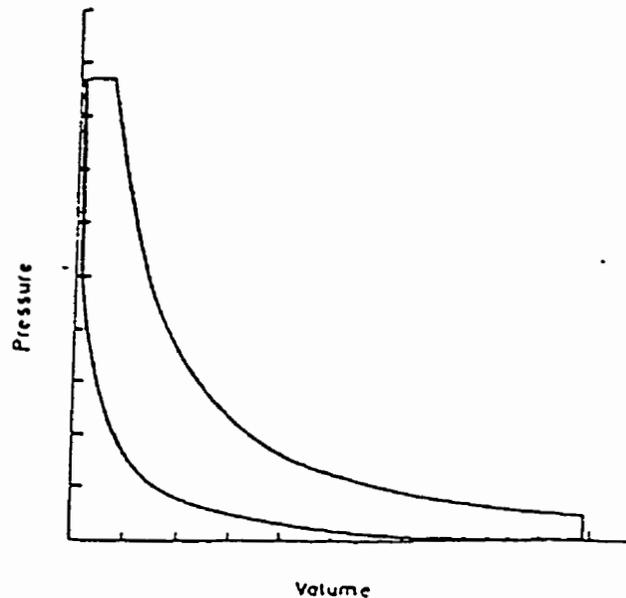
Figure 2.3:   Ideal dual combustion cycle.

Figure 2.4 shows the variation of thermodynamic work corresponding to three advanced injection angles on a P - V process diagram for a two-stroke engine. Comparing the areas of the enclosed curves shown in Figure 2.4 it is seen that there is an optimum injection angle that yields the greatest thermodynamic work (i.e., maximum area), and thus,
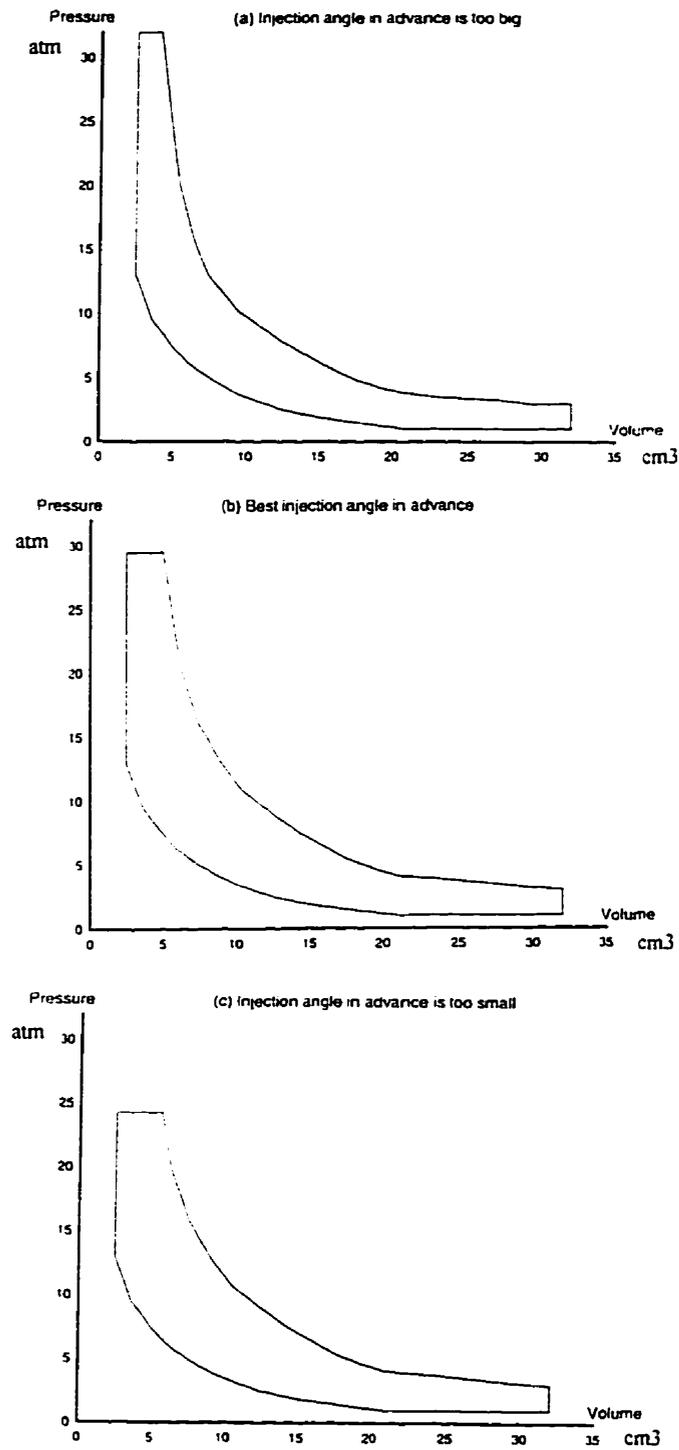
Figure 2.4: Thermodynamic work for a two-stroke engine [Benson, 1979]
Larger diesel cycle enclosed area corresponds to greater
engine combustion efficiency.

highest efficiency (all other parameters constant) in a given engine cycle. In particular, when the advance injection angle is too small, the combustion process does not occur at the highest pressures possible resulting in reduced power and efficiency. Alternatively, when the advance injection angle is too early (e.g., -20^0) more work is needed for compression which in turn lowers efficiency [Benson, 1979; Heywood, 1988; Weaving, 1990; Whitelaw, 1988].

A heavily delayed (e.g., positive angle) injection or flame quenching by the chamber wall will both increase pollutant emissions because of incomplete fuel combustion. The latter effect, flame quenching by chamber walls, reveals a need to control in-cylinder-fluid flow in order to control autoignition and subsequent flame locations. It will be found that the high-pressure natural gas injection jet in general dominates diesel engine chamber flows up to the time of autoignition. In summary, autoignition delay time and ignition location are critical parameters in establishing diesel engine timing and emission values, respectively.

2.3. Review of Experimental Work

The first study of the autoignition of methane[1]-oxygen mixtures in a shock tube was carried out by Skinner and Ruehrwein in 1959. Since then many investigators, such as Cooke and Williams [1975], Heffington *et al.* [1977], Tsuboi and Wagner [1975], Matula *et al.* [1973],

---

[1] Recall, natural gas is primarily methane. Commercial grade natural gas is nominally 93% methane.

Olson and Gardiner [1977], etc., have reported on methane-oxygen studies based on shock tube experiments. Shock tube studies provide aspects of premixed chemical reaction such as autoignition delay time, activation energy, temperature trends, pressure trends, and the effect of additives. Shock tube studies can also ascertain if the ignition processes of any two fuels are coupled to each other. Such studies are limited to the low pressures (typically 1-4 atm) and high temperatures (1300-2100 K) of shock tube data, however, they do not simulate the higher pressure, lower temperatures at fuel injection, inhomogeneous charge conditions, found in diesel engine combustion chambers. For example, in a real engine, fuel and air are still mixing when autoignition occurs in a turbulent flow that is highly multi-dimensional, not one-dimensional like shock tube studies. The only available data on the autoignition of natural gas under diesel like pressures and temperatures is that of Fraser *et al.* [1991] and Naber *et al.* [1994].

The objective of this section is to present the experimental work of Fraser *et al.* [1991] and Naber *et al.* [1994]. These experiments form the foundation for this work, i.e., they provide experimental data with which the modelling work will ultimately be compared in an attempt to validate the overall code.

An experiment into the autoignition of methane and natural gas in a simulated diesel engine environment was first reported by Fraser *et al.* [1991]. Fraser *et al.*'s experiment simulates a diesel engine combustion chamber by injecting fuel into a diesel engine size, pancake shape, combustion vessel at in-cylinder diesel engine like temperatures and pressures. Turbulence levels of diesel engines are not simulated in an attempt to provide easier to simulate data and hence, hopefully, the physics of kinetics and mixing can more easily be extracted. In effect Fraser *et al.*'s experiment decouples

the effects of natural gas injection and the strong turbulent fluid flow created by piston movement. The experiments yield autoignition properties in a field of non-uniform fuel/air mixture and include the injection process. They also examine the influence of additives on ignition delay times.

Naber *et al.*'s experiment is an extension of the earlier research by Fraser *et al.* Fraser *et al.* experimentally investigated the autoignition of simple methane and binary methane-ethane mixtures at lower ambient pressures (0.5 - 5.5 Mpa) than Naber *et al.* Naber *et al.*'s work considers a broader range of thermodynamic conditions that include engine TDC conditions, realistic NG fuel compositions, and a fuel injector that is more characteristic of current DI NG engine development efforts. These more recent NG autoignition experiments also expand on the work of Fraser *et al.* in several ways: they investigate the effects of ambient densities (from 6.2 to 32.6 kg/m^3) for several natural gas compositions; they more clearly quantify the effects of pressure, density, and temperature; they attempt to investigate the interaction of stoichiometry and chemical kinetics at ignition; they assess the maximum reduction in ignition delay possible with increases in ethane, propane, and *n*-butane concentrations; and they assess the impact of the experimental technique themselves on the measured ignition delays.

A more detailed discussion of the experimental work done by Fraser *et al.* and Naber *et al.* will be given in the following sections. Present research focuses primarily on modelling the experiments of Fraser *et al.*

2.3.1 Experimental Procedure

The experiments of Fraser *et al.* were conducted in a constant-volume combustion vessel designed by Volkswagen Research in West Germany [Siebers, 1987]. Figure 2.5 shows a schematic cross-section of the combustion vessel used. The vessel has a pancake shaped
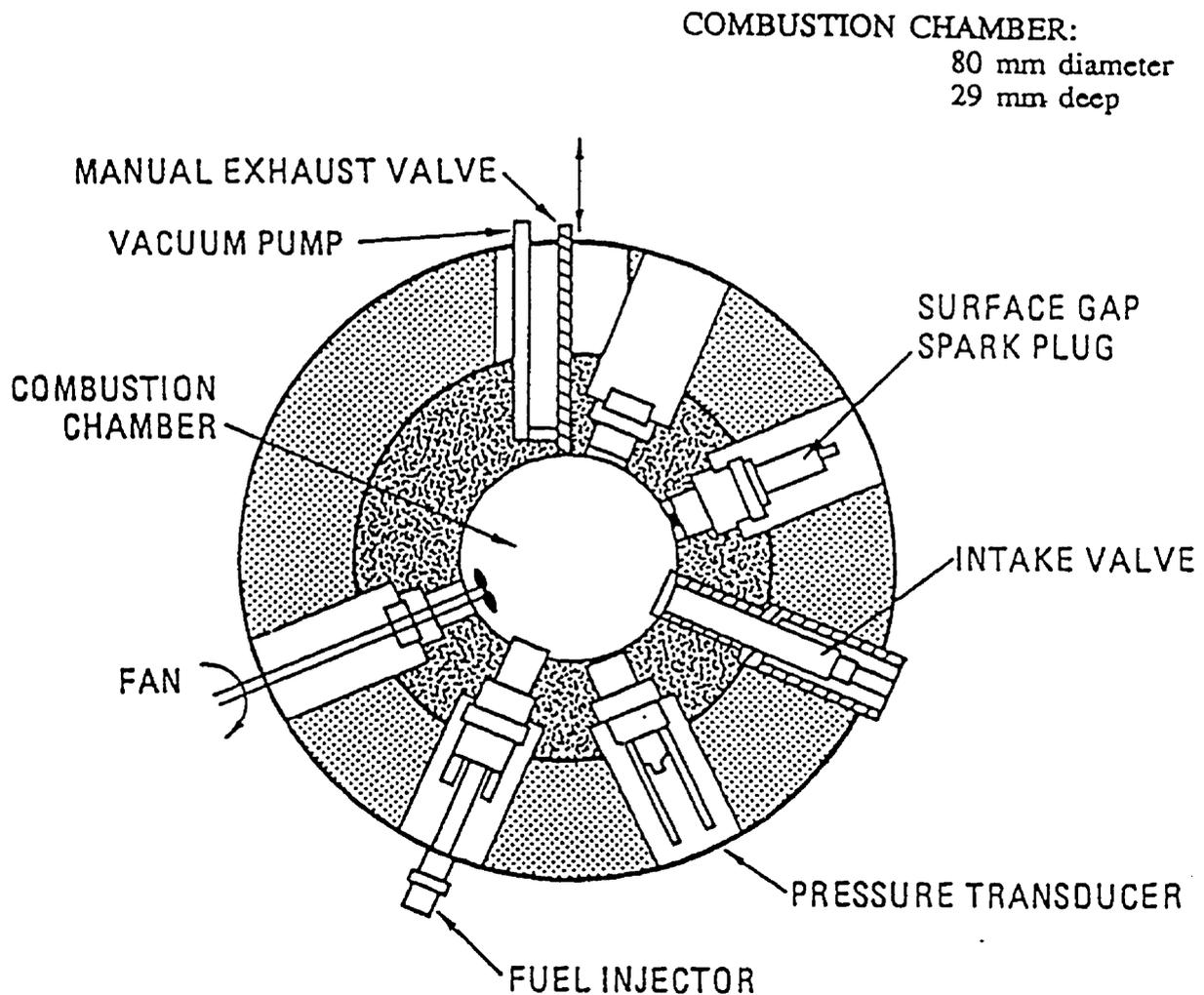
Figure 2.5: Constant-volume combustion vessel system used by Fraser et al. [1991].

combustion chamber 80 mm in diameter and 29 mm in deep and was designed for pressures up to 100 atm. Naber *et al.*'s [1994] experimental vessel was 114 mm in diameter and 28.6 mm in width and was designed to simply be an enlarged version of the Volkswagen combustion vessel that could withstand pressures up to 200 atm. Sapphire windows at each end of the vessel permit full field line-of-sight optical access to the chamber. As shown in Figure 2.5, there are five interchangeable access ports and one injector port on the circumference of the vessel (Naber *et al.*'s experiment has two injector ports). Mounted in the five interchangeable access ports are the following: two air operated valves, one for intake and another for exhaust; a surface gap spark plug; a pressure transducer; and a mixing fan. The mixing fan maintains a homogeneous temperature throughout the combustion vessel. The introduced turbulence is much lower than that found in diesel engines. Walls are kept at a realistic 444 K.

A two step combustion process is used to simulate quiescent diesel TDC combustion processes in the constant-volume combustion vessel. The first step is to generate a high-pressure, high-temperature environment by the spark ignition and combustion of a precharge lean premixed combustible gas mixture. When the products of this first combustion event cool from their high temperature to a preselected pressure and temperature state, the fuel injector is fired. Obtainable pressure-temperature states for injection are pre-determined by the pre-charge pressure. The ensuing fuel jet autoignites and burns as it would in a diesel engine. The experimental model thus simulates a practical diesel engine environment, less the cylinder turbulence, by using precharging to establish the temperature and pressure conditions at the time of natural gas injection. The entire process is computer controlled.

2.3.1.1 Precharging

Each experiment begins by evacuating, via a vacuum pump, the combustion vessel. It is then filled with the precharge gas mixture of hydrogen-ethylene-oxygen-nitrogen (see Table 2.1) [Fraser *et al.*, 1991]. At the desired pressure, the intake valve is closed. After filling, the pre-charge gases in the vessel are at a uniform and known temperature, i.e., the wall temperature, 444 K. Accurate determination of the gas density can therefore be made from the ideal gas law using the fill pressure, the wall temperature, and the known premixed gas composition and hence molecular weight. This premixed charge is then spark ignited and burned yielding a high temperature, high pressure, pre-injection environment within the combustion vessel. (Naber *et al.*'s experiment shows that the premixed burn reaches a peak pressure of 10.4 Mpa and a mass average bulk gas temperature of 1800 K). The product environment is compositionally similar to air (i.e., 21 % O_2, 79 % inerts, primarily N_2 , see Table 2.1).

The combustion-vessel mixing fan runs throughout the entire event. The function of the fan is three fold: (a) to keep the temperature uniform during the premixed gas fill process, (b) to increase the flame speed during the premixed burn, and most important, (c) to keep the temperature in the vessel uniform after the premixed burn up to the point of the natural gas injection event. Without the mixing fan the lean premixed burn will take several hundred milliseconds, and after the burn, severe temperature in-homogeneity exists as a result of vertical thermal stratification of the gas in the vessel.

Table 2.1. Predicted equilibrium combustion products for

a premixed charge of $C_2H_4/H_2/O_2/N_2$ / (Product species

with mole fractions less than 0.001 not listed)

Reactants		Products	
Pressure (atm)	10.6	Pressure (atm)	40.7
Temperature (K)	444	Temperature (K)	1146
Mol. Wt. (g/mol)	27.59	Mol. Wt. (g/mol)	28.43
Species (mole fraction)		Species (mole fraction)	
N_2	0.648	N_2	0.666
O_2	0.278	O_2	0.208
H_2	0.059	H_2O	0.092
C_2H_4	0.015	CO_2	0.031
		NO	0.003

2.3.1.2.   Natural Gas Injection

After the premixed burn local mean velocities range from 1.7 m/s directly in front of the fan

to approximately zero in the centers of the fan generated double vortices. A representative

mean and rms velocity are 0.9 m/s and 0.7 m/s, respectively. These measured velocities,

which are more than two orders of magnitude less than the gas jet velocity ($\approx$ 400 m/s) at

the injector orifice, indicate that the fluid motion created by the fan should have very little impact on the transient gas jet injection and natural gas combustion processes.

After the diesel environment is established, natural gas is injected through a solenoid actuated gas injector as shown in Figure 2.6 [Fraser *et al.*, 1991] (The injector used
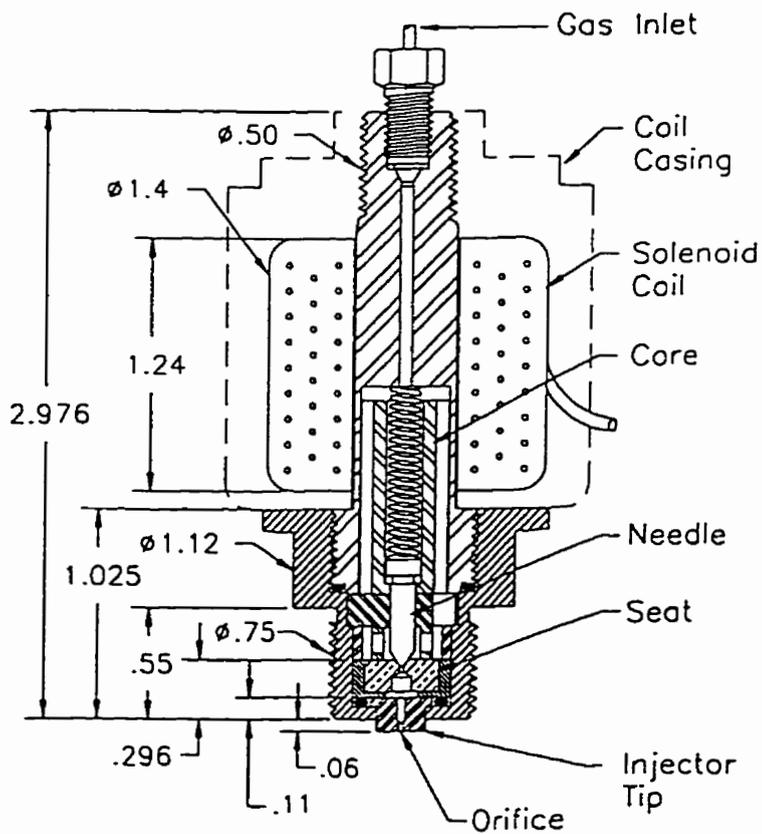
Figure 2.6:   Solenoid actuated gas injector

in Naber *et al.*'s experiment is different [Naber *et al.*, 1994].). This is a single shot, fast-acting, high pressure (gas inlet pressure: ≈3000 psia or 204 atm), gaseous fuel injector capable of injecting the required mass of fuel (i.e., 30 mg) in an acceptable time (i.e., 7 ms). The design of the gas injector is much more complex than that of a liquid injector due to the need for high pressure seals, the need for a source of high pressure gas, the limitation of short injection time, the minimum dead volume between injector tip and orifice, the structural integrity required for safety, etc.

For example, in real engines the injection time is around 3 to 4 ms. The solenoid gas injector could not satisfy this requirement because it took the solenoid spring and upstream gas pressure a minimum of 5 ms to move the needle and core back to the closed position. As another example, the solenoid actuated gas injector has a dead volume 0.025 cm^3. The dead volume generates an uncertainty in the initial composition of the fuel injected as it traps uncombusted gases from the pre-charging process. This initial fuel composition uncertainty is assumed negligible. The second effect of the dead volume is to create a lag between the start of injection and the time the fuel mixture actually enters the chamber volume, i.e., the dead volume gas is first compressed and then expelled into the combustion chamber. For injection times on the order of milliseconds the buffering action of the dead volume is considerable.

The injection system injects natural gas at a pressure about 200 atm into the combustion chamber pressures on the order of 25 atm through an orifice of diameter 0.57 mm and length 6.35 mm. The orifice is constructed as a convergent-divergent nozzle with the flow through the nozzle being underexpanded. A succession of expansion and compression waves occur outside the nozzle during steady state operation. However, when

the injection is unsteady an entirely different wave structure is observed as shown in Figure 2.7 [Nakahira, 1992].

The autoignition process in a diesel engine environment is an unsteady, compressible, turbulent fluid flow problem with chemical reactions. Integrating into a numerical model each of these complex physical phenomena is the challenge tackled in this work.
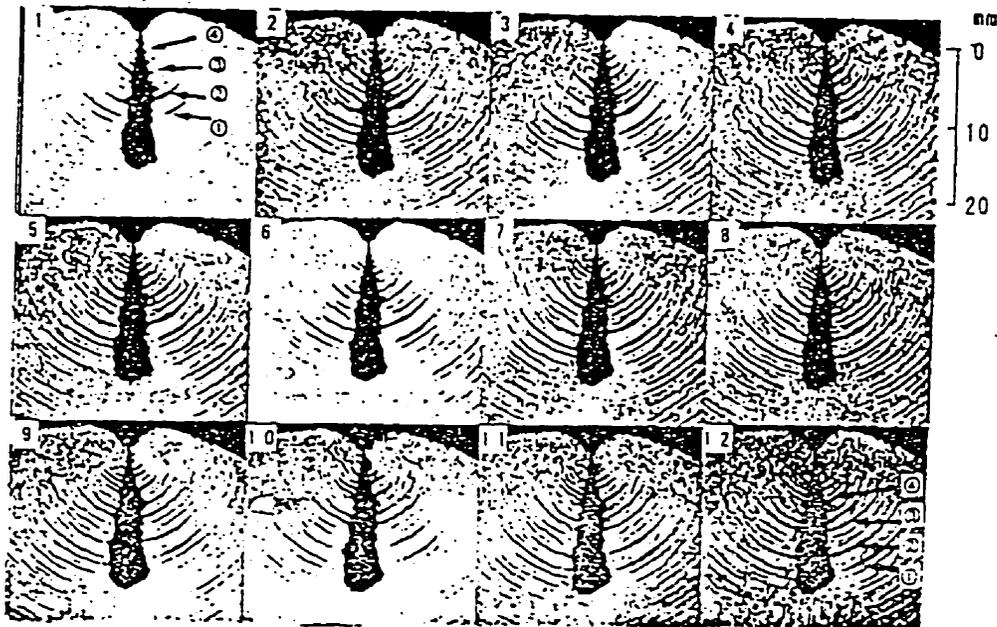
Figure 2.7: Framing photographs of the shock wave generation at the tip of the injection nozzle [Nakahira, 1992].

2.3.2. Autoignition Delay Time

Two ignition delay times are defined in Fraser *et al.* and Naber *et al.*'s experiments: the pressure delay time and the luminous delay time.

As its name suggests the pressure delay time is was determined from combustion vessel pressure measurements. The pressure delay is determined from data as exampled in Figure 2.8 which shows the net pressure-rise after injection versus time for four diesel
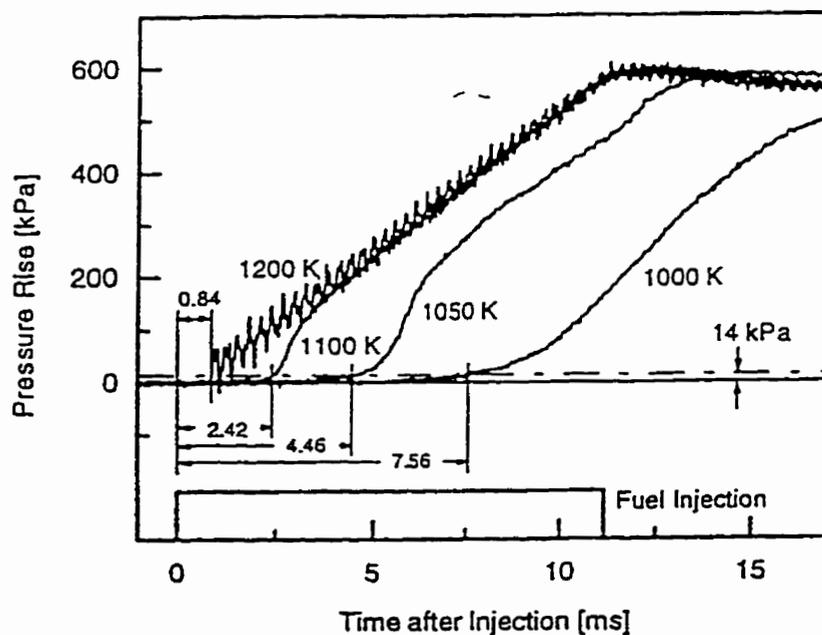
Figure 2.8: Pressure-rise from the direct-injection of natural gas and subsequent combustion [Naber et al., 1994].

burns. The net pressure-rise is the difference between the pressure measured during the diesel burn and the pressure determined by extrapolating the decaying pressure curve just prior to fuel injection[2]. Use of the net pressure-rise removes the pressure change resulting from heat loss to the chamber walls induced by the mixing fan fluid motion in the vessel, leaving only the pressure change caused by injection of the cold fuel, combustion, and additional heat losses caused by gas jet induced fluid motions after the injection.

The four net pressure-rise histories in Figure 2.8 from Naber *et al.* [1994] are for injections of mean natural gas into core temperatures of 1000, 1050, 1100, and 1200K at a density of 20.4 kg/m^3. For each injection event, 14.0 mgs of the mean natural gas mixture were injected through a 0.25 mm hole at an injection pressure of 20.7 MPa during an 11 ms period. The pressure delay is defined as the time from the start of injection to when the pressure-rise exceeds a set value. The set-value pressure-rise used is 14 kPa (0.25 atm in Fraser *et al.*'s experiment) which corresponds to a heat release from approximately 0.33 mg of fuel or 2.5 % of the total mass injected. The pressure delays using this definition for the four NG injections with core temperatures of 1000, 1050, 1100, and 1200 K are 7.56, 4.46, 2.42, and 0.84 ms, respectively.

The luminous delay time is defined as the time from injector opening until the first luminosity is sensed by a photodiode. Figure 2.9 shows consistency between delay times measured using pressure and luminosity for natural gas. Thus pressure delay times also mirror the chemical kinetics as indicated by the luminous delay in Fraser *et al.*'s and Naber *et al.*'s experiments. Only at the highest temperatures (shortest delay times, i.e., less than

---

[2] The extrapolation is based on the fit of pressure versus time just prior to fuel injection to a decaying exponential. Within the noise of the pressure measurements, the extrapolation is good for 10's of ms.

0.2 ms) does the luminous delay time tend to be smaller than the pressure delay time. It seems reasonable to expect this deviation at high temperatures where there is less fuel in the chamber at the time of autoignition. If the mass of injected fuel is insufficient to result in a 0.25 atm pressure rise corresponding to Fraser *et al.*'s set-value pressure then the measured autoignition pressured-delay time will be delayed until a sufficient mass of fuel has been
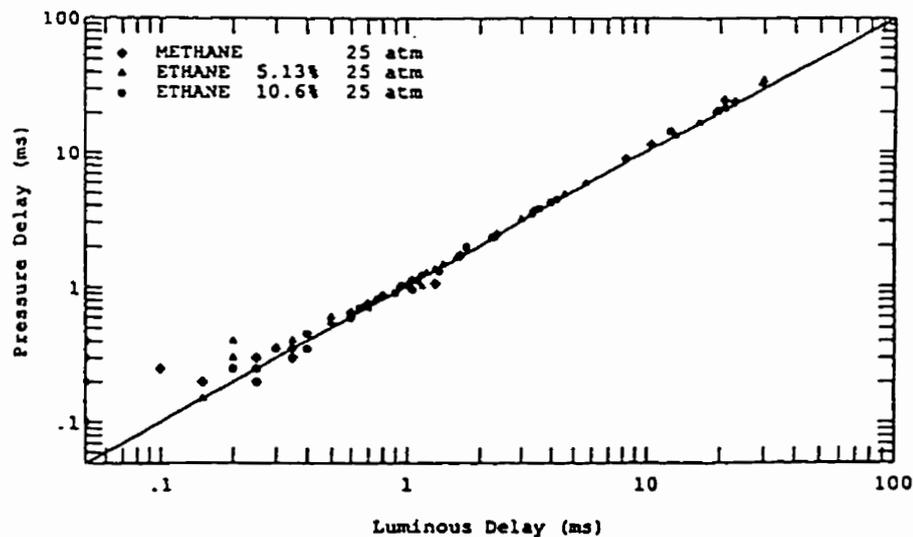
Figure 2.9: Correlation between the pressure and luminosity autoignition delay times for natural gas [Fraser et al., 1991].

injected and delayed with respect to the luminosity-delay time. In addition, the pressure sensor cannot be located exactly at the ignition site. This results in an additional time lag between ignition and detection. Pressure detection is limited by the speed of sound, while the luminosity delay is negligibly delayed by the speed of light. For example, the radius of the combustion vessel divided by the speed of sound yields an estimate for this delay

$$\tau = \frac{r}{\sqrt{\gamma RT}} = \frac{0.057m}{720m/s} = 0.08ms.$$

This 0.08 ms time delay is significant at higher autoignition temperatures (where, for example, autoignition delay times at 1400^0C are 0.3 - 0.4 ms).

The results for natural gas contrast with the results using liquid fuel such as methanol, ethanol, isooctane, and cetane [Siebers, 1987], where the luminous delay time is consistently smaller than the pressure delay time (see Figure 2.10) for delay times less than about 10 ms. One explanation is that the latent heat required to vaporize the liquid spray delays the observed liquid fuel pressure rise. This effect is not present with gaseous injection.

In modelling natural gas autoignition, the variables, such as pressure, temperature etc., will be assigned to the nodes of the mesh. There is no direct variable showing luminosity in the numerical study, but the local temperature should approximate the luminosity delay as the luminosity is temperature dependent. Consequently, it is expected that a temperature delay time should follow the pressure delay time in a fashion similar to the luminosity delay time as shown in Figure 2.9.
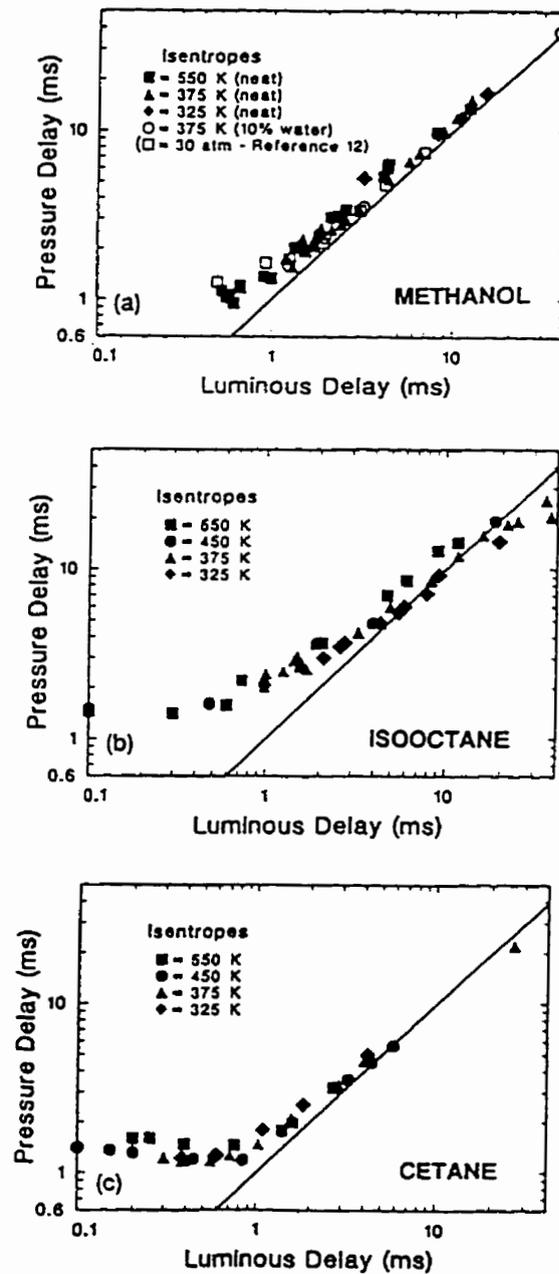
Figure 2.10: Correlation between the pressure and luminosity autoignition delay times for (a) methanol, (b) isooctane, and (c) cetane [Siebers, 1987].

2.3.3. Autoignition Characteristics

The autoignition characteristics of natural gas are significantly different from that of diesel fuel. Figure 2.10 shows the temperature-pressure domain characteristics of natural gas autoignition [Fraser *et al.*, 1991]. Similar plots reported by Sieber and Edwards [1987] for methanol, ethanol, isooctane, and cetane are shown in Figure 2.11. The conditions for which the fuels could not be ignited are indicated by cross-hatching. For the natural gas fuel blends tested (methane and ethane mixture), the autoignition region extends above temperatures of 1000 K. Furthermore, the lower the ethane concentration, the higher the minimum temperature for autoignition. As a pragmatic guideline, autoignition delay times for a practical diesel engine are 2 ms or less. The natural gas two millisecond boundaries correspond to approximately horizontal lines with respect to pressure at temperatures of 1250 K, 1225 K, and 1200 K for ethane concentrations of 0 %, 5.13 %, and 10.6 %, respectively. As with the no-ignition boundaries, the 2 ms boundaries also correlate lower ethane concentration fuel blends with the higher autoignition temperatures. To achieve the aforementioned temperatures at TDC in a naturally-aspirated diesel engine with a bottom-dead-centre (BDC) temperature of 325 K would require compression ratios in excess of 29:1, 27:1, and 26:1, respectively, assuming isentropic compression. These compression ratio estimates are a lower limit to what is needed by a real engine without ignition assist since ideal compression is assumed, the injection event is of finite duration while the TDC temperature (which corresponds to the peak cylinder temperature for non-reactive compression) occurs only for an instant, and it is common to displace the injection event from TDC to control power and emissions. Also, these high compression ratios are
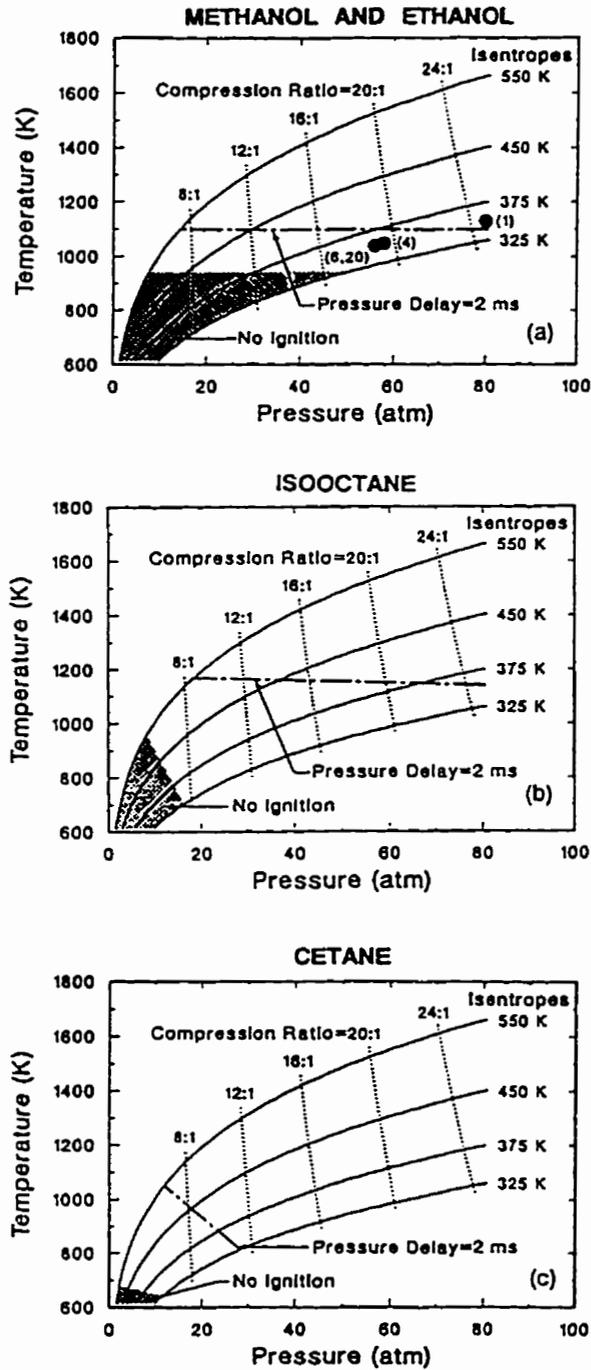
Figure 2.11: Temperature and pressure autoignition regimes for (a) methanol and ethanol, (b) isooctane, and (c) cetane [Siebers, 1987].

impractical because of efficiency killing friction from tighter piston ring sealing. Therefore, the use of natural gas as a diesel fuel that depends solely on compression for ignition appears impractical. Undoubtedly, some ignition assist will be required. For example, dual-fuel injection, suitable additive(s), or the use of exhaust gas recirculation (EGR) are possibilities.

2.4. Review of Natural Gas Autoignition Modelling Work

The first study of the autoignition of methane-oxygen mixtures in a shock tube was carried out by Skinner and Ruehrwein [1959]. Since then many investigators, such as Cooke and Williams [1971, 1975], Heffington *et al.* [1977], Tsuboi and Wagner [1975], Matula *et al.* [1973], Olson and Gardiner [1977], Westbrook *et al.* [1977, 1979] and etc., have reported many studies in the literature based on shock tubes. The chemical reaction behind the shock is in general the focus of these works. A typical experiment has a shock sweeping through a premixed, stoichmetric, gas mixture which may or may not lead to ignition. The delay time is calculated from the time of shock sweeping to the time ignition appears. Modelling efforts on shock initiated ignition typically report autoignition delay times based on temperature. Because flame propagation speed is much less than shock wave speed, the influence of upstream reactions on the down stream is ignored.

In 1994, Naber *et al.* assumed a constant volume combustion vessel in numerical calculations that utilized the approach used by Westbrook and Pitz [1986, 1987] to

determine induction times. Naber *et al.* characterized the temperatures and pressures that result in autoignition for natural gas/air mixtures. The constant volume combustion vessel assumption effectively views the combustion vessel as a continuously stirred constant volume reactor. These computations start with a stoichiometric fuel/oxidizer mixture at a given initial temperature and pressure. Initial mixture temperature is deduced assuming constant-pressure, adiabatic mixing of fuel and oxidizer where the initial fuel temperature differs from the initial oxidizer temperature. The initial oxidizer temperature is the combustion vessel's core temperature. Initial oxidizer species concentrations at the start of the induction time calculation are determined by following the same pressure-temperature decay observed in the experiments from the end of the premixed burn to the start of injection. The pressure-temperature decay in the model is matched to the experiment by adjusting a heat transfer term in the model. All species concentrations (e.g., H_2O, CO_2, OH, CO, etc.) during the simulated temperature decay are predicted to be near equilibrium.

Two typical induction time calculations from Naber *et al.* are shown in Figure 2.12. They are for oxidizer temperatures of 950 and 1000 K and a natural gas fuel temperature of 450 K, which for an equivalence ratio of 1.0 results in mixture temperatures of 890 and 920 K, respectively. Plotted is the mixture temperature versus time from the start of the computation. The lower temperature case does not ignite while the higher temperature one does. In the igniting case, the temperature initially begins to decrease due to heat loss to the vessel walls. It then rises as ignition begins, slowly at first, then very rapidly. The predicted induction time, defined as the time at which the steep temperature rise occurs, is 24.7 ms for this case.
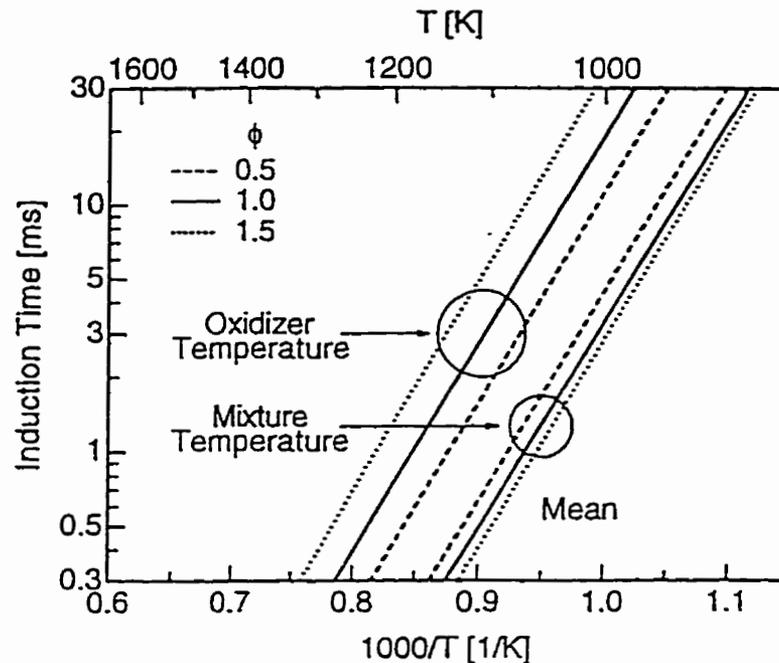
Figure 2.12: Predicted induction times of the mean NG fuel [Naber et al., 1994].

In 1997, Agarwal and Assanis numerically investigated the effect of natural gas composition on ignition delay by using both detailed and reduced chemical kinetic mechanisms under a closer diesel engine environment [Agarwal and Assanis, 1997]. Their results reveal a strong dependence of ignition delay on natural gas composition, with pure methane having the highest delay, followed by blends with increasing percentages of higher hydrocarbons.

Natural gas autoignition numerical modelling, whether in shock tubes or in Naber *et al.*'s combustion vessel, does not involve much of the physics associated with the direct injection of natural gas in a diesel engine. In particular, the effects of injection, mixing, and pressure wave propagation on the ignition process are ignored. These

previous autoignition models mainly focus on detailed chemical kinetic mechanisms (or chemical ignition delay) rather than fluid flow, turbulent mixing, and convective heat transfer. These models will hence forth be referred to as chemical kinetic based models. Many investigators, especially Westbrook *et al.* [1977, 1979, 1981, 1987], use a chemical kinetic based model to estimate ignition and knock. Recently, very detailed kinetics have been developed to describe the reactions of specific hydrocarbon fuels both in low and intermediate temperature ranges (i.e., < *1000 K*) [Refael, 1989, Sloane, 1989] as well as for higher temperatures [Bilger, 1990, Peters, 1987]. Good low and intermediate temperature range kinetics are critical for accurate autoignition predictions. In *1987* Westbrook and Pitz modeled the chemical kinetics of hydrocarbon autoignition computing the autoignition delay time of selected fuel-air mixtures under conditions similar to those found in internal combustion engines. These autoignition delay time computations assessed the influence of initial pressure, temperature, and fuel composition (*i.e.*, the ratio of methane to ethane). Although the model employs one of the most complete chemical kinetic reaction mechanisms available, to admit a numerical solution, they still must make many major assumptions as follows:

(1)   uniform premixed fuel-air mixture in the entire volume at the initial state,

(2)   constant volume (reaction during the compression stroke of an engine is assumed to be negligible),

(3)   no viscous fluid flow action,

(4)   no convection heat transfer, and

(5)   no turbulence action.

With these assumptions the model has not been very successful in predicting observed engine ignition, especially in a compression-ignition engine. However, it has predicted observed autoignition delay time and engine knock trends fairly well for changes in fuel composition, pressure, and temperature.

With the development of high speed computers, approaches that include fluid flow will be possible providing better predictions of the compression-ignition characteristics of natural gas. This thesis is one such attempt to include fluid flow with ignition chemistry.

Typical internal combustion engine flows are complicated by their inherent three dimensionality. In addition, no unified models exist that consistently represent realistic turbulent combustion. Many researchers [Dwyer, 1983, Jeske, 1992, Jones, 1982, Peters, 1987, etc.] have worked on multidimensional modelling of gas or natural gas flow and combustion in internal combustion engine cylinders. The chemical kinetic/fluid flow interaction modelling was limited by computational speed and computer memory. Dwyer [1983] modeled the spark-ignition and flame propagation with adaptive numerical grids; Jeske [1992] modeled the natural gas injection process in a two-stroke diesel engine without reaction processes; Jones [1980] modeled the reacting turbulent flows in gas-turbine combustion chambers without considering the ignition process; Peters [1987] computed stretched laminar methane-air diffusion flames using a reduced four-step mechanism; Kono *et al.* [1987, 1990] developed a two-dimensional computational model for analysis of the ignition mechanism of premixed charge by short duration sparks; and Mantel [1991] extended Kono's study to three dimensions. Recently Kong, Ayoub, and Reitz [1992] modeled combustion in compression-ignition homogeneous charge engines

by using KIVA, a code from Los Alamos [Amsden, 1985]. Belardini, Bertoli, Corcione, and Valentino used the second version of KIVA to perform numerical computations of combustion systems. Kuo and Reitz [1992] calculated combustion and flow in a premixed charge, direct injection, two-stroke engines using a laminar and turbulent characteristic-time combustion submodel, again using KIVA. The direct modelling of natural gas injection autoignition process in diesel engine environment by other researchers has not been found in the public literature except that of Ouellette and Hill [1995], who are using KIVA too and a steady state injection boundary condition, as well as Papageorgakis *et al* [1996], who are using a single step global mechanism to simulate methane combustion, and implementing methane injection and glow plug ignition models in KIVA-3 code. Papageorgakis *et al*'s parametric studies of injector hole orientation and number of holes indicate that an optimum injection strategy is important in ensuring desirable fuel-air mixing and combustion. The focus of this thesis is the study of natural gas injection autoignition in diesel engine environments. Zhang *et al.* [1994] is based on this work and represents the first detailed study of the natural gas injection process into a diesel engine type environment.

2.5 Closure

This chapter had three major focuses: diesel engine operation, review of natural gas experimental work, and review of natural gas numerical modelling work as they pertain to autoignition. Heavily delayed injection, or flame quenching by the chamber wall, will both increase pollutant emission because of incomplete fuel combustion. Consequently,

autoignition delay time and location are critical parameters in establishing diesel engine timing and emission values, respectively.

The review of experimental work has revealed that the data of Fraser *et al.* and Naber *et al.* are the only available results detailing the autoignition process of natural gas in diesel engines. Fraser *et al.*'s experiment decouples the effects of natural gas injection and the strong turbulent fluid flow created by piston movement. The experiment yields autoignition properties in a field of inhomogeneous fuel/air mixture, includes the injection process, and spans diesel engine type in-cylinder pressure and temperature. Naber *et al.*'s work considers a broader range of thermodynamic conditions that include engine TDC conditions, realistic natural gas fuel compositions, and a fuel injector that is more characteristic of current DI natural gas engine development efforts.

Finally, a review of previous modelling attempts identifies little success in predicting, from fundamentals, engine ignition, particularly in a compression-ignition engine. An autoignition numerical study that more closely reflects diesel engine flow, geometry, temperature, and pressure conditions is necessary. The present study detailed in this thesis includes the interaction of fluid flow and chemical kinetics as well as ignition delay and ignition location versus fluid flow feature for the autoignition of natural gas under diesel engine type conditions.

Chapter 3.

Modeling Natural Gas Autoignition

3.1. Overview

This chapter presents the mathematical models used in the solution of the natural gas autoignition in diesel engine geometry. The mathematical models involve the governing equations for mass, momentum, and energy, the turbulence model, and the reaction mechanism.

Fundamental assumptions are given. A compressible flow form of the k-ε turbulence equations in conjunction with the governing equations is described and the corresponding model constants are chosen. This k-ε model is a special turbulence model which has been specifically designed for and used by engine fluid flow modelling. A two-step Arrhennius, five-species reaction model for natural gas oxidation is implemented to model the natural gas autoignition process. Finally the initial and boundary conditions are detailed.

3.2. Fundamental Assumptions

The process of natural gas autoignition in diesel engines is very complicated and the selection of designs large. The assumptions described herein make the problem tractable.

Combustion chamber geometry can be U-type, ω-type, etc. [Benson, 1979]. For high speed, low power diesel engines, a duel combustion chamber (or vortex flow combustion chamber) is usually utilized for efficiency and emission reduction purposes [Benson, 1979]. Injector location and injection direction are varied to match a given combustion chamber geometry. Injector location and injection direction are selected to minimize injecting fuel onto a cold cylinder wall or piston top. since this can lead to incomplete combustion. For example, the ω-type combustion chamber requires that the injector be located top center with multi-holes [Benson, 1979]; the U-type combustion chamber has a side-located injector [Benson, 1979]; and the duel combustion chamber needs the injector located on the circumference of the vortex flow combustion chamber instead of in the main combustion chamber.

During the compression stroke, piston movement drives the in-cylinder turbulent flow. The intensity and the appearance of in-cylinder turbulent flow depends on the intake port geometry, the speed of piston movement, and the geometry of combustion chamber(s). Strong turbulent fluid flow may affect the process of natural gas autoignition through its effect on mixing. The presence of a strong turbulent flow severely complicates any modelling effort. In order to decouple in-cylinder turbulence effects on natural gas autoignition this study merely focuses on the effects of natural gas injection on autoignition. That is, the injection process is assumed to dominate the mixing process.

This is consistent with the work of Fraser et al. and Naber et al. whose experimental data will be used to validate this modelling effort. Also consistent with the experiments a low level initial condition turbulence intensity will exist in the combustion chamber when modelling.

Injector design can strongly affect the injection process. The magnitude of the dead volume of the injector causes the different injection distances in time. Diesel injectors usually have multi-holes injection structure. The natural gas injector of Fraser et al. and Naber et al., however, have used a single -hole injection. For both structures, manufacturers try to make the dead volume as small as possible. The reason is that the dead volume makes the smooth change of fuel injection rate at the period of starting and ending injection. When the needle of the injector lifts to inject fuel, the dead volume buffers fuel injection immediately to reach maximum fuel injection rate and when the needle starts to close, the high pressure in the dead volume makes a later fuel injection for a certain time period. The later fuel injection rate comparing with normal fuel injection rate is lower. Much more fuel is located around injector tip and is burnt incompletely due to rich fuel in this area. The incomplete burn causes high temperature at injector tip and HC accumulation on injector tip and also in dead volume. The dead volume geometry made from manufacturing is complicated in structure. Only does the magnitude of the dead volume of injector have influence on fuel injection. Therefore it is not necessary to model the complicated dead volume geometry. A pipe with same volume as the dead volume is assumed for the computational model.

The needle valve volume has a structure (see Figure 2.6). The various structures of the needle valve volumes may not produce big difference in fuel injection as long as

they have similar volume in which the pressure decreasing is not very much at the fuel injection period. According to above point of view, two approximations can be made for computational model. The one is assuming a constant pressure behind the needle of injector during the fuel injection process. The approximation has the weakness of determining fuel velocity distribution cross the needle. The other is making a big volume cylinder which is long enough to prevent expansion wave from reaching the end of the cylinder during fuel injection process. Therefore a wall boundary conditions or a Neumann boundary conditions of pressure and velocity can be assumed at the end of this cylinder.

It is possible to simulate injector needle lift and closing spring force, needle mass, needle geometry, flow about the needle, and the pressure forces across the needle. The present study, however, does not include a detailed model of needle opening or closing movement for the following two reasons:

(1) Determining the flow about the needle and the instantaneous pressure about the needle would require computational resources (e.g., memory and speed) not available given the focus on the natural gas autoignition process.

(2) The flow through the injector orifice quickly becomes choked [Fraser et al.] and hence quickly becomes the fuel flow rate determining factor, not the needle dynamics.

In the experiments of Fraser et al. [1991] and Naber et al. [1994] the injector was situated to maximize the time before the injected natural gas jet struck the cylinder wall. In fact, once the jet hits the wall Fraser et al. and Naber et al. observed wide fluctuations in autoignition times which led them to reject this data as corrupted by wall/jet interaction effects. As seen in Figure 2.5 this results in a 3-dimensional flow problem. In this work

the combustion chamber is assumed cylindrical but with the injection along the cylinder's axis (see Figure 2.5). The problem then reduces to a more manageable axisymmetric one. In essence, it is assumed that the wall effects are negligible in the natural gas jet dominated flow. This is consistent with Fraser et al.'s and Naber et al.'s rejection of wall affected data.

Liss *et al.* [1992] observed that the composition of commercially available natural gas under normal delivery practices varies widely across the north America with extremes of *75-98%* for methane, *0.5-13%* for ethane, and *0-2.6%* for propane. For propane/air peak shaving practices, they found that the composition variations could be even more extreme with methane concentrations as low as *56%* and propane concentration as high as *24%*. The study of natural gas autoignition in diesel engines with various composition of natural gas needs to employ a detailed chemical kinetic model. The computational fluid dynamics study of the natural gas injection process with a detailed chemical kinetic model is currently impractical due to computational time and computer memory limitations. For this study, a global reaction model is therefore used in the modelling of natural gas autoignition. The present work assumes *100%* methane for natural gas.

The heat conduction from the combustion chamber boundary during natural gas injection and autoignition period can be estimated. The metal of the combustion chamber wall has a conductivity higher than that of the gas. Therefore, it is reasonable to assume a uniform wall temperature. However, this wall temperature is in general unknown. If the cylinder could be assumed adiabatic it would greatly aid in establishing appropriate boundary conditions. Consider Naber et al.'s experiment [1994]. The pressure history just after premixed combustion reaches a peak of 4.2 Mpa. The pressure decreases due to

a temperature decrease from heat loss to the chamber walls. Let us estimate the pressure reduction by heat transfer through combustion boundaries in a 7 ms natural gas injection period. The chamber completely cools in about 0.225 s. A linear approximation yields

$$dp = 4.2 \ Mpa \times \frac{0.007s}{0.255s} = 0.115 \ Mpa.$$

Suppose that at injection, the combustion chamber pressure and temperature are 6 Mpa and 1200 K, respectively, and if the effect of injecting a small, but finite, mass of natural gas is neglected, a constant density cooling process results that follows

$$\frac{p}{T} = Const.$$

Differentiating and rearranging a percentage form of this expression is obtained.

$$\frac{dT}{T} = \frac{dp}{p}.$$

Consequently, a temperature reduction of only 2 % is experienced during a 7 ms injector period. Further, since pragmatic autoignition delays are around 2 ms or less the temperature variation in the combustion chamber is only 0.6 % before autoignition. Therefore an adiabatic combustion vessel can be assumed.

Again, consistent with the experiments of Fraser et al. [1991] and Naber et al. [1994] a uniform thermal environment is initially assumed. Naber et al. and Fraser et al. maintained a uniform temperature using a small fan. Temperature measurements made with fine wire (0.25 μm) platinum/platinum-rhodium thermocouples show in Naber et al.'s experiment that in the core region of the combustion vessel (defined as the inner 90 % of the vessel volume) a temperature uniformity of ± 2 % is observed. The rms temperature fluctuation is ± 6 % of the temperature difference between the core gas and the wall. The remaining outer 10 % of the vessel volume is occupied by a 1-2 mm thick wall boundary layer with steep temperature gradients. Therefore, a uniform thermal environment within the combustion chamber before natural gas injection is a reasonable assumption.

Radiation heat transfer is not significant because the gas radiation is mainly influenced by carbon oxide CO_2 and water steam H_2O which do not exist in large quantities prior to ignition. Also, it is well known that the intensity of radiation heat transfer is a function of temperature. Before ignition, local gas temperature differences are not high and thus yield little radiation heat transfer. At ignition high temperature differences (e.g., $> 1000^0$ C) do appear however this numerical study stops as soon as ignition starts. That is, the autoignition event is modelled but not subsequent combustion and flame propagation. Therefore, radiation heat transfer is assumed negligible.

The natural gas fuel, air, and their combustion products are all assumed to behave as ideal gases with temperature varying specific heats. This is reasonable given compressibility factors of $Z = 1.03$, 1.06, 1.09, respectively, being so nearly equal 1.0.

External body forces are not significant. From the experiment the mixing fan removes buoyancy effects. Furthermore, the high pressure injection jet dominates the fluid flow and pressure distribution inside the combustion chamber.

In addition Fick's law is usually applied for species diffusion and written

$$Y_k U_{d,k,i} = -D_k \frac{\partial Y_k}{\partial x_i} = -D \frac{\partial Y_k}{\partial x_i} \tag{3.1}$$

where the D is independent of species. It can be written as

$$D = \frac{\mu_{eff}}{\rho S_c}$$

where S_c is Schmidt number (≈ 0.7), and μ_{eff} the effective viscosity.

3.3. Governing Equations

The unsteady Reynolds time-averaged compressible turbulent equations expressed in conservative form are considered. The conservation equations are those of mass, momentum, energy, and species. Due to the axisymmetry of the problem all equations are two-dimensional. Mean flow properties are denoted without an overbar for equation

simplicity e.g., u_x, not $\overline{u_x}$. The differential equations representing mass, momentum, energy, and species conservation under Cartesian frame are then

Mass:

$$\frac{\partial \rho}{\partial t} + \left[\frac{\partial}{\partial x} \left(\rho u_x \right) + \frac{\partial}{\partial y} \left(\rho u_y \right) \right] = 0 \qquad (3.2)$$

Momentum:

$$\frac{\partial}{\partial t} \left(\rho u_x \right) + \left[\frac{\partial}{\partial x} \left(\rho u_x^2 \right) + \frac{\partial}{\partial y} \left(\rho u_x u_y \right) \right] + \frac{\partial p}{\partial x} - \left[\frac{\partial}{\partial x} \left(2 \mu_{eff} \frac{\partial u_x}{\partial x} \right) \right.$$

$$\left. + \frac{\partial}{\partial x} \left(\mu_{eff} \frac{\partial u_y}{\partial x} + \mu_{eff} \frac{\partial u_x}{\partial y} \right) \right] = 0$$

$$(3.3)$$

$$\frac{\partial}{\partial t} \left(\rho u_y \right) + \left[\frac{\partial}{\partial x} \left(\rho u_y u_x \right) + \frac{\partial}{\partial y} \left(\rho u_y^2 \right) \right] + \frac{\partial p}{\partial y} - \left[\frac{\partial}{\partial x} \left(\mu_{eff} \frac{\partial u_y}{\partial x} + \mu_{eff} \frac{\partial u_x}{\partial y} \right) \right.$$

$$(3.4)$$

$$\left. + \frac{\partial}{\partial y} \left(2y \, \mu_{eff} \frac{\partial u_y}{\partial y} \right) \right] = 0$$

Energy:

$$\frac{\partial}{\partial t}\left(\rho E\right) + \frac{\partial}{\partial x}\left[\left(\rho E + p\right)u_x - \mu_{eff}\left(2u_x\frac{\partial u_x}{\partial x} + u_y\frac{\partial u_y}{\partial x} + u_y\frac{\partial u_x}{\partial y}\right)\right.$$

$$\left.-\frac{c_p\mu_{eff}}{\sigma_t}\frac{\partial T}{\partial x}\right] + \frac{\partial}{\partial y}\left[\left(\rho E + p\right)u_y - \mu_{eff}\left(u_x\frac{\partial u_y}{\partial x} + u_x\frac{\partial u_x}{\partial y}\right.\right. \tag{3.5}$$

$$\left.\left.+2u_y\frac{\partial u_y}{\partial y}\right) - \frac{c_p\mu_{eff}}{\sigma_t}\frac{\partial T}{\partial y}\right] + \sum(h_k\omega_k) = 0$$

$$E \equiv e + \frac{1}{2}\,v\cdot v = c_v T + \frac{1}{2}\left(u_x^2 + u_y^2\right)$$

Fuel Mass Fraction:

$$\frac{\partial}{\partial t}\left(\rho Y_k\right) + \left[\frac{\partial}{\partial x}\left(\rho Y_k u_x\right) + \frac{\partial}{\partial y}\left(\rho Y_k u_y\right)\right] = \left[\frac{\partial}{\partial x}\left(\frac{\mu_{eff}}{S_C}\frac{\partial Y_k}{\partial x}\right)\right.$$

$$\left. + \frac{\partial}{\partial y}\left(\frac{\mu_{eff}}{S_C}\frac{\partial Y_k}{\partial y}\right)\right] + \omega_k \tag{3.6}$$

$$\nabla\cdot v \equiv \left[\frac{\partial}{\partial x}\left(u_x\right) + \frac{\partial}{\partial y}\left(u_y\right)\right];$$

$$\mu_{eff} \equiv \mu_t + \mu$$

respectively where the pressure, p, the velocities, u_x and u_y, the density, ρ, the temperature, T, and the mass fractions, Y_k, are the dependent variables. The fluid is assumed to be Newtonian and to obey Stokes' law. The effective viscosity is the addition of the turbulence viscosity and the molecular viscosity and the thermal conductivity is related to Prandtl number ($\sigma_t \approx 0.7$). In addition the fluid is assumed to be a calorically perfect gas which obeys the equation of state given by

$$p = \rho R T \qquad (3.7)$$

where R is the gas constant

$$R = \frac{\Re}{M}.$$

where

$\Re$ is the universal gas constant (= 8314.3 J/(kgmole•K), and

M is the molar mass (kg/kgmole).

The specific heat at constant volume can be obtained from specific heat at constant pressure and the gas constant as follows:

$$c_v = c_p - R,$$
$$c_p = \sum (Y_k c_{p,k}), \text{ and}$$
$$c_{p,k} = a_k + b_k T + c_k T^2 .$$

The above polynomial expression for $c_{p,k}$ is an approximate equation that fits experimental data over any fairly wide temperature range. The a_k, b_k, and c_k are experimentally determined coefficients. Table 3.1 [Reynolds, 1977] gives values for several gases. These equations fit the data with an average deviation of less than 1 percent and a maximum deviation of about 2 percent over the temperature range indicated.

Table 3.1 Mass specific heats at constant pressure for the ideal gas state
(300 to 1500 K) $c_p = a + b\,T + c\,T^2$ [adopted from Reynolds, 1977]

Gas	Formula	a (J/kg K)	b x 10^3(J/kg K^2)	c x 10^6(J/kg K^3)
Carbon dioxide	CO_2	591.2	989.04	- 339.26
Carb. monoxide	CO	959.8	871.21	- 29.302
Methane	CH_4	884.6	4720.8	- 1125.0
Nitrogen	N_2	975.2	186.88	- 0.1495
Oxygen	O_2	804.2	405.78	- 120.74
Water	H_2O	1687.4	534.41	65.813

The specific enthalpy (includes the chemical energy) of the kth component is denoted h_k. It can be expressed as

$$h_k = h_{0,k} + \int_{T_0}^{T} c_{p,k}\, dT \,,$$

where $h_{0,k}$ is the specific enthalpy of the kth component at an arbitrary temperature T_0. At the temperature of 298 K, specific enthalpy values are listed in Table 3.2 [Weast, 1969].

Table 3.2 Specific enthalpy at temperature of 298 K [Weast, 1969]

Gas	Formula	$h_{298\ K}$ (J/kg)
Carbon dioxide	CO_2	- 8.9478 x 10^6
Carbon monoxide	CO	- 3.9491 x 10^6
Methane	CH_4	- 4.6802 x 10^6
Oxygen	O_2	0.0
Water	H_2O	- 13.442 x 10^6

Therefore the energy-source term, $\Sigma\ h_k\ \omega_k$, due to chemical reaction can be expressed in terms of above approximate polynomial equations of specific heat $c_{p,k}$ as

$$\sum h_k \omega_k = \sum \left[\left(h_{0,k} + \int_{T_0}^{T} c_{p,k}\, dT \right) \omega_k \right]$$

$$= \sum \left\{ \left[h_{0,k} + \int_{T_0}^{T} (a_k + b_k\, T + c_k\, T^2)\, dT \right] \omega_k \right\}$$

$$= \sum \left\{ \left[h_{0,k} + a_k(T - T_0) + \frac{b_k}{2}(T^2 - T_0^2) + \frac{c_k}{3}(T^3 - T_0^3) \right] \omega_k \right\}$$

where $h_{0,k} = h_{298\ K,k}$ and $T_0 = 298$ K. The mass reaction rate, ω_k, will be discussed in Section 3.5.

3.4. Turbulence Model

The k - ε turbulence model used is based on El Tahry's [1983] modified version specifically designed for modelling piston driven internal combustion engines. The transport equation for k is then written as

$$\frac{\partial \rho k}{\partial t} + \frac{\partial \rho U_j k}{\partial x_j} = \frac{\partial}{\partial x_j}\left[\left(\frac{\mu_t}{\sigma_k} + \mu\right)\frac{\partial k}{\partial x_j}\right] - \overline{\rho u_i' u_j'}\frac{\partial U_i}{\partial x_j} - \rho \varepsilon \tag{3.8}$$

The ε-transport equation becomes

$$\begin{aligned}
\frac{\partial \rho \varepsilon}{\partial t} + \frac{\partial \rho U_j \varepsilon}{\partial x_j} &= \frac{\partial}{\partial x_j}\left[\left(\frac{\mu_t}{\sigma_\varepsilon} + \mu\right)\frac{\partial \varepsilon}{\partial x_j}\right] + \frac{\varepsilon}{k}C_1 \mu_t \frac{\partial U_i}{\partial x_j}\left(\frac{\partial U_i}{\partial x_j} + \frac{\partial U_j}{\partial x_i}\right) \\
&- \frac{2\varepsilon}{3k}\frac{\partial U_l}{\partial x_l}\left(C_1' \mu_t \frac{\partial U_k}{\partial x_k} + C_1'' \rho k\right) - C_2 \rho \frac{\varepsilon^2}{k} + C_3 \rho \varepsilon \frac{\partial U_l}{\partial x_l} + C_4 \frac{\rho \varepsilon}{\mu}\frac{\partial \mu}{\partial t}
\end{aligned} \tag{3.9}$$

the turbulent (or eddy) viscosity is given by

$$\mu_t = C_\mu \rho \frac{k^2}{\varepsilon}, \tag{3.10}$$

where the constants are assigned the following values

$$C_\mu = 0.09, \; C_l = 1.44, \; C_l^{'} = 1.44, \; C_l^{''} = 1.44, \; C_2 = 1.92, \; C_3 = -1/3, \; C_4 = 1$$
$$\sigma_k = 1.0, \; \sigma_\varepsilon = 1.30, \; \sigma_l = 0.7, \tag{3.11}$$

and the molecular viscosity is a function of temperature and is expressed by Sutherland formula

$$\mu = \frac{C_5 T^{1.5}}{T + C_6}$$

where $C_5 = 1.458 \times 10^{-6}$ kg/(m·s·K$^{0.5}$) and $C_6 = 110.4$ K. Therefore the derivative of molecular viscosity μ is given by

$$\frac{\partial \mu}{\partial t} = \frac{C_5}{2} T^{0.5} \frac{T + 3C_6}{(T + C_6)^2} \frac{\partial T}{\partial t} \;.$$

In spite of its high Reynolds number and jet flow limitations [Wilcox, 1989], the k - ε model is currently the most reasonable choice for most combustion flows because of its general acceptance by the engine community in light of there being no obviously better candidate [El. Tahry, 1983]. For the turbulent flux of scalar quantities a gradient diffusion model is used, viz.,

$$\overline{\rho u_j^{'} \phi^{'}} = -\frac{\mu_t}{\sigma_t} \frac{\partial \Phi}{\partial x_j}. \tag{3.12}$$

The reaction rates ω_i in equations (3.5) and (3.6) are a source of considerable difficulty, particularly when considering turbulent effects on the reaction rates ω_i. Suppose that the reaction rates ω_i are expressed in second order Arrhennius form, i.e.,

$$\omega_i = \frac{\rho^{a+b} M_i}{M_i^a M_j^b} Y_i^a Y_j^b A \exp\left(\frac{-E}{\Re T}\right) \tag{3.13}$$

where for discussion simplicity $a = b = 1$ is assumed. Here M_i is molecular weight of species i, A the frequency factor, E the activation energy for the reaction, and $\Re$ the universal gas constant. The mean rate expression is obtained by employing Reynolds decomposition of the terms into their mean and fluctuating components (e.g., $\overline{Y_i}$, Y_i'). expand the expression, and then average it. The result has the form [Bilger, 1976]

$$\overline{\omega_i} = \frac{\overline{\rho^2}}{\overline{M_i}} \overline{Y_i}\, \overline{Y_j} A \exp\left(\frac{-E}{\Re \widehat{T}}\right)$$

$$\left\{ 1 + \frac{\overline{\rho'^2}}{\overline{\rho}^2} + \frac{\overline{Y_i' Y_j'}}{\overline{Y_i Y_j}} + \frac{2\overline{\rho' Y_i'}}{\overline{\rho} \overline{Y_j}} + \frac{E}{\Re \widehat{T}}\left[\frac{\overline{Y_i' T'}}{\overline{Y_i T}} + \frac{\overline{Y_j' T'}}{\overline{Y_j T}} + \left(\frac{E}{2\Re \widehat{T}} - 1\right)\frac{\overline{T'^2}}{\overline{T^2}} \right] + \ldots \right\} \tag{3.14}$$

The continuation is for terms involving triple correlations of the form $\overline{Y_i' Y_j' T'}$, $\overline{Y_i' T'^2}$, etc. Equations can be derived for the double correlations, $\overline{Y_i' Y_j'}$, $\overline{Y_i' T'}$, etc. in terms of higher order correlations but the number of variables increase and the "closure" problem arises.

Do turbulent effects on the reaction rates ω_i need to be considered in the model? Before answering, consider the following two aspects of the problem. First, a major

effect in determining reaction rate is the temperature due to its pressure in the exponential factor of equation (3.14). Before ignition, the factor $\exp(-E/\Re\,\overline{T})$ is very small and results in a very small reaction rate $\overline{\omega}_i$. When ignition occurs, the temperature increases dramatically at any ignition location(s). However, this work is concerned only with reaction up to the time of ignition where the temperature is much lower than the temperature of diffusion flames. Second, the degree that such components affect the chemical reactions and heat release rate in a combustion system depends upon the relative characteristic times associated with each of the individual elements. The characteristic time of the chemical reactions before ignition is much longer than a characteristic time associated with the fluid-mechanical fluctuations. The fluid mechanics therefore has a major effect on the chemical reaction rate and energy release rates. Therefore it is not necessary to consider the turbulent effects of reaction rates ω_i in the study of natural gas autoignition.

3.5   Reaction Models

The combustion model must provide a method of evaluating the mean formation and destruction rate of each relevant species present. In addition it must admit the calculation of mean fluid temperature and density as well. Under ideal circumstances we can handle reacting flows comprising of many components in which reactions may occur via a large number of finite-rate reaction steps. For example, the mechanism of Miller *et al.* [1984] involves *16* species and *58* reaction steps. In general, this would necessitate the solution

of conservation equations for the mean value of each species, i.e., 15 transport equations. The species formation/destruction rates are highly nonlinear functions of temperature and species concentrations which often necessitate small time steps. Handling a large number of reacting species leads to excessively large computer storage requirements, which, when coupled to small time steps also leads to excessively long run times. Fortunately, in reaction systems the rate of change of many species concentration is very small in comparison with the rates of their creation and destruction. In such situations global reaction mechanisms can often be produced that preserve the gross characteristics of the reaction, e.g., yield the proper energy release rate. However, global reaction mechanisms are typically limited in their range of applicability and must be, in general, empirically adapted to a specific problem situation. The use of a global two-step mechanism model is the approach adopted to model reactions in this work and is detailed in the next section.

3.5.1.   Two-Step Reaction Mechanism

Based on the experimental data of Naber et al. [1994], the combustion submodel of reacting natural gas is formulated. A two-step kinetic mechanism is used. The first of the two global rate equations controls the disappearance of methane, the second controls the oxidation of carbon monoxide. These two reactions each account for a significant portion of the energy release. The reaction equations are [Naber et al., 1994]

$$2CH_4 + 3O_2 = 2CO + 4H_2O$$
$$2CO + O_2 = 2CO_2 \tag{3.15}$$
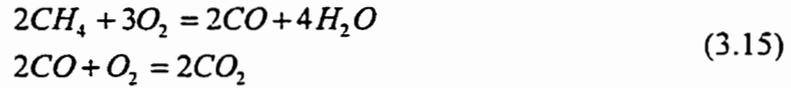
The reaction rates can be expressed in Arrhenius form as follows:

$$-\frac{d[CH_4]}{dt} = 2.0 \times 10^{10} \exp\left(\frac{-2.3668 \times 10^4}{T}\right)[CH_4]^{0.7}[O_2]^{0.8}$$

$$-\frac{d[CO]}{dt} = 1.423 \times 10^- \exp\left(\frac{-1.9639 \times 10^4}{T}\right)[CO][O_2]^{0.25}[H_2O]^{0.5} \tag{3.16}$$

T is in *Kelvin* and concentrations are in units of *moles/m³*. The Arrhenius constants and activation energies of both the methane and carbon monoxide global reactions have been selected to fit experimental data by Naber et al. [1994].

According to expression (3.16), the mass reaction rates for species CH_4, O_2, CO. CO_2, and H_2O are as follows

$$\omega_{CH_4} = -0.287 x 10^{10} \rho^{1.5} \exp\left(\frac{-2.3668 x 10^4}{T}\right) Y_{CH_4}^{0.7} Y_{O_2}^{0.8} ;$$

$$\omega_{O_2} = -0.8615 x 10^{10} \rho^{1.5} \exp\left(\frac{-2.3668 x 10^4}{T}\right) Y_{CH_4}^{0.7} Y_{O_2}^{0.8}$$

$$- 0.8058 x 10^7 \rho^{1.75} \exp\left(\frac{-1.9639 x 10^4}{T}\right) Y_{CO} Y_{O_2}^{0.25} Y_{H_2O}^{0.5} ;$$

$$\omega_{CO} = 0.5026x10^{10} \, \rho^{1.5} \exp\left(\frac{-2.3668x10^4}{T}\right) Y_{CH_4}^{\ 0.7} \, Y_{O_2}^{\ 0.8}$$
$$- 1.41x10^6 \, \rho^{1.75} \exp\left(\frac{-1.9639x10^4}{T}\right) Y_{CO} \, Y_{O_2}^{\ 0.25} \, Y_{H_2O}^{\ 0.5} \, ;$$

$$\omega_{CO_2} = 0.2216x10^7 \, \rho^{1.75} \exp\left(\frac{-1.9639x10^4}{T}\right) Y_{CO} \, Y_{O_2}^{\ 0.25} \, Y_{H_2O}^{\ 0.5} \, ;$$

$$\omega_{H_2O} = 0.6461x10^{10} \, \rho^{1.5} \exp\left(\frac{-2.3668x10^4}{T}\right) Y_{CH_4}^{\ 0.7} \, Y_{O_2}^{\ 0.8} \, .$$

3.6. Conservation Equations in Curvilinear Coordinate Systems

An analytic solution of a physical problem usually depends on the equations being cast in some specialized form. On the other hand, a numerical solution can be based on more general forms of the equations derived from fundamental principles. In applying a numerical technique, however, the form of a starting point equation is dictated by the requirements of an analytic solution. Other forms of the equations are ideally suited to the numerical technique. The numerical technique is extended in its range of applicability. It means that the numerical technique based on a uniformly spaced squared computational grid can be employed in a non-uniformly spaced irregular physical grid by the transformations of independent variables. In the case of moving grid or adaptive grid, the grid in the physical domain is moved whereas the grid in the computational domain is

fixed. The independent variable transformation between both domains makes it possible to apply a much simplified numerical technique.

A completely general transformation of the form can be considered as

$$
\begin{aligned}
\tau &= t \\
\xi &= \xi(t, x, y) \\
\eta &= \eta(t, x, y)
\end{aligned}
$$

(3.17)

which can be used to transform the differential equations from the physical domain (t, x, y) to the computational domain (τ, ξ, η). Using the chain rule of partial differentiation, the partial derivatives become

$$
\begin{aligned}
\frac{\partial}{\partial t} &= \frac{\partial}{\partial \tau} \\
\frac{\partial}{\partial x} &= \xi_x \frac{\partial}{\partial \xi} + \eta_x \frac{\partial}{\partial \eta} \\
\frac{\partial}{\partial y} &= \xi_y \frac{\partial}{\partial \xi} + \eta_y \frac{\partial}{\partial \eta}
\end{aligned}
$$

(3.18)

The metrics (ξ_x, η_x, ξ_y, η_y) appearing in these equations can be determined in the following manner.

$$
\begin{bmatrix} d\tau \\ d\xi \\ d\eta \end{bmatrix} = \begin{bmatrix} 1 & 0 & 0 \\ \xi_t & \xi_x & \xi_y \\ \eta_t & \eta_x & \eta_y \end{bmatrix} \begin{bmatrix} dt \\ dx \\ dy \end{bmatrix}
$$

(3.19)

Another like manner is

$$
\begin{bmatrix} dt \\ dx \\ dy \end{bmatrix} = \begin{bmatrix} 1 & 0 & 0 \\ x_\tau & x_\xi & x_\eta \\ y_\tau & y_\xi & y_\eta \end{bmatrix} \begin{bmatrix} d\tau \\ d\xi \\ d\eta \end{bmatrix}
\tag{3.20}
$$

Therefore,

$$
\begin{bmatrix} 1 & 0 & 0 \\ \xi_t & \xi_x & \xi_y \\ \eta_t & \eta_x & \eta_y \end{bmatrix} = \begin{bmatrix} 1 & 0 & 0 \\ x_\tau & x_\xi & x_\eta \\ y_\tau & y_\xi & y_\eta \end{bmatrix}^{-1} = J \begin{bmatrix} \dfrac{1}{J} & 0 & 0 \\ -\dfrac{\partial(x,y)}{\partial(\tau,\eta)} & y_\eta & -x_\eta \\ \dfrac{\partial(x,y)}{\partial(\tau,\xi)} & -y_\xi & x_\xi \end{bmatrix}
\tag{3.21}
$$

Thus, the metrics are

$$
\begin{pmatrix} \xi_t \\ \xi_x \\ \xi_y \\ \eta_t \\ \eta_x \\ \eta_y \end{pmatrix} = \begin{pmatrix} -J(x_\tau y_\eta - x_\eta y_\tau) \\ J y_\eta \\ -J x_\eta \\ J(x_\tau y_\xi - x_\xi y_\tau) \\ -J y_\xi \\ J x_\xi \end{pmatrix}
\tag{3.22}
$$

where J is the Jacobian of the transformation

$$
J \equiv \frac{\partial(\xi,\eta)}{\partial(x,y)}
\tag{3.23}
$$

In the computational domain, the grid is fixed in time, i.e.,

$$\begin{pmatrix} \dfrac{d\xi}{dt} \\ \dfrac{d\eta}{dt} \end{pmatrix} = \begin{pmatrix} \xi_x \dfrac{dx}{dt} + \xi_y \dfrac{dy}{dt} + \xi_t \\ \eta_x \dfrac{dx}{dt} + \eta_y \dfrac{dy}{dt} + \eta_t \end{pmatrix} = \begin{pmatrix} 0 \\ 0 \end{pmatrix} \tag{3.24}$$

Therefore

$$\begin{pmatrix} \xi_t \\ \eta_t \end{pmatrix} = \begin{pmatrix} -\xi_x \dfrac{dx}{dt} - \xi_y \dfrac{dy}{dt} \\ -\eta_x \dfrac{dx}{dt} - \eta_y \dfrac{dy}{dt} \end{pmatrix} \tag{3.25}$$

3.6.1.   Equations in Axisymmetric Coordinates

With reference to the structure of injector and the simplification of combustion chamber, the governing and turbulent equations [Lilley, 1979] can be expressed in axisymmetric coordinate (r, z) as follows

Mass:

$$\frac{\partial r\rho}{\partial t} + \left[\frac{\partial}{\partial z}\left(r\rho u_z\right) + \frac{\partial}{\partial r}\left(r\rho u_r\right) \right] = 0 \tag{3.26}$$

Momentum:

$$\frac{\partial}{\partial t}\left(r\rho\,u_z\right) + \left[\frac{\partial}{\partial z}\left(r\rho\,u_z^2\right) + \frac{\partial}{\partial r}\left(r\rho\,u_z\,u_r\right)\right] + \frac{\partial}{\partial z}\left(rp\right)$$

$$-\left[\frac{\partial}{\partial z}\left(2r\,\mu_{\it eff}\frac{\partial u_z}{\partial z}\right) + \frac{\partial}{\partial r}\left(r\,\mu_{\it eff}\frac{\partial u_r}{\partial z} + r\,\mu_{\it eff}\frac{\partial u_z}{\partial r}\right)\right] = 0$$

(3.27)

$$\frac{\partial}{\partial t}\left(r\rho\,u_r\right) + \left[\frac{\partial}{\partial z}\left(r\rho\,u_r u_z\right) + \frac{\partial}{\partial r}\left(r\rho\,u_r^2\right)\right] + \frac{\partial}{\partial r}\left(rp\right)$$

$$-\left[\frac{\partial}{\partial z}\left(r\,\mu_{\it eff}\frac{\partial u_r}{\partial z} + r\,\mu_{\it eff}\frac{\partial u_z}{\partial r}\right) + \frac{\partial}{\partial r}\left(2r\,\mu_{\it eff}\frac{\partial u_r}{\partial r}\right)\right] - p$$

(3.28)

$$+ \,2\,\mu_{\it eff}\,\frac{u_r}{r} \,=\, 0$$

Energy:

$$\frac{\partial}{\partial t}\left(r\rho E\right) + \frac{\partial}{\partial z}\left[r\left(\rho E + p\right)u_z - r\mu_{\it eff}\left(2u_z\frac{\partial u_z}{\partial z} + u_r\frac{\partial u_r}{\partial z} + u_r\frac{\partial u_z}{\partial r}\right)\right.$$

$$\left.- r\frac{c_p\mu_{\it eff}}{\sigma_t}\frac{\partial T}{\partial z}\right] + \frac{\partial}{\partial r}\left[r\left(\rho E + p\right)u_r - r\mu_{\it eff}\left(u_z\frac{\partial u_r}{\partial z} + u_z\frac{\partial u_z}{\partial r}\right.\right.$$

(3.29)

$$\left.\left.+2u_r\frac{\partial u_r}{\partial r}\right) - r\frac{c_p\mu_{\it eff}}{\sigma_t}\frac{\partial T}{\partial r}\right] + r\sum\left(h_k\omega_k\right) \,=\, 0$$

$$E \equiv e + \frac{1}{2}\,v\cdot v \,=\, c_v T + \frac{1}{2}\left(u_z^2 + u_r^2\right)$$

Fuel Mass Fraction:

$$\frac{\partial}{\partial t}\left(r\rho Y_k\right) + \left[\frac{\partial}{\partial z}\left(r\rho Y_k u_z\right) + \frac{\partial}{\partial r}\left(r\rho Y_k u_r\right)\right] = \left[\frac{\partial}{\partial z}\left(r\frac{\mu_{eff}}{S_C}\frac{\partial Y_k}{\partial z}\right)\right.$$

$$\left. + \frac{\partial}{\partial r}\left(r\frac{\mu_{eff}}{S_C}\frac{\partial Y_k}{\partial r}\right)\right] + r\omega_k \tag{3.30}$$

$$\nabla \cdot v \equiv \frac{1}{r}\left[\frac{\partial}{\partial z}\left(r u_z\right) + \frac{\partial}{\partial r}\left(r u_r\right)\right];$$

$$\mu_{eff} \cong \mu_t + \mu$$

Turbulent Kinetic Energy:

$$\frac{\partial}{\partial t}\left(r\rho k\right) + \left[\frac{\partial}{\partial z}\left(\rho r u_z k\right) + \frac{\partial}{\partial r}\left(\rho r u_r k\right)\right] = \left[\frac{\partial}{\partial z}\left(\frac{r\mu_t}{\sigma_k}\frac{\partial k}{\partial z}\right) + \right.$$

$$\frac{\partial}{\partial r}\left(\frac{r\mu_t}{\sigma_k}\frac{\partial k}{\partial r}\right)\right] + r\mu_t\left[2\left(\frac{\partial u_z}{\partial z}\right)^2 + 2\left(\frac{\partial u_r}{\partial r}\right)^2 + 2\left(\frac{u_r}{r}\right)^2 \tag{3.31}$$

$$+ \left(\frac{\partial u_z}{\partial r} + \frac{\partial u_r}{\partial z}\right)^2\right] - \frac{2}{3}r\nabla \cdot v\left(\mu_t\nabla \cdot v + \rho k\right) - r\rho\varepsilon$$

Turbulent Dissipation Rate:

$$
\begin{aligned}
\frac{\partial}{\partial t}\left(r\rho\varepsilon\right) &+ \left[\frac{\partial}{\partial z}\left(\rho r u_z \varepsilon\right) + \frac{\partial}{\partial r}\left(\rho r u_r \varepsilon\right)\right] = \left[\frac{\partial}{\partial z}\left(\frac{r\mu_t}{\sigma_\varepsilon}\frac{\partial\varepsilon}{\partial z}\right) + \right. \\
&\frac{\partial}{\partial r}\left(\frac{r\mu_t}{\sigma_\varepsilon}\frac{\partial\varepsilon}{\partial r}\right)\left.\right] + \frac{C_1 r\mu_t\varepsilon}{k}\left[2\left(\frac{\partial u_z}{\partial z}\right)^2 + 2\left(\frac{\partial u_r}{\partial r}\right)^2 + 2\left(\frac{u_r}{r}\right)^2\right. \\
&+ \left.\left(\frac{\partial u_z}{\partial r} + \frac{\partial u_r}{\partial z}\right)^2\right] - \frac{2}{3}r\frac{\varepsilon}{k}\left(\nabla\cdot v\right)\left[C_1'\mu_t\left(\nabla\cdot v\right) + C_1''\rho k\right] - C_2 r\rho\frac{\varepsilon^2}{k} + \\
&C_3 r\rho\varepsilon\left(\nabla\cdot v\right) + C_4\frac{r\rho\varepsilon}{\mu}\frac{\partial\mu}{\partial t}
\end{aligned}
$$

$$(3.32)$$

Ideal Gas:

$$
p = \rho RT \tag{3.33}
$$

where t is the time; ρ is the density; r is the radius; z is the axial distance; u_z is the axial velocity; u_r is the radial velocity; p is the pressure; μ is the molecular viscosity; K is defined by $\frac{c_p \mu_{eff}}{\sigma_t}$; c_v is the constant volume heat capacity; T is the temperature; k is the turbulent kinetic energy per unit mass; ε is the turbulent dissipation rate per unit mass; S_c is the Schmidt number set equal 0.7 [Williams, 1985]; and μ_t is defined by $C_\mu\frac{\rho k^2}{\varepsilon}$. The k - ε turbulence model constants are shown in Table 3.3.

Table 3.3 k - ε turbulence model constants
[Ahmadi-Befrui, Gosman, and Watkins, 1984, and El Tahry, 1983]

C_μ	σ_k	σ_ε	C_1	$C_1{}'$	$C_1{}''$	C_2	C_3	C_4
0.09	1.0	1.3	1.44	1.44	1.44	1.92	-1/3	1.0

3.7. Closure

In this chapter the fundamental assumptions which reasonably approximate the physical problem into the mathematical model are detailed. The governing equations which represent mass, momentum, energy and species conservation, the turbulence model which is presented by a typical k - ε model for compressible flows, and the reaction mechanism which involves the two-step global reaction mechanism, are discussed. The differential conservation equations based on the coordinate system frames are addressed. The governing equations and the k - ε equations under the curvilinear coordinate system frames are presented and their detailed derivation is shown in Appendix D. The transformation of the axisymmetric uniform-spaced coordinate frame for the computational domain and the curvilinear coordinate frame for the physical domain is especially useful for the modeling of the problem.

Chapter 4.

Approaches To Solve Reacting Flows

4.1. Overview

In this chapter the numerical scheme selected to solve the natural gas injection and autoignition problem is detailed. It involves the discretization of the conservation equations of mass, momentum, energy, and species. The linearization of these non-linear equations using an implicit method [Chen and Pletcher, 1991], an explicit method, Newton-Raphson linearization, and positive coefficient linearization [Schneider, 1992] are discussed. Also, the iteration methodology which includes segregated iteration (e.g., SIMPLE), global, and semi-global iteration, (i.e., a global iteration for mass and momentum conservation and another global iteration for energy and species conservations), are addressed. Both fluid flow and reaction time scales for the natural gas injection and autoignition problem are analyzed in order to select a suitable iteration scheme.

Throughout the development of the algebraic equations a number of approximations are introduced. As such the resulting algebraic equations only approximate the differential equations. These approximations are made in both space and time. Therefore, it must be remembered that the resulting numerical solutions can only be as good as these approximations permit.

4.2. Discretization of the Conservation Equations

In order that the differential equations be rendered suitable for solving flows of arbitrary geometry, for more easily admitting the implementation of an adaptive moving grid in future work, and for simplifying the area or volume calculation in a volume-weighted skew upwind scheme [Sheu, et al., 1991], these equations are transformed to a generalized coordinate system where ξ and η are the new coordinate directions and are defined functionally by

$$\xi = \xi(x,r) \quad \eta = \eta(x,r)$$

This new coordinate system is not required to be orthogonal and the discretization lengths, $\Delta\xi$ and $\Delta\eta$, are set equal to unity in the transformed domain.

The strong conservative form of the equations is retained by using the chain rule to place all metric terms arising from the transformation inside the derivatives. Double cross- derivatives are assumed to be equivalent regardless of the order in which they are evaluated, and metric identities are then used to eliminate terms not expressed in conservative form. The resulting transformed equations then assume the following form

$$\frac{\partial}{\partial t}\frac{\rho\phi}{J} + \frac{\partial}{\partial \xi_1}\frac{\rho U_1 \phi}{J} + \frac{\partial}{\partial \xi_2}\frac{\rho U_2 \phi}{J} = \frac{\partial}{\partial \xi_1}\left[\frac{\Gamma}{J}\left(c_1 \frac{\partial}{\partial \xi_1}\frac{\phi}{J} - c_2 \frac{\partial}{\partial \xi_2}\frac{\phi}{J}\right)\right]$$
$$+ \frac{\partial}{\partial \xi_2}\left[\frac{\Gamma}{J}\left(c_3 \frac{\partial}{\partial \xi_2}\frac{\phi}{J} - c_2 \frac{\partial}{\partial \xi_1}\frac{\phi}{J}\right)\right] + S$$
(4.1)

where U and V denote the contravariant velocities in the generalized coordinate system

$$U_1 = u_1 \frac{\partial x_2}{\partial \xi_2} - u_2 \frac{\partial x_1}{\partial \xi_2}$$

$$U_2 = u_2 \frac{\partial x_1}{\partial \xi_1} - u_1 \frac{\partial x_2}{\partial \xi_1}$$

$$c_1 = \left(\frac{\partial x_1}{\partial \xi_2}\right)^2 + \left(\frac{\partial x_2}{\partial \xi_2}\right)^2$$
(4.2)

$$c_2 = \frac{\partial x_1}{\partial \xi_1}\frac{\partial x_1}{\partial \xi_2} + \frac{\partial x_2}{\partial \xi_1}\frac{\partial x_2}{\partial \xi_2}$$

$$c_3 = \left(\frac{\partial x_1}{\partial \xi_1}\right)^2 + \left(\frac{\partial x_2}{\partial \xi_1}\right)^2$$

and where J is the Jacobian of the transformation defined by

$$J = \frac{\partial x_1}{\partial \xi_1}\frac{\partial x_2}{\partial \xi_2} + \frac{\partial x_2}{\partial \xi_1}\frac{\partial x_1}{\partial \xi_2}$$
(4.3)

4.2.1 Finite Volume Formulation

To this point, the governing equations have been presented in differential form. However, for the reasons presented earlier, a formulation based on the finite volume or

control volume approach is to be used for the numerical discretization of the equations. While the differential forms in transformed coordinates are mathematically equivalent to the familiar equations in x and y, they do not immediately lend themselves to a straightforward integral expression. Metric terms such as J, ξ_x , etc., do not, at first glance, have direct meaning in the more physically based finite volume methodology. Since the differential equations of motion are derived from a control volume expression in the limit where the volume goes to zero it must be that a physical equivalence can be established. To clarify the meaning of the metric terms in the finite volume formulation, and to establish the connection between the differential and integral forms of the governing equations, a finite volume is examined from the standpoint of both the differential and integral form of the continuity equation.

If the Γ and S are zero, and ϕ is one in expression 4.1, then the differential form of the continuity equation in the generalized coordinate system may be expressed as:

$$\frac{\partial}{\partial t} \frac{\rho}{J} + \frac{\partial}{\partial \xi_1}\left(\frac{\rho}{J}(\frac{\partial \xi_1}{\partial x_1} u_1 + \frac{\partial \xi_1}{\partial x_2} u_2)\right) + \frac{\partial}{\partial \xi_2}\left(\frac{\rho}{J}(\frac{\partial \xi_2}{\partial x_1} u_1 + \frac{\partial \xi_2}{\partial x_2} u_2)\right) = 0. \qquad (4.4)$$

Remembering that $\Delta\xi_1$ and $\Delta\xi_2$ are both unity, the equation can be integrated over the volume, $\Delta\xi_1\Delta\xi_2$, giving

$$\frac{\Delta\rho}{J\Delta t}\Delta\xi_1\Delta\xi_2 + \left(\frac{\rho}{J}(\frac{\partial \xi_1}{\partial x_1} u_1 + \frac{\partial \xi_1}{\partial x_2} u_2)\right)\Bigg|_w^e + \left(\frac{\rho}{J}(\frac{\partial \xi_2}{\partial x_1} u_1 + \frac{\partial \xi_2}{\partial x_2} u_2)\right)\Bigg|_s^n = 0.$$

$$(4.5)$$

This expression can then be compared with the control volume form of the equations in the x-y plane

$$\frac{\Delta\rho}{\Delta t}\Delta V + \left.\left(\rho\left(u_1\,n_x + u_2 n_y\right)dS\right)\right|_w^e + \left.\left(\rho\left(u_1\,n_x + u_2\,n_y\right)dS\right)\right|_s^n = 0. \qquad (4.6)$$

where w, e, s, and n represent, respectively, the west, east, south and north faces of the two dimensional control volume in the x-y plane, and the surface normal vector $n = n_x\,i + n_y\,j$ with i and j being the unit vectors in the x and y directions. By comparing the volume integral and the surface integral over only the east face of control volume, the following identities arise

$$\frac{1}{J} = \Delta V, \qquad \frac{1}{J}\left(\frac{\partial\xi_1}{\partial x_1}i + \frac{\partial\xi_1}{\partial x_2}j\right) = \left(n_x\,i + n_y\,j\right)dS \qquad (4.7)$$

with similar identities for the west, south and north faces. This shows the inverse of the Jacobian of the transformation to be equivalent to the volume of the integral in the two dimensional x-y plane, and the vector $\dfrac{1}{J}\left(\dfrac{\partial\xi_1}{\partial x_1}i + \dfrac{\partial\xi_1}{\partial x_2}j\right)$ is the normal surface vector with length equal to the east face. This result, when carried out over all faces of the cell, yields the connection between the differential and integral forms of the governing equations in transformed coordinates.

From purely physical grounds, the surface normal vector for the east face may also be shown to be

$$n dS = \Delta x_2\,i - \Delta x_1\,j = \frac{\partial x_2}{\partial\xi_2}i - \frac{\partial x_1}{\partial\xi_1}j \qquad (4.8)$$

when $\Delta\xi_1$ and $\Delta\xi_2$ are both equal to unity across each volume. Similar results also applying to the remaining faces. Not surprisingly, this result is the same as if the metric identity

$$\begin{pmatrix} \dfrac{\partial \xi_1}{\partial x_1} & \dfrac{\partial \xi_1}{\partial x_2} \\[2mm] \dfrac{\partial \xi_2}{\partial x_1} & \dfrac{\partial \xi_2}{\partial x_2} \end{pmatrix} = J \begin{pmatrix} \dfrac{\partial x_2}{\partial \xi_2} & -\dfrac{\partial x_1}{\partial \xi_2} \\[2mm] -\dfrac{\partial x_2}{\partial \xi_1} & \dfrac{\partial x_1}{\partial \xi_1} \end{pmatrix} \tag{4.9}$$

had been used. However, in the case of the finite volume approach, all of the information has been derived physically from volume geometry and integral requirements. These relationships allow us to identify the contravariant velocities as the volumetric fluxes across the faces of each cell.

$$\frac{1}{J} U_1 = V \bullet n\, dS \text{ on west and east faces,}$$

$$\frac{1}{J} U_2 = V \bullet n\, dS \text{ on south and north faces}$$

where V is the total velocity vector and n is the surface normal vector.

The differential equation in transformed coordinates as expressed in equation 4.1 can now be placed in integral form by multiplying the equation by J and integrating over a finite, two-dimensional volume, ΔV.

$$\int_{\Delta V} \left\{ \frac{\partial}{\partial t} \frac{\rho \phi}{J} + \frac{\partial}{\partial \xi_1} \frac{\rho U_1 \phi}{J} + \frac{\partial}{\partial \xi_2} \frac{\rho U_2 \phi}{J} = \frac{\partial}{\partial \xi_1} \left[\frac{\Gamma}{J} \left(c_1 \frac{\partial}{\partial \xi_1} \frac{\phi}{J} - c_2 \frac{\partial}{\partial \xi_2} \frac{\phi}{J} \right) \right] \right. $$
$$\left. + \frac{\partial}{\partial \xi_2} \left[\frac{\Gamma}{J} \left(c_3 \frac{\partial}{\partial \xi_2} \frac{\phi}{J} - c_2 \frac{\partial}{\partial \xi_1} \frac{\phi}{J} \right) \right] + S \right\} J\, dx_1\, dx_2 \tag{4.10}$$

Converting the integral to the transformed plane, and assuming the vector properties to be constant within the volume, ΔV, may be written as

$$\frac{\partial}{\partial t}\frac{\rho\phi}{J} + \int_{\Delta V}\left\{\frac{\partial}{\partial\xi_1}\frac{\rho U_1\phi}{J} + \frac{\partial}{\partial\xi_2}\frac{\rho U_2\phi}{J} = \frac{\partial}{\partial\xi_1}\left[\frac{\Gamma}{J}\left(c_1\frac{\partial}{\partial\xi_1}\frac{\phi}{J} - c_2\frac{\partial}{\partial\xi_2}\frac{\phi}{J}\right)\right]\right.$$
$$\left. + \frac{\partial}{\partial\xi_2}\left[\frac{\Gamma}{J}\left(c_3\frac{\partial}{\partial\xi_2}\frac{\phi}{J} - c_2\frac{\partial}{\partial\xi_1}\frac{\phi}{J}\right)\right]\right\}d\xi_1\,d\xi_2 + S \tag{4.11}$$

Green's Theorem in vector form for a vector field $G(x,y) = M(x,y)i + N(x,y)j$ is

$$\oint_S G\bullet n\,dS = \int_{\Delta V}\nabla\bullet G\,dx\,dy \tag{4.12}$$

but may be more conveniently expressed in component form for control volume applications as

$$\oint_S (M\,dx + N\,dy) = \int_{\Delta V}\left(\frac{\partial N}{\partial x} + \frac{\partial M}{\partial y}\right)dx\,dy \tag{4.13}$$

and then used to transform the volume flux integrals of equation 4.11 to surface integrals.

$$\frac{\partial}{\partial t}\frac{\rho\phi}{J} + \int_S \frac{\rho U_1\phi}{J}d\xi_2 + \int_S \frac{\rho U_2\phi}{J}d\xi_1 = \int_S\left[\frac{\Gamma}{J}\left(c_1\frac{\partial}{\partial\xi_1}\frac{\phi}{J} - c_2\frac{\partial}{\partial\xi_2}\frac{\phi}{J}\right)\right]d\xi_2$$
$$+ \int_S\left[\frac{\Gamma}{J}\left(c_3\frac{\partial}{\partial\xi_2}\frac{\phi}{J} - c_2\frac{\partial}{\partial\xi_1}\frac{\phi}{J}\right)\right]d\xi_1 + S \tag{4.14}$$

Recalling that the coordinate direction ξ_1 is constructed so as to coincide with the cell's east and west faces, and the ξ_2 direction coincides with the north and south faces, then by definition the transformed flux vectors are normal to these respective surfaces. This leaves

$$\frac{\partial}{\partial t}\frac{\rho\phi}{J} + \left(\frac{\rho U_1\phi}{J}\right)\Big|_w^e + \left(\frac{\rho U_2\phi}{J}\right)\Big|_s^n = \left[\frac{\Gamma}{J}\left(c_1\frac{\partial}{\partial\xi_1}\frac{\phi}{J} - c_2\frac{\partial}{\partial\xi_2}\frac{\phi}{J}\right)\right]\Big|_w^e$$
$$+ \left[\frac{\Gamma}{J}\left(c_3\frac{\partial}{\partial\xi_2}\frac{\phi}{J} - c_2\frac{\partial}{\partial\xi_1}\frac{\phi}{J}\right)\right]\Big|_s^n + S \tag{4.15}$$

When discretizing the equations in the finite volume form described above care must be taken to use the proper metric terms for the flux evaluation. For the transient and convective terms this is straightforward, since the metric terms required for their calculation are physically defined by volume itself. However, by inspection of the viscous fluxes, there exist many terms involving cross derivatives that do not contain physically defined metric terms. For these terms, a fictitious cell is constructed at the surface in question based on the geometries of the adjacent cells.

4.2.2 Volume-Weighted Skew Scheme

In equation 4.1, a curvilinear coordinate system is used for all governing equations in order to more easily admit the implementation of an adaptive grid (or moving grid) in future work, and to simplify the area or volume calculation in a volume-weighted skew scheme [Sheu, Lee, Yang and Chiou, 1991].

Most numerical methods for convection-diffusion problems suffer from severe false diffusion when the flow direction is at a finite angle to the grid lines. These diffusion errors are usually produced from the local one-dimensional treatment for multi-dimensional problems. The resulting discretization error tends to augment the transport of dependent variables in a direction normal to the local streamline. Improvement, therefore, can be made by employing a flow-oriented scheme such that the real physics is not masked. The first approach considered for reducing the false diffusion error was the skew upwind scheme of Raithby [1976]. In this study, however, a volume-weighted

skew upwind differencing scheme [Sheu, Lee, Yang and Chiou, 1991] is used instead of

the line interpolation skew scheme of Raithby [1976].

The discretization equations are obtained by integrating the governing equations

over a control volume. For a typical control volume around the point P, shown in Figure

4.1, integration of equation 4.1 with $\Delta \xi_1 = \Delta \xi_2 = 1$ gives
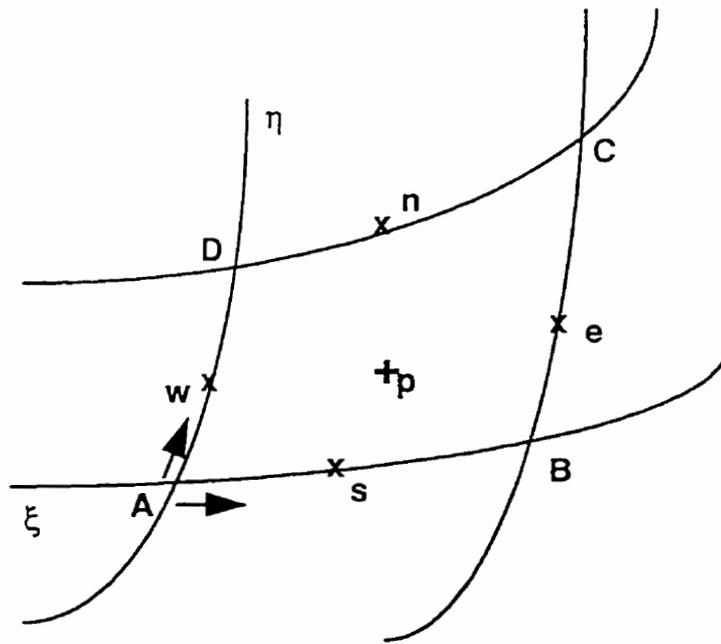
Figure 4.1:   Basic element for a finite-volume method

$$\frac{1}{\Delta\tau}\left[(\rho\phi)_P^{n+1} - (\rho\phi)_P^n\right] + \left[\rho U_1\phi - \frac{\Gamma}{J}\left(c_1\frac{\partial\phi}{\partial\xi_1} - c_2\frac{\partial\phi}{\partial\xi_2}\right)\right]_e^{n+1} - \left[\rho U_1\phi - \frac{\Gamma}{J}\left(c_1\frac{\partial\phi}{\partial\xi_1} - c_2\frac{\partial\phi}{\partial\xi_2}\right)\right]_w^{n+1}$$

$$+\left[\rho U_2\phi - \frac{\Gamma}{J}\left(c_3\frac{\partial\phi}{\partial\xi_2} - c_2\frac{\partial\phi}{\partial\xi_1}\right)\right]_n^{n+1} - \left[\rho U_2\phi - \frac{\Gamma}{J}\left(c_3\frac{\partial\phi}{\partial\xi_2} - c_2\frac{\partial\phi}{\partial\xi_1}\right)\right]_s^{n+1} - JS_P^{n+1} = 0$$

$$(4.16)$$

Equation 4.16 involves implicit integration. Values and gradients of dependent variables at the control-volume surfaces are classified using the subscripts e, w, n, s to denote the east, west, north, or south face, respectively, and by the subscript P to denote the control-volume center. The source term, viscous terms, and convecting velocities of equation 4.16 are approximated by a central differencing scheme. The convected quantities $\rho\phi$ at the surface of cell can be approximated by introducing two upstream volumes A_0, and A_1 as weighting factors. The following discussion focuses only on the west face. Volumes A_0 and A_1 in Figure 4.2 are bounded by a line connecting the centers of adjacent upstream control volume cells and two lines parallel to the contravariant velocity vector[1], V, at the center of control surface. These parallel lines start from the corners of the control volume and extend all the way back to a line connecting the centers of two adjacent cells. The interpolated values can be expressed as

$$\phi_w = \frac{A_0\cdot\phi_1 + A_1\cdot\phi_2}{A_0 + A_1}$$

$$(4.17)$$

---

[1] It has been proven by differential geometry that the direction of contravariant velocity in computational space corresponds to the direction of velocity in physical space.
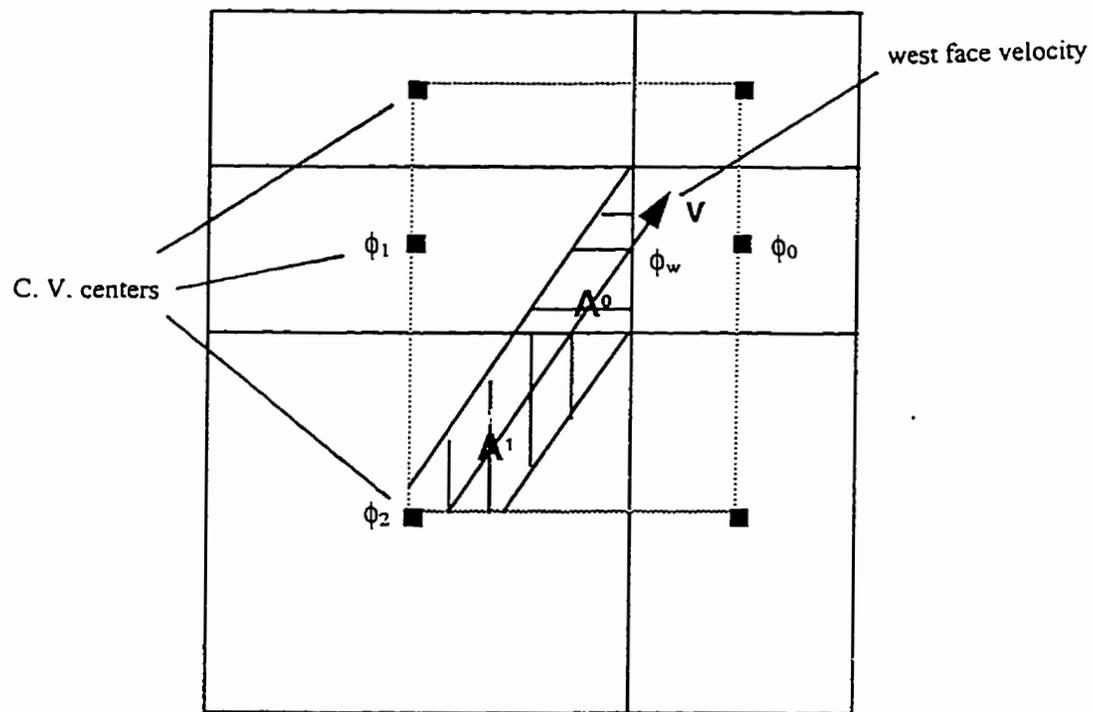
Figure 4.2:   Illustration of volume-weighted skew upwind scheme [Sheu et al., 1991]

After discretization of equation 4.1 all non-linear terms are linearized by the Newton-Raphson method. It should be noted that an equivalent formulation can also be developed using conventional Jacobian matrices. In addition, the linearization error can be effectively removed by iterating at each time level for unsteady-state calculations.

After linearization of equation 4.16, the nine dependent variables, u, v, p, T and five species $(Y_{CH_4}, Y_{H_2O}, Y_{CO}, Y_{CO_2}, Y_{O_2})$, appear in all of the equations and the resulting equations take the following form:

$$A_{i,j}^6 q_{i-1,j-1} + A_{i,j}^5 q_{i+1,j-1} + A_{i,j}^4 q_{i+1,j-1} + A_{i,j}^7 q_{i-1,j} + A_{i,j}^9 q_{i,j} + A_{i,j}^3 q_{i+1,j}$$
$$+ A_{i,j}^8 q_{i-1,j+1} + A_{i,j}^1 q_{i,j+1} + A_{i,j}^2 q_{i+1,j+1} = b_{i,j}$$

$$(4.18)$$

and can be expressed in a matrix form as

$$[A]q = b \qquad (4.19)$$

where

$$[A] = \begin{bmatrix} A_{1,1}^9 & A_{1,1}^3 & & A_{1,1}^1 & A_{1,1}^2 & & & & \\ A_{i,j}^6 & A_{i,j}^5 & A_{i,j}^4 & A_{i,j}^7 & A_{i,j}^9 & A_{i,j}^3 & A_{i,j}^8 & A_{i,j}^1 & A_{i,j}^2 \\ & & A_{im,jm}^6 & A_{im,jm}^5 & & A_{im,jm}^7 & A_{im,jm}^9 \end{bmatrix} \qquad (4.20)$$

is the coefficient matrix with a 9×9 block in each element (a detailed expression for matrix [A] is not shown here due to complexity) and

$$q = \left[\left(u,v,p,T,Y_k \right)_{1,1}^T, \ldots, \left(u,v,p,T,Y_k \right)_{i,j}^T, \ldots, \left(u,v,p,T,Y_k \right)_{im,jm}^T \right]^T$$

and   (4.21)

$$b = \left[\left(b_u,b_v,b_p,b_T,b_{Y_k} \right)_{1,1}^T, \ldots, \left(b_u,b_v,b_p,b_T,b_{Y_k} \right)_{i,j}^T, \ldots, \left(b_u,b_v,b_p,b_T,b_{Y_k} \right)_{im,jm}^T \right]^T$$

are the unknown vector and the right-hand side vector, respectively.

4.3. Boundary Conditions

A general boundary condition expression in physical space can be written as

$$C_1 \frac{\partial \phi}{\partial n} + C_2 \phi = C_3 \qquad (4.22)$$

where n is a normal unit vector ($n_x i$, $n_y j$), C_1, C_2, and C_3 are constants, and ϕ is a general variable.   Our objective is to find the corresponding general boundary condition expression in computational space so that the boundary condition equation can be directly utilized by equation 4.16. In equation 4.22, $\frac{\partial \phi}{\partial n}$ is the unique term that needs to be rewritten in computational space. The normal derivative is equal to an inner product of the gradient ϕ and a normal unit vector n, i.e.,

$$\frac{\partial \phi}{\partial n} = \nabla \phi \bullet n = \left(\frac{\partial \phi}{\partial x}, \frac{\partial \phi}{\partial y} \right) \bullet \begin{pmatrix} n_x \\ n_y \end{pmatrix}. \tag{4.23}$$

The gradient in computational space is then expressed as

$$\left(\frac{\partial \phi}{\partial x}, \frac{\partial \phi}{\partial y} \right) = \left(\frac{\partial \phi}{\partial \xi}, \frac{\partial \phi}{\partial \eta} \right) \bullet \frac{\partial(\xi, \eta)}{\partial(x, y)}.$$

Finally, the general boundary condition expression in computational space becomes

$$C_1 (n_x, n_y) \cdot \left[\frac{\partial(\xi, \eta)}{\partial(x, y)} \right]^T \begin{pmatrix} \dfrac{\partial \phi}{\partial \xi} \\ \dfrac{\partial \phi}{\partial \eta} \end{pmatrix} + C_2 \, \phi = C_3. \tag{4.24}$$

For a specific boundary geometry and grid distribution the coefficient vector, $C_1 (n_x, n_y) \cdot \left[\dfrac{\partial(\xi, \eta)}{\partial(x, y)} \right]^T$, can easily be calculated.

The specific boundary conditions used in the natural gas autoignition problem are as follows. As was mentioned, an adiabatic boundary condition at the cylinder wall is assumed, i.e., $\dfrac{\partial T}{\partial n}\bigg|_{wall} = 0$. In addition, fluid velocities, pressure gradient, and species gradient are equal to zero on wall boundaries, that is,

$$u_{wall} = v_{wall} = 0,$$

$$\left.\frac{\partial p}{\partial n}\right|_{wall} = 0, \ and \tag{4.25}$$

$$\left.\frac{\partial Y_k}{\partial n}\right|_{wall} = 0.$$

The turbulence boundary conditions on the wall boundary are obtained by making the following assumptions:

(1)   the flow is in equilibrium in the log-law region, i.e.,

$$-\overline{uv}\frac{\partial U}{\partial y_n} = \varepsilon. \tag{4.26}$$

(2)   there is a constant stress layer $(\overline{uv} = -U_\tau^2)$, and

(3)   the turbulent viscosity relation [Wilcox, 1994] is valid.

Therefore, a log-law equation can be written

$$\frac{U}{U_\tau} = \frac{1}{\kappa}\ln\left(\frac{y_n U_\tau}{\upsilon}\right) + C \tag{4.27}$$

where $\kappa = 0.41$ and $C = 5.2$. y_n is the distance normal to the wall. In computational space, the log-law equation 4.27 becomes

$$y_n = \left| n \cdot \begin{pmatrix} \Delta x \\ \Delta y \end{pmatrix} \right| = \left| n \cdot \left[\frac{\partial(\xi, \eta)}{\partial(x, y)} \right]^{-1} \begin{pmatrix} \Delta \xi \\ \Delta \eta \end{pmatrix} \right| \tag{4.28}$$

where n represents a normal unit vector. In order to calculate U_τ of the log-law equation an estimate of U_τ is used which is obtained from the following expression (a derivative of equation 4.27)

$$\frac{U_\tau}{\kappa y_n} = \frac{\partial U}{\partial y_n} = (n_x, n_y) \cdot \left[\frac{\partial(\xi, \eta)}{\partial(x, y)} \right]^{T} \begin{pmatrix} \dfrac{\partial U}{\partial \xi} \\ \dfrac{\partial U}{\partial \eta} \end{pmatrix} . \tag{4.29}$$

Applying the Newton-Raphson iteration scheme to equation 4.27 yields U_τ. Finally, substituting equation 4.29 into the following expressions

$$k = \frac{U_\tau^2}{\sqrt{c_\mu}} \qquad and \qquad \varepsilon = \frac{U_\tau^3}{\kappa y_n} \tag{4.30}$$

one obtains the values for k and ε at the wall boundary layer.

4.4. Integration Time Step

It is desirable to employ a variable integration time step. The reason is that in the initial fuel/air mixing period the time step will be relatively long in contrast to the needed time step when the exponential reaction rate terms begin to play a major role in the energy and species equations. Varying the time step saves computer time when two different characteristic time scales are present. A detailed time stepping analysis is described in Appendix E.

4.5. Ignition

A steep rise in temperature as used by Naber et al. is used to identify ignition. It is not necessary, however, to check the temperature in the computational domain at each time step to know whether ignition occurs. An empirical, critical time step (i.e., $\Delta t_c \approx 0.05$ µs) can be evaluated to justify whether or not a temperature check is needed. When the time step for a convergent solution is longer than the critical time step, i.e., $\Delta t > \Delta t_c$, a temperature check is not necessary because in this case ignition is impossible. After $\Delta t < \Delta t_c$ a temperature check for ignition is performed at each time step. This approach ultimately saves computational time.

4.6. Fluid Flow and Reaction Time Scales

Fluid flow and reaction time scales strongly depend on the stability of the numerical method used to solve the differential equations. Stability is closely coupled to the propagation of round off error or any other computational errors. Any numerical scheme that allows an error to grow, eventually swamping the true solution, is unstable. Instability problems must be avoided by restrictive action, such as limiting the interval size, adopting an alternative numerical method, etc. The interval size is governed by grid density and time step. In unsteady flow, it is, in general, necessary to keep the Courant number small by selecting a small enough time step. Due to reaction process within the fluid flows the time step must be very small to maintain stability. This situation can be seen in the following analysis of a linear system with an explicit algorithm (because an implicit, real system analysis is much more complicated.).

First, consider the stability of a linear partial differential equation (e.g., equation 4.21). The connection between truncation errors and computational stability can be determined for such a linear equation. Take, for instance, the equation

$$\frac{\partial u}{\partial t} + a \frac{\partial u}{\partial x} = v \frac{\partial^2 u}{\partial x^2} \qquad (4.31)$$

which describes both the convection and diffusion of a function $u(x, t)$. The convection velocity, a, and diffusion coefficient, v, are assumed constant. Solutions to this equation are bounded.

A simple finite difference (e.g., central difference) discretization of equation 4.31 yields

$$\frac{u_j^{n+1} - u_j^n}{\Delta t} = -\frac{a}{2\Delta x}\left(u_{j+1}^n - u_{j-1}^n\right) + \frac{v}{\Delta x^2}\left(u_{j+1}^n - 2u_j^n + u_{j-1}^n\right) \tag{4.32}$$

where u_j^n denotes $u\ (j\Delta x,\ n\Delta t)$.

Observe that the difference equation 4.32 propagates an effect from each datum point $(j\Delta x,\ n\Delta t)$ into a region bounded by lines passing through that point and having slopes $\pm\Delta x/\Delta t$. These lines are not true characteristic lines along which the signals propagate, but they do play an important role in this stability analysis.

The difference equation 4.32 is linear with constant coefficients, hence, its stability can be examined by the Fourier method. A single Fourier component of u_j^n, say

$$r^n \exp(i\,k\,j\,\Delta x) \tag{4.33}$$

satisfies equation 4.33 provided [Hirt, 1968]

$$r = 1 - \left(\frac{ia\Delta t}{\Delta x}\right)\sin(k\Delta x) - \left(\frac{2v\Delta t}{\Delta x^2}\right)[1 - \cos(k\Delta x)] \tag{4.34}$$

If r has a magnitude greater than unity for any value of k then the difference equation is unstable since that Fourier component will grow exponentially with n, i.e., with time. A study [Hirt, 1968] of equation 4.34 shows that the magnitude of r is less than unity for all k if the following two conditions are satisfied

$$\frac{2v\Delta t}{\Delta x^2} \leq 1, \tag{4.35}$$

$$v \geq \frac{1}{2}a^2\Delta t \tag{4.36}$$

These two inequalities are stability conditions for equation 4.32. For given values of v, a, and Δx they define a range of permissible Δt values.

The fluid flow and reaction differential equations are coupled and nonlinear. Discretization approximations for these equations are easily constructed, but they frequently suffer from computational instabilities. The usual Fourier method of testing for stability pertains to perturbations about stationary and uniform flows. However, there is some recourse as the frozen coefficient method can be used to evaluate stability over a very short time period using the Fourier method [Hirt, 1968]. The a of equation 4.31 can be considered as the frozen coefficient of the convection terms. In the reaction case, source terms must be added to the energy and species equations. With the frozen coefficient method the source term can be written as $c_s u$ in which the u represents temperature or mass fraction. Therefore equations 4.31 and 4.32 can be represented by

$$\frac{\partial u}{\partial t} + a\frac{\partial u}{\partial x} = v\frac{\partial^2 u}{\partial x^2} + c_s u \tag{4.37}$$

and

$$\frac{u_j^{n+1} - u_j^n}{\Delta t} = -\frac{a}{2\Delta x}\left(u_{j+1}^n - u_{j-1}^n\right) + \frac{v}{\Delta x^2}\left(u_{j+1}^n - 2u_j^n + u_{j-1}^n\right) + c_s u_j^n \qquad (4.38)$$

respectively. The corresponding Fourier analysis r is then

$$r = 1 + c_s\Delta t - \left(\frac{ia\Delta t}{\Delta x}\right)\sin(k\Delta x) - \left(\frac{2v\Delta t}{\Delta x^2}\right)[1 - \cos(k\Delta x)] \qquad (4.39)$$

The above expression shows that Δt should be very short for stability of the numerical method if c_S is very large in order to limit r less than unity. It means that, in this case, the fluid flow time scale is much greater than that for the reactions. Although this analysis has been applied to an explicit numerical method the conclusion is similarly valid in any implicit scheme [Hirt, 1968].

In other hand, time step selection is directly related to integration accuracy for transient problems, especially for a first order (in time) of integration scheme. A detailed discussion is shown in Appendix E.

4.7. Autoignition

Current segregate solving methods lead to very slow convergence speeds for the strongly coupled nonlinear differential equations [Chen et al., 1991]. In order to ensure convergence for a large range of problems it is desirable to seek positive coefficient linearization. Unfortunately, its guaranteed convergence with large time steps is

countered by the fact that the convergence speed with positive coefficient linearization is very slow.

Section 4.6 concludes that there is a large difference between the time scale for fluid flows and the time scale for reactions. One reasonable approach then is to separately solve the fluid flow equations, i.e., the mass and momentum equations, and the reaction equations, i.e., the energy and species equations, in a so-called semi-global method. This approach solves mass and momentum equations with a larger time step than that used to solve the energy and species equations resulting in a time efficient approach. Several time steps in the solution of the reaction equations are computed before the next time step in the solution of fluid flow equations is updated. This advantage can be obtained when the number of reaction equations is much less than the number of fluid flow equations. However, when multiple species concentrations are considered this method does not appear to have this advantage and may result in a coupling problem between variables. For instance, the number of fluid flow equations is three for the two-dimensional case and four for the three-dimensional case. For a two-step reaction mechanism of natural gas oxidation with five species, the global solving method which attempts to solve the fluid flow and reaction equations simultaneously only increases by one-third the number of equations over the two-dimensional case. For a more detailed reaction model the percentage increase in the number of equations will be larger. It means that the global solving method does not dramatically increase computer memory and computational time. On the other hand, it couples all unknown variables together and results in a faster convergence in each nonlinear iteration cycle.

In the study of natural gas injection and subsequent autoignition in a diesel engine type environment the computation is only continued until autoignition occurs. For a large fraction of the injection process (e.g., 90 % period of the total time) effectively no reaction occurs, e.g., convection and diffusion dominates the fluid flow. Therefore, for the global solving method the initial time step can be chosen large, i.e., reflecting the longer fluid flow time scale.

The methodology employed to solve the autoignition of natural gas problem is as follows: In each time step the equations of mass, momentum, energy, and species are solved globally (i.e., simultaneously) by using the Newton-Raphson nonlinear iteration method. When convergence is reached, the variables of pressure, velocities, temperature, and species mass fractions are updated and then the updated variables are substituted into k-ε equations. After that, the k-ε equations in which coefficients are updated are solved to update turbulence viscosity μ_t. In both cases, the linear systems, generated by linearizing the algebraic equations of mass, momentum, energy, and species and the algebraic k-ε equations, are solved by the newly developed conjugate gradient solvers, Bi-CGSTAB [Von Der Vorst, 1992] and TFQMR [Freund, 1991], through block and sparse data structures which will be detailed in next Chapter.

4.8. Closure

This chapter briefly outlined the approaches used to solve the mass, momentum, energy, and species equations for the natural gas diesel engine autoignition problem. There are three major parts to this Chapter. The first part presents the discretization of the

differential equations. The second part reveals concerns of stability arising from the large difference between the fluid flow and reaction characteristic time scales. The reaction time scale is the smaller and hence more restrictive. The third part outlines methodologies suitable for tackling the multi-time scale problem. For the solution of natural gas injection and subsequent autoignition the global solving method is selected.

Chapter 5.

Conjugate Gradient Iterative Solvers

5.1. Overview

Most heat transfer and fluid flow modeling efforts use the Newton-Raphson method for solving fully-coupled nonlinear equations. The Jacobian matrix, generated by the Newton-Raphson method, is usually quite large size (e.g., 10^5) and sparse in structure for most realistic problems. The common rule of thumb is that if the size of a linear system is smaller than 10^5 the direct Gaussian elimination method may perform as well as a indirect (i.e., iterative) preconditional conjugate gradient (PCG) method. In practice, the total CPU time of the PCG method, which is composed of total inner iterations for an entire sequence of nonlinear iterations for a matrix size around 10^4 would be shorter than that provided by a direct solver for the nonlinear system. The reason for this is that the residual tolerance of a linear iteration cycle need not be small before the iteration goes back to a nonlinear iteration cycle. This large residual tolerance greatly reduces the large

number of inner iterations in the linear iteration cycle. Another advantage of the PCG method in comparison with other iterative methods, e.g., ADI (Alternative Direction Implicit) and multigrid methods, is that it can easily be used to solve the problems on unstructured grids. In this chapter, the general features of the preconditional conjugate gradient solver package, PCGPACKAGE, which was developed by the author using four acceleration technologies (ORTHOMIN, CGS, Bi-CGSTAB, and TFQMR) are briefly introduced.

5.2. Acceleration Techniques

The PCGPACKAGE developed involves four different acceleration techniques: ORTHOMIN [Vinsome, 1976], CGS [Sonneveld, 1989], Bi-CGSTAB [Von Der Vorst, 1992], and TFQMR [Freund, 1991].

The ORTHOMIN acceleration technique is an orthogonalization-minimization method for non-Hermitian (or nonsymmetric) linear systems. This technique accelerates the convergence rate by minimizing the sum of the squares of residuals along orthogonal vectors. The procedure has the following major features: (1) it is suitable for strongly nonsymmetric systems; (2) both the minimization and orthogonalizations have a pronounced effect on the convergence rate; and (3) the number of orthogonalizations required is problem dependent and is specified by a user input parameter.

The CGS algorithm, called as conjugate gradient square algorithm, first yields a polynomial system effectively equivalent to the ORTHOMIN procedure and then derives the squares of the polynomials to accelerate the convergence rate. This method has been

found to be more efficient than the ORTHOMIN algorithm in general, but it often leads to rather irregular convergence behaviour. The irregular convergence behaviour may even lead to severe cancellation problems, particular, in situations when the starting iteration is close to the solution.

Another CGS related method is to predefine the form of the CGS polynomial, select suitable constants, and combine pair results from successive iteration steps. This method often leads to a more stable and more efficient algorithm than the simple CGS approach. Because of its similarity to CGS and its favourable stability properties it is named Bi-CGSTAB.

After the Bi-CGSTAB was created, Freund [1991] generated an even more stable approach, named the transpose-free quasi-minimal residual algorithm (TFQMR). TFQMR is very stable, however it requires more CPU time than Bi-CGSTAB. Both Bi-CGSTAB and TFQMR are recent, very efficient, iterative solvers.

5.3. Sparse Data Structure

It is impractical to install all elements of the matrix. The reason is that 400 MB memory must be used to store all variables for a 10^4 by 10^4 matrix using only single precision for the natural gas autoignition problem. Another alternative approach is to use a banded data structure to store data. However, banded data storage still installs a lot of zero elements for problem of complicated geometry, particularly for unstructured grids, and hence also needs large amounts of memory. Sparse data storage only installs non-zero

elements of the matrix. It needs at most 0.2 MB to install the data for a 10^4 by 10^4 matrix. The sparse data structure is described next.

Suppose that each element of a resulting sparse matrix, A (see Figure 5.1), is a real number (zero or non-zero) and that the distribution of non-zero elements in matrix A is irregular. Non-zero element locations are dependent on grid structure and grid number ordering, especially for unstructured grids. Let all non-zero elements be recorded in a one dimensional array $a(i)$ that sweeps from the left column to the right column and from the first row to the last row. The i represents a sequential number of non-zero elements.

ir (1) = 1, jc (1) = 1   jc (2) = 4

ir (2) = 3, jc (3) = 2

ir (3) = 5, jc (5) = 1   jc (4) = 4

$$
A \equiv \begin{pmatrix}
a(1) & 0 & 0 & a(2) & 0 \\
0 & a(3) & 0 & a(4) & 0 \\
a(5) & 0 & a(6) & 0 & 0 \\
a(7) & 0 & 0 & a(8) & 0 \\
0 & a(9) & 0 & 0 & a(10)
\end{pmatrix}
$$

ir (4) = 7, jc (7) = 1   jc (6) = 3   jc (10) = 5

ir (5) = 9, jc (9) = 2   jc (8) = 4
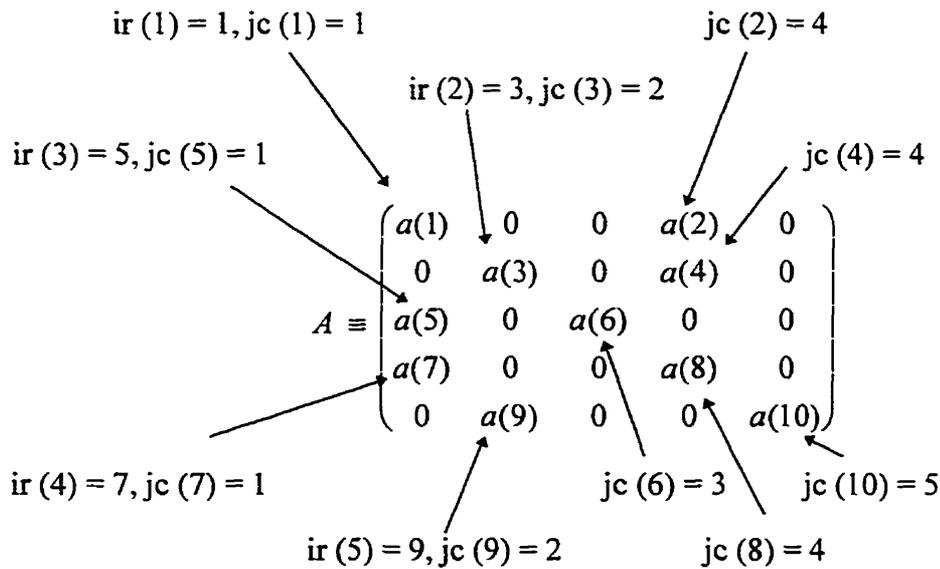
Figure 5.1:   Example of a sparse matrix A

The non-zero element positions in matrix A are identified by two integer arrays, *ir(k)* and *jc(i)*. The integer array *ir(k)* records the sequential number of the first non-zero element of each row where k is a row number. The integer array *jc(i)* points to the column number of every non-zero element. Consequently, the three arrays, *a(i), ir(k), and jc(i)* compactly record the sparse matrix A completely. When section 5.2 conjugate gradient approaches are employed all the operations (consisting of matrix-vector multiplications, matrix-matrix multiplications, forward/backward substitutions, and incomplete LU decompositions) can be performed on one-dimensional arrays.

5.4. A Block Sparse Data Structure

When we solve a set of strongly coupled equations the discretization coefficients for each node are blocked into submatrices. It means that in above sparse matrix A, a block or submatrix replaces each nodal element (see Figure 5.2). It should be noted that block size may vary because the number of equations associated with each node may not be same (for example, the number of equations on the boundaries may not be equal to the number of equations inside for a free surface problem). On the diagonal of sparse matrix A, however, all the blocks must be square. The other blocks may be square or rectangular, depending on the corresponding diagonal block sizes. The data in each non-zero block are written in a one dimensional array while block size is recorded in another integer array. All operations, such as block-block multiplication, taking the block inverse, etc.

are performed on one-dimensional arrays. The advantages of a block preconditional conjugate gradient solver are as follows: (1) it maintains a strong coupling between equations by applying a direct solver (i.e., Gaussian elimination method) to each diagonal block; (2) it is able to use pivoting in each diagonal blocks to optimize the matrix and to remove undesirable zero elements on the diagonal of matrix A; and (3) it is efficient because only small block matrices are inversed.

$$A \equiv \begin{pmatrix} [\ldots]_{n1 \times n1} & 0 & 0 & [\ldots]_{n1 \times n4} & 0 \\ 0 & [\ldots]_{n2 \times n2} & 0 & [\ldots]_{n2 \times n4} & 0 \\ [\ldots]_{n3 \times n1} & 0 & [\ldots]_{n3 \times n3} & 0 & 0 \\ [\ldots]_{n4 \times n1} & 0 & 0 & [\ldots]_{n4 \times n4} & 0 \\ 0 & [\ldots]_{n5 \times n2} & 0 & 0 & [\ldots]_{n5 \times n5} \end{pmatrix}$$

Figure 5.2:   Example of a block sparse matrix A

5.5. Incomplete LU Factorization

The aim of partial factorization is to optimize the matrix so that the number of iterations needed for convergence of the iterative methods is effectively reduced. A more accurate LU factorization scheme will need fewer iterations to converge, but it also requires more

work to calculate the factorization and to do the forward and backward substitution. Hence, an optimal situation exists between full and no LU factorization, i.e., partial or incomplete factorization. Partial factorizations can be obtained by performing one or more steps of the Gaussian elimination process on the matrix A.

The simplest partial factorization possible is that obtained by carrying out only one step of Gaussian elimination on the matrix A, changing only the diagonal elements (or blocks) of matrix A, and not adding any extra elements (or blocks). The factors L, D, and U retain the sparsity structure of matrix A. Such a partial factorization is known as DKR (Dupont-Kendall-Rachford) factorization [Freund, 1991].

For a block structured matrix, when partial factorizations are done, it is important that the partial elimination procedure be carried out in a block sense. That is, each block should be considered a unit when Gaussian elimination is done, and divisions should be replaced by matrix inverses.

Incomplete LU factorization is performed only once at the beginning of the linear system solution procedure.

For large problems using the PCGPACKAGE solvers in place of a direct solver (1) a large amount of computer memory can effectively be saved, and (2) the CPU time for the solution of the project is substantially decreased.

5.5. Closure

This chapter focused on matrix solvers, in particular conjugate gradient iterative solvers which were created to deal with a large sized matrix resulting from fully coupled non-linear equations that must be solved in the natural gas autoignition problem. Four different acceleration techniques are identified. The Bi-CGSTAB and TFQMR acceleration techniques are deemed the most effective and efficient methods. In addition, a block sparse data structure is introduced that maintains a strong coupling between equations which permits better matrix condition optimization and hence reduces the number of iterations needed. The sparse data structure identified also makes efficient use of computer memory.

The discretized partial differential equation after linearization may be stiff or ill-conditional. Consequently, many iterations may be required for a converged solution. The incomplete LU factorization presented is able to optimize the matrix so that the number of iterations needed for convergence is reduced. Though a more accurate LU factorization will need fewer iterations to converge it has the disadvantage of requiring more operations to calculate the factorizations in the first place. Simple partial factorization, i.e., DKR factorization, is therefore used.

Chapter 6.

Natural Gas Injection and Autoignition

6.1. Overview

Direct injected natural gas diesel engines are currently being developed. Numerical analyses results are presented for 20.0 MPa ($\approx$3000 psia; 200 atm), 444 K, natural gas injection into 4.0 MPa cylinder air where the ambient turbulence field is representative of diesel engines. Two very important, non-intuitive, observations are made. First, the seemingly reasonable spatially uniform velocity profile currently used at the injector exit is *not* appropriate, rather a double-hump profile is correct. Second, a spatially uniform, injector exit, temperature profile results in local temperature overestimates as large as 300 K. Considering the strong role of temperature on chemical kinetics, this second observation may have profound implications on the validity of conclusions reached using uniform exit profiles.

The 3-D modelling of in-cylinder phenomena such as mixing, ignition delay time, etc., are already computationally very expensive if not prohibitive. As such, there is a strong incentive to simplify the details of injector operation by applying reasonable injector exit (i.e., injector/cylinder interface) boundary conditions. The literature on steady-state [Abramovich, 1963] and low-speed transient [Tsang, 1968] jets is well established. Unfortunately, the literature on high-speed transient jets is virtually non-existent. To compensate for this lack of knowledge, current modellers of diesel engine natural gas injection processes [Jeske et al., 1992 and Abraham, 1993] assume educated guesses for the exit boundary conditions such as uniform temperature, pressure, and velocity profiles. The uniform (or box hat) profile assumption is used extensively in computational studies of the far field region of jets [Launder et al., 1973 and Chen et al., 1979]. It is also a fair first approximation to observed turbulent pipe flow velocity profiles [Abdel-Rahman, 1987]. Diesel engine natural gas jets, however, are highly compressible in nature resulting in some doubt as to the appropriateness of these assumed exit profiles.

The objective of this chapter is to establish the correct boundary conditions (i.e., velocity, temperature, and pressure profiles) to be applied at the exit plane of a high-speed, natural gas injector as used in DI diesel engines. This objective is pursued by modelling the turbulent fluid flow within the injector, through the orifice, and into the cylinder. Operating conditions (e.g., 20.0 MPa and 444 K for the upstream natural gas), and injector and cylinder geometry, are roughly based on those found in the diesel engine like environment, injected natural gas, autoignition experiments of Fraser et al. [1991].

This work would have been sufficiently significant if its only conclusion was to confirm the appropriateness of currently assumed injector exit boundary conditions. It is

shown, however, that actual exit property profiles are not as have been assumed. Though the importance of this work's results are discussed, a detailed analysis of their impact on the conclusions reached by other researchers using assumed profiles is beyond the scope of this work.

In the next section, the injector configurations modelled are described. Following this, computations revealing transient injector exit boundary conditions for a DI diesel engine natural gas injector are presented. Given the lack of experiments for comparison, a discussion outlining the major checks on the validity of the solutions follows leading to several new insights into transient, high-speed, gas jets. An attempt is made to incorporate and improve the model. The experimental measurements of Fraser et al. and Naber et al. are used as the basis for improving the model. Finally, the comparison of ignition delay time between the present computation and experiment as well as the ignition location are presented.

6.2. Computational Model

An in-house developed, 2-D compressible flow, finite-volume based code is used in this study [Zhang et al., 1992, 1993, and Chapter 3 and 4]. The finite-volume approach requires that the conservation laws be satisfied locally over each control-volume as well as globally. Recognizing this important characteristic of the finite-volume approach is crucial to appreciating the physical discussions presented to explain the non-intuitive exit boundary condition results observed. In particular, explanations on the origin of the resulting velocity

profile rely heavily upon determining the relative contribution of the various momentum and energy balance terms as they apply to a local control volume.

The Base Case axi-symmetric injector/cylinder configuration is shown in Figure 6.1. A sample grid pattern is also shown. As mentioned, system dimensions such as orifice length and diameter, and cylinder wall location, are based upon the experiments of Fraser et al. [1991]. Adapting the non-axi-symmetric injector/cylinder arrangement in the experiments of Fraser et al. to an axi-symmetric model is accomplished by preserving both the nearest injector to cylinder wall dimension (i.e., 29 mm) and the cylinder volume (i.e., 149 cm^3). The high-pressure natural gas (20.0 MPa) and cylinder air (4.0 MPa) are initially at rest, separated by a fictitious diaphragm. The diaphragm is then instantaneously removed and the subsequent flow development calculated. Heat transfer to the walls is neglected by applying adiabatic wall boundary conditions. This is often reasonable for high speed flows [Anderson, 1990] and greatly simplifies the problem by removing the need to model thermal transients in the wall. The adiabatic boundary condition is initially superior to the isothermal boundary condition since it permits, via a simple review of the wall temperature, a qualitative measure on the degree of cooling or heating generated by the flow. The injection process is followed for a maximum of 2 ms. Since the computations reported in this work are non-reacting, and since practical diesel engine autoignition times are on the order of 2 ms or less [Fraser et al., 1991], jet development is followed for a maximum of 2 ms.
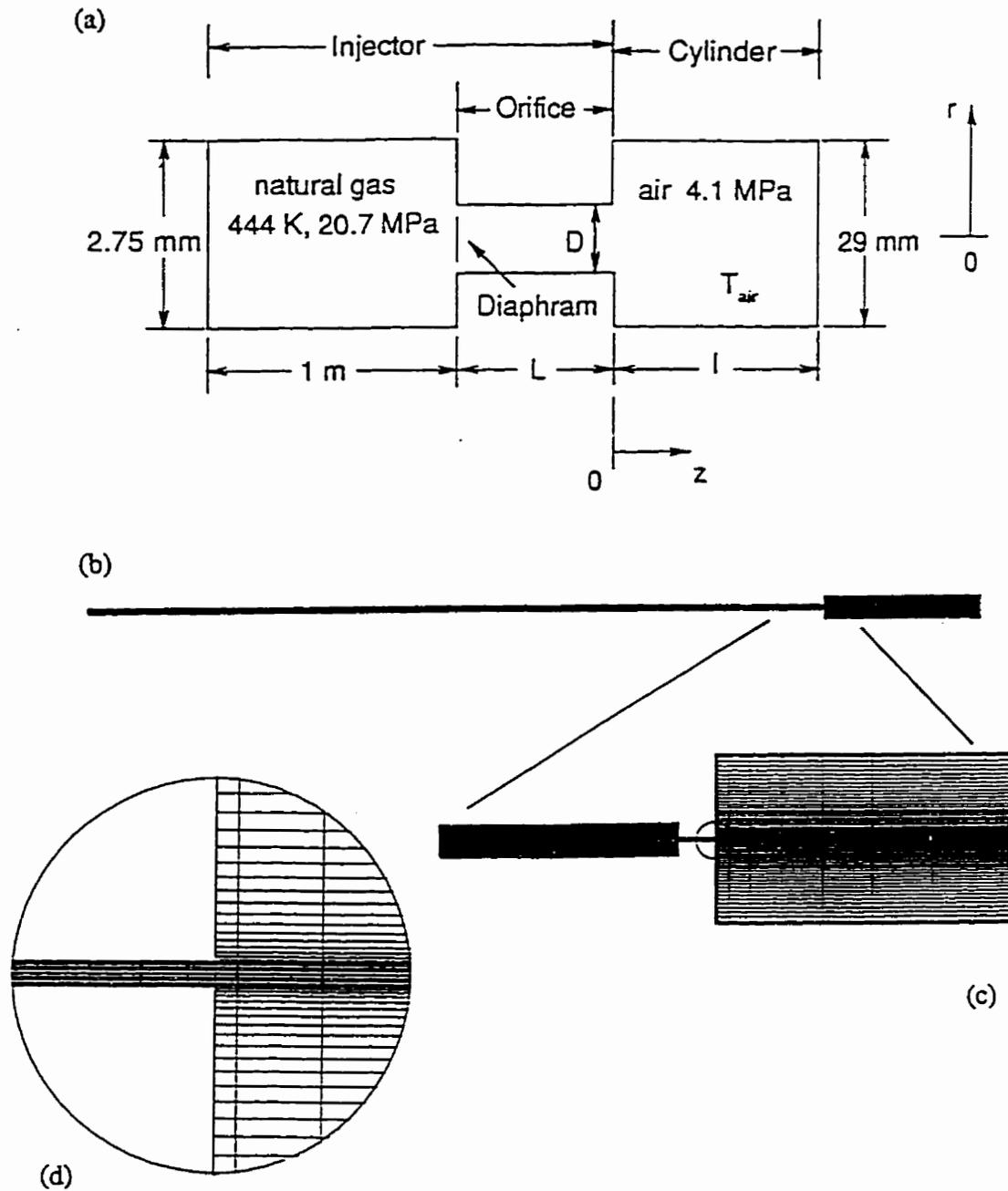
Figure 6.1:   An axisymmetric injector/cylinder configuration

All other configurations studied involve parametric changes to the Base Case. Changes in geometry, coordinate system, grid, turbulence levels, etc. are as summarized in Table 6.1. Reference to Figure 6.1 is required for definitions of Table 6.1 listed geometric parameters. The two geometries investigated are the 2-D axi-symmetric and 2-D Cartesian-plane configurations.

The governing conservation equations of mass, momentum, and energy are solved in conjunction with a compressible flow form of the $k - \varepsilon$ turbulence equations [Ahmadi-Befrui et al., 1984 and El Tahry, 1983], a fuel mass fraction equation, and the ideal gas equation of state. Chapter 3 presents the 2-D axi-symmetric form of these equations. Similar equations are used for the 2-D Cartesian-plane problem results presented.

It is computationally advantageous [Chen et al., 1991 and Karki et al., 1989] to transform Equations 3.24 to 3.31 to an axi-symmetric, body-fitted, coordinate system where they are then discretized using a collocated finite-volume numerical scheme similar to that employed by Karki and Patankar [1989].

Table 6.1 **Injector/Cylinder Configurations** **(Refer to Figure 6.1)**
CASE #	Geometry	L (mm)	D (mm)	L/D	l (mm)	T_{AIR} (K)	Comments
BASE	AXIS[1]	6.35	0.572	11.1	220	444	
1	AXIS					1200[2]	Turb[3]
2	2-D Plane						Uniform[4]
3	2-D Plane						FULL[5]; Uniform
4	2-D Plane						Low Speed[6]; Uniform
5							Turb
6	2-D Plane						
7	2-D Plane						FULL
8							Fine Grid[7]
9						1200	
10						1200	Low Turb[8]
11						800	
12							Turb; Uniform
13		12.7		22.2			
14			1.144	5.55			
15		12.7		22.2			Turb
16			1.144	5.55			Turb

[1] 2-D axi-symmetric.
[2] Only initial cylinder air is at 1200 K. Initial orifice air is at 444 K.
[3] Initial cylinder k=0.5 m²/s² and ε =500 m²/s³ => turbulent viscosity, μ_T=5.2 x 10^{-4} kg/m×s ($\mu_{AIR,1200K}$=4.6 x 10^{-5} kg/m×s). Base Case initial k and ε are essentially zero.
[4] Uniform temperature, pressure, and velocity (600 m/s) profiles are applied at injector exit.
[5] Full griding: the complete two-dimensional domain is solved over.
[6] Low speed of 18 m/s is applied at the injector exit.
[7] Grid resolution is approximately doubled.
[8] Initial cylinder k=0.125 m²/s² and ε =250 m²/s³ => μ_T=6.5 x 10^{-5} kg/m×s

Volume-weighted skew upwinding [Sheu et al., 1991] and fully-implicit differencing schemes are employed in order to ensure numerical stability at relatively high Courant numbers. With maximum time steps of 10^{-6} seconds, and minimum spatial dimensions of about 0.05 mm, the corresponding maximum Courant number realized in this work is

$CFL = \dfrac{a\Delta t}{\Delta x} \approx 10$ (Δx and Δt are space and time increments, respectively; a is the

local speed of sound). At each time step the discretized equations of mass, momentum, and

energy are solved simultaneously using the Block-CGSTAB conjugate gradient iterative

solver as described in section 5.2. The turbulent kinetic energy, turbulent energy dissipation

rate, and fuel mass fraction are then determined. Most computations were performed on a

66 MHz PC, or on a PC equipped with a special i860 board, resulting in computation times

of about 2 days per configuration per 2 ms of injection process development.

6.3. Profiles on Injector/Cylinder Surface [Zhang et al., 1994]

Case 1 (see Table 6.1) configuration selection is an attempt to model a reasonable facsimile

of a DI diesel engine natural gas injection process. Geometry, initial pressure distribution,

and initial temperature distribution, are based on the simulated diesel engine environment,

high-speed, natural gas injection, autoignition experiments of Fraser et al. [1991]. To

isolate autoignition physics, however, these experiments removed the complicating factor of

high-level, in-cylinder turbulence characteristic of I.C. engines. In addition, Case 1 includes

I.C. engine level turbulence.

It is well established for automotive engines that the turbulence intensity, u', and

turbulence integral length scale, L, near top-dead-centre (TDC) are on the order of 1 m/s

and 1 mm, respectively [Hall, 1987 and Fraser et al., 1992]. Consistent with this

expectation, an initial turbulence intensity and turbulence integral length scale of 1 m/s and

2 mm were chosen for the ambient in-cylinder turbulence level of Case 1. Corresponding

estimates for the turbulent kinetic energy, k ($\equiv 1/2\,u'^2$), and turbulent kinetic energy dissipation rate, ε ($\equiv u'^3/\Lambda$), are 0.5 m^2/s^2 and 500 m^2/s^3, respectively.

The simulated diesel engine environment experiments performed by Fraser et al. [1991] determined that 1200 K is approximately the minimum cylinder air temperature required for injected natural gas to autoignite unassisted in 2 ms. It is worth noting, however, that an actual engine operating on injected natural gas need not reach this high pre-ignition temperature if, for example, it uses dual-fuel injection [Jeske et al., 1992 and Hodgins et al., 1992]. Therefore, 1200 K is on the high end of pre-ignition air temperatures that may be experienced. Correspondingly, the 444 K initial air temperature used by some configurations is on the low end. The 800 K temperature used in Case 11 is representative of the autoignition temperature utilized by liquid-fuelled diesel engines [Siebers et al., 1987].

Case 1 injector exit-plane profiles of velocity, temperature, pressure, and mass fraction are shown in Figure 6.2. The exit plane property values plotted in Figure 6.2 are taken from control volume grid nodes 0.5 mm upstream (z/D = -0.87) of the actual exit plane. Also shown in Figure 6.2 are corresponding profiles immediately outside the injector orifice exit (i.e., 0.5 mm downstream). In effect, Figure 6.2 shows the property profiles seen at the injector exit as well as the relative rate of change in the various properties as they exit the injector. Injector exit profile resolution is $\approx$ 0.05 mm radially for a total of 10 control volumes across the injector orifice.
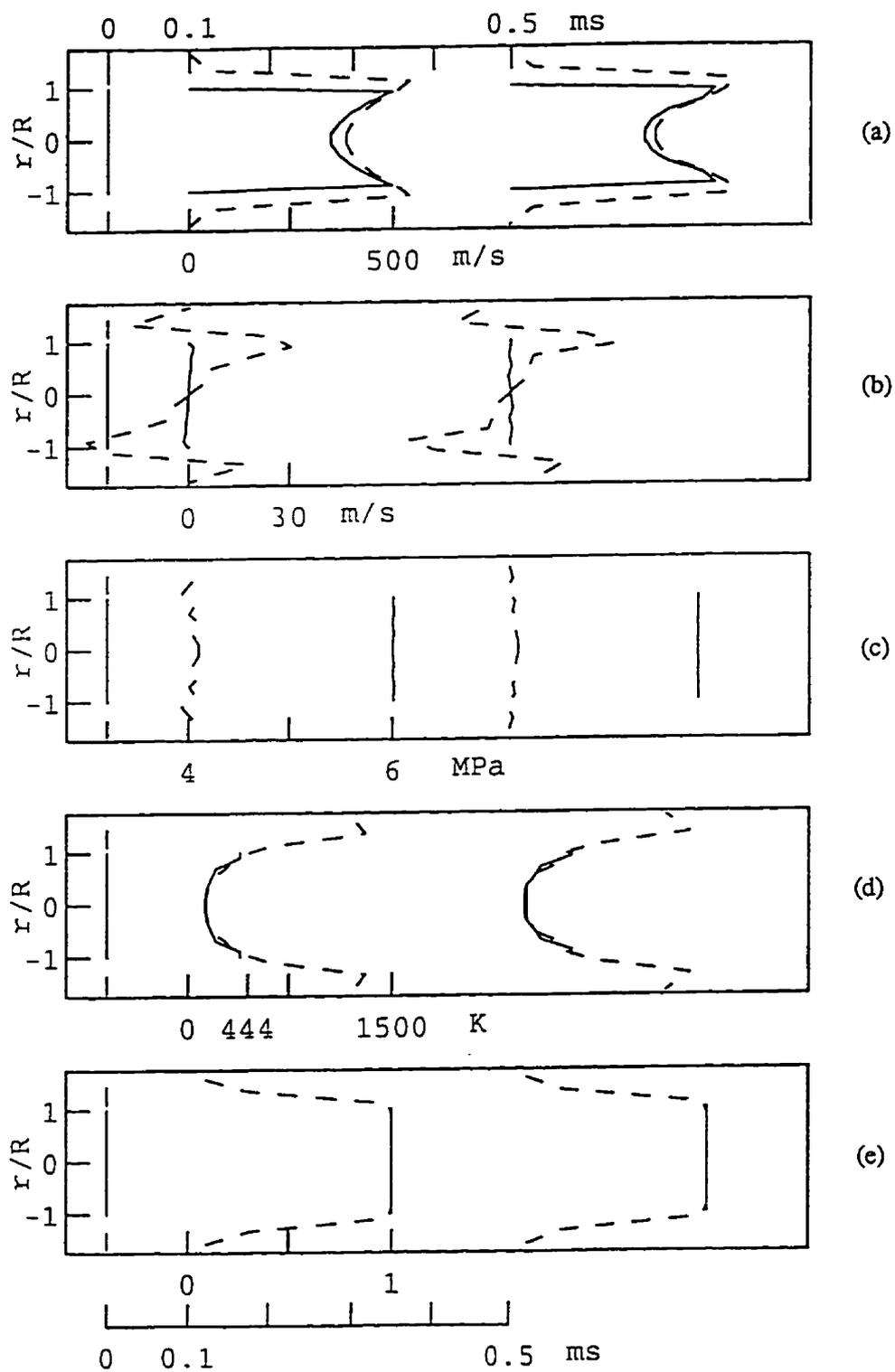
Figure 6.2: Case 1 injector exit profiles at 0. 0.1, and 0.5 ms for (a) axial velocity, (b) radial velocity, (c) static pressure, (d) static temperature, and (e) fuel mass fraction. R is the injector orifice radius. (———— z/D = -0.87; - - - - - - - z/D = 0.87)

The most striking feature of the chronological snapshots shown in Figure 6.2 is that some profiles differ noticeably from the previously expected turbulent pipe flow (box hat like) [Jeske et al., 1992], or steady-state, on-design, turbulent gas jet (also box hat like) [Abramovich, 1963]. They also bear no resemblance to the familiar parabolic like profiles seen in laminar flow. For example, the axial velocity trace reveals an unexpected double-hump feature. In addition, the resulting, far from uniform, exit plane total temperature distribution dips significantly to a low of about 200 K (or about half the initial static, and total, 444 K temperature) and peaks at slightly above 550 K within the orifice and at 1250 K just outside the orifice. This is in stark contrast to familiar one-dimensional compressible flow results that state that the total temperature, for a calorically perfect gas, is constant in isentropic flow through a variable area duct, or across a stationary normal shock [Anderson, 1990].

In short, the calculated injector exit-plane boundary conditions do not support the uniform exit-plane profiles assumed previously by other researchers.

Given that the results of Case 1 are counter intuitive, two very important questions must be answered. First, are the results in error for computational reasons? Second, what is the physical explanation for the results? These two questions are discussed in the next section. Once these questions are addressed, this work will then return to the problem of establishing natural gas, DI diesel engine, injector exit-plane, boundary conditions.

6.4   Injector Exit Profiles

It is legitimate to ask, given the lack of experimental data for verification, if the reported Case 1 results are physically reasonable? Is the centerline velocity deficit a materialization of a boundary condition problem? Etc.

First, let it be noted that there are related problems that also display multiple-hump velocity profiles. For example, low-speed, transient jet experiments indicate the presence of a multiple-hump mean velocity profile in the vicinity of the start-up vortex [Tsang, 1968]. Second, two potential flow vortices circulating in opposite directions are characterized by multiple-hump velocity profiles [Currie, 1974].

Injector exit-plane profiles of velocity, temperature, pressure, and fuel mass fraction for the Base Case are shown in Figure 6.3. These profiles may be compared with the corresponding Case 1 profiles of Figure 6.2. All Base Case and Case 1 profiles are qualitatively identical. Case 1 differs from the Base Case by increasing the initial in-cylinder temperature and turbulence level (see Table 6.1). It is not surprising to find that Figures 6.2 and 6.3 reveal little sensitivity to cylinder temperature and turbulence level since the injector exit flow is momentum dominated, i.e., diffusive effects are secondary. Figure 6.4 provides a visual picture of overall Case 5 flow through the use of velocity vectors and streamlines. For the Base Case a strong double-hump velocity profile is observed at both the injector exit and in the vicinity of the leading edge of the jet. In contrast, the higher turbulence levels of Case 5 noticeably weakens the double-hump profile in the vicinity of the jet's leading edge ($z/D = 47$, $t = 0.1$ ms).
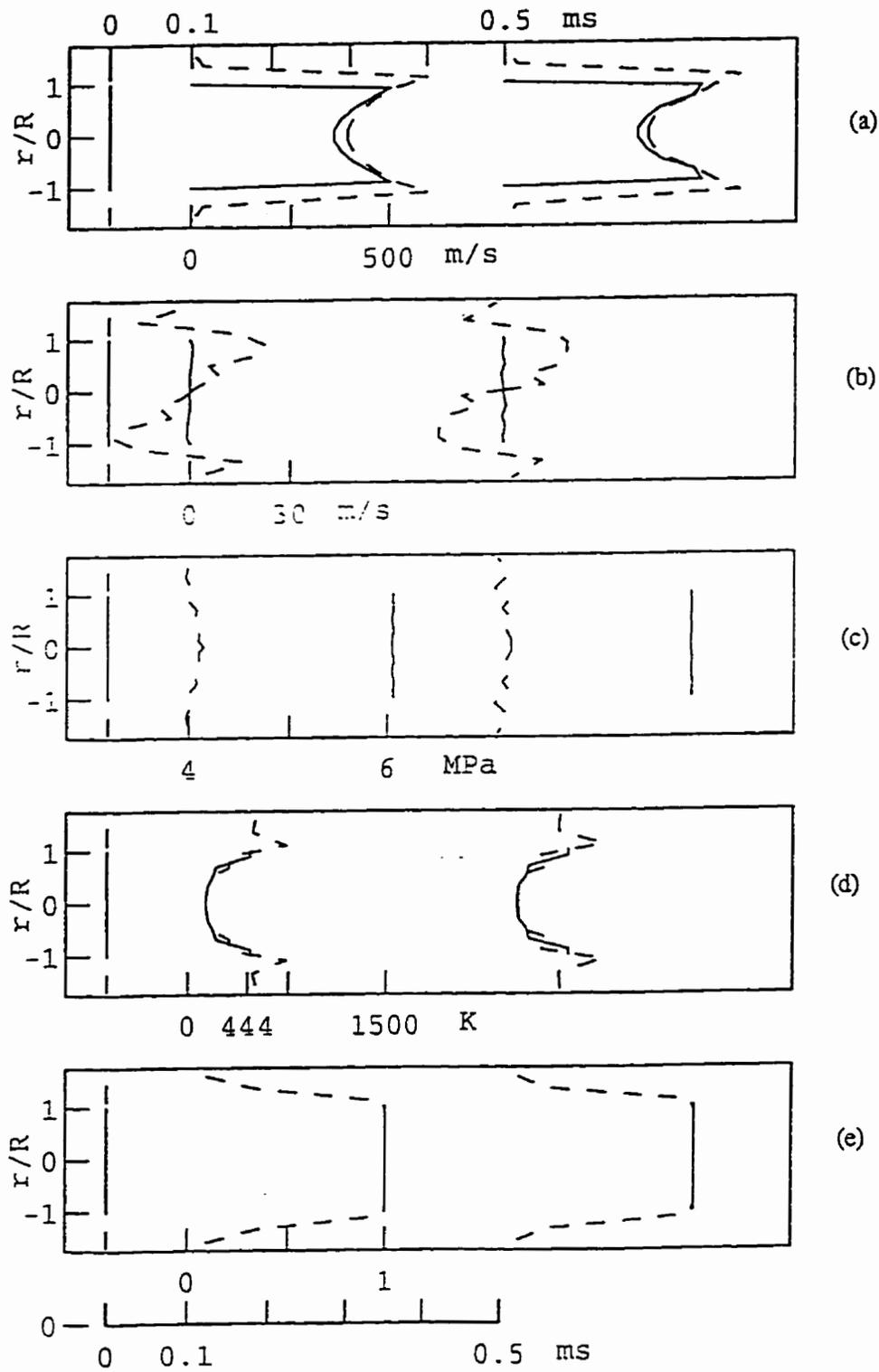
Figure 6.3: Base case injector exit profiles at 0. 0.1, and 0.5 ms for (a) axial velocity, (b) radial velocity, (c) static pressure, (d) static temperature, and (e) fuel mass fraction. R is the injector orifice radius. (——— z/D = -0.87; - - - - - - - z/D = 0.87)
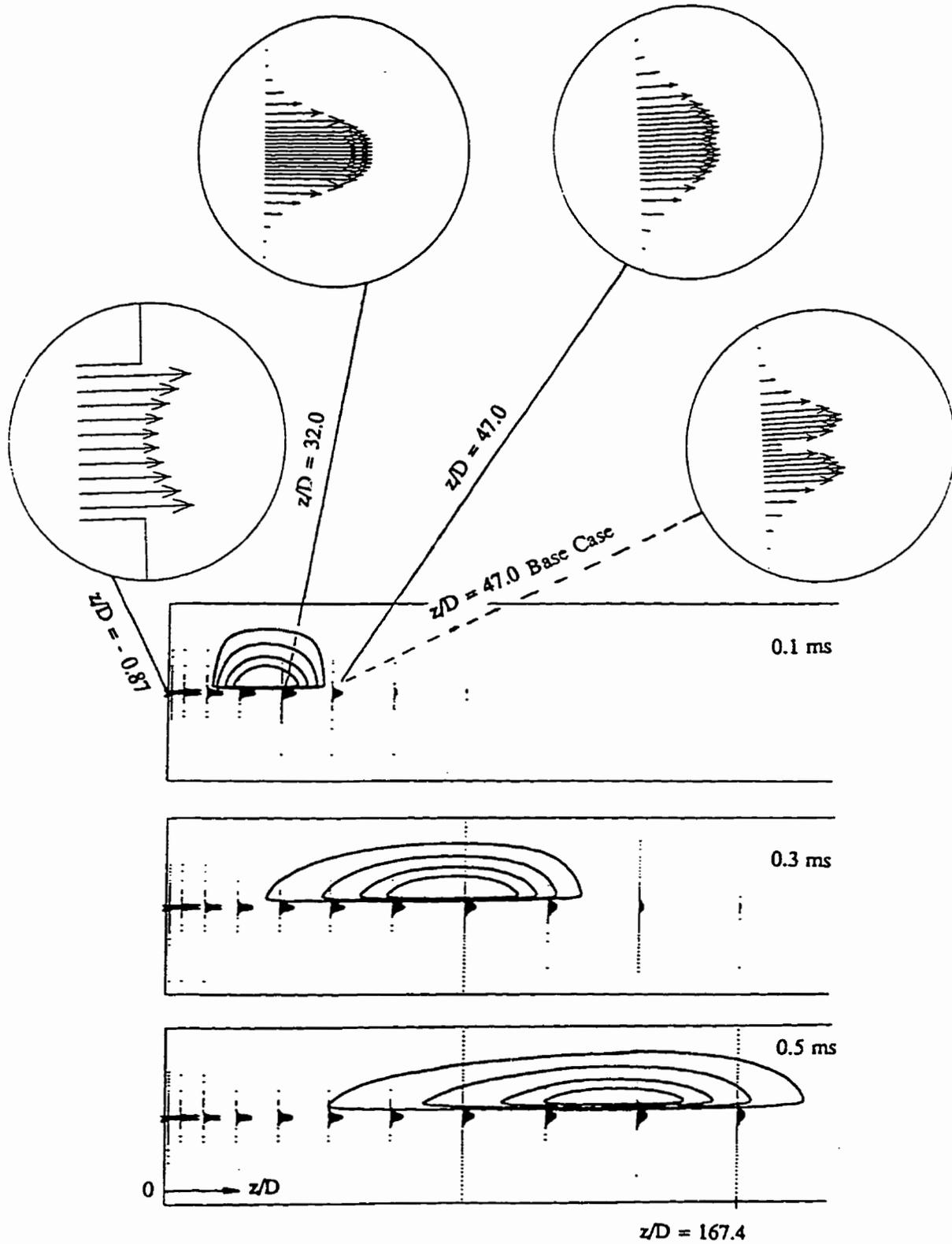
Figure 6.4: Case 5 velocity profiles at 0.1, 0.3, and 0.5 ms. A base case velocity profile
is also shown for z/D = -0.87, 32.0, and 47.0

Between the injector exit and the jet's leading edge turbulent diffusion acts to create a parabolic like velocity profile ($z/D = 32$, $t = 0.1$ ms).

The Base Case, injector exit ($z/D = -0.87$), centerline velocity deficit (quantified as the peak velocity minus the centerline velocity all divided by the peak velocity for a given axial location) is observed to asymptote towards a constant non-zero magnitude. This behaviour is made clear in Figure 6.5.

velocity deficit
$(1 - u_{centre} / u_{max})$

$z/D = -0.87$

$z/D = 32.0$

0.75

0.50

0.25

0.00

0.00   0.10   0.20   0.30   0.40   0.50   t (ms)
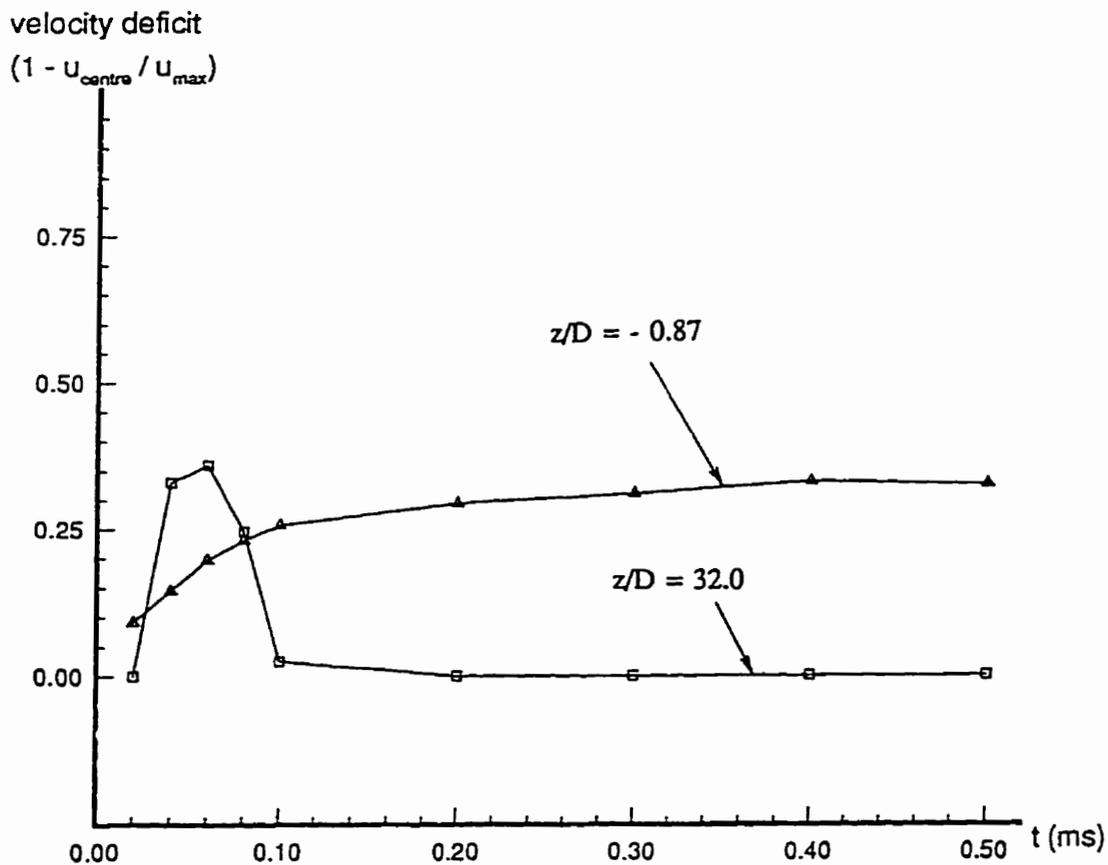
Figure 6.5:   Base case velocity deficit development

The initially large velocity deficit observed at z/D = 32.0 is start-up vortex generated. Once the vortex is far removed, transients die out, and only the steady-state result remains. The z/D = 32.0 velocity deficit asymptotically approaches to a zero magnitude due to the diffusive effects of jet induced turbulence. Therefore, the double-hump velocity profile is characteristic of the injector exit and vortex regions of the jet, but not in between. In effect, the steady-state injector exit velocity deficit is not sustained by the start-up vortex.

6.4.1 More Code Validation

One of the first areas of concern investigated was the handling of the axi-symmetric code's symmetry axis boundary conditions. This is of concern since this boundary coincides with the centre of the initially suspicious velocity deficit. Cases 6 and 7 reveal a similar velocity deficit to the Base Case (see Figure 6.6). Case 6 checks the axi-symmetric code against a symmetric 2-D Cartesian code by showing that the presence of a velocity deficit is not a function of the coordinate system. Case 7 checks the 2-D Cartesian code, and indirectly the axi-symmetric code, axis boundary condition by solving over the entire fluid flow domain (i.e., the need to specify a boundary condition on the axis of symmetry is completely removed). As required, Case 6 and Case 7 velocity, temperature, pressure, and mass fraction distributions are identical.

A second area of concern in the code was the handling of the boundary conditions at the sharp corners of the injector exit, especially given the large pressure drop across the

exit. Cases 2 and 3 are similar to Cases 6 and 7 except that the injector is replaced by uniform velocity, temperature, pressure, and fuel mass fraction boundary conditions.

Since the double-hump velocity profile also develops in the presence of uniform boundary conditions (see Figure 6.7), where code handling of the corner is markedly different, indications are that the corner is not a problem with respect to the trends observed. As a quantitative check on the code's handling of the corner the number of grid points is approximately doubled (Case 8). If the corner is a problem then this finer spatial resolution should translate into differences in velocity profile development. As can be seen in Figure 6.8, Case 8 profiles match the coarser, corresponding, Case 5 profiles well. The maximum difference between Case 5 and Case 8 velocities occurs on the centerline and is 6%. Therefore, it is concluded that the sharp injector exit corner is not a major problem.

Interestingly, it is also revealed in Figure 6.7 that the impact the uniform exit profile boundary condition is for the uniform profile to compete with velocity deficit, with the uniform profile eventually dominating the flow. That is, when the start-up vortex is far downstream, the velocity deficit is eventually replaced with a jet structure characteristic of uniform boundary condition steady-state jets [Abramovich, 1963].

6.4.2 Double-Hump Velocity Profile Origin

Case 2 proved very useful. It enabled the author to identify at least one physical reason for the double-hump axial velocity profile. This was achieved by solving the discretized conservative equations by hand in the vicinity of the injector exit. First, as required, mass, momentum, and energy conservation were confirmed to hold for each computational control volume. It was then established that the velocity deficit begins to
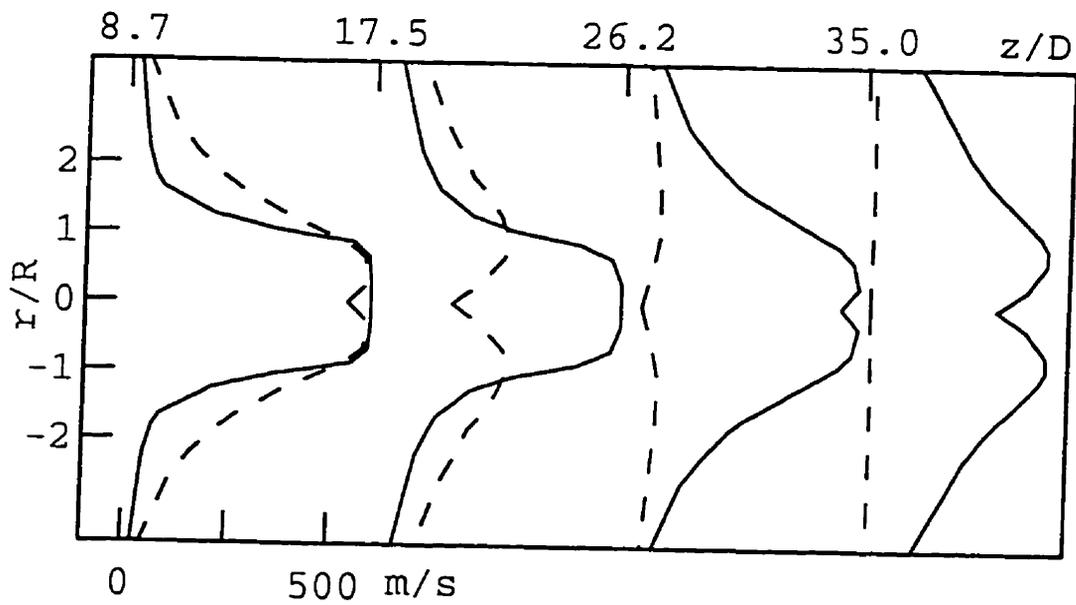
Figure 6.7: Existence of double-hump axial velocity profile for uniform injector exit boundary condition; Cases 2 and 3. R is orifice radius (- - - - 0.04 ms; ——— 0.1 ms).
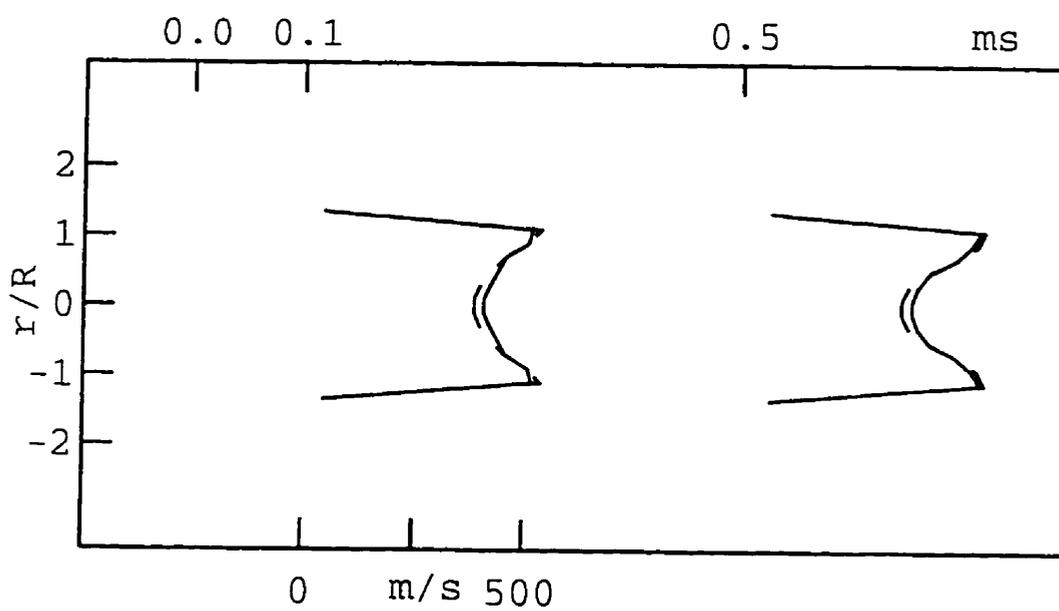
Figure 6.8: Effect of doubling grid resolution on velocity profile at z/D = 0.87.
(——— Case 8; - - - - Case 5).

form immediately. This should be of no surprise since the start-up vortex also begins to form immediately.

For Case 2 consider two control volumes just outside the injector exit. One adjacent to the axis-of-symmetry and the second radially adjacent to the first control volume. The axial velocity is constant across the injector-side face of both control volumes. Viscous effects are negligible as momentum dominates the flow. Radial expansion is driven by a radial pressure gradient. Pressure initially peaks on the axis of symmetry. By symmetry, no axial momentum is convected radially across the axis-of-symmetry, however, axial momentum is convected radially out across the common surface between the two control volumes being considered. It is next found that the axial momentum convected in and out of the second control volume is nearly balanced. Therefore, given that the axial convected axial momentum contribution is near equivalent for each control volume, then the second control volume's axial momentum must be greater than that of the control volume adjacent to the axis-of-symmetry. If the effects of density and temperature are neglected, then the axial velocity in the second control volume must also be greater. That is, a centerline axial velocity deficit is formed resulting in a double-hump velocity profile. In other words, the much smaller radial convection velocity can actually govern net control volume momentum. Though this discussion has been simplified by neglecting density and temperature effects, it is noted that the inclusion of these properties does not change the essence of this explanation.

In short, the injector exit double-hump velocity profile appears to be a by-product of the pressure distribution's control over the radial velocity combined with radial momentum convection dominance. In essence, expansion effects cause the double-hump

near the injector exit. Now, for Case 5, Figures 6.4 and 6.5 reveal a double-hump profile at the injector exit and at the head of the start-up vortex, but not in between. Therefore, it appears that the double-hump profile has at least two physical origins; the start-up vortex flow pattern and injector exit expansion effects.

If pressure plays a crucial role in establishing the double-hump velocity profile, how then can the double-hump profile extend to the interior of the injector orifice? That is, how can pressure information from downstream expansion travel upstream into the orifice given that Mach numbers greater than one are found within the orifice (see Figure 6.9)? The answer lies in the two-dimensional nature of the problem. In-cylinder pressure information first travels radially towards the orifice (radial Mach numbers are less than 0.02 everywhere) before propagating upstream through the orifice boundary layer.

Finally, the double-hump velocity profile is not an upstream effect. When starting, the orifice velocity profile is initially pipe flow like. Second, the velocity deficit is observed to gradually propagate up the orifice until a near steady-state situation is reached where the double-hump velocity profile extends only part way into the orifice.
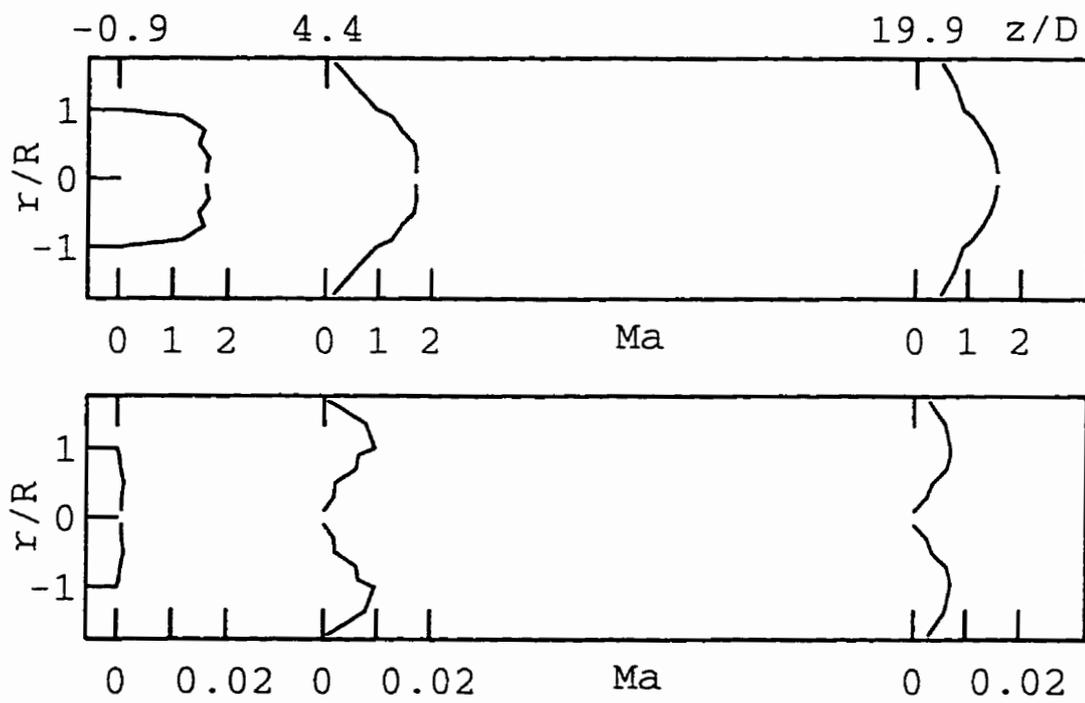
Figure 6.9: Base Case Mach number profiles after 0.5 ms in
the (a) axial and (b) radial directions.

6.5   Temperature

It is observed in Figure 6.2 for Case 1 that the injector exit static temperature profile is highly non-uniform varying from about 150 K to 1250 K. The peak temperature exceeds the initial total temperature of 444 K, even after the steady-state solution has been reached. The reason for the large temperature peaks and valleys is closely coupled to the pressure distribution. In particular, flow work [Reynolds et al., 1977] determines fluid parcel temperature.

It is easy to appreciate the importance of flow work on temperature in transient, compressible flows by considering the classical transient shock tube problem. Refer to Figure 6.10 for a schematic of classic one-dimensional shock tube velocity, temperature, and pressure profiles [Anderson, 1990]. Evidently, the local temperature *can* exceed the initial total temperature in transient compressing flows. The increase in temperature behind the transient shock is due primarily to flow or compression work. It can be shown that dissipative effects within a shock contribute little to the temperature increase across a shock [Anderson, 1984].

Considering the strong role of temperature on chemical kinetics, the fact that the injector exit-plane temperature profile ($z/D = -0.87$) varies by about 300 K may have profound implications on the validity of reacting flow conclusions reached using uniform exit profiles (see Figures 6.2 and 6.3). Ascertaining these implications is beyond the scope of this work.

Case 9 differs from the Base Case by starting with an initial cylinder air temperature of 1200 K instead of the base 444 K. The initial pressure in the cylinder is

kept constant through a compensating decrease in density. As can be seen in Figure 6.11, jet penetration is greater for Case 9 than the Base Case after 0.1 ms. The trend of increased jet penetration given increased cylinder temperature is further substantiated by Case 1 and Case 10 results also shown in Figure 6.11. Results for Case 11, not shown, are also consistent with this trend. If molecular viscosity decreased with temperature then the added retarding force could possibly explain this trend.
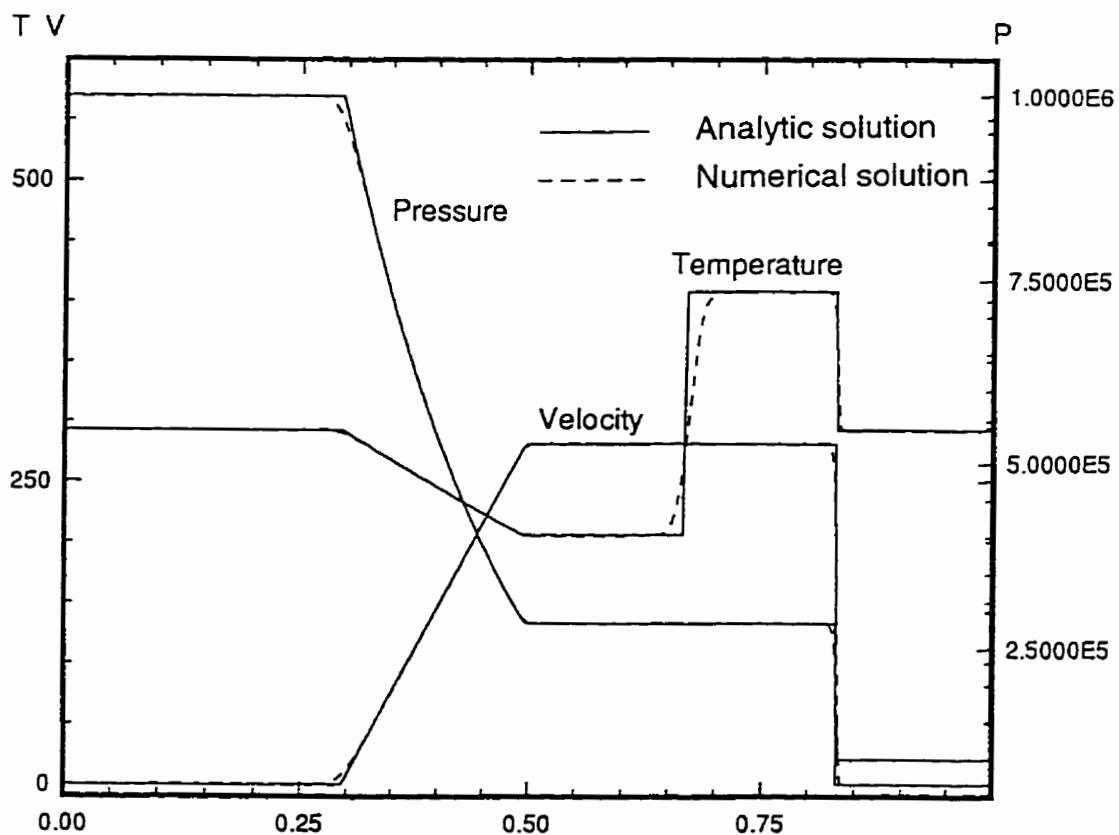

Figure 6.10: Classical one-dimensional shock tube velocity, temperature and pressure profiles.
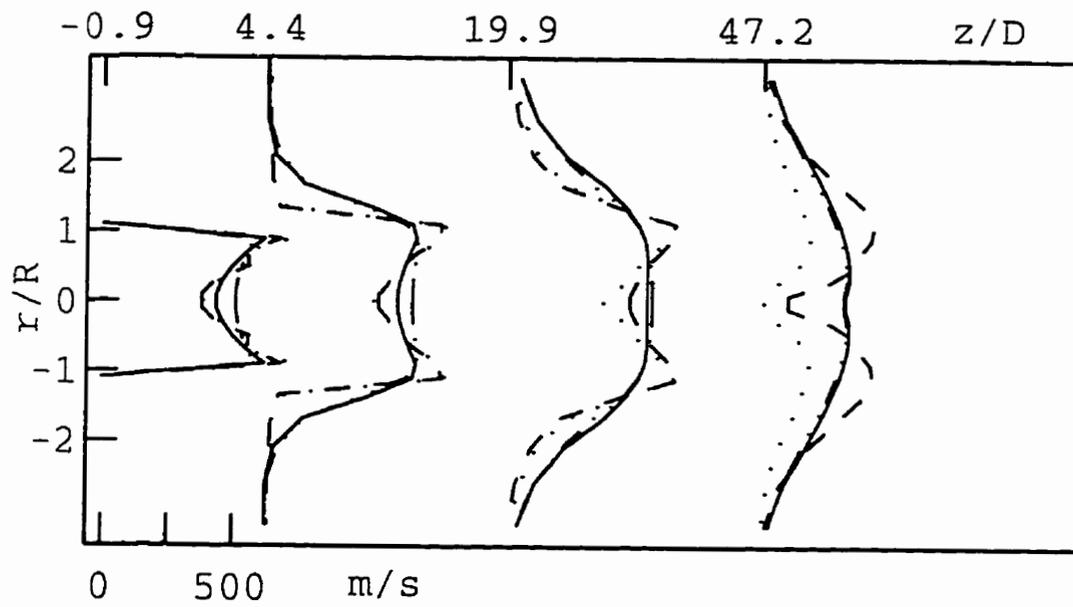
Figure 6.11: Effect of temperature and turbulence on jet profiles
for the Base Case (· ·⁣·· · ··) and Cases 1 (————)
9 (- - - - -) and 10 (—··— ··—) after 0.1 ms.

Unfortunately, the molecular viscosity of air almost doubles between 444 K to 1200 K (Sutherland formula [Anderson, 1984]). The explanation for increasing jet penetration with temperature seems to be related to the increase in sound speed associated with higher temperatures. In effect, information about the injection process travels downstream faster at 1200 K than 444 K. Figure 6.11 also reveals that an increase in cylinder temperature has a noticeable effect on the injector exit velocity profile.

Lastly, notice that the static wall temperature within the orifice (Figures 6.2 and 6.3) is below the initial wall temperature in Case 1, and above the initial wall temperature in the Base Case. Correspondingly, Case 1 has a net cooling effect on the injector. The Base Case is reversed in having a slight heating effect.

6.6 Turbulence and High Temperature

Confidence in the existence of the double-hump velocity profile first observed for Case 1 has been fairly well established as discussed above. This work now returns to diesel engine related considerations.

It is realized that the injector configurations discussed are only partial representations of actual DI diesel engine natural gas injection. Even Case 1 is limited by its omission of reacting flow considerations. Nevertheless, avoiding such complicating factors has proven very useful in isolating underlying physical processes. Of interest now is the influence of the complicating factor of turbulence.

Increasing in-cylinder turbulence levels is expected to increase the diffusive transport of mass, momentum, and energy. The results for Cases 1, 9, and 10 are shown

in Figure 6.11 confirm this expectation. For example, in the absence of initial cylinder turbulence Case 9 displays a strong double-hump velocity profile at z/D = 47.2. In contrast, the presence of high cylinder turbulence levels in Cases 1 and 10 smoothes this double-hump profile at z/D = 19.9 to such an extent that it is completely removed. Notice, that the presence of in-cylinder turbulence levels typical of I.C. engines has a significant impact on jet mixing and development downstream of the injector exit. Regardless, turbulence does not remove the velocity-deficit profile seen at the injector exit i.e., a strong double-hump profile still exists. The differences observed in the injector exit velocity profiles between Cases 1, 9, and 10 in Figure 6.11 are significant, however, in the sense that they complicate the task of identifying a universal velocity profile applicable over a reasonable range of diesel engine operating conditions. Injector exit profiles are sensitive to cylinder temperature and turbulence levels.

It is observed in Figure 6.4 for Case 5 and in Figure 6.11 for Cases 1 and 10 that in-cylinder turbulence levels representative of I.C. engines yield smooth, parabolic like velocity profiles. This characteristic of turbulence to yield velocity profiles more in line with those of uniform injector exit boundary conditions is important, because, it suggests that conclusions based on uniform type boundary conditions made by other modellers of natural gas DI engine injection may not be in such serious error, though this still needs to be confirmed. As mentioned previously, such confirmation is beyond the scope of this work.

6.7 Distribution of Species Concentration Without Reaction

Gas jet penetration distance and jet width are quantified. These quantities are defined in Figure 6.12. Gas jet penetration is determined from the maximum axial extent of the 5% and 50% fuel mass fraction contours. Similarly, jet width is determined from the maximum width of the 5% and 50% fuel mass fraction contours. Another parameter of practical importance is the total mass of fuel injected.
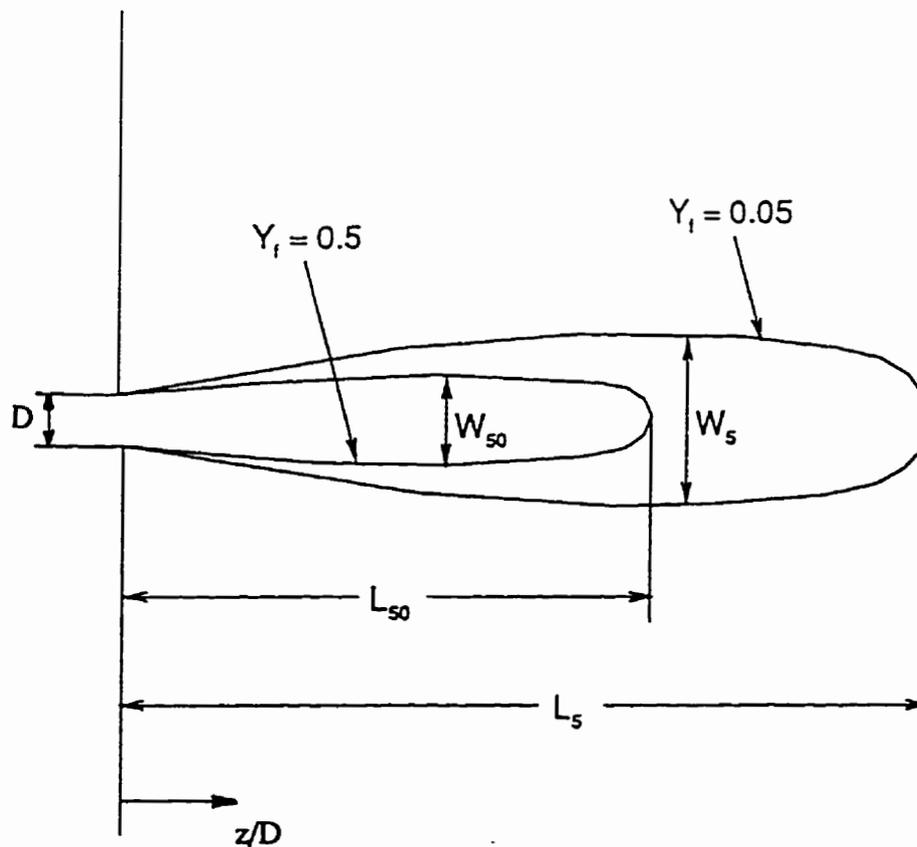

Figure 6.12: Schematic defining jet penetration distance and jet width. Y_f is the fuel mass fraction.

Figure 6.13 shows plots of jet penetration distance, jet width, and injected fuel mass as functions of time for the Base Case and Cases 5, 13, 14, 15, and 16. These cases investigate the influence of orifice geometry on jet behaviour as well as providing a handle on the impact of in-cylinder turbulence.

It is seen in Figures 6.13a and 6.13b that the effect of turbulence is to retard jet penetration, L, and to broaden the jet's width, W. This is not surprising. The injected fuel mass diffuses sideways faster in the presence of turbulence, consequently, by conservation of mass, the penetration distance cannot be as great. Second, jet penetration increases slightly with decreasing L/D as shown in Figure 6.13c. This is inconsistent with the notion of increased frictional losses within the longer orifice. But it is consistent with the hypothesis that the larger diameter orifice used to decrease L/D decreases the back-pressure seen by the orifice in Cases 14 and 16 more than in Cases 13 and 15. The decreased back-pressure decreases injector exit velocity and hence jet penetration. Inspection of injector exit velocity confirms this decrease. Third, the mass injected varies little for all cases with similar orifice diameter. Figure 6.13d, however, reveals that a doubling in orifice diameter increases the mass flow by more than the associated increase in orifice area. A more than four fold mass flow increase is expected since the volume to surface area ratio of the orifice is also increased, i.e., the percentage contribution from orifice wall friction effects is correspondingly decreased.

Data as shown in Figure 6.13 are presented only as a potential aid to those familiar with liquid-fuel diesel engine injection [Bracco, 1985] and who would like to attempt to draw comparisons.
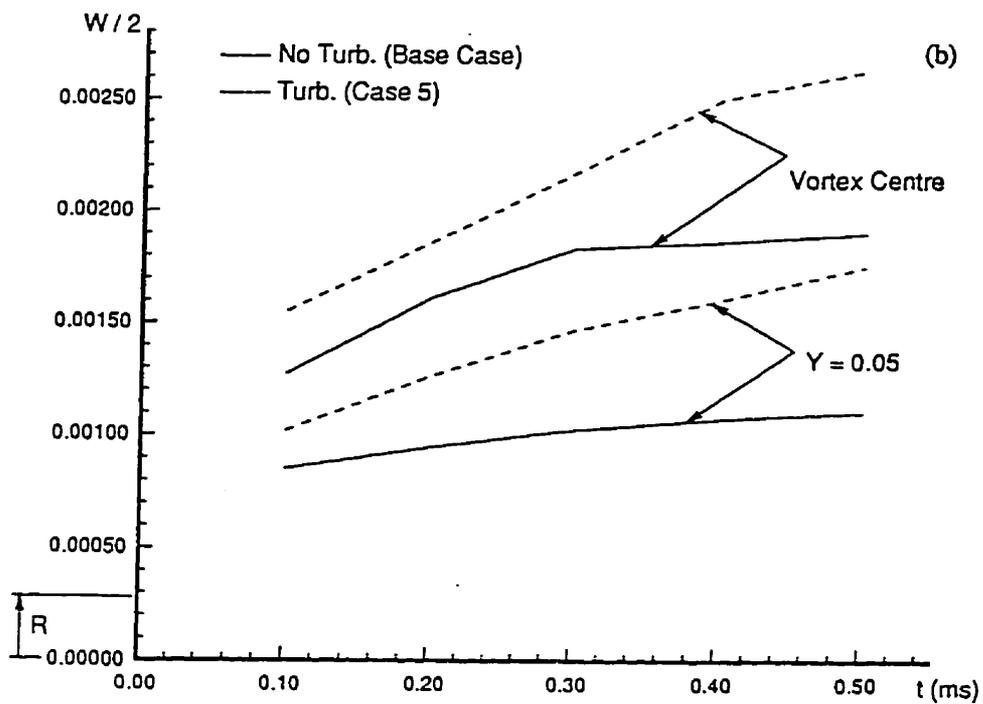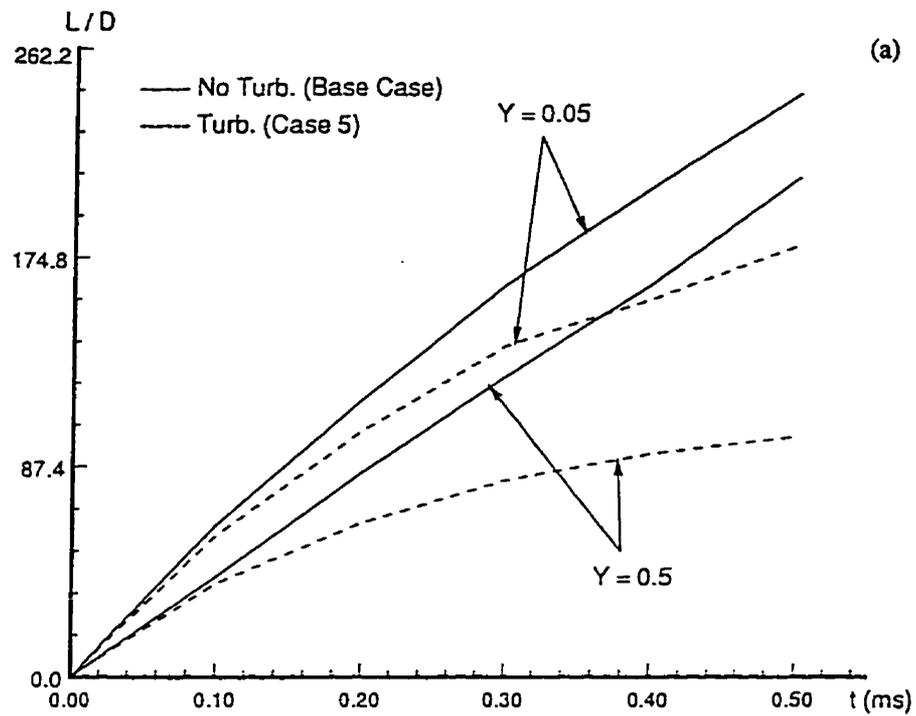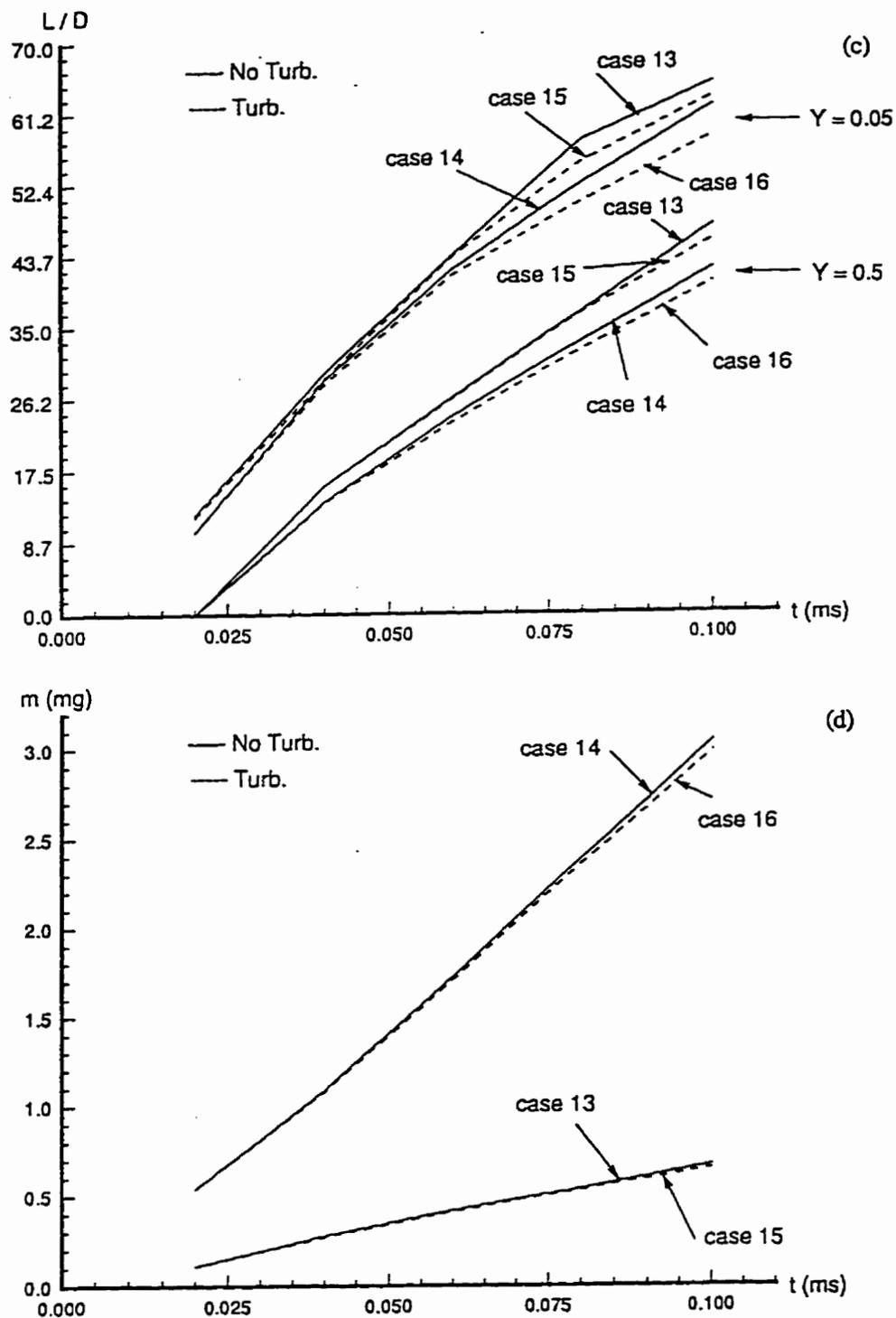
Figure 6.13: Jet development as measured by jet penetration, L, jet width, W, and net injected mass for the base case and case 5, 13, 14, 15, and 16.

6.8. Optimized Reaction Model

A review of previous simplified reaction models found that no global ignition models for natural gas autoignition exist. Many global models do exist for systems after ignition, but these models cannot be expected to be able to capture the low temperature reactions responsible for ignition. One way to generate an ignition model is to modify an existing reaction model by using numerical regression or numerical optimization.

The natural gas ignition model selected for optimization is the combustion submodel of Naber et al. [1994]. This submodel is based upon a large pool of after ignition experimental data. It assumes a two-step kinetic mechanism to account for the oxidation of methane.

Comparing natural gas autoignition computations using the reaction submodel of Naber et al. [1994] and the experimental data of Naber et al. [1994] reveal large disagreements. This is not surprising given the post ignition origin of the reaction submodel. The approach to be pursued have to improve computational and experimental agreement will be to modify the reaction submodel's Arrhenius constants and activation energies.

The first of the two global reaction rate equations, Equation (3.14) controls the disappearance of methane and generates carbon monoxide. The reaction equation plays a preconditional role, it is the rate limiting step that primarily establishes the autoignition delay time. Therefore, the Arrhenius constant and the activation energy of Equation (3.14) are optimized first.

The optimization procedure utilized is as follows. Naber et al.'s experimental results show three curves representing ignition delay time versus temperature for three different initial densities: 6.4 kg/m³, 20.2 kg/m³, and 32.6 kg/m³. From each curve three points are selected, as shown in Figure 6.14. A least-squares minimization fitting expression can be written as

$$\chi^2 \equiv \sum_{i=1}^{9} (\tau_i' - \tau_i)^2 \tag{6.1}$$

where the τ_i' models the delay time which corresponds to a particular initial temperature and density. The goal is to obtain the maximum likelihood estimate of the two model parameters, Arrhenius constant A and activation energy E, by minimizing residual χ^2. Here τ_i' is a function of A and E, but the function cannot be expressed by a mathematical formula. Making it impossible to explicitly evaluate the derivatives of $\chi^2(A, E)$. One possible solution is to select parameter intervals of A and E,

$$\begin{aligned} A_1 &\leq A \leq A_2 \\ E_1 &\leq E \leq E_2 \,. \end{aligned} \tag{6.2}$$

These intervals represent a rectangular area. In each step of the search for a converged estimate of the optimum A and E, the four points in this rectangular area are selected by Golden section method, which generates the following expressions

$$A_1^{\ 1} = 0.382\ (A_2 - A_1),$$

$$A_2^{\ 1} = 0.618\ (A_2 - A_1),$$

$$E_1^{\ 1} = 0.382\ (E_2 - E_1), \hspace{2cm} (6.3)$$

$$E_2^{\ 1} = 0.618\ (E_2 - E_1),$$

$$A_1\ <\ A_1^{\ 1}\ <\ A_2^{\ 1}\ <\ A_2\ ,\ \text{and}$$

$$E_1\ <\ E_1^{\ 1}\ <\ E_2^{\ 1}\ <\ E_2$$

Suppose that test results are written as

$$\chi^2\big|_{11}^{\ 1}(A_1^{\ 1}, E_1^{\ 1}),$$

$$\chi^2\big|_{12}^{\ 1}(A_1^{\ 1}, E_2^{\ 1}),$$

$$\chi^2\big|_{21}^{\ 1}(A_2^{\ 1}, E_1^{\ 1}), \hspace{2cm} (6.4)$$

$$\chi^2\big|_{22}^{\ 1}(A_2^{\ 1}, E_2^{\ 1})$$

and $\chi^2\big|_{22}^{\ 1}$ is a minimum value for the four χ^2s, i.e.,

$$\chi^2\big|_{22}^{\ 1} < \chi^2\big|_{11}^{\ 1},\ \chi^2\big|_{12}^{\ 1}\ \text{and}\ \chi^2\big|_{21}^{\ 1}. \hspace{2cm} (6.5)$$

The next A and E interval to be tested is reduced in size to

$$A_1^1 \leq A \leq A_2$$
$$E_1^1 \leq E \leq E_2 \; .$$

$$(6.6)$$

This rectangular area is only approximate 37.8 % of the last one. This procedure of reducing the interval size is continued until acceptable accuracy is obtained for the estimates of the least-square minimizing optimized A and E. The optimized model obtained using the Golden search method is

$$-\frac{d[CH_4]}{dt} = 6.5 \times 10^8 \exp\left(\frac{-2.6000 \times 10^4}{T}\right) [CH_4]^{0.7} [O_2]^{0.8}$$

$$-\frac{d[CO]}{dt} = 1.423 \times 10^7 \exp\left(\frac{-1.9639 \times 10^4}{T}\right) [CO][O_2]^{0.25} [H_2O]^{0.5}$$

$$(6.7)$$

Figure 6.14 compares the zero-dimensional, detailed kinetics, modeling effort of Naber et al. [1994] to their experimental results. Although the agreement is poor the expected trend of decreasing ignition delay time with increasing density is observed. It is not surprising that this model does not work well as it cannot account for jet mixing contributions. Figure 6.15 shows the status of this work's attempt at obtaining a global kinetic scheme that works in combination with the detail modelling of injection jet fluid flow. The agreement between model and experiment shown in Figure 6.15 is better than that of Figure 6.14, but it is still poor. One possible explanation for the poor agreement in Figure 6.15 is that varying the Arrhenius constant and activation energy in Equation (6.7) provides insufficient flexibility to bring least-square closer to zero.
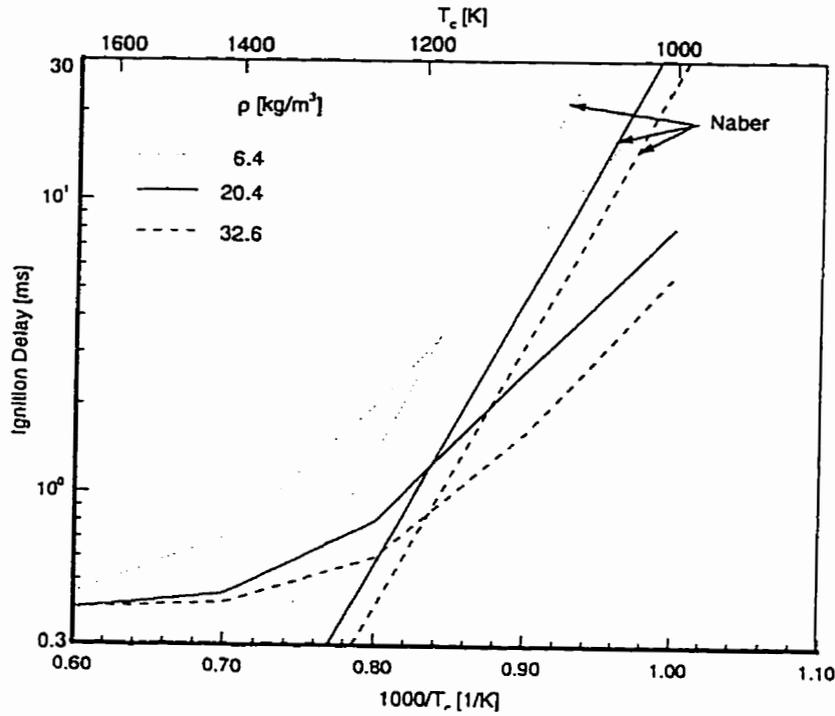
Figure 6.14: Comparison of Naber et al.'s [1994] kinetic model and experiment results.
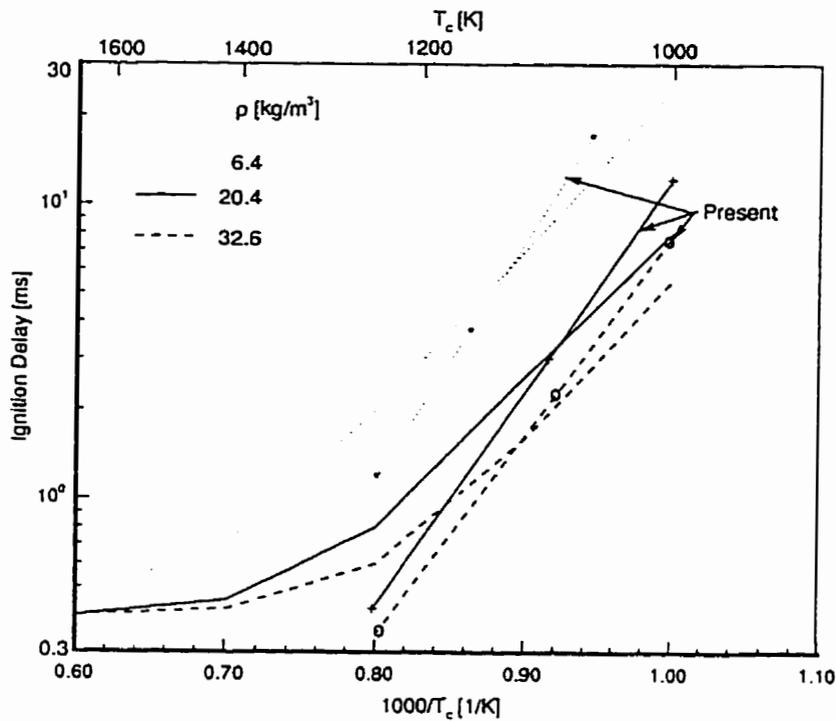
Figure 6.15: Comparison of present model and Naber et al.'s [1994] experiment results.

All possible parameters for use in the least-square minimization search would be much more expensive in computer time and should be the subject of future study. It may also be that the two-step global reactions of Equations (3.14) are incapable of capturing the ignition physics and that some other unknown set of equations need to be used. It is computationally prohibitive, however, to use a detailed set of elementary equations, a global reaction scheme needs to be found.

6.9. Ignition Delay and Ignition Location

Thermal considerations play the key role in the ignition processes. In addition, a specific range of fuel-air ratios is a necessary condition for ignition. A local reaction rate depends upon local temperature, local mixing rate, local molecular diffusivities, and local concentrations. When the rate of thermal energy release by the reaction is greater than the rate of thermal energy loss an ignition condition exists. When the opposite condition exists, ignition is impossible. When the two energy rates are equal, a critical thermal ignition condition ignition exists. There are two induction periods [Kuo, 1986], or ignition delay times, associated with the ignition of a premixed charge. First, there is the chemical time τ_c required for the charge to build up a critical concentration of radicals. Second, there is the thermal time τ_t associated with the time it takes for the system to reach the thermal ignition condition. Natural gas injection and subsequent autoignition,

however, is not a premixed charge situation and involves another induction time, the jet convection with turbulent mixing time.

To identify the location of autoignition two macro conditions must be met: (1) a high temperature on the order of the adiabatic flame temperature; and (2) a fuel-air concentration within flammability limits. Figure 6.16 summarizes observations concerning the location at which injected natural gas autoignites. The vortex referred to in Figure 6.16 is the start up donut vortex that accompanies, but trails slightly, the head of the natural gas jet. One consistent feature concerning autoignition site location is that it is always behind the vortex center. Another consistent feature is that autoignition occurs nearer the jet centerline than the vortex center.

Locations A, B, C, D, and E around vortex center are highlighted in Figure 6.17. The high temperature condition is satisfied at almost all locations. There are, however, large concentration differences between location A, B, C, D, and E. Locations B and E always present lean fuel concentrations. Note that the injection process is an unsteady state process that leads to vortex center forward-movement in time. Therefore, it is impossible for ignition to occur in locations B and E. Locations C, D, and A are possible autoignition sites. One-dimensional shock tube analysis points out that shock speed is always faster than contact surface speed. In other words, pressure propagation speed is much faster than any local flow speed. In the case of two-dimensional or axi-symmetric injection, pressure information generates the vortex and pushes it ahead. It is therefore difficult for the natural gas fuel to reach the vortex center, hence, the lean fuel status at locations D and A. At location C (see Figure 6.18), high temperature fresh air merges with the incoming natural gas fuel and combines via turbulent mixing.
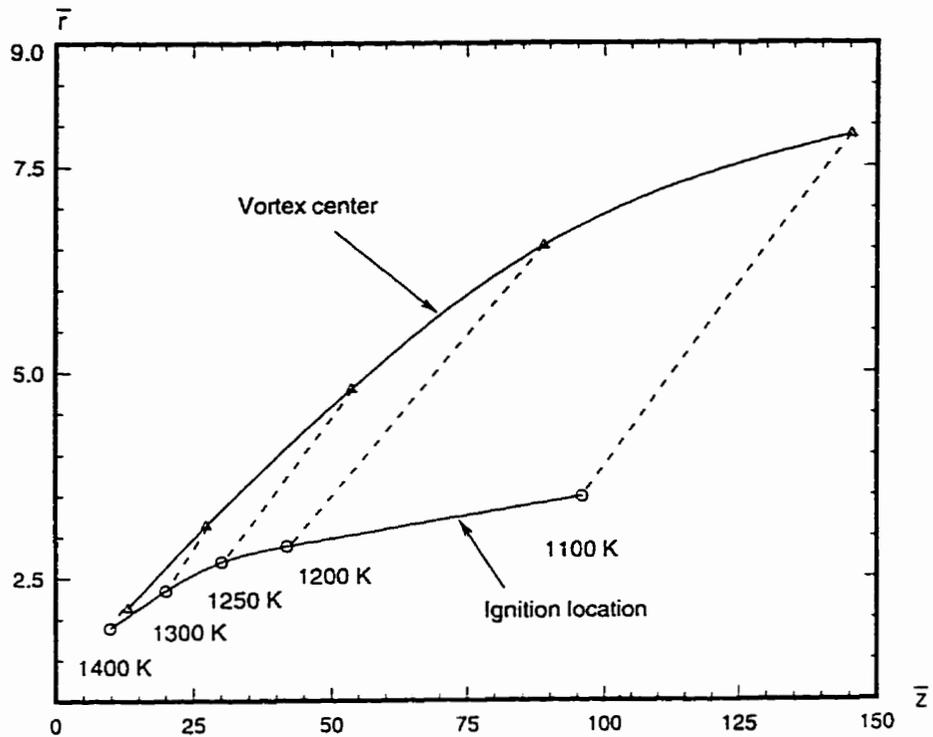
Figure 6.16: Computational results of autoignition location and vortex center.
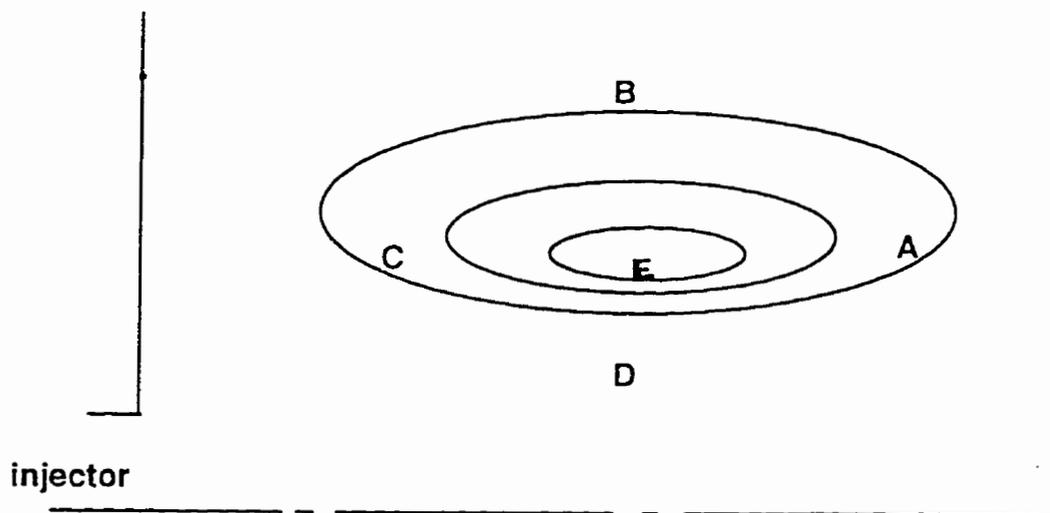
Figure 6.17: Analysis of ignition location around vortex.

The temperature and fuel-air concentration at location C are well suited for building up to a critical radical concentration and to the thermal ignition condition. Consequently, location C is the most probable ignition site. Experimental verification of this model prediction does not exist but is critical in order to better ascertain our modelling capabilities.

Finally, it is observed that as soon as the ignition occurs at location C the resulting high pressure source reduces the intensity of the startup vortex while also generating a second vortex behind ignition location C (see Figure 6.19).
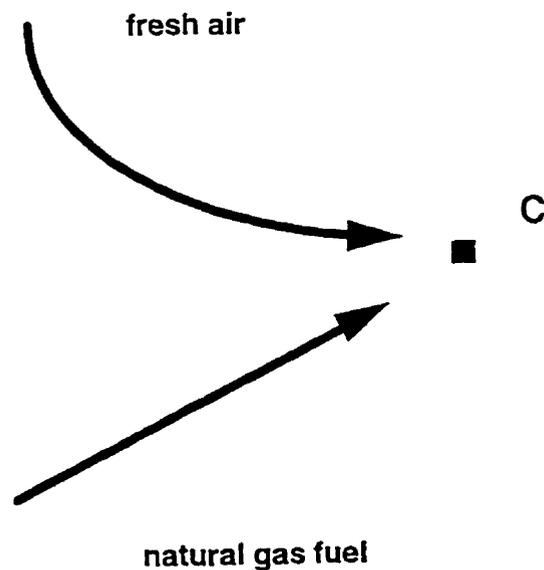
Figure 6.18: Mixing around ignition site.
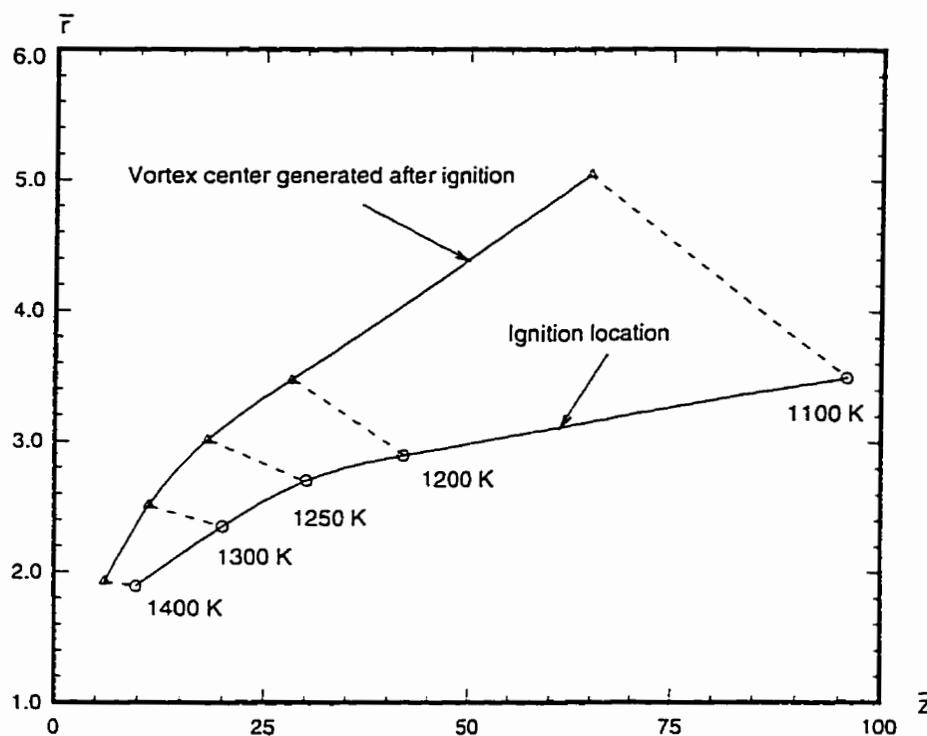
Figure 6.19: Vortex generated behind ignition site after ignition.

6.10. Closure

This work's first objective was to establish the injector/cylinder interface boundary conditions appropriate for diesel engine modelling purposes. The establishment of appropriate injector/cylinder boundary conditions is of interest since it will hopefully remove the need to model the finer details of injector operation, thus permitting future computational efforts to focus on in-cylinder mixing and combustion processes. The complexity of the injection process, however, has prevented the identification of a universal

set of injector exit profiles characteristic of natural gas injection into diesel engines. This work investigated in some detail the non-intuitive injector exit velocity, temperature, and pressure profiles observed. The major conclusions reached are as follows:

1)   The uniform injector exit velocity and temperature profiles currently used in the modelling of diesel engine, high-pressure, transient, natural gas injection are *not* even good first approximations to the actual profiles. Velocity displays a double-hump profile with peak values occurring within the jet mixing layer. Temperature variations greater than 300 K are observed at the injector exit. These profile complications are a direct result of the jet being underexpanded.

2)   Cylinder turbulence at levels characteristic of diesel engines quickly dominates the jet's velocity field. This may imply that modellers of diesel engine, natural gas, jet mixing processes need not be overly concerned about the dissimilarities noted in conclusion 1 above. This implication, however, still needs to be verified.

3)   Given the strong role of temperature on chemical kinetics, the temperature dissimilarities noted in conclusion 1 should be of serious concern. In particular, it may have profound implications on the validity of reacting flow conclusions reached using uniform exit profiles.

4)   The non-uniform temperature profile observed at the injector exit is primarily a result of compressibility effects, or more specifically, flow work. The origin of the non-uniform velocity profile is more difficult to explain beyond noting an apparent close coupling to the pressure field.

The impact of these findings on the conclusions reached by modellers assuming uniform profiles is beyond the scope of this work, and as such, is yet to be determined. The

two greatest needs at the moment are profile verification, ideally through experiment, and more information on injector construction and operation.

Section 6.8 presents a modified kinetic mechanism based on a previous proposed reaction model [Naber et al., 1994]. The numerical results using the modified reaction submodel yields improved agreement between modelling efforts and the experimental data of Naber et al. [1994]. Autoignition location is computationally studied and found to be consistent with physical expectations. The most likely autoignition location is behind startup vortex closer to the jet centerline than the vortex centre.

Finally, this work has idealized the start-up phase of injection as an instantaneous event. This omission may not be insignificant with respect to its control over initial fuel-air mixing and subsequent autoignition. However, without a more detailed knowledge of injector construction and operation, this omission cannot easily be critiqued further. Since this work omits reacting flow and concentrates on momentum dominated, pressure driven, jet dynamics, concern over injector start-up is assumed minimal. In addition, injector closing has been completely ignored. In short, there is a definite need to have more information on injector construction and operation.

Chapter 7.

Closure

7.1. Summary

This work attempts to model the autoignition process for high pressure natural gas injected into a diesel engine type environment. Corresponding experimental data measured over a wide range of initial pressure, density, and temperature conditions is used for model evaluation. Previously proposed detailed and simplified models have yielded poor predictions of injected natural gas autoignition delay times. This is no doubt due to the fact that these models all ignore the influence of the jet mixing process. This work overcomes this weakness by including a detailed simulation of the jet injection fluid mechanics, hence, the first phase of this work concentrated on the fluid mechanics of the problem without reactions. Two major results of this phase are the identification of a double-humped injector exit velocity and temperature profile, and the observation that fuel injected at 444 K reaches a peak temperature due to compression effects of about 300 K higher in absence of chemical reactions. This latter observation may play a critical role

in natural gas autoignition given temperature's dominant role in kinetics. The second phase of this work adds kinetics to the problem. Numerical regression is used to optimize the simplified kinetic scheme used in order to better match experiment.

A review of the literature shows that almost all numerical autoignition studies are restricted to shock tubes. Shock tube studies provide properties for premixed chemical reaction such as autoignition delay time, activation energy, temperature, and pressure trends and the effect of additives. Such studies, however, do not simulate the majority of conditions found in diesel engine combustion chambers. For example, in a real engine, fuel and air are not fully premixed, flows are not one-dimensional, and turbulent mixing is involved. In addition these numerical studies cannot predict the ignition location which is very useful for design purposes and for gaining insights into the physics of gaseous combustion in diesel engines.

A review of previous simplified reaction models found that many simplified reaction models do exist that consider the reaction after ignition, but these models are of little use. Ignition being a low temperature phenomenon involves different dominant reactions than the high temperature reaction process. The development of a simplified reaction model therefore become a requirement of this research.

The process of natural gas autoignition in diesel engines is very complicated, correspondingly model simplifications are needed. A constant volume combustion chamber based on the experimental work of Fraser et al. [1991] is used. A cylindrical shaped chamber that is 2-D axisymmetric is used in place of the experiments 3-D disk/injector geometry however. This geometry change should not affect the characteristics of natural gas injection and autoignition as long as injected gas does not

impinge on the wall of combustion chamber before autoignition occurs. Another important assumption is that the turbulent kinetic energy in the combustion chamber is far less than that actually observed in diesel engines. That is, the in-cylinder turbulence has been decoupled from the problem for both the computations and the experiments, thus permitting the flow to be jet dominated. Several computations, however, did include turbulent intensities typical of diesel engines for comparison purposes.

In order to solve the natural gas autoignition problem it was also necessary to incorporate suitable numeric calculation strategies. This included the use of computational space methods and an evaluation of linear equation solvers. Two iteration solvers were particularly attractive due to their low storage requirements. Ultimately a new conjugate gradient solver called B-CGSTAB was developed in this work. B-CGSTAB is a block preconditional conjugate gradient solver with low storage requirements, stability, and an ability to maintain a strong coupling between equations via the use of a direct solver for each diagonal block. Pivoting is used in the preconditioning.

Local supersonic flow has been identified as the cause of the unexpected double-hump velocity and temperature profile at the injector/cylinder interface (i.e., boundary condition). Initially the injector orifice velocity profile is pipe flow like. It then quickly forms a velocity deficit that propagates up the orifice. The double-hump velocity profile forms as this velocity deficit passes but extends only slightly into the orifice. The importance of this double-hump profile on the autoignition process is not fully understood but it certainly reveals that previously assumed parabolic and box-hat exit profiles are inappropriate should, for example, the 300 K temperature increase associated

with the double-hump severely impact the kinetics. The double-hump profile persists due to radial expansion from the supersonic jet.

Local reaction rates depend on local species concentrations and local temperature. For natural gas injection the mixing process directly impacts on both of these. Based on a two-step global kinetic mechanism and experimental data a model for injected diesel engine natural gas autoignition is presented. This model is obtained by optimizing the Arrhenius constant and activation energy such that the squared deviation between computed and experiment autoignition times are minimized.

Finally, a first attempt at identifying the location of the autoignition site is undertaken. Controlling the ignition site may prove useful in improving subsequent combustion, e.g., an ignition site that immediately impinges on the wall may experience more quenching. Preliminary results indicate that the most probable initial ignition site is located behind the injection jet's start-up vortex and toward the jet centerline.

7.2. Recommendations for Future Research

There are three major areas for future research that will either improve or greatly extend this work. They are as follows:

(1)   The global kinetic model should be further optimized allowing for variable activation energy, Arrhenius constant, concentration exponents, perhaps a pre-exponential temperature exponent, and more iterations.

(2)   Piston motion and more complex geometries indicative of commercial diesel

         engines need to be investigated using expected in-cylinder turbulence levels.

(3)   Mixing effects on autoignition site control can be investigated.

References

[1]   Abramovich, G.N., The Theory of Turbulent Jets, MIT Press, Cambridge, Massachusetts, 1963.

[2]   Agarwal, A and D.N. Assanis, "Modeling the Effect of Natural Gas Composition on Ignition Delay under Compression Ignition Conditions," SAE Technical Paper No. 971711, Dearborn, Michigan, May 5-8, 1997.

[3]   Ahmadi-Befrui, B., A.D. Gosman and A.P. Watkins, "Prediction of In-Cylinder Flow and Turbulence with three Versions of k-e Turbulence Model and Comparison with Data," Flows in Internal Combustion Engines -II, ASME, New York, pp. 27-37, 1984.

[4]   Allen, J.S. and S.I. Cheng, "Numerical Solutions of the Compressible Navier-Stokes Equations for the Laminar Near Wake," Physics of Fluids, Vol. 13, No.1, pp.37-52, 1970.

[5]   Amsden, A.A., J.D. Ramshaw, P.J. O'Rourke, and J.K. Dukowitz. "KIVA - A Computer Program for Two and Three Dimensional Fluid Flows with Chemical Reactions and Fuel Sprays," LOS ALAMOS National Laboratories, Report LA-10245-MS, 1985.

[6]   Anderson, J.D., Jr., <u>Modern Compressible Flow With Historical Perspective</u>, 2nd Ed., McGraw-Hill, Toronto, 1990.

[7]   Beck, N.J., "Natural Gas-A Rational Approach to Clean Air," SAE Paper 902228, 1990.

[8]   Bilger, R.W., S.H. Starner, and R.J. Kee, "On Reduced Mechanisms for Methane-Air Combustion in Nonpremixed Flames," Combustion and Flame, Vol..80, p.135-149, 1990.

[9]   Bradshaw, P., Topics in Applied Physics, Vol.12, Turbulence, Springer-Verlag, New York, 1976.

[10]   Brandt, A., "Multi-Level Adaptive Solutions to Boundary-Value Problems," Math. Comput., Vol.31, 1977.

[11]   Carey, G.F., K.C. Wang, and W.D. Joubert, "Performance of Iterative Methods for Newtonian and Generalized Newtonian Flows," Internat. J. Numer. Methods Fluids, Vol.9, p.127-150, 1989.

[12]   Chen, K.-H. and R.H. Pletcher, "Primitive Variable, Strongly Implicit Calculation Procedure for Viscous Flows at All Speeds," AIAA Journal, Vol. 29, No. 8, pp. 1241-1249, August 1991.

[13]   Cooke, D.F. and A. Williams, "Shock Tube Studies of Methane and Ethane Oxidation," Combustion and Flame, Vol.24, p.245, 1975.

[14] Dandy, D.S. and L.G. Leal, "A Newton's Method Scheme for Solving Free-Surface Flow Problems," Internat. J. Numer. Methods Fluids, Vol.9, p.1469-1486, 1989.

[15] Demirdzic, I., Z. Lilek, and M. Peric, "Fluid Flow and Heat Transfer Test Problems for non-Orthogonal Grids: Bench-Mark Solutions," International Journal for Numerical Methods in Fluids, Vol.15, pp.329-354, 1992.

[16] Dwyer, H.A., B.R. Sanders, and F. Raiszadek, "Ignition and Flame Propagation Studies with Adaptive Numerical Grids," Combustion and Flame, Vol.52, p.11-23, 1983.

[17] El Tahry, S.H., "k-e Equation for Compressible Reciprocating Engine Flows," Journal of Energy, Vol. 7, No. 4, pp. 345-353, 1983.

[18] Fraser, R.A., C.J. Edwards, and D.L. Siebers, "Autoignition of Methane and Natural Gas in a Simulated Diesel Environment," SAE Paper No. 910227, 1991.

[19] Freund, R.W., "A Transpose-Free Quasi-Minimal Residual Algorithm for Non-Hermitian Linear Systems," Submitted to SIAM Journal on Scientific and Statistical Computing, 1991.

[20] Harten, A., J.M. Hyman, and P.D. Lax "On Finite Difference Approximations and Entropy Conditions for Shocks," Communications on Pure and Applied Mathematics, Vol.29, pp.297-322, 1976.

[21] Heffington, W.M., G.E. Parks, K.G.P. Sulzmann, and S.S Penner, "Studies of Methane-Oxidation Kinetics," Sixteenth Symposium (International) on Combustion, p.997, The Combustion Institute, Pittsburgh, 1977.

[22] Hirt, C.W., "Heuristic Stability Theory for Finite-Difference Equations," J. of Compu. Physics, Vol.2, pp.339-355, 1968.

[23]   Howard, D., W.M. Connolley, and J.S. Rollett, "Unsymmetric Conjugate Gradient Methods and Sparse Direct Methods in Finite Element Flow Simulation," Internat. J. Numer. Methods Fluids, Vol.10, p.925-945, 1990.

[24]   Hutchinson, B.R. and G.D. Raithby, "A Multigrid Method based on the Additive Correction Strategy," Numerical Heat Transfer, Vol.9, 1986.

[25]   Hutchinson, B.R., S.R. Elias, and S.D. McMillan, "The Evaluation of A Numerical Error Estimation Technique For Engineering Flows," CFD 96, Ottawa, Ontario, Canada, June 2-6, 1996.

[26]   Ishii, K., M. Kono, K. Niu, T. Tsukamoto, and Y. Ujiie, "Analysis of Ignition Mechanism of Combustible Mixtures by A Short Duration Sparks," International Symposium COMODIA, p.153-158, 1990.

[27]   Jeske, F.R. and M. J. Jennings, "Modelling of the Natural Gas Injection Process in a Two-Stroke Diesel Engine," SAE Technical Paper 920192, 1992.

[28]   Jiang, R.W., S.M. Gao, and J.K. Wu, "Linear Algebra (Chinese)" People's Education Publishing Company, 1978.

[29]   John, J.E.A., Gas Dynamics, Second Edition, Allyn and Bacon, Inc. 1984.

[30]   Jones, W.P., "Models for Turbulent Flows with Variable Density and Combustion", Imperial College, London, England, 1973.

[31]   Jones, W.P. and B.E. Launder, "The Prediction of Laminarisation with A Two Equation Turbulence Model," Int. J. Heat Mass Transfer, Vol.15, p.301, 1972.

[32]   Jones, W.P. and J. McGuirk, "Mathematical Modelling of Gas-Turbine Combustion Chambers," AGARDC, p.275, 1980.

[33] Jones, W.P. and J.H. Whitelaw, "Calculation Methods for Reacting Turbulent Flows: A Review," Combustion and Flame, Vol.48, p.1-26, 1982.

[34] Kansa, E.J., "Shock Computations With Adaptive Mesh Refinement and Moving Grids," Comput. Math. Applic., Vol. 15, No. 6-8, pp.623-634, 1988.

[35] Karki, K.C. and S.V. Patankar, "Pressure Based Calculation Procedure for Viscous Flows at All Speeds in Arbitrary Configurations," AIAA Journal, Vol. 27, No. 9, pp. 1167-1174, September 1989.

[36] Kong, S.C., N. Ayoub, and R.D. Reitz, "Modeling Combustion in Compression Ignition Homogeneous Charge Engines," SAE Technical Paper 920512, 1992.

[37] Kono, M., K. Niu, T. Tsukamoto, and Y. Ujiie, "Mechanism of Flame Kernel Formation Produced by A Short Duration Spark," Twenty Second Symposium (International) on Combustion, p.1643-1649, 1987.

[38] Kou, T.W. and R.D. Reitz, "Three-Dimensional Computations of Combustion in Premixed-Charge and Direct-Injected Two-Stroke Engines," SAE Technical Paper 920425, 1992.

[39] Launder, B.E., "Progress in the Modelling of Turbulent Transport," Lecture Series 76, von Karman Institute for Fluid Dynamics, Belgium, 1972.

[40] Lax, P.D. and B. Wendroff, "Systems of Conservation Laws," Communication on Pure and Applied Mathematics, Vol.23, pp.217-237, 1960.

[41] Lilley, D.G., "Computer Modeling of Turbulent Reacting Flows in Practical Combustion Chamber Design," 17th Aerospace Sciences Meeting, New Orleans, January, 1979.

[42]   Liss, W.E., W.H. Thrasher, G.F. Steinmetz, P. Chowdiah, and A. Attari, "Variability of Natural Gas Composition in Select Major Metropolitan Areas of the United States," GRI Report GRI-92/0123, March, 1992.

[43]   Lumley, J.L., "Computational Modelling of Turbulent Flows," in Advances in Applied Mechanics No.18, Academic Press, New York, 1978.

[44]   MacCormack, R.W., "The Effect of Viscosity in Hypervelocity Impact Cratering," AIAA Paper No.69-354, 1969.

[45]   Majda, A. and S. Osher, "Numerical Viscosity and the Entropy Condition," Communications on Pure and Applied Mathematics, Vol.32, pp.797-838, 1979.

[46]   Mantel, T. and R. Borghi, "A New Model of Premixed Wrinkled Flame Propagation Based on A Scaler Dissipation Equation," Thirteenth International Colloquium on the Dynamics of Explosion and Reactive Systems, Nagoya University, 1991.

[47]   Matula, R.A., H.J. Gangloff, and K.L. Maloney, "Ignition Delays in Hydrocarbon Systems," Paper Presented at the Symposium on Hydrocarbon Combustion Chemistry, Division of Petroleum Chemistry, Inc., American Chemical Society, Dallas, 1973.

[48]   McNally, W.D. and P.M. Sockol, "Computational Methods for Internal Flows with Emphasis on Turbomachinery," NASA-TM-82764, Washington, D.C., 1981.

[49]   Miller, J.A., R.J. Kee, M.D. Smooke, and J.F. Grcar, Paper WSS/DI 84-10, Western States Section of the Combustion Institute, Spring Meeting 1984.

[50]   Naber, J.D., D.L. Siebers, J.A. Caton, C.K. Westbrook, and S.S. DiJulio, "Natural Gas Autoignition Under Diesel Conditions: Experiments and Chemical Kinetic Modeling," the 1994 SAE Fuels & Lubricants Meeting, Baltimore, Maryland, 1994.

[51]   Nakahira, T., M. Komori, M. Nishida, and K. Tsujimura, "The Shock Wave Generation Around the Diesel Fuel Spray with High Pressure Injection," SAE Technical Paper 920460, 1992.

[52]   Naterer, G.F. and G.E. Schneider, "Use of the Second Law in A Predictive Capacity for Compressible Fluid Flow Discrete Analysis," AIAA-92-2942, AIAA 27th Thermophysics Conference, July 6-8, 1992.

[53]   Olson, D.B. and W.C. Gardiner, Jr., "An Evaluation of Methane Combustion Mechanisms," J. Phys. Chem., Vol.81, p.2514, 1977.

[54]   Papageorgakis, G., A. Agarwal, G. Zhang, and D.N. Assanis, "Multi-Dimensional Modeling of Natural Gas Injection, Mixing and Glow Plug Ignition Using the KIVA-3 Code," ASME 1996 Spring Technical Conference, Youngstown, Ohio, April 21-24, 1996.

[55]   Palumbo, D.J. and E.L. Rubin, "Solution of the Two-Dimensional, Unsteady, Compressible Navier-Stokes Equations Using A Second-Order Accurate Numerical Scheme," Journal of Computational Physics, Vol.9, pp.466-495, 1972.

[56]   Patankar, S.V., "Numerical Heat Transfer and Fluid Flow," Hemisphere Publishing Corporation, 1980.

[57]   Peters, N. and R.J. Kee, "The Computation of Stretched Laminar Methane-Air Diffusion Flames Using A Reduced Four-Step Mechanism," Combustion and Flame, Vol.68, p.17-29, 1987.

[58]   Peyret, R. and H. Viviand, "Computation of Viscous Compressible Flows Based on the Navier-Stokes Equations," AGARD-AG-212, 1975.

[59] Pulliam, T.H., "Artificial Dissipation Models for the Euler Equations," AIAA Journal, Vol.24, No.12, pp.1931-1940, 1986.

[60] Raithby, G.D., "Prediction of Dispersion by Surface Discharge," Report to Canada Centre for Inland Waters, Basin Investigation and Modelling Section, Burlington, Ontario, 1976.

[61] Refael, S. and E. Sher, "Reaction Kinetics of Hydrogen-Enriched Methane-Air and Propane-Air Flames," Combustion and Flame, Vol.78, p.326-338, 1989.

[62] Roache, P.J., "Perspective: A Method for Uniform Reporting of Grid Refinement Studies," Journal of Fluids Engineering, 116:405-413, 1994.

[63] Robichaud, M.P. and P.A. Tanguy, "Finite Element Solution of Three-Dimensional Incompressible Fluid Flow Problems by A Preconditioned Conjugate Residual Method," Internat. J. Numer. Methods Engrg., Vol.24, p.447-457, 1987.

[64] Schneider, G.E. and E. Kochavi, "A Control Volume Based Finite Element Formulation of The Compressible Flow Equations With Application to The Shock Tube Problem," AIAA, 1989.

[65] Shapiro, A.H., "The Dynamics and Thermodynamics of Compressible Fluid Flow," Volume II, Robert E. Krieger Publishing Company, 1983.

[66] Sheu, T.W.H., S.-M. Lee, K.O. Yang, and B.J.Y. Chiou, "A Non-Oscillating Solution Technique for Skew Upwind and QUICK-Family Schemes," Computational Mechanics, Vol. 8, pp. 365-382, 1991.

[67] Siebers, D.L. and C.F. Edwards, "Autoignition of Methanol and Ethanol Sprays under Diesel Engine Conditions," SAE Transactions, Vol. 96, pp. 5.140-5.152, 1987.

[68]   Siebers, D.L. and C.F. Edwards, "A Study of the Autoignition Process of a Diesel Spray via High Speed Visualization," SAE Technical Paper 920108, 1992.

[69]   Sloane, T.M., "Ignition and Flame Propagation Modeling With An Improved Methane Oxidation Mechanism," Combustion Science and Technology, Vol.63, p.287, 1989.

[70]   Thompson, J.F., "A Survey of Dynamically-Adaptive Grids in the Numerical Solution of Partial Differential Equations," Applied Numerical Mathematics Vol.1, p.3-27, 1985.

[71]   Tsao, K.C. and Z. Han, SAE Technical Paper Series 930312, 1993.

[72]   Tsuboi, T. and H.G. Wagner, "Homogeneous Thermal Oxidation of Methane in Reflected Shock Waves," Fifteenth Symposium (International) on Combustion, p.883, The Combustion Institute, Pittsburgh, 1975.

[73]   Tsuji, H. and I. Yamaoka, Thirteenth Symposium (International) on Combustion, The Combustion Institute, p.723, 1971.

[74]   Van der Vorst, H.A., "Bi-CGSTAB: A Fast and Smoothly Converging Variant of Bi-CGS for the Solution of Nonsymmetric Linear Systems," SIAM J. Sci. Stat. Comput., Vol. 13, No. 2, pp.631-644, 1992.

[75]   Van Doormaal, J.P., " Numerical Methods for the Solution of Incompressible and Compressible Fluid Flows," Ph.D. Thesis, University of Waterloo, 1985.

[76]   Wang, D.R., "Solution Algorithms for Non-Linear Equations (Chinese)" Education Publishing Company, 1983.

[77]   Westbrook, C.K., "An Analytical Study of the Shock Tube Ignition of Mixtures of Methane and Ethane," Combustion Science and Technology, Vol.20, p.5-17, 1979.

[78]   Westbrook, C.K., "Simplified Reaction Mechanisms for the Oxidation of Hydrocarbon Fuels in Flames," Combustion Science and Technology, Vol.27, p.31-43, 1981.

[79]   Westbrook, C.K., J. Creighton, C. Lund, and F.L. Dryer, "A Numerical Model of Chemical Kinetics of Combustion in A Turbulent Flow Reactor", J. Phys. Chem., Vol.81, p.2542, 1977.

[80]   Westbrook, C.K. and W.J. Pitz, "High Pressure Autoignition of Natural Gas/Air Mixtures and the Problem of Engine Knock", Gas Research Institute Technical Report No. GRI-87/0264, 1987.

[81]   White, F.M., Viscous Fluid Flow, McGraw-Hill, Toronto, 1974.

[82]   Williams, F.A., Combustion Theory, Benjamin/Cummings Publishing, Don Mills. Ontario, 1985.

[83]   Young, D.P., F.T. Melvin, F.T. Johnson, L.B. Wigton, and S.S. Samant, "Application of Sparse Matrix Solvers as Effective Preconditioners," SIAM J. Sci. Statist. Comput., Vol.10, p.1186-1199, 1989.

[84]   Zedan, M. and G.E. Schneider, "Investigation into the Simultaneous Variable Solution of Velocity and Pressure in Incompressible Fluid Flow Problems," AIAA Paper No. 83-1519, 1983.

[85]   Zhang, J.-F., "Comparison of Solver Performance," A Research Report, Dept. of Mech. Eng., Univ. of Waterloo, 1991.

[86]   Zhang, J.-F., R.A. Fraser, and A.B. Strong, "Numerical Study of the Autoignition of Natural Gas in Diesel Engines: Use of Adaptive Griding," Spring Technical

Meeting of the Combustion Institute, Canadian Section, Quebec City, Quebec, May 9-12, 1993.

[87]   Zhang, J.-F., R.A. Fraser, and A.B. Strong, "Numerical Study of the Autoignition of Natural Gas in Diesel Engines: Code Development Phase," Spring Technical Meeting of the Combustion Institute, Canadian Section, Edmonton, Alberta, May 10-13, 1992.

[88]   Zhang, J.-F., R.A. Fraser, and A.B. Strong, "Modeling Diesel Engine Natural Gas Injection: Injector/Cylinder Boundary Conditions," SAE Paper No. 940329. February 1994.

[89]   Zhang, J.-F., R.A. Fraser, and A.B. Strong, "Modeling Diesel Engine Natural Gas Injection: Injector/Cylinder Boundary Conditions with Reaction," Spring Technical Meeting of the Combustion Institute, Canadian Section, Kingston, Ontario, 1994.

[90]   Zhang, X.D., J.-Y. Trepanier, and R. Camarero, "An Error Estimation of Finite Volume Method For Hyperbolic Equations," CFD 96, Ottawa, Ontario, Canada. June 2-6, 1996.

Appendix A

Code Verification

A.1. Overview

This appendix outlines several code verification tests. This includes the driven cavity test, flow around a blunt body test, and a steady state turbulence gas jet comparison. These tests cover fluid flow computations from subsonic to supersonic. These problems are defined below and are chosen so as to include the most important features of the complex flows encountered in engineering practice.

A.2. Lid-Driven Cavity Flow Test

The lid-driven cavity flow test involves a quadrilateral domain with parallel walls, one pair of which is inclined as shown in Fig A.1. A non-orthogonal grid is used. Non-orthogonality is the limiting in many solution methods. An angle of 45^0 is chosen. As far as grid non-orthogonality is concerned, this case is likely to cover all of the relevant effects to be experienced in the natural gas autoignition problem. Laminar flow is induced by the movement of one wall (hence the name lid-driven cavity flow). Specifically the test case corresponds to an angle $\beta = 45^0$, a length $L = 1$ m, a density $\rho = 1$ kg/m^3, and a lid velocity $U = 1$ m/s. The Reynolds number, defined by using the lid velocity, U, and cavity length, L, is 1. Mach number is varied from 0.0034 to 0.2 by changing temperature. A comparison of centerline velocity profiles with bench mark
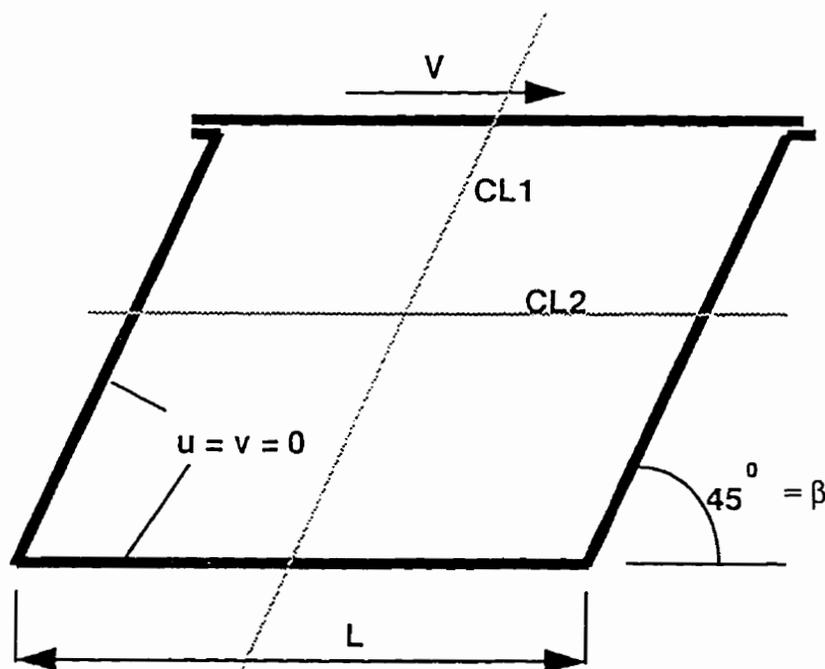

Figure A.1: Geometry and boundary conditions for test case

results [Demirdzic et al, 1992] is shown in Figures A.2 and A.3. Results for three different Mach numbers are shown. Computations were stopped in all three cases after the same number of iterations, 1000. Test case 3 with a Mach number of 0.2 yielded rapid convergence with its final results being very close to the benchmark results. When the Mach number was reduced to 0.03 (test case 2) and 0.0034 (test case 1), system stiffness in this density based formulation (see Appendix E.4) increases, thus slowing convergence speed. The Mach numbers 0.03 and 0.0034 results in Figures A.2 and A.3 are not converged to a predefined relative error tolerance but rather were stopped by the maximum iteration number. That is, though cases 1 and 2 are expected to converge to the benchmark solution given more iterations, the results shown are not converged.
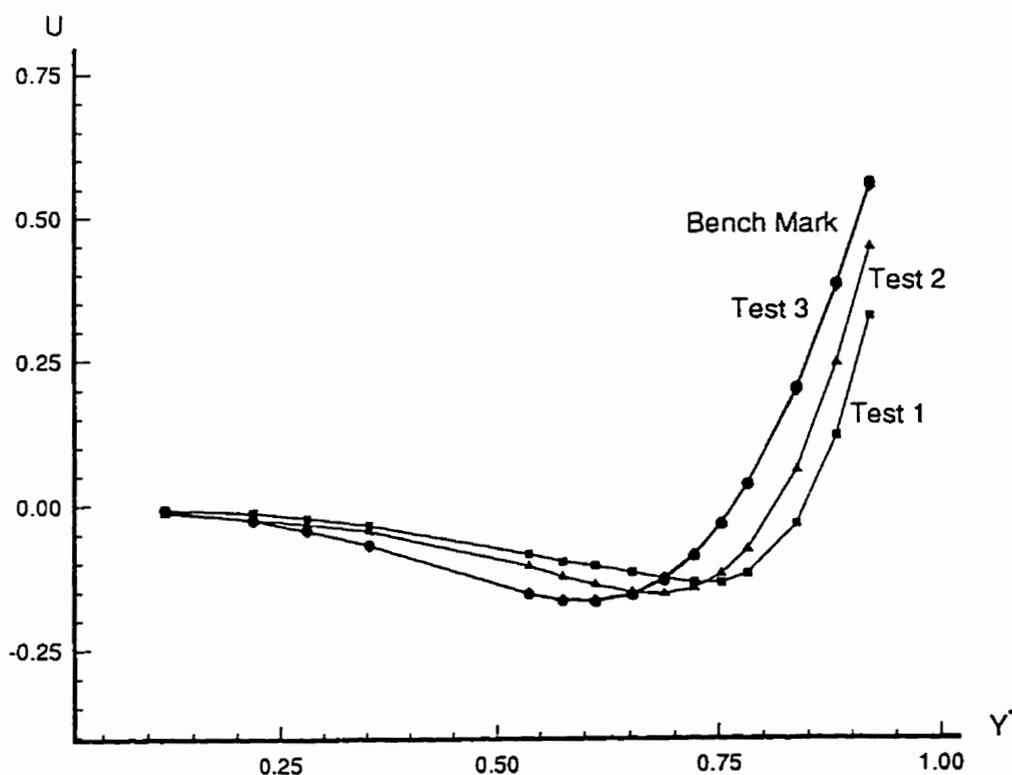
Figure A.2: Variation of the centreline velocity profiles of U-component.
Test 1 ---- Mach number 0.0034; Test 2 ---- Mach number 0.03;
Test 3 ---- Mach number 0.2; Bench Mark [Demirdzic et al., 1992].
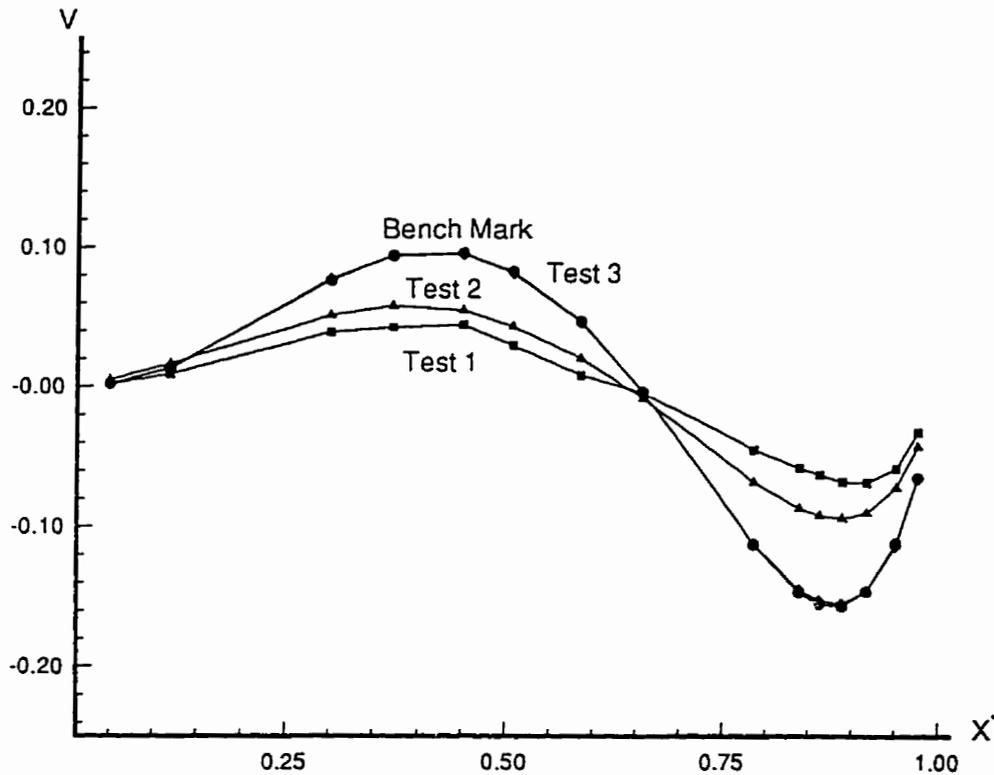
Figure A.3: Variation of the centreline velocity profiles of V-component.
Test 1 —— Mach number 0.0034; Test 2 —— Mach number 0.03;
Test 3 —— Mach number 0.2; Bench Mark [Demirdzic et al., 1992].

A.3. Flow Around A Blunt Body

The second case involves a two-dimensional channel flow with a blunt body at its center (see Figure A.4). The purpose of this test case is to evaluate supersonic flow capabilities of the code. The boundary conditions are such that the inlet Mach number is Ma = 2, the inlet velocity is U = 587 m/s, the Reynolds number is Re = 3.4 x 10^6, outlet pressure is P = 10^5 Pa, and wall no-slip condition holds. Isothermal laminar flow is considered. The fluid temperature is T = 300 K.
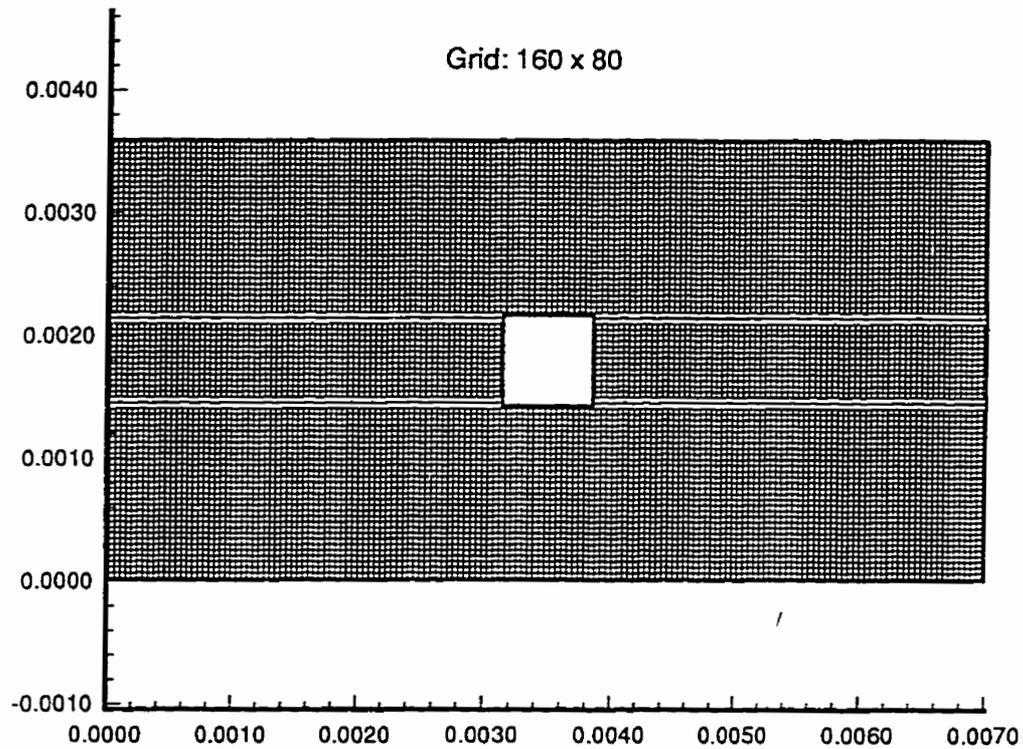
Figure A.4: Two-dimensional channel flow with a blunt body at its center.

Figure A.5 shows the velocity vector distribution for the test case supersonic flow. An oblique shock is generated at the leading edge of the inlet due to boundary layer effects. The oblique shock-wave angle is around 35^0C with respect to the horizontal which matches the chart data on oblique shocks charts [Anderson, 1990]. The figure also exhibits a detached shock wave, a reflection shock wave, an expansion wave, and reveals an interaction between the shock wave and the boundary layer, all as expected. The corresponding Mach number contour and the pressure contour of this supersonic internal flow are shown in Figure A.6 and A.7, respectively.

U = 587 m/s, M = 2.0, T = 300K, μ = 2 x 10^{-5} kg/m s

P = 10^5 Pa, Re = 3.4 x 10^6, Block: 0.1 x 0.1 m
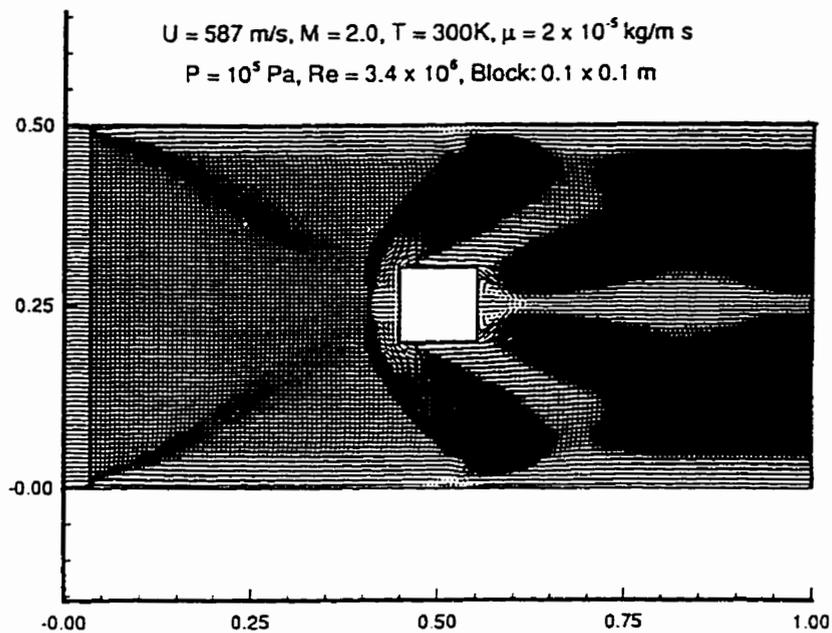
Figure A.5:   Velocity vector distribution.

Mach Number Contour
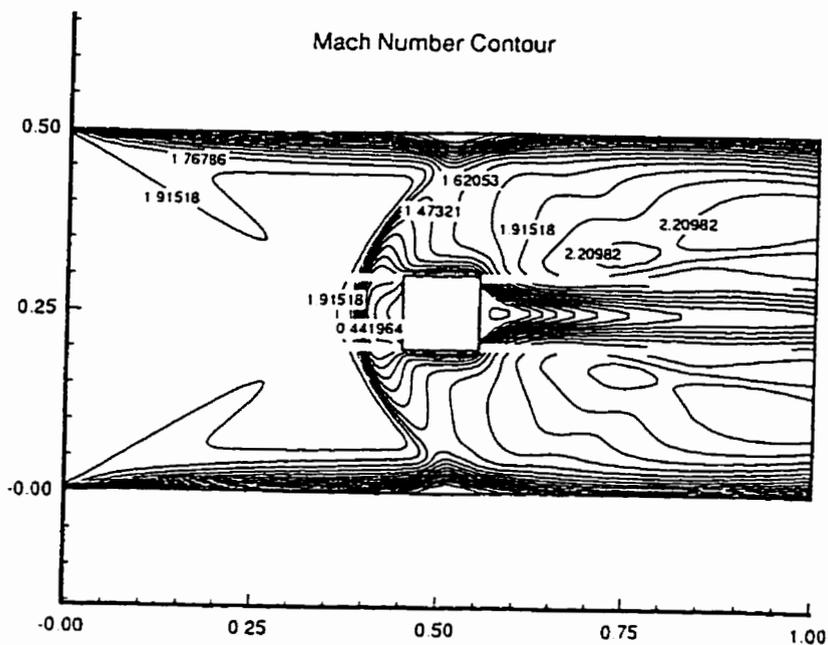
Figure A.6:   Mach number contour
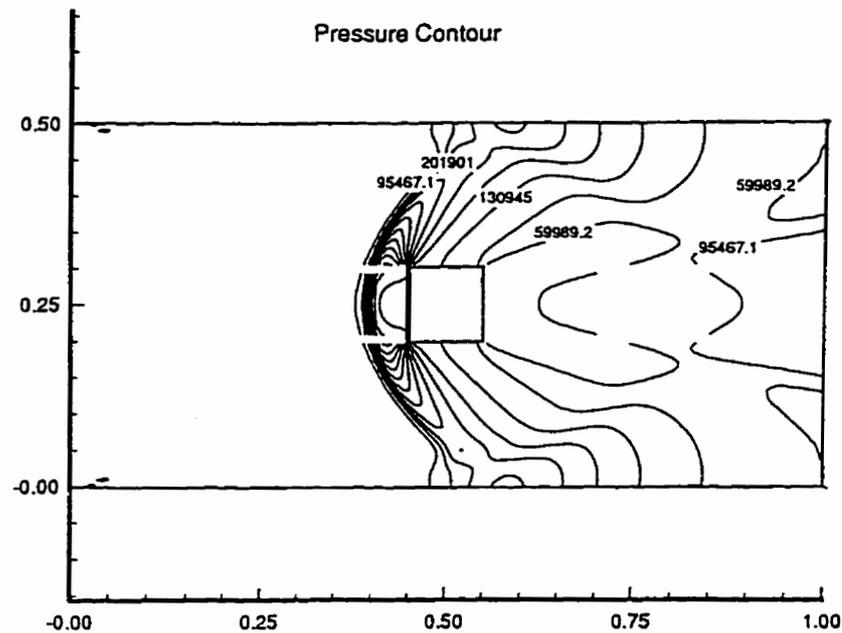
Figure A.7:   Pressure contour

A.4. Steady-State Turbulent Gas Jet Comparison

Abramovich's high-speed, steady-state, profile data [Abramovich, 1963] provide a classic

reference on turbulent jets.   Abramovich presents an extensive theoretical treatment,

supported by numerous experiments, of 2-D planar, steady-state, high-speed, turbulent,

gas jets.   The high-speed jets modeled are on-design resulting in uniform velocity,

temperature, and pressure profiles at the jet exit plane.   In other words, the experiments

are specifically designed to yield near uniform jet exit profiles.   If the unsteady state case

of natural gas injection into combustion chamber is permitted to reach steady-state (which

would require wall removal and a longer jet development time) then the solution should

agree with the results of Abramovich. A steady-state solution match is a good check on a code's ability to capture high-speed jet physics.

Abramovich [Abramovich, 1963] provides analytic expressions for velocity and temperature profiles in the mixing region near the exit orifice of steady-state, high-speed, turbulent jets. These profiles are non-dimensionalized collapsing the data to a single curve. Figure A.8 plots the semi-empirical, analytic, non-dimensional velocity profile of Abramovich along with corresponding near steady-state results for the natural gas injection. The agreement between the computations and the analytic expression are within the scatter of the data used to validate the analytic profiles. It is concluded from Figure A.8 that the developed code can model on-design, steady-state, turbulent, high-speed, gas jets reasonably well.
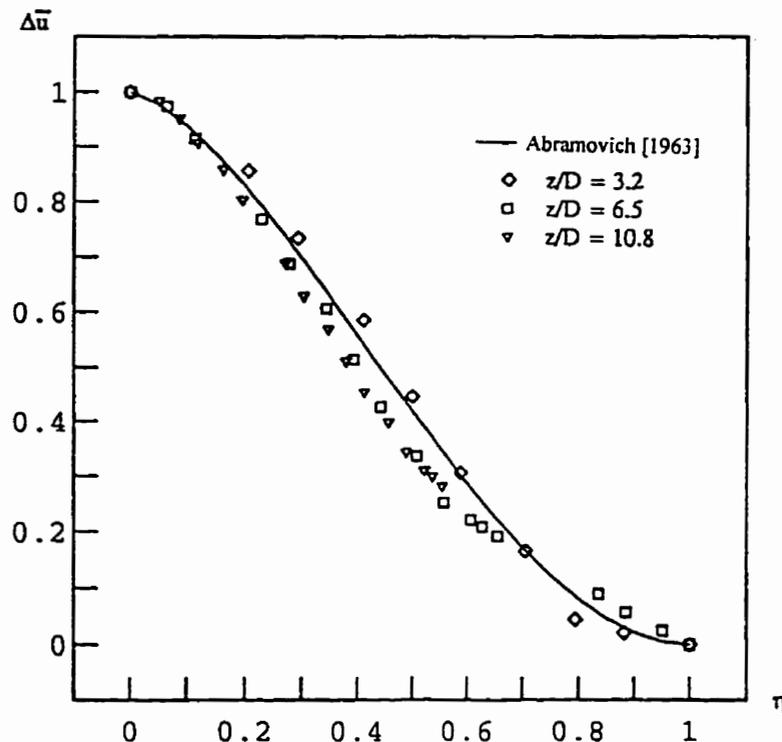
Figure A.8: Natural gas near steady-state, high-speed, turbulent, gas jet, mixing layer velocity profile for case 2 after 0.1 ms. η and Δu are the non-dimensional radius and velocity, respectively, defined by Abramovich [1963].

Another check on the prediction capabilities of the code involved the modelling of a low speed jet. Theoretically based analytic expressions exist for low speed, steady-state, jets [White, 1974]. A comparison between theoretical and calculated profiles is exampled in Figure A.9. It is again seen that velocity profile agreement is good.
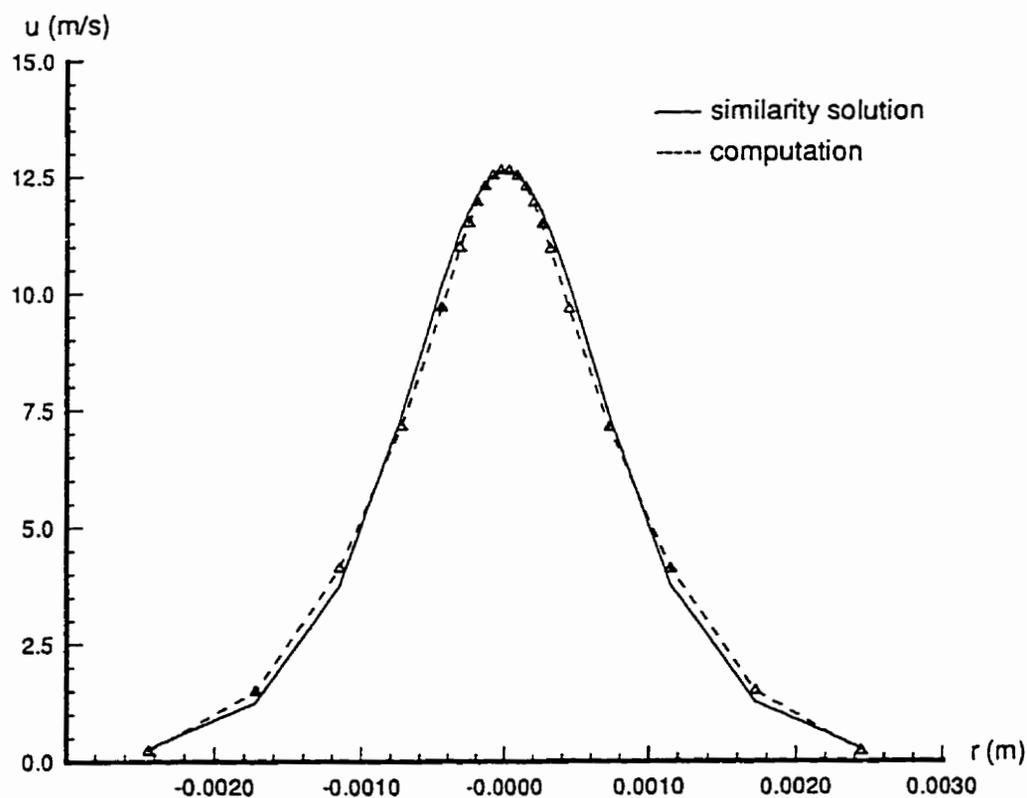
Figure A.9: Low speed gas jet velocity profile comparison between computation and analytic similarity solution.

A.5. Closure

This appendix presents a brief of the more important code validation tests. These test looked at subsonic laminar flow in a lid-driven cavity, at supersonic, laminar flow for an inner flow passing around a blunt body, and at a turbulence gas jet comparison with existing data. The comparison between the computations and bench mark results show good agreement with a maximum error 1% for lid driven cavity when Ma = 0.2 and a maximum error 7% for figures A.8 and A.9. These tests have established a level of confidence in the in-house code that indicates it to be suitable to model natural gas injection into a combustion chamber.

Appendix B.

Shock Wave Studies

B.1. Overview

In the course of addressing the natural gas injection problem an entropy production rate scheme was developed to model moving shocks, compression waves, and contact surfaces. This scheme employs an entropy production rate formula within a finite volume method such that second law of thermodynamics is locally satisfied. For this scheme, it is proven impossible for Gibb's phenomena like oscillations to form in the vicinity of shock front and contact surface discontinuities. This scheme is not hindered by the need to incorporate artificial viscosity or an assumed shock shape analytic function as is the norm. Furthermore, this idea is extendible to two and three dimensions. The entropy production rate analysis is located on entropy control volumes. The entropy production rate formula is used to determine surface values or integration point values for each control volume from neighbour node values. Results are presented for an unsteady shock problem.

Computations confirm the absence of oscillations (including overshot and undershot) with results of comparable quality to artificial viscosity techniques. When adaptive griding is utilized the spatial sharpness of shocks and contact surfaces is greatly improved.

B.2. Modeling Shock Waves

The high pressure injection of natural gas into a combustion chamber leads to a group of unsteady shock waves or compression waves. In the search for an effective numerical method for modelling the problem this one-dimensional entropy production rate scheme was developed for shock tube flows. It is beyond the scope of this work to actually incorporate this scheme into the natual gas injection at this point in time, but to do so is certainly a future possibility.

Numerically predicting heat transfer and fluid flow requires solving a set of differential equations: conservation of mass, momentum and energy. The differential equations are discretized to a set of approximate algebraic equations. The need to solve the differential equations is therefore replaced by the need to solve a set of algebraic equations [Patankar, 1980]. The discrete solution can represent the solution of the differential equations if and only if the discretized equations (i.e., a set of non-linear algebraic equations) are first and foremost physically reasonable. The question, "How to make a physically reasonable discretization?", has been the subject of much research in computational fluid dynamics.

In order to model a shock by using the Euler equations, numerical methods require the discretized equations with certain, inherent, numerical diffusions (such as viscous diffusion and thermal diffusion) in the vicinity of the shock. The reason these diffusions are needed is that the Euler equations do not provide any natural diffusion mechanism. However, most of the numerical methods may either not have sufficient or may even locally generate negative diffusions. Most methods violate the entropy condition (or Second Law of Thermodynamics) and produce locally non-physical solutions, such as oscillation, overshoot, and undershoot in the vicinity of shock. Much research work has focused on numerical methods which satisfy the entropy condition.

A number of different numerical schemes [Anderson, 1990, Kansa, 1988, Schneider et al, 1989] have been proposed to accommodate shock waves and contact surfaces. In 1957, the pioneering work of Lax pointed out that weak solutions of hyperbolic conservation laws are not uniquely determined by their initial values and an entropy condition is needed to pick out the physically relevant solution. Harten *et al* in 1976 showed that a monotone finite-difference approximation converges to the physically relevant solution and does satisfy the entropy condition. However, the monotone finite-difference scheme is necessarily of first-order accuracy. For accuracy, most of the numerical methods which have order of accuracy higher than one are not monotone. The solutions to these numerical methods in conservation form may converge to non-physically relevant solutions and may violate the entropy condition.

Following Harten *et al*'s early work [Harten et al, 1976], Majda and Osher [Majda, 1979] have demonstrated that the operation by adding a non-linear artificial diffusion to the standard Lax-Wendroff difference scheme [Lax, 1960] can satisfy the entropy condition. It

means that the use of artificial diffusion can effectively improve the property of the Lax-Wendroff scheme near the shock. Consequently, oscillation solutions in the vicinity of shock do not appear. In 1986, Pulliam employed the technique of adding artificial diffusion models to two dimensional Euler equations and analyzed many artificial diffusion models. With a central difference algorithm the effect of these models on accuracy, stability, and convergence rates were investigated. Linear and non-linear diffusion models have been studied by using an implicit approximate factorization code for transonic airfoils. All these artificial diffusion approaches have one thing in common: they require empirical constants. In 1989 Schneider and Kochavi showed an empirical constant free artificial diffusion model. After that, Naterer and Schneider [Naterer and Schneider, 1992] extended the model to two dimensional shock capturing. Their artificial diffusion is evaluated by an entropy-based criterion. In order to compensate for a negative entropy production rate their numerical method forces, in the vicinity of the shock, entropy production by increasing the diffusion. This method ensures that the local entropy production rate is greater than or equal to zero.

A local entropy production rate greater than zero is a necessary condition, but it is not a sufficient condition. This is because the entropy production rate may take on different positive values depending on the irreversibility mechanism and strength. The difficulties associated with calculating the local entropy production rate increase stem from the complexities of the irreversible processes, such as irreversible thermal diffusion and viscous friction in shock. The entropy production rate scheme developed later in this appendix determines the local entropy production rate increase. The performance of the entropy production rate scheme is revealed through a test problem of section B5.

B.3 Oscillation(s) and Entropy Production Rate

Oscillations usually occur in the vicinity of discontinuities, such as at a shock and or contact surface. An oscillation solution is one example of a non-physical solution which violates the second law of thermodynamics. Euler equation and Navier-Stock equation may, numerically, not obtain the physical solutions of a shock problem if some limit conditions are not added. The reason is that the Euler's equations do not include any viscous diffusion or heat diffusion terms necessary for entropy production. The Navier-Stock's equations have diffusion terms, but values for these diffusivities in the vicinity of shock are unknown. An entropy limitation condition can effectively be used to produce physical relevant solutions of Euler's and Navier-Stock's equations. The entropy transport equation can be written as

$$\frac{\partial(\rho s)}{\partial t} + \nabla \cdot (\rho s v + \frac{q''}{T}) = \wp_s \tag{B.1}$$

where $\wp_s$ is the entropy production rate, ρ is the density, s is the entropy, v is the velocity, T is the temperature, and q'' is the heat flux. For a reversible processes, $\wp_s = 0$. For irreversible processes $\wp_s > 0$. Processes for which $\wp_s < 0$ are never observed. The relation between oscillations and entropy production rates is discussed next.

B.3.1 Oscillation Around Shock

In this section equation (B.1) is considered for adiabatic flow ($q'' = 0$). The solid line shown in Figure B.1 represents a density distribution at time t_1; the dashed line is the physical solution of density at time t_2 ($t_2 = t_1 + \Delta t$); a non-physical solution is assumed with the dash-dot line.
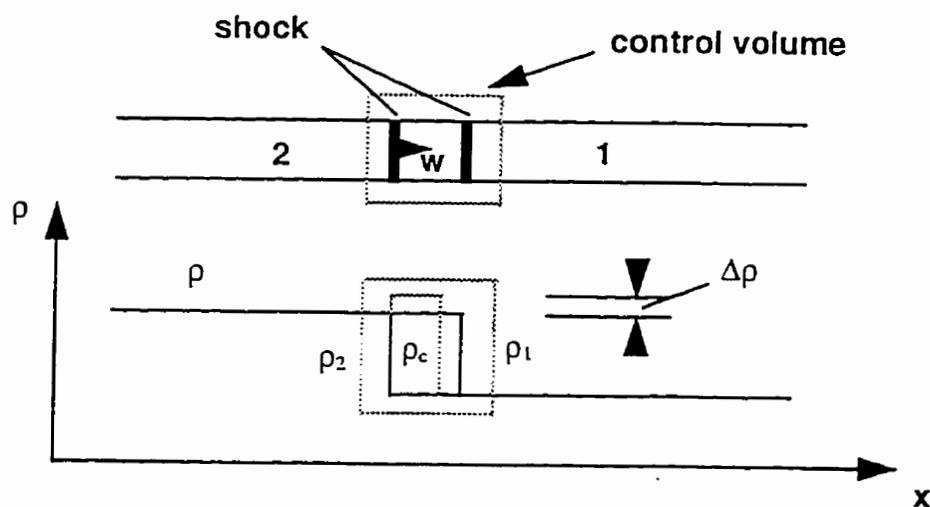
Figure B.1: Density distribution around a shock at times t_1 and $t_1 + \Delta t$.

After the shock sweeps a distance $w\Delta t$, the parameters in the swept area are defined by subscript c. A physically relevant solution should present $u_c = u_2$, $p_c = p_2$, $T_c = T_2$, and $r_c = r_2$. The entropy production rate can therefore be written as

$$\wp_s = [(\rho s)_2 - (\rho s)_1]w + (\rho u s)_1 - (\rho u s)_2 \qquad (B.2)$$

where s is a generalized entropy, i.e.,

$$s = Ln\left[\frac{(p/p_{ref})^{1/r}}{\rho/\rho_{ref}}\right] \qquad (B.3)$$

In order to generate a non-dimensional entropy production rate, we assume that $u_1 = 0$, $p_1 = p_{ref}$, $r_1 = r_{ref}$, and $a_1 = a_{ref}$. The non-dimensional entropy production rate is then given by

$$\overline{\wp}_s \equiv \frac{\wp_s}{\rho_{ref}a_{ref}} = \overline{\rho}_2 s_2(\overline{w} - \overline{u}_2) \qquad (B.4)$$

where

$$\overline{w} \equiv \frac{w}{a_{ref}}, \quad \overline{u}_2 \equiv \frac{u_2}{a_{ref}} \quad and \quad \overline{\rho}_2 \equiv \frac{\rho_2}{\rho_{ref}}. \qquad (B.5)$$

A physically relevant solution should satisfy

$$\overline{w} - \overline{u}_2 = M_2 \frac{a_2}{a_{ref}} = M_2 \sqrt{\frac{T_2}{T_{ref}}} = M_2 \sqrt{\overline{T}_2}, \quad where \quad M_2 \cong \frac{w - u_2}{a_2}. \tag{B.6}$$

Substituting into equation (B.4) one obtains

$$\overline{\wp} = \overline{\rho}_2 s_2 M_2 \sqrt{\overline{T}_2} = s_2 M_s \tag{B.7}$$

We define the expression (B.7) as the non-dimensional critical entropy production rate, i.e.,

$$\overline{\wp}_{s(cr)} = s_2 M_s \tag{B.8}$$

It is worth noting that the non-dimensional critical entropy production rate is always greater than zero around shock.

The entropy production rate of a non-physically relevant solution can be expressed as

$$\wp_s = (\rho_c s_c - \rho_1 s_1)w + \rho_1 u_1 s_1 - \rho_2 u_2 s_2 \tag{B.9}$$

Its non-dimensional form becomes

$$\overline{\wp}_s = \overline{\rho}_c s_c \overline{w} - \overline{\rho}_2 s_2 \overline{u}_2 \tag{B.10}$$

The entropy production rate is studied next in accordance with expressions (B.8) and (B.10). The entropy production rate variation may be defined as

$$\Delta \overline{\wp}_s \equiv \overline{\wp}_s - \overline{\wp}_{s(cr)} = \overline{\rho}_c s_c \overline{w} - \overline{\rho}_2 s_2 M_s \tag{B.11}$$

The $\overline{\rho}_c$, s_c *and* $\overline{w}$ can be obtained from mass conservation, momentum conservation and energy conservation in this control volume. These conservation equations are, respectively, as follows:

$$\overline{\rho}_c = \frac{\overline{\rho}_2 \overline{u}_2}{\overline{w}} + 1 \tag{B.12}$$

$$\overline{\rho}_c \overline{u}_c = \frac{\overline{p}_2 / \gamma - 1/\gamma + \overline{\rho}_2 \overline{u}_2^2}{\overline{w}} \tag{B.13}$$

$$(\overline{\rho}_c \overline{u}_c)^2 = 2\overline{\rho}_c [(\frac{1}{\gamma - 1}\overline{p}_2 \overline{u}_2 + \frac{1}{2}\overline{\rho}_2 \overline{u}_2^3)\frac{1}{\overline{w}} + \frac{1}{\gamma(\gamma - 1)}(1 - \overline{p}_c)] \tag{B.14}$$

Substituting equation (B.13) into (B.14) one obtains

$$\frac{A_l^2}{\overline{w}^2} = 2\overline{\rho}_c \left[\frac{A_2}{\overline{w}} + \frac{1}{\gamma(\gamma-1)}(1-\overline{p}_c) \right]$$ (B.15)

where

$$A_l = (\overline{p}_2 - 1)\frac{1}{\gamma} + \overline{\rho}_2 \overline{u}_2^2 \quad and \quad A_2 = \frac{\overline{p}_2 \overline{u}_2}{\gamma-1} + \frac{1}{2}\overline{\rho}_2 \overline{u}_2^3$$ (B.16)

If the density jump Δr is small, expression (B.11) can be approximated by

$$\Delta \overline{\wp}_s \approx d(\overline{\rho}_c s_c \overline{w}) = s_2 M_s d\overline{\rho}_c + \overline{\rho}_2 s_2 d\overline{w} + \frac{\overline{\rho}_2 M_s}{\gamma \overline{p}_2} d\overline{p}_c - M_s d\overline{\rho}_c$$ (B.17)

Differentiating expressions (B.12) and (B.15), we obtain

$$d\overline{\rho}_c = -\frac{\overline{\rho}_2 \overline{u}_2}{M_s^2} d\overline{w}$$ (B.18)

and

$$\left(\frac{\overline{\rho}_2 A_2}{M_s^2} - \frac{A_l^2}{M_s^3} \right) d\overline{w} = \left[\frac{A_2}{M_s} + \frac{1}{\gamma(\gamma-1)}(1-\overline{p}_2) \right] d\overline{\rho}_c - \frac{\overline{\rho}_2}{\gamma(\gamma-1)} d\overline{p}_c$$ (B.19)

respectively. Equations (B.18) and (B.19) present approximate linear differential relations between the variables $\overline{\rho_c}$, $\overline{p_c}$ and $\overline{w}$. These variables satisfy mass, momentum and energy conservation and the differential approximates are acceptable when Δr is small. The non-dimensional variables with subscripts 1 and 2 in equations (B.17), (B.18), and (B.19) are initial and boundary conditions in this analysis and have to satisfy normal shock relations with moving shock Mach number M_S. By using equations (B.18) and (B.19) and normal shock relations [Anderson, 1990], equation (B.17) becomes

$$\Delta \overline{\wp_s} \approx -\left\{ \frac{2\,M_s(\,M_s^2-1)(\gamma-1)}{2\gamma\,M_s^2-\gamma+1} + \frac{s_2\,M_s\,[(\gamma-1)\,M_s^2+2]}{2(\,M_s^2-1)} \right\} d\overline{\rho_c} = -C^{\bullet}\,d\overline{\rho_c} \tag{B.20}$$

where

$$C^{\bullet} = \frac{2\,M_s(\,M_s^2-1)(\gamma-1)}{2\gamma\,M_s^2-\gamma+1} + \frac{s_2\,M_s\,[(\gamma-1)\,M_s^2+2]}{2(\,M_s^2-1)} \tag{B.21}$$

The moving shock Mach number is greater than one and the non-dimensional entropy s_2 greater than zero. Therefore, the factor C^{*} is always greater than zero. The relation between the factor C^{*} and a moving shock at Mach number M_S is shown in Figure B.2.

Equation (B.20) reveals that a positive fluctuation of density will result in a reduction in entropy production rate and a positive $\Delta \overline{\wp_s}$ that will smear shock. In accordance with equations (B.18) and (B.19) and the equation of state, a relation between

density fluctuation and pressure fluctuation and a relation between density fluctuation and temperature fluctuation can be obtained, i.e.,

$$d\bar{p}_c = \frac{\gamma(2 M_s^2 + \gamma - 1)[(\gamma - 1) M_s^2 + 2]}{(\gamma + 1)^2 M_s^2} d\bar{\rho}_c \qquad (B.22)$$

$$d\bar{T}_c = \frac{(\gamma - 1)[(\gamma - 1) M_s^2 + 2]^2}{(\gamma + 1)^2 M_s^4} d\bar{\rho}_c \qquad (B.23)$$
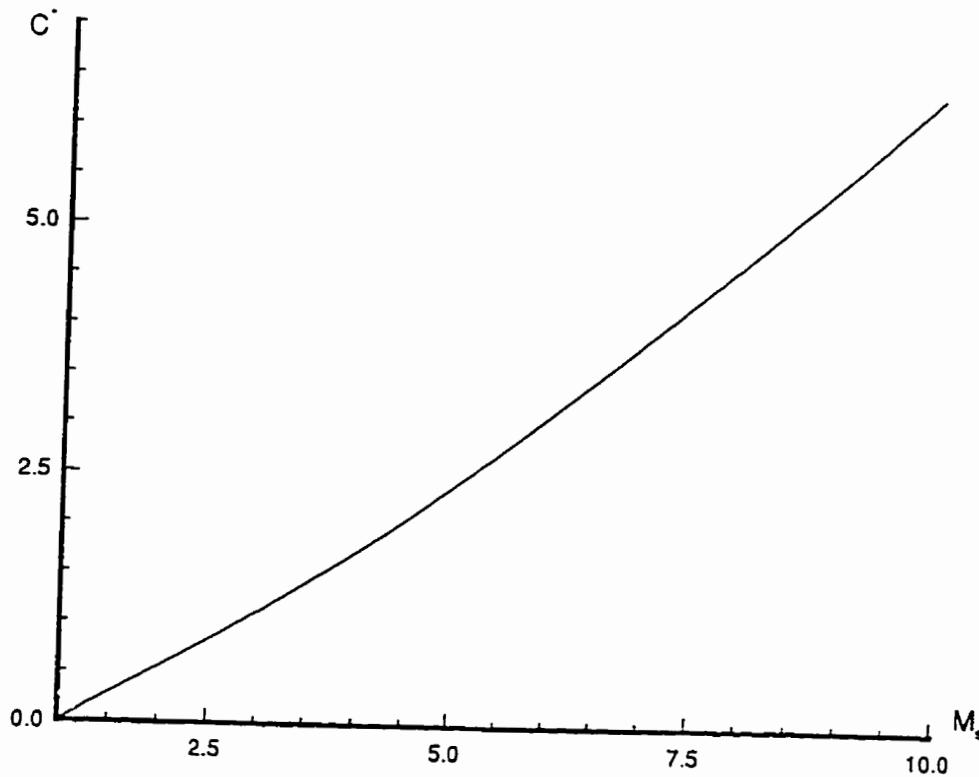

Figure B.2: Relationship between the factor C^* and a moving shock Mach number M_s.

Equations (B.22) and (B.23) show that a positive fluctuation in density will, in the meantime, cause a positive fluctuation in pressure and temperature. This means that a density oscillation in the vicinity of shock must result in pressure and temperature oscillations. The above only shows, however that these conclusions are correct only under the condition of a small density variation. When the density variation is not small, the results of equations (B.11), (B.12), (B.13), and (B.14) utilizing a Newton iteration solver are shown in Figure B.3. $\gamma = 1.4$ is assumed. Figure (B.3) confirms that the local oscillation in density, pressure or temperature must result in a reduction in the entropy production rate, i.e., $\Delta \overline{\wp}_s < 0$. In effect, an oscillation solution results in less entropy production rate than the critical entropy production rate. Correspondingly a greater entropy production rate than the critical entropy production rate will result in oscillation free solutions. Therefore, the condition to be satisfied for oscillation free solutions is

$$\Delta \overline{\wp}_s \geq 0$$

or

$$\wp_s \geq \wp_{s(cr)} > 0 \qquad\qquad (B.24)$$

where $\wp_{s(cr)} > 0$ is consistent with the normal shock relations.
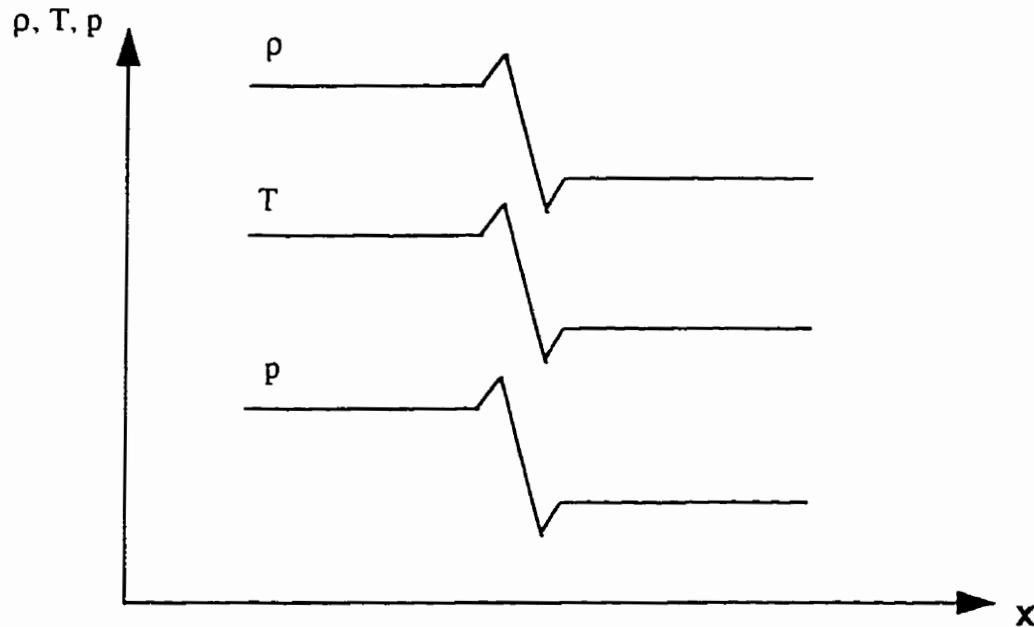
Figure B.3: Relationships between pressure, density, and temperature, across a
computed shock with oscillations for a finite density oscillation.

B.3.2 Oscillations Around a Contact Surface

Pressure and velocity remain unchanged across a contact surface, i.e., $u_2 = u_1 = u$ and $p_2 = p_1 = p$. Normalizing the conservation equations of mass, momentum and energy for the control volume shown in Figure B.4, one obtains

$$(\overline{\rho_c} - 1)\overline{w} + (1 - \overline{\rho_2})\overline{u} = 0 \qquad (B.25)$$

$$(\overline{\rho_c}\overline{u_c} - \overline{u})\overline{w} + (1 - \overline{\rho_2})\overline{u}^2 = 0 \qquad (B.26)$$

$$[\frac{1}{2}\overline{\rho_c}\overline{u_c}^2 - \frac{1}{2}\overline{u}^2 + \frac{1}{\gamma(\gamma - 1)}(\overline{p_c} - 1)]\overline{w} + \frac{1}{2}(1 - \overline{\rho_2})\overline{u}^3 = 0 \quad (B.27)$$
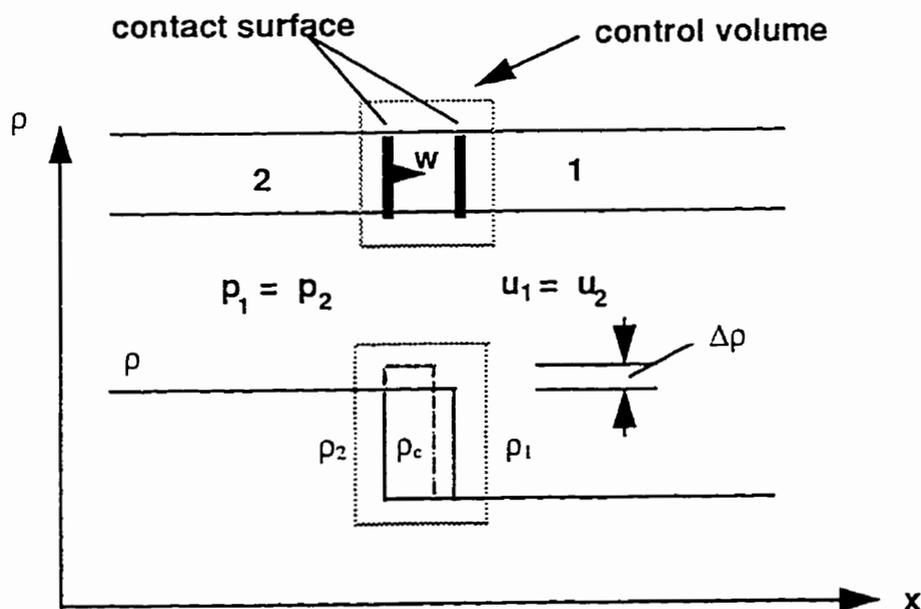
Figure B.4: Control volume around a contact surface.

where the reference variables are defined by

$$\rho_{ref} \equiv \rho_1 \quad and \quad a_{ref} \equiv a_1 \tag{B.28}$$

The non-dimensional entropy production rate in this case becomes

$$\overline{\wp}_s \equiv \frac{\wp_s}{\rho_{ref} a_{ref}} = \overline{\rho}_c s_c \overline{w} - \overline{\rho}_2 s_2 \overline{u} \tag{B.29}$$

where $s_1 = 0$. In the critical case $\overline{\rho}_c = \overline{\rho}_2$, $\overline{w} = \overline{u}$, due to mass conservation. Therefore, the non-dimensional critical entropy production rate becomes

$$\overline{\wp}_{s(cr)} = \overline{\rho}_c s_c \overline{w} - \overline{\rho}_2 s_2 \overline{u} = 0 \tag{B.30}$$

In an oscillation case, i.e., $\overline{\rho}_c > \overline{\rho}_2$, let us study the variation of the non-dimensional entropy production rate. Equations (B.26) and (B.27) can be rearranged as

$$\overline{\rho}_c \overline{u}_c = \frac{(\overline{\rho}_2 - 1)\overline{u}^2}{\overline{w}} + \overline{u} , \tag{B.31}$$

and

$$(\bar{\rho_c}\bar{u_c})^2 = 2\bar{\rho_c}[\frac{1}{2}(\bar{\rho_2} - 1)\bar{u}^3\frac{1}{w} + \frac{1}{2}\bar{u}^2 + \frac{1}{\gamma(\gamma-1)}(1-\bar{p_c})] \qquad (B.32)$$

respectively. Substituting equation (B.31) into (B.32) to remove $\bar{u_c}$ we obtain

$$[\frac{(\bar{\rho_2}-1)\bar{u}^2}{w} + \bar{u}]^2 = 2\bar{\rho_c}[\frac{1}{2}(\bar{\rho_2} - 1)\bar{u}^3\frac{1}{w} + \frac{1}{2}\bar{u}^2 + \frac{1}{\gamma(\gamma-1)}(1-\bar{p_c})] \qquad (B.33)$$

Substituting the mass conservation equation (B.25) into the above equation to delete $\bar{w}$ yields

$$\bar{p_c} = 1 \quad or \quad p_c = p_1 = p_2 \qquad (B.34)$$

In accordance with expression (B.34) and momentum conservation equation (B.26) one can obtain

$$\bar{u_c} = 1 \quad or \quad u_c = u_1 = u_2 = u \qquad (B.35)$$

Expressions (B.34) and (B.35) reveal that an oscillatory solution has no influence on pressure and velocity in the vicinity of the contact surface. According to the equation of

state, a relation ship between density and temperature can, due to constant pressure, be written as

$$\overline{T}_c = \frac{1}{\overline{\rho}_c} \tag{B.36}$$

Equation (B.36) can be differentiated into

$$d\overline{T}_c = -\frac{1}{\overline{\rho}_2} d\overline{\rho}_c \tag{B.37}$$

Equation (B.37) reveals that a density oscillation must generate a temperature oscillation. This relation is shown in Figure B.5. Furthermore, according to expression (B.34) and mass conservation equation (B.25), the entropy production rate can be presented as

$$\overline{\wp}_s = [\overline{\rho}_c s_c(\overline{\rho}_2 - 1) - \overline{\rho}_2 s_2(\overline{\rho}_c - 1)] \frac{\overline{u}}{\overline{\rho}_c - 1} \tag{B.38}$$

or

$$\frac{\overline{\wp}_s}{\overline{u}} = \frac{\overline{\rho}_c s_c(\overline{\rho}_2 - 1) - \overline{\rho}_2 s_2(\overline{\rho}_c - 1)}{\overline{\rho}_c - 1} \tag{B.39}$$

where $s_c = -ln(\overline{\rho}_c)$. Figure B.6 shows results from equation (B.39). According to Figure B.6, the following condition has to be satisfied to obtain oscillation free solutions in the vicinity of a contact surface
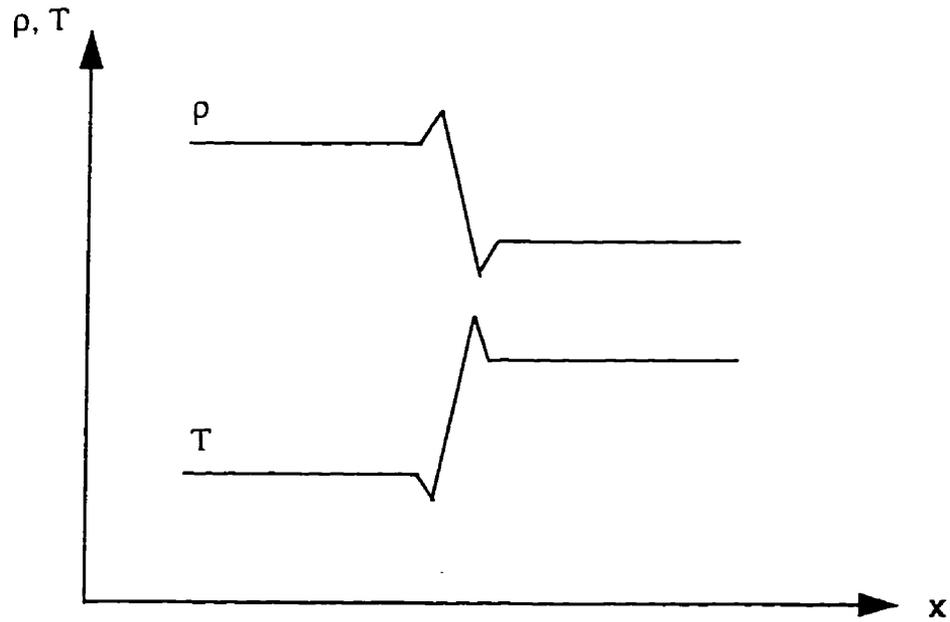
Figure B.5: Relationship between density and temperature oscillations.

$$\wp_s \geq \wp_{s(cr)} = 0 \qquad\qquad (B.40)$$

where the critical entropy production rate is equal to zero in contact surface.

Combining expressions (B.24) and (B.40), we finally obtain the following condition
of oscillation free solutions

$$\wp_s \geq \wp_{s(cr)} \qquad\qquad (B.41)$$

which defines the *entropy production rate condition.* This result represents a major new

contribution in the attempt to utilize the second law of thermodynamics in computations to

identify physically realistic solutions. The entropy production rate scheme presented next

details a practical implementation of this result.
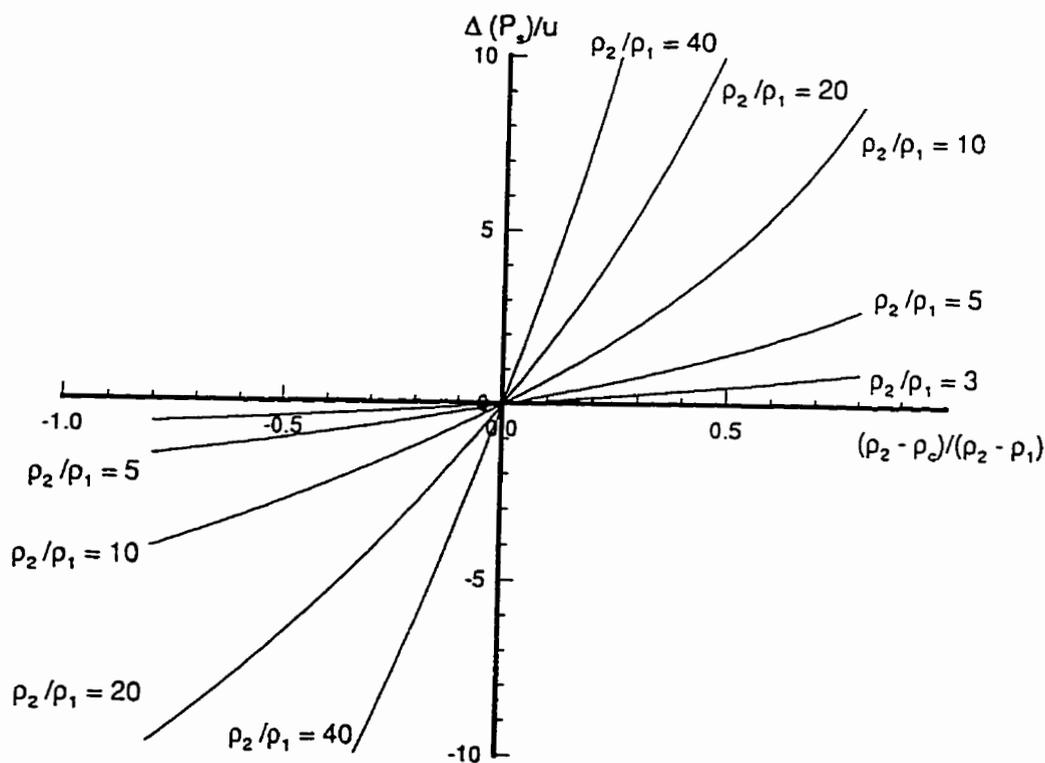
Figure B.6: Relationship between entropy production rate and density
around a contact surface.

B.4 Finite Volume Scheme with Entropy Production Rate Limitation

The entropy production rate condition (B.41) provides a quantitative way to discriminate between possible state changes and impossible ones. The condition can be employed to drive a numerical method which completely the satisfies second law of thermodynamics without adding any artificial diffusion terms (in present work). Another numerical method which adds an artificial diffusion terms [Naterer and Schneider, 1992] can be seen to also satisfy the entropy production rate condition and hence also always satisfy the second law of thermodynamics. This research develops for the first time a numerical method which does not include any artificial diffusion terms, or *a priori* knowledge of a shock wave's structure (e.g., its discontinuity behaviour), in the modelling of transient shock waves.

In this section, the calculation of a local critical entropy production rate is first described, then an oscillation free numerical method is explained. The study is restricted to the one-dimensional shock problem.

B.4.1 Local Critical Entropy Production Rate

Physically a shock can be considered a discontinuity surface due to its very small scale [John, 1984, Shapiro, 1983]. However, numerical solutions always involve control volumes of finite size which tend to smear the shock over several control volumes. The physical

states on two neighbour control volume nodes can be related to the local critical entropy production rate if a step type function replaces the wave curve (Figure B.7).
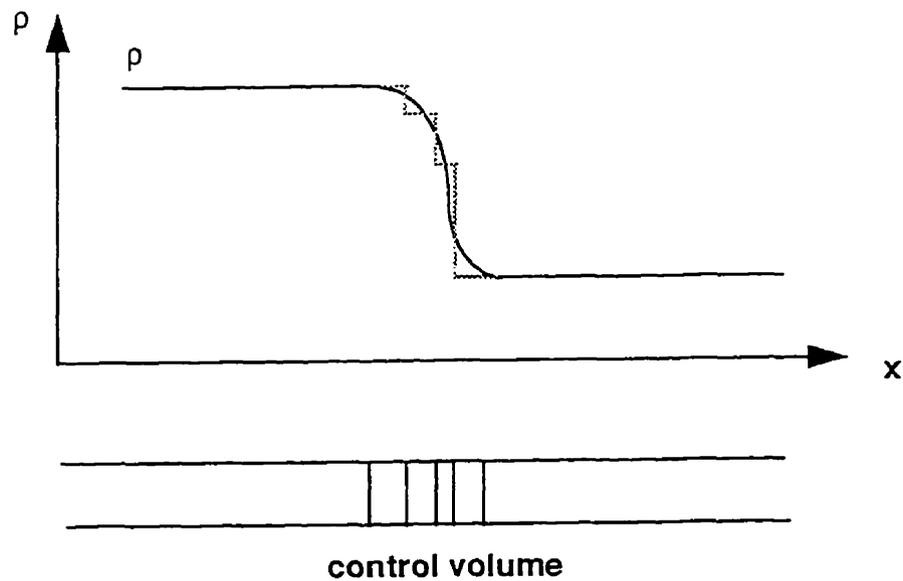
Figure B.7:   Discretizing a shock front using control volumes.

Figure B.8 shows an example control volume node distribution around a shock. The crossing points between the smooth shock solution and the horizontal dashed lines are node locations while the crossing points of the solid line and the vertical dashed lines identify control volume surfaces (or integration surfaces). Here we define the shaded area as the entropy control volume. The entropy control volume crosses two neighbour control

volumes. The two neighbour nodes are on the surfaces of the entropy control volume. It looks like staggered control volume [Patankar, 1980].
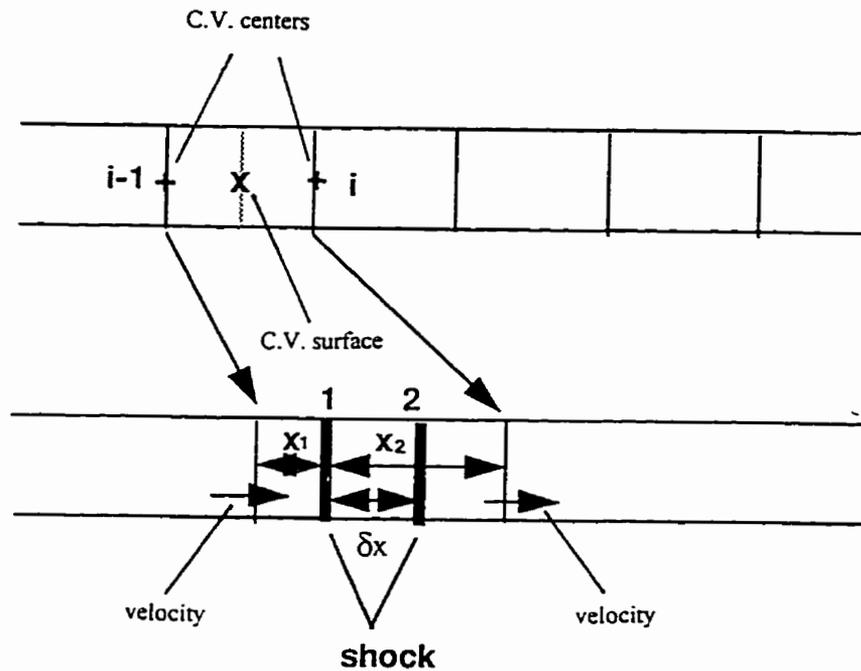
Figure B.8: Node distribution around a shock.

Because the entropy control volume numerically covers part of the shock wave, we can envision part of shock wave moving from location 1 to location 2 within the entropy control volume in a time step (see Figure B.8). So, the local critical entropy production rate can be presented as

$$\wp_{s(cr)_k} = (ms)_i^{j-\omega} - (ms)_{i-1}^{j+\omega} + \frac{\int_{i-1}^{i}(\rho s)^{j-1}dx - \int_{i-1}^{i}(\rho s)^{j}dx}{\Delta t} \tag{B.42}$$

where $0 \leq w \leq 1$. An explicit method is selected, i.e., $w = 0$. The subscripts k and i refer to the entropy control volume number and node number, respectively, and the superscripts j and $j+1$ are time steps. The mass fluxes and non-dimensional entropies on the surfaces of the entropy control volume are

$$m_{i-1} = \rho_{i-1}u_{i-1} ; \quad m_i = \rho_i u_i \tag{B.43}$$

and

$$s_{i-1} = \ln\left[\frac{\left(p_{i-1}/p_{ref}\right)^{1/\gamma}}{\rho_{i-1}/\rho_{ref}}\right] ; \quad s_i = \ln\left[\frac{\left(p_i/p_{ref}\right)^{1/\gamma}}{\rho_i/\rho_{ref}}\right], \tag{B.44}$$

respectively. According to Figure B.8, the entropies of this entropy control volume at time j and time $j+1$ can be written as

$$\int_{i-1}^{i}(\rho s)^{j}dx = \rho_{i-1}s_{i-1}x_1 + \rho_i s_i x_2, \tag{B.45}$$

and

$$\int_{i-1}^{i}(\rho s)^{j+1}dx \;=\; \rho_{i-1}s_{i-1}(x_{1} \,+\, \delta x) \,+\, \rho_{i}s_{i}(x_{2} \,-\, \delta x) \,, \qquad \text{(B.46)}$$

respectively. By substituting expressions (B.43), (B.45) and (B.46) into (B.42), we obtain the following expression for the local critical entropy production rate

$$\wp_{s(cr)_{k}} \;=\; \rho_{i-1}s_{i-1}(\frac{\delta x}{\Delta t} \,-\, u_{i-1}) \,-\, \rho_{i}s_{i}(\frac{\delta x}{\Delta t} \,-\, u_{i}) \qquad \text{(B.47)}$$

where $\dfrac{\delta x}{\Delta t}$ is the shock velocity which is given by [John, 1984]

$$\frac{\delta x}{\Delta t} \;=\; a_{i}\sqrt{\frac{\gamma+1}{2\gamma}(\frac{p_{i-1}}{p_{i}} \,-\, 1) + 1} \;+\; u_{i} \qquad \text{(B.48)}$$

Equation (B.47) is a local critical entropy production rate expression. If a numerical scheme satisfies

$$\wp_{s_{k}} \;\geq\; \wp_{s(cr)_{k}} \,, \qquad k \;=\; 1, 2, \ldots, N \qquad \text{(B.49)}$$

over every entropy control volume, this numerical scheme will be non-physical oscillation free.

B.4.2   An oscillation Free Numerical Method

In the numerical solution of Navier-Stocks equations the convection terms are often very difficult to handle. As a first approximation, an exact solution for steady one-dimensional flow in which only convection and diffusion terms are present is usually employed to evaluate the surface values (or integration points) of control volumes [Patankar, 1980]. A approximate models that attempt to improve upon the 1-D exact solution include the exponential model, the hybrid model, the power-law model, Raithby's approximation formula, etc. [Karki and Patankar, 1989, Raithby, 1976]. All these models use a non-dimensional number, Peclet number, when calculating the values of physical variables at integration points.

The Euler equations have no diffusion terms and hence are physically invalid in the vicinity of shock. The Navier-Stocks equations have diffusion terms, however, diffusivities in the vicinity of the shock are generally unknown. Therefore, the Peclet number can not be employed to evaluate variables at integration points in the vicinity of a shock.

The proposal in this work is to use the local entropy production rate to evaluate variables at integration points in the vicinity of a shock. The method yields local numerical diffusion (viscous diffusion and heat diffusion) which is both physically required in the vicinity of a shock and satisfies the entropy production rate condition. That is, the scheme will produce a physical relevant solution (or oscillation free solution).

Consider the entropy control volume shown in Figure B.9. The integration points p_k and ρ_k are unknown, but they can be bounded, i.e.,

$$p_{i-1} \leq p_k \leq p_i \qquad when \ \ p_{i-1} \leq p_i$$
$$p_{i-1} \geq p_k \geq p_i \qquad when \ \ p_{i-1} \geq p_i \qquad \text{(B.50)}$$

and

$$\rho_{i-1} \leq \rho_k \leq \rho_i \qquad when \ \ \rho_{i-1} \leq \rho_i$$
$$\rho_{i-1} \geq \rho_k \geq \rho_i \qquad when \ \ \rho_{i-1} \geq \rho_i \qquad \text{(B.51)}$$

The above expressions can be replaced by the following equations

$$p_k = C_p p_{i-1} + (1 - C_p) p_i \qquad 0 \leq C_p \leq 1$$
$$\rho_k = C_\rho \rho_{i-1} + (1 - C_\rho) \rho_i \qquad 0 \leq C_\rho \leq 1 \qquad \text{(B.52)}$$
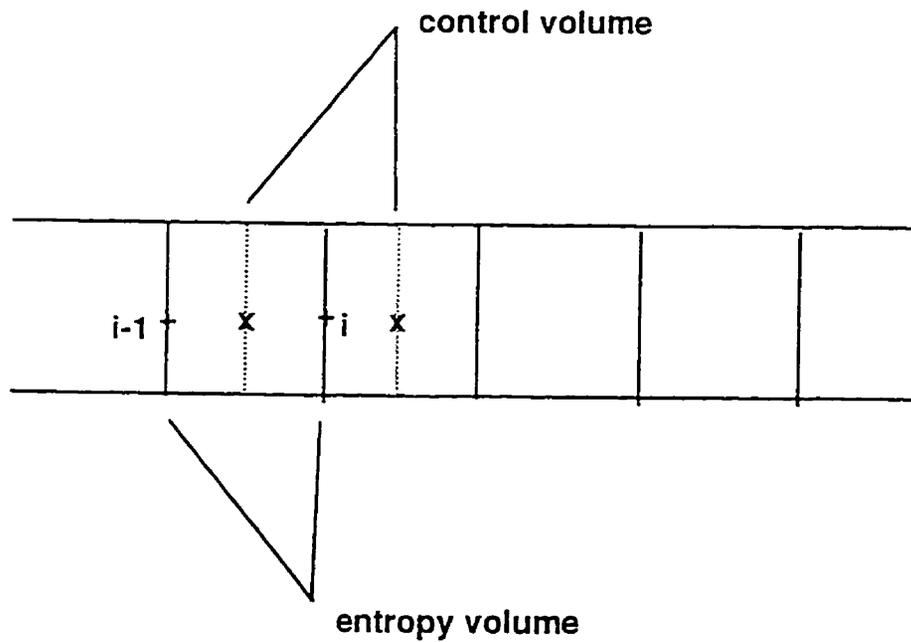
Figure B.9:   Sample entropy volume and sample control volume.

Substituting equations (B.52) into entropy production equation

$$\wp_{s_k} = (ms)_i^j - (ms)_{i-1}^j + \frac{(ms)_k^{j+1} - (ms)_k^j}{\Delta t}$$

(B.53)

where $\Delta x = x_i - x_{i-1}$,

$$s_l^j = ln\left[\frac{\left(p_l / p_{ref}\right)^{1/\gamma}}{\rho_l / \rho_{ref}}\right]^j \qquad l = i-1, \, i, \, or \, k, \tag{B.54}$$

and

$$s_k^{j+1} = ln\left[\frac{\left(\dfrac{C_p p_{i-1} + (1-C_p) p_i}{p_{ref}}\right)^{1/\gamma}}{\dfrac{C_\rho \rho_{i-1} + (1-C_\rho) \rho_i}{\rho_{ref}}}\right]. \tag{B.55}$$

The two coefficients, C_p and C_ρ, in equation (B.55) imply that an additional equation is required. Momentum and energy conservation can not be used to yield this additional equation due to their unknown diffusivities. Mass conservation is therefore used. The entropy control volume then yields

$$\rho_k^{j+1} = \rho_k^j - \frac{[(\rho u)_i^j - (\rho u)_{i-1}^j]\Delta t}{\Delta x} \tag{B.56}$$

Finally, we can express inequality (B.49) as follows

$$\wp_{s_k} = C_s \wp_{s(cr)_k} \qquad\qquad C_s \geq 1 \tag{B.57}$$

Equations (B.47), (B.48), (B.53), (B.54), (B.55), (B.56), and (B.57) are solved to determine the pressure and the density, or the temperature, at the integration point. The velocity at the integration point is determined utilizing a standard approach since the velocity does not directly impact on the computed entropy production rate.

B.5 Numerical Test

A fully implicit calculation procedure is employed in order to admit a larger time step than would be admitted using an explicit scheme. Compatibility with a dynamically adaptive grid is also pursued.

First, the conservative form governing equations are transferred from physical space to computational space. The governing equations in computational space are still conservative. The set of equations is discretized in computational space. Although grids in physical space are moving in time, grids in computational space are fixed. The entropy

production rate scheme is employed to determine pressure and temperature at the integration points. The non-linear algebraic equations produced by discretizing the differential equations are simultaneously computed using the Newton iteration method. This approach uses primitive variables *(u, p, T)* rather than the more traditional conservative variables *(ρ, ρu, e)* as unknowns. No artificial diffusion terms are added to the governing equations. The linear system produced by Newton-Raphson linearization is solved by block TDMA.

After replacing the density by pressure and temperature, and after using the equation of state *(ρ = p/RT)*, the unsteady state, one-dimensional Euler equations in computational space can be written as

$$\frac{\partial Q(q)}{\partial \tau} + \frac{\partial E(q)}{\partial \xi} = 0 \tag{B.58}$$

where

$$q = \begin{bmatrix} u \\ p \\ T \end{bmatrix} \tag{B.59}$$

$$Q = \frac{1}{J} \begin{bmatrix} \dfrac{pu}{RT} \\[2ex] \dfrac{p}{RT} \\[2ex] \left(\dfrac{c_p}{R} - 1\right)p + \dfrac{1}{2}\dfrac{pu^2}{RT} \end{bmatrix} \tag{B.60}$$

$$E = \frac{1}{J} \begin{bmatrix} \dfrac{puU}{RT} + p\xi_x \\[2ex] \dfrac{pU}{RT} \\[2ex] \left(\dfrac{c_p}{R}p + \dfrac{1}{2}\dfrac{pu^2}{RT}\right)U - p\xi_t \end{bmatrix} \tag{B.61}$$

$$U = \xi_t + \xi_x u$$

Here, J is the Jacobian of the mapping; x is the physical coordinate; ξ is the mapping coordinate; u is the Cartesian velocity; ρ is the density; p is the static pressure; T is the static temperature; R is the gas constant; c_p is the constant pressure specific heat; and

$$R = 287 \ (J \, / \, kg \, K), \qquad \gamma = 1.4 \tag{B.62}$$

The discretization will be described for the form of the equations given by Eq. (B.58). The equations are integrated over a control volume in computational space. For a typical control volume around point P, the integration of equation (B.58) with $\Delta x = 1$ gives

$$[Q(q)]_p^{j+1} - [Q(q)]_p^{j} + \{[E(q)]_e^{j+\omega} - [E(q)]_w^{j+\omega}\} \Delta\tau = 0 \qquad \text{(B.63)}$$

where $0 \le w \le 1$. $w = 1$ is selected for an implicit scheme in time. Although a larger time step or Courant number can be made within the implicit scheme, the adaptive grid may produce smaller control volumes in some regions.

A collocated numerical scheme is used. The variables at integration points are evaluated by the entropy equations (B.51) and (B.57) and mass conservation equation (B.56). This technique replaces the conventional methods which utilize Peclet number to calculate integration point property values.

For the one-dimensional problem, the adaptive griding scheme of Dwyer [Dwyer et al, 1983] is convenient to calculate. In addition, no kinked grids will occur in the one-dimensional case. Dwyer's adaptive gridding scheme can be written as

$$\xi(x,t) = \frac{\int_0^x (1 + c_p^a |\partial p / \partial x| + c_T^a |\partial T / \partial x|) dx}{\int_0^{x_{max}} (1 + c_p^a |\partial p / \partial x| + c_T^a |\partial T / \partial x|) dx} \qquad \text{(B.64)}$$

where the c_p^a and c_T^a are the "buffering" coefficients. For the case $c_p^a = c_T^a = 0$, a uniform distribution of grids is obtained. High grid resolution about the moving shock field and the contact surface is expected, hence both control variables, pressure and temperature, are used to reset to a new grid distribution. In all cases, the integrals in equation (B.64) are evaluated using the trapezoidal rule. If the previous pressure and temperature are employed

to determine the grid distribution, it will permit the shock wave and contact surface to move out of the fine-mesh region within a given time step. A prediction-correction scheme is used to overcome this problem. The prediction-correction scheme used is given by

$$x_i^{j+1} = \frac{1}{2}(x_i^{\bar{j}} + x_i^{\overline{j+1}})$$

(B.65)

$x_i^{\bar{j}}$ ---------- *produced by previous pressure and temperaure*

$x_i^{\overline{j+1}}$ --------- *produced by predict pressure and temperature*

where *j* is a time step number.

After discretizing, all non-linear terms are linearized by a Newton-Raphson method. However, it is noted that an equivalent formulation can be developed using conventional Jacobian matrices. The representations for two typical non-linear terms, such as the time term in the continuity equation and one of the convective terms in the momentum equation are illustrated by

$$\left(\frac{p}{T}\right)^{j+1,n+1} \approx \left(\frac{1}{T}\right)^{j+1,n} p^{j+1,n+1} - \left(\frac{p}{T^2}\right)^{j+1,n} T^{j+1,n+1} + \left(\frac{p}{T}\right)^{j+1,n}$$

(B.66)

$$\left(\frac{puU}{JT}\right)^{j+1,n+1} \approx \left(\frac{pU}{JT} + \frac{pu}{T}\right)^{j+1,n} u^{j+1,n+1} + \left(\frac{uU}{JT}\right)^{j+1,n} p^{j+1,n+1}$$
$$- \left(\frac{puU}{JT^2}\right)^{j+1,n} T^{j+1,n+1} + \left(\frac{puU}{JT}\right)^{j+1,n}$$

(B.67)

where n is the iteration index and j indicates the time step. For the transient problem, the linearization error can be effectively removed by iterating at each time step.

After linearization, the three variables, u, p, and T, appear in all of the equations and the resulting equations can be expressed in a matrix form as

$$[A]q = b \qquad\qquad (B.68)$$

where $[A]$ is the tri-diagonal block (3×3) coefficient matrix which can be solved by block TDMA and

$$q = [(u, p, T)_1^T, \dots, (u, p, T)_i^T, \dots, (u, p, T)_{i_{max}}^T]^T \qquad (B.69)$$

$$b = [(b_u, b_p, b_T)_1^T, \dots, (b_u, b_p, b_T)_i^T, \dots, (b_u, b_p, b_T)_{i_{max}}^T]^T$$

are an unknown vector and a right-hand side vector, respectively.

Consider a *1 m* long shock tube that has a diaphragm at its centre separating the tube into two sections with initial pressures of *1000 kPa* on the left and *100 kPa* on the right. A uniform temperature of *293 K* and zero velocity are considered as initial conditions with a specific gas constant $R = 285.7$ *J/kg K* and $c_p = 1000$ *J/kg K*. A maximum Courant number ($a \, \Delta t/\Delta x$) is specified to control the time-step-length and a minimum grid ratio (minimum grid size/maximum grid size) is also specified to obtain the "buffering" coefficients. The solution at $t = 0.58$ *ms* is computed.

If a central difference scheme is used on the pressure term, then the results shown in Figure B.10 are obtained.
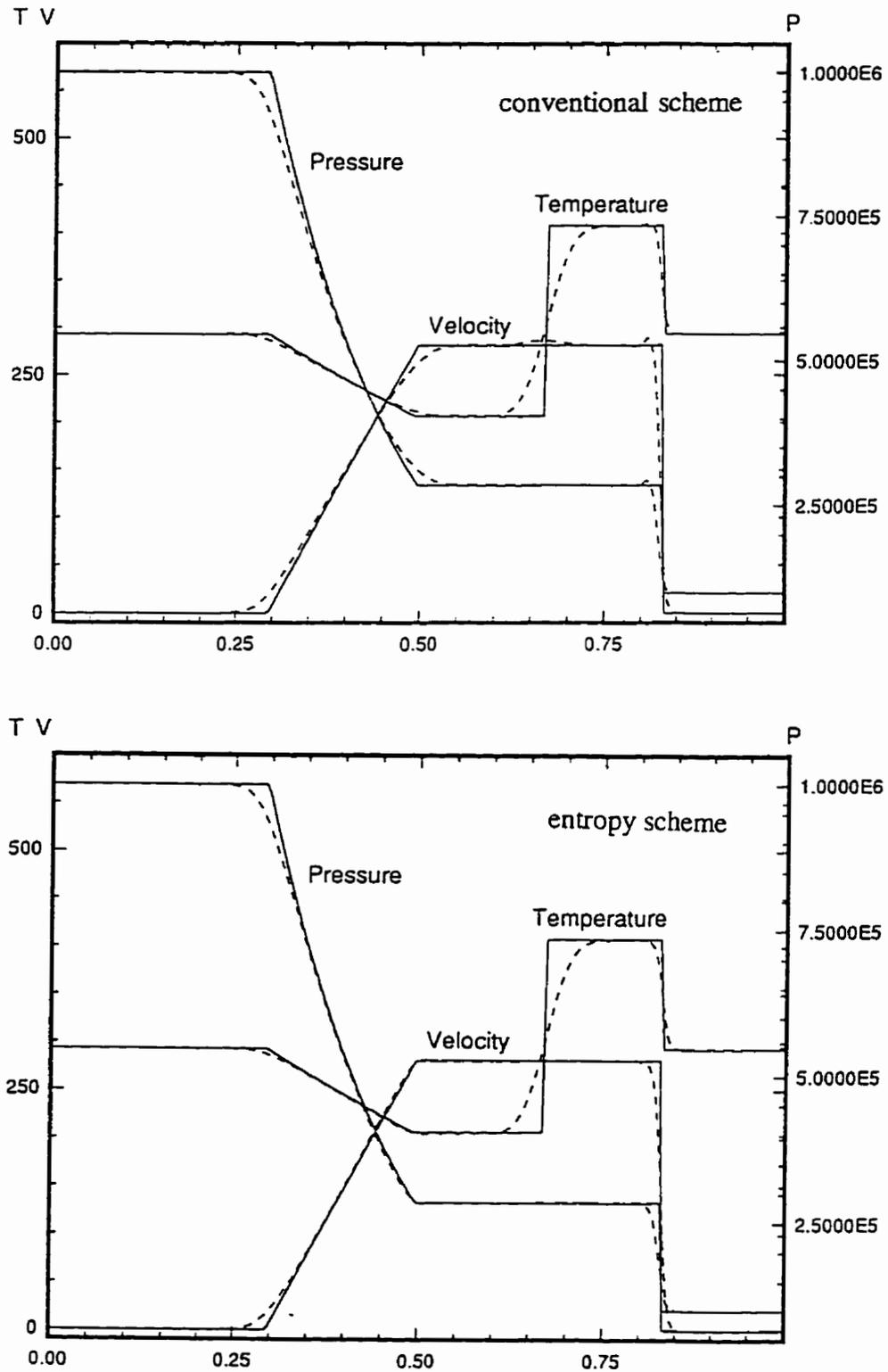
Figure B.10: Comparison of results between a conventional central difference method and the entropy production rate method.

Oscillation still occurs on the shock wave. Figure B.10 also presents solutions obtained by the entropy production rate scheme in which case the numerical method locally satisfies the entropy production rate condition (B.41), therefore, no oscillations occur in its result. The shock wave and contact surface are smeared. Adaptive moving grids can effectively make very fine grids locally around the shock wave and contact surface which would then yield numerical solutions much closer to the exact solutions. This is demonstrated in Figure B.11.
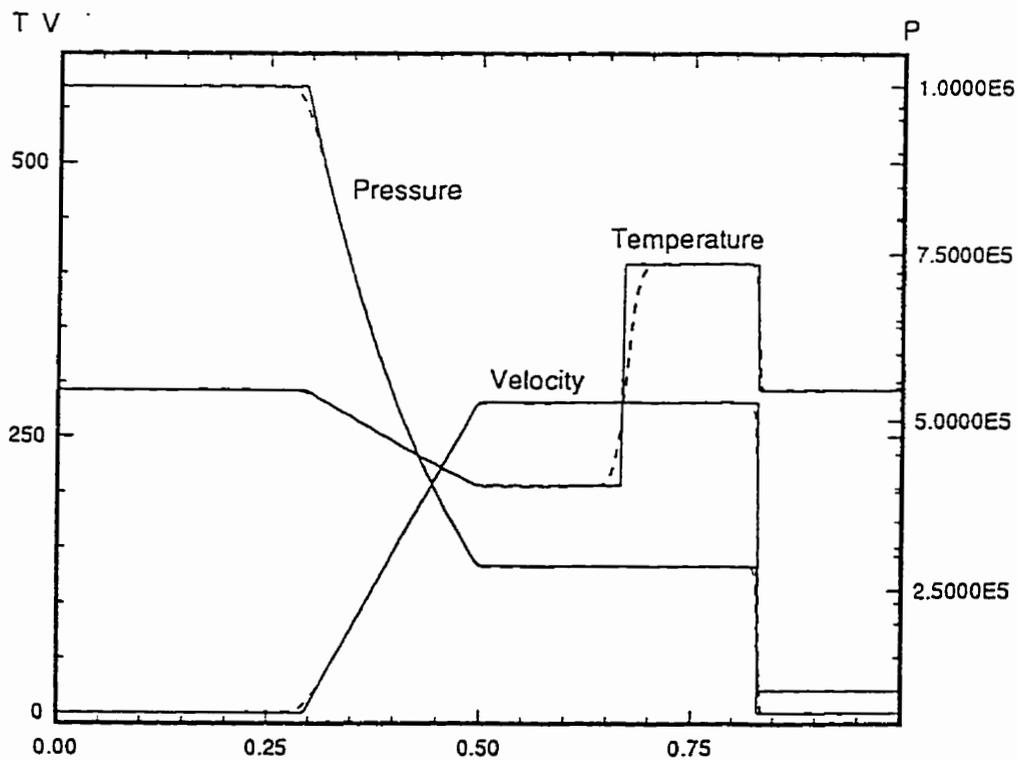
Figure B.11: Results using the entropy production rate method with adaptive gridding.

Using node-variables to interpolate integration-point-variables is the key of a collocated scheme. A reasonable approximation will only result in a local entropy production rate increase and hence non-physical oscillation solutions will still be prohibited. Any non-reasonable collocated grid interpolation approximations may cause oscillatory solutions.

B.6 Closure

A detailed analysis of the relationship between numerical solution oscillations and entropy production rate in the vicinity of a shock and a contact surface is presented. It is proved that a critical entropy production rate could provide a quantitative measure on the amount of numerical diffusion necessary to produce physically relevant solutions. The local entropy production rate in any numerical method has to be equal to or greater than the local critical entropy production rate, i.e.,

$$\wp_{s_t} \geq \wp_{s(cr)_t} \tag{B.70}$$

to ensure that the numerical method results in oscillation free solutions. This quantitative measure demands that the Second Law of Thermodynamics be satisfied locally as well as globally. Equation (B.70) represents a major new contribution advance in an attempt to incorporate the second law of thermodynamics into numerical computations.

When modelling shock wave problems, Peclet number loses its utility. The conventional evaluation of property values at integration points, using such techniques as

the exponential, hybrid or power-law approximate formula, can not be used in the vicinity of a shock. Based on the entropy production rate inequality (equation B.70), a finite volume entropy production rate scheme is developed.   The scheme numerically guarantees satisfaction of the Second Law of Thermodynamics on each control volume.   Thus the solutions produced by this scheme can prevent under- and over-shoots in the vicinity of shock and a contact surfaces.   With the addition of adaptive griding techniques, the entropy production rate scheme has very strong potential as a way to achieve good shock resolution with relatively few grid points.   Sample 1-D shock tube solutions are presented using the entropy production rate scheme (i.e., no artificial diffusion terms) showing very good agreement with exact solutions.

Appendix C

Grids and Adaptive Grids

C.1. Overview

In this appendix numerical grid generation and dynamically adaptive grid generation are discussed. This work was pursued because it was realized early that steep property gradient problems may have been encountered in the natural gas injection problem. In the use of end this adaptive grid technique was not required with the accuracy of the solutions to the natural gas problem obtained and detailed in the main text of this thesis.

The partial differential equations connected with elliptic grid generation are numerically solved so that a group of smoothly changing, orthogonally-closed, grids are generated. Particular attention is given to systems using elliptic grid generation based on variational principles. Adaptive grids are coupled with the physical solution being such that the grid points continually move in the course of the solution in order to resolve developing gradients, or regions of existing steep gradients, within the solution. It is

noted that dynamic grid adaptation can remove solution oscillations common when strong gradients exist on fixed grids, and it appears that when the grid adapts to the solution most numerical solution algorithms work well. Finally, adaptive grid tests in two- and three-dimensional domain are presented.

C.2. Body Fitted Elliptic Grids

In general, the generation of a boundary-conforming coordinate system is accomplished by a determination of curvilinear coordinate values in a region from specified values and/or slopes of the coordinate lines on the boundary of that region. One coordinate will be constant on each segment of the physical boundary curve or surface in three-dimensions, while the other varies monotonically along the segment. The problem in the transformed region is the determination of values of the physical coordinates in the interior of the transformed region from specified values on the boundary of the transformed region.

Now, the generation of field values of a function from boundary values can be done by solving a set of partial differential equations [Zhang et al, 1993]. The solution of such a boundary-value problem takes the coordinates to be solutions of a system of partial differential equations. If the coordinate points and/or slopes are specified on the entire closed boundary of the region, the choice of equations must be elliptic, while if the specification is on only a portion of the boundary the choice would be hyperbolic. This latter case would occur, for instance, when an inner boundary of a region is specified, but

a surrounding outer boundary is arbitrary. The present discussion, however, treats the case of a completely specified boundary, so it requires an elliptic partial differential system.

The important property in regard to coordinate system generation is the inherent smoothness that prevails in the solutions of the elliptic system. Furthermore, boundary slope discontinuities do not propagated into the field. There are then a number of advantages to using a system of elliptic partial differential equations as a means of coordinate system generation.

C.2.1.   Differential Equations

The simplest elliptic partial differential system that exhibits considerable smoothness is the Laplace system [Thompson, 1985]

$$\nabla^2 \xi_i = \left(\frac{\partial^2 \xi_i}{\partial x_1^2} \right) + \left(\frac{\partial^2 \xi_i}{\partial x_2^2} \right) + \left(\frac{\partial^2 \xi_i}{\partial x_3^2} \right) = 0 \qquad (i = 1,\ 2,\ 3) \qquad \text{(C.1)}$$

where ξ_1, ξ_2, and ξ_3 represent the coordinates in the computational domain and x_1, x_2, and x_3 the coordinates in the physical domain. This generation system guarantees a one-to-one mapping for boundary-conforming curvilinear coordinate systems on general closed boundaries. If control terms are added to the right side of equations (C.1), the elliptic generating system becomes the Poisson system

$$\nabla^2 \xi_i = p_i \qquad (i = 1,\ 2,\ 3) \qquad\qquad \text{(C.2)}$$

This system still possesses elliptic properties if the inhomogeneous functions p_i do not change sign in the field. Negative values for the control function p_i will cause the ξ_i-lines to tend to move toward lines with lower values of ξ_i. Since the boundary values are fixed, the ξ_i-lines cannot change points of intersection with the boundary. The effect of the control function p_i at the boundary is thus to change the angle of intersection causing the ξ_i-lines to rotate toward lines with lower values of ξ_i. Control of p_i by with the fluid flow parameters, *i.e.*, velocity and/or temperature, is called dynamic control or dynamic adaptation. Dynamic adaptation will be discussed in section C.3.

Generalizing the Poisson system of equations (C.2) to three-dimensions, yields, with the Cartesian and curvilinear coordinates denoted by x_i and ξ_I, respectively,

$$\nabla^2 \xi_i = p_i(\xi_j, \frac{\partial \xi_j}{\partial x_k}, x_k) \qquad\qquad \text{(C.3)}$$

where i, j, and k all range over 1-3. In the transformed plane, this system becomes

$$\sum_{i=1}^{3}\left(\sum_{j=1}^{3} g^{ij} \frac{\partial^2 x_k}{\partial \xi_i \partial \xi_j} + p_i \frac{\partial x_k}{\partial \xi_i} \right) = 0 \qquad\qquad \text{(C.4)}$$

where

$$g^{ij} = \frac{1}{g}(g_{km}g_{ln} - g_{kn}g_{lm}) \tag{C.5}$$

with (i, k, l) and (j, m, n) cyclic, *i.e.*,

$$k = i + 1\ (\equiv 3\,),\ l = i + 2\ (\equiv 3\,),\ m = j + 1\ (\equiv 3\,),\ \text{and}\ n = j + 2\ (\equiv 3\,), \tag{C.6}$$

and

$$g_{ij} = \frac{\partial x_1}{\partial \xi_i}\frac{\partial x_1}{\partial \xi_j} + \frac{\partial x_2}{\partial \xi_i}\frac{\partial x_2}{\partial \xi_j} + \frac{\partial x_3}{\partial \xi_i}\frac{\partial x_3}{\partial \xi_j} \tag{C.7}$$

$$g \equiv J^2 = \left|\frac{\partial(x_1,x_2,x_3)}{\partial(\xi_1,\xi_2,\xi_3)}\right|^2$$

If p_i is not a function of the coordinate derivatives, the system is linear in the physical domain, but quasi-linear in the transformed domain. Our interest is in the transformed domain, that is, to solve the non-linear differential equations (C.4). The equations are more complicated in general in the transformed region.

C.2.2.   Boundary Conditions

The simplest boundary conditions are Dirichlet boundary conditions where the grid points are fixed on the boundary. However, most numerical methods require orthogonal grid

boundary, or Neumann boundary, conditions on some parts of the boundary. The orthogonal boundary condition in the computational domain can be expressed in two-dimensions as

$$\left.\frac{dy}{dx}\right|_{\xi_1} \cdot \left.\frac{dy}{dx}\right|_{\xi_2} = -1 \tag{C.8}$$

where $\left.\dfrac{dy}{dx}\right|_{\xi_1}$ and $\left.\dfrac{dy}{dx}\right|_{\xi_2}$ represent the direction derivatives along the ξ_1 line and the ξ_2 line, respectively. In generally, derivatives follow the following relation

$$\frac{dy}{dx} = \frac{\partial y}{\partial \xi_1} \cdot \frac{d\xi_1}{dx} + \frac{\partial y}{\partial \xi_2} \frac{d\xi_2}{dx} \tag{C.9}$$

On the ξ_1 line, ξ_1 is a constant and the direction derivative along ξ_1 line becomes

$$\left.\frac{dy}{dx}\right|_{\xi_1} = \frac{\partial y}{\partial \xi_2} \cdot \frac{d\xi_2}{dx} = \frac{\partial y}{\partial \xi_2} \bigg/ \frac{dx}{d\xi_2} = \frac{\partial y}{\partial \xi_2} \bigg/ \frac{\partial x}{\partial \xi_2} \tag{C.10}$$

where $\dfrac{dx}{d\xi_2} = \dfrac{\partial x}{\partial \xi_2}$ along the ξ_1 line. In the same way, ξ_2 is a constant along the ξ_2 line. The direction derivative along the ξ_2 line is

$$\frac{dy}{dx}\bigg|_{\xi_2} = \frac{\partial y}{\partial \xi_1} \cdot \frac{d\xi_1}{dx} = \frac{\partial y}{\partial \xi_1} \bigg/ \frac{dx}{d\xi_1} = \frac{\partial y}{\partial \xi_1} \bigg/ \frac{\partial x}{\partial \xi_1} \qquad (C.11)$$

Substituting expressions (C.10) and (C.11) into expression (C.8), the orthogonal boundary condition is obtained,

$$\frac{\partial y}{\partial \xi_1} \cdot \frac{\partial y}{\partial \xi_2} + \frac{\partial x}{\partial \xi_1} \frac{\partial x}{\partial \xi_2} = 0 \qquad (C.12)$$

C.2.3.   Solving Methods

The partial differential equations (C.4) are non-linear since g^{ij} is a function of $\frac{\partial x_m}{\partial \xi_n}$ (m, n = 1, 2, 3). One linearization method is to substitute the guessed x_i into the discretized form of g^{ij} where the finite difference scheme applied to g^{ij} assumes that p_i is not a function of x_i. If p_i is a function of x_i, use the guess x_i in p_i too. The linear algebraic equations yield a sparse coefficient matrix which is solved by using the Gauss eliminate method or a sparse conjugate gradient solver. Solver choice depends on how large the number of grid points. Initial grids are generated by using an algebraic interpolation method. Iteration is then employed until the maximum x_i difference is less than a given tolerance.

C.2.4.   Sample Results

Figure C.1 shows the grid which is a static mesh region for free surface flow passing over a half cylinder. A moving mesh will be added on the top boundary *AB* to match the free surface requirement. The *BC* line actually is not a boundary of the mesh. It requires an orthogonal boundary condition, i.e., Neumann condition, which is different from the other boundary conditions due to symmetry considerations.
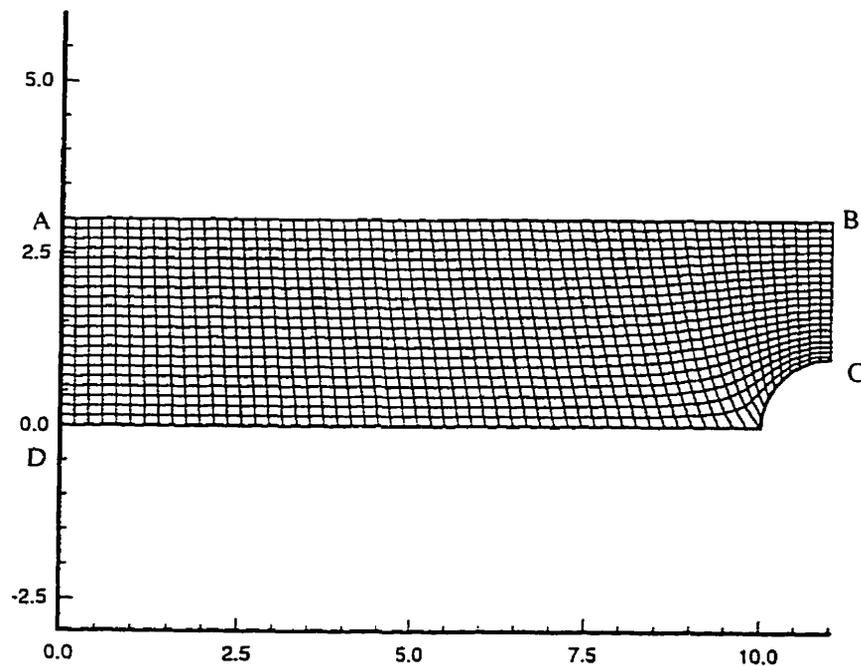
Figure C.1:   A fixed mesh part for free surface flow passing over a half cylinder.

In Fraser *et al.*'s experiment [1989] it is noted that the combustion chamber is a circular cylinder and that the fuel injector is located on the circular boundary of the chamber. Mesh generation is needed for only a quarter of the circular cylinder due to symmetric consideration. A fine mesh is needed at the injector orifice *AB* shown on Figure C.2. Surfaces *1* and *22* are two boundaries of the quarter combustion chamber.
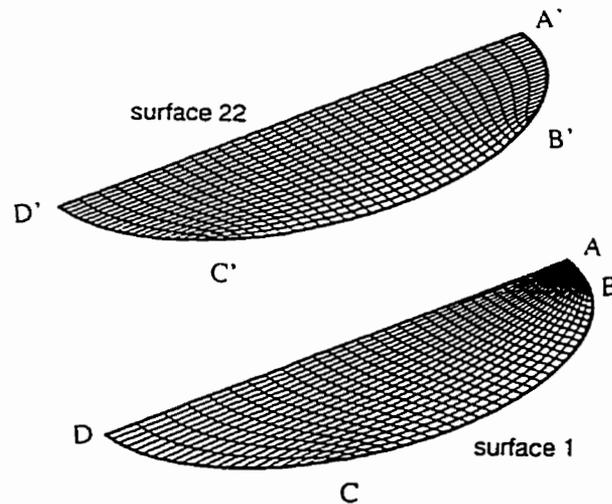
Figure C.2:   Grid distribution of combustion chamber

C.3. Adaptive Grids

In an adaptive grid, the physics of the problem at hand must ultimately direct the grid points to congregate such that an improvement in solution accuracy is obtained. The mathematics controls the points by sensing the gradients in the evolving physical solution, evaluating the accuracy of the discrete representation of the solution, communicating the needs of the physics to the points, and, finally, by providing mutual communication among the points as they respond to the physics.

The basic techniques involved are

(1) distributing points over the field in an orderly fashion such that neighbors may be easily identified and data can be stored and handled efficiently,

(2) communicating between points such that a smooth distribution is maintained as points shift their positions,

(3) representing continuous functions by discrete values on a collection of points with sufficient accuracy, and evaluating the error in this representation, and

(4) communicating the need for a re-distribution of points in light of the error evaluation, and controlling this re-distribution.

In the present discussion, some features of two adaptation schemes are noted. A grid speed simplification which results in a reduction in computation in each time step is then discussed. It is noted that the idea of equal-distribution is the unifying feature of adaptive grids in general, and is equivalent to solving the Euler equations arising from a variational principle.

C.3.1.   Dwyer's Method

In this method the lines of constant ξ_2 are fixed in the two-dimensional case and the adaptation is done along line ξ_1, and vice versa.   In effect, the method is quasi-one-dimensional and it relies on the model having sufficient qualitative knowledge about the solution to be able to fix a set of coordinates which are roughly normal to any steep fronts in the solution. An expression of this adaptation system can be taken as

$$\Delta \xi_1 = \frac{\int_{x_i}^{x_{i+1}} w(x) dx}{\int_0^1 w(x) dx} = const. \leq 1 \qquad (C.13)$$

where x is the length along the fixed line, and w is the weight function given, for example, by

$$w = 1 + \alpha \left| T_x' \right| + \beta \left| f(T_{xx}'') \right| \qquad (C.14)$$

α and β are the adjustable constants used for optimization of the grid distribution. For the case $\alpha = \beta = 0$ a uniform distribution of points along the fixed line result. For large values of α and β, the mesh intervals are determined such that the same change in the dependent variable T, i.e., temperature, occurs between mesh points. The coefficients α and β can be thought of as buffers. That is, α and β are chosen so that not all of the mesh points are concentrated at the steep gradient or front region. Some are in regions of

relatively uniform T, and there is a smooth progression of mesh interval sizes when moving away from a front. The weighting function is evaluated explicitly and the mesh transformation is held fixed throughout the time step. The integrals in expression (C.13) can be evaluated by using the trapezoidal rule.

The method is simpler than one of solving the partial differential equations (C.4). However, it may cause severe grid distortion, especially in three-dimensional grid generation cases.

C.3.2.　Anderson's Method

Anderson's method [Thompson, 1985] provides an effective way to produce a fine mesh in large gradient variation regions of physical parameters. The question is how to use physical parameters, such as temperature T and velocity V to control the function p_i of equation (C.3). The control function considered is

$$p_i = g^{ii} \frac{\left(\frac{\partial w}{\partial \xi_i}\right)}{w} \tag{C.15}$$

where g^{ii} is given in equation (C.4) and w is a weighting function given, foe example, by

$$w = 1 + \alpha_1 \sum_{i=1}^{3} \left(T_{\xi_i}\right)^2 + \alpha_2 \sum_{i=1}^{3} \left(V_{\xi_i}\right)^2 \tag{C.16}$$

where α_1 and α_2 are adjustable coefficients (or buffers).

An important difference between Anderson's method and Dwyer's method [Dwyer et al, 1983] is that Anderson's method adapts to large rates of change in the gradient while Dwyer's method adapts to large gradients. For instance, Figure C.3 shows a 1-D temperature distribution, an example of how Dwyer's scheme would adapt to this distribution, and an example of how Anderson's scheme would adapt. Anderson's scheme should, in general, outperform Dwyer's scheme.
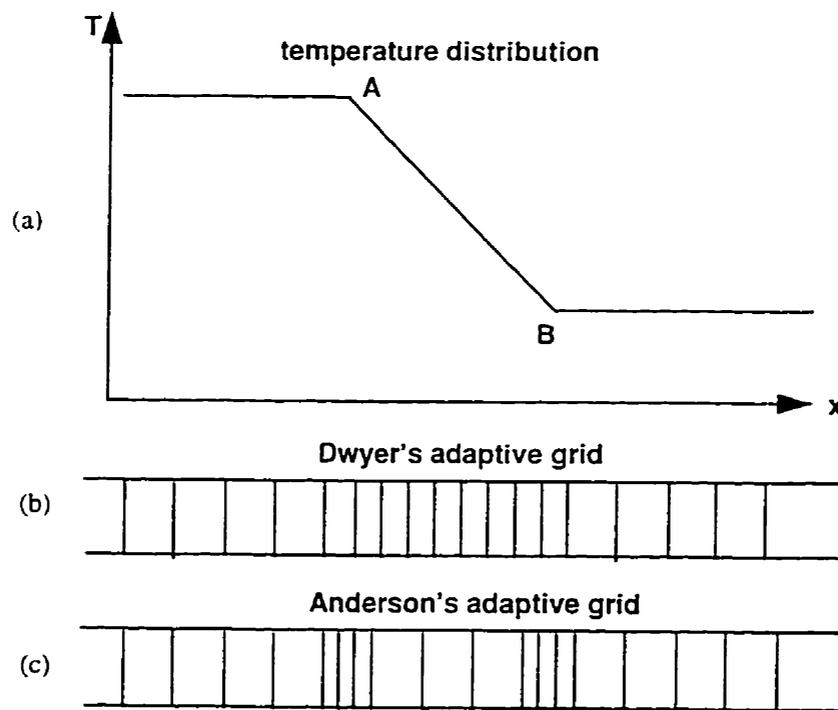
Figure C.3: Grid adaptations to (a) a temperature distribution using (b) Dwyer's adaptation and (c) Anderson's adaptation.

The number of grid points in the physical domain are established initially and usually does not change during the course of a calculation. However, the grid can always be restructured. In order to construct a mesh which is appropriate for a specific problem, *a priori* the knowledge of the solution is required at the outset. High mesh point densities are desirable in high gradient regions, but if the locations of these regions are unknown, it is difficult to establish a suitable grid. Unfortunately, the exact details of a solution are seldom know before it is computed and unexpected behavior frequently occurs. A method for the construction of an appropriate grid will be discussed in Section C.3.4.

C.3.3.   Moving Boundary Grids

Some important considerations surrounding moving boundaries are discussed in this section. In some realistic problems the boundary may not be fixed in time. For instance, the top surface of piston considered as the parts of boundary of a combustion chamber moves in time in connection with the rotation speed of the crank shaft. In this case the movement of boundary grid is a function of engine speed. If the speed of crank shaft is constant and known, the boundary grid location can easily be determined in time. However, the speed of crank shaft depends on the combustion chamber pressure which accelerates or decelerates the piston and hence the crank shaft. In this case the moving grid location is uncertain or implicit. Explicit movement independent of the physical process are simpler, but generally correction. Implicit handling is coupled with physical process and may require much more computer memory and run time.

C.3.4.   Grid Speed Approaches

Adaptive griding solves a set of non-linear partial differential equations. The solution to these non-linear equations must be determined iteratively. Furthermore, adaptive grids change with time in a transient problems. It is therefore computationally expensive and impractical to solve these nonlinear equations for each time step in order to update the grid. Noted, however, that grid point location accuracy does not significantly affect the computational accuracy of the fluid flow and reaction problem provided the grid is close to the desired location. An alternative approach, therefore, is to differentiate the above non-linear equations with respect to time yielding, for a one-to-one mapping, the following equations:

$$S[Z] = R$$

$$Z = (\frac{d\,x_1}{dt}, \frac{d\,x_2}{dt}, \frac{d\,x_3}{dt}) \quad and \quad R = \sum_{k=1}^{3} g^{kk} F_{kt} r_{\xi_k} \qquad (C.17)$$

S is a matrix operator which, due to its complexity, will not be shown here. The approach to be adopted first solves the non-linear grid generation system for the initial grid points. All other grids at future times are generated by solving the above linear grid speed equations with the prediction-correction scheme. The prediction-correction scheme is given as follows

$$x_k^{\overline{n+1}} = x_k^n + \Delta t \, \frac{dx_k^n}{dt}$$

$$x_k^{n+1} = \frac{1}{2}(x_k^n + x_k^{\overline{n+1}} + \Delta t \, \frac{dx_k^{\overline{n+1}}}{dt}) \, . \tag{C.18}$$

where n is the temporal iteration step number. This approach is computationally much cheaper than solving the non-linear adaptive generation system directly.

C.3.5.   Sample Results

Figure C.4 shows the implementation of adaptive griding for a high temperature gas jet injected into a cooler ambient gas where only half the chamber is used for the computations due to symmetry considerations. The figure shows, (a) the initial uniform mesh; (b) the temperature control function; and (c) is an adaptive mesh.

Figure C.5 shows a three-dimensional case which employs a normal distribution of temperature as a control function with 1000^0C at the center of the chamber quarter and 20^0C on the boundaries. For clarity, the figure only presents selected surfaces.
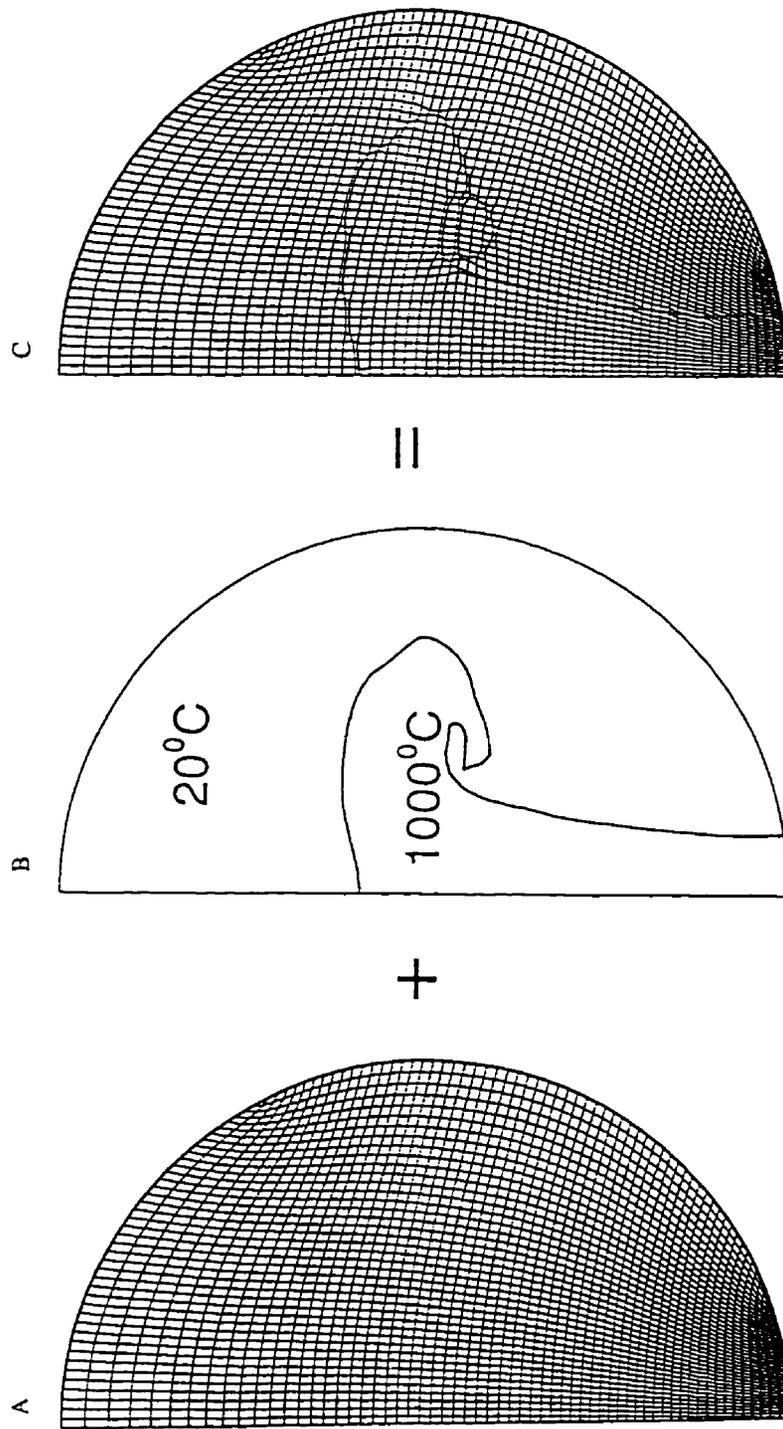
Figure C.4: Adaptive gridding for a high temperature gas jet injected into a cooler ambient gas. (A) initial mesh, (B) controlling temperature distribution, and (C) adapted mesh.

surface 22

surface 1

surface 17

surface 6

surface 17

surface 11

surface 6
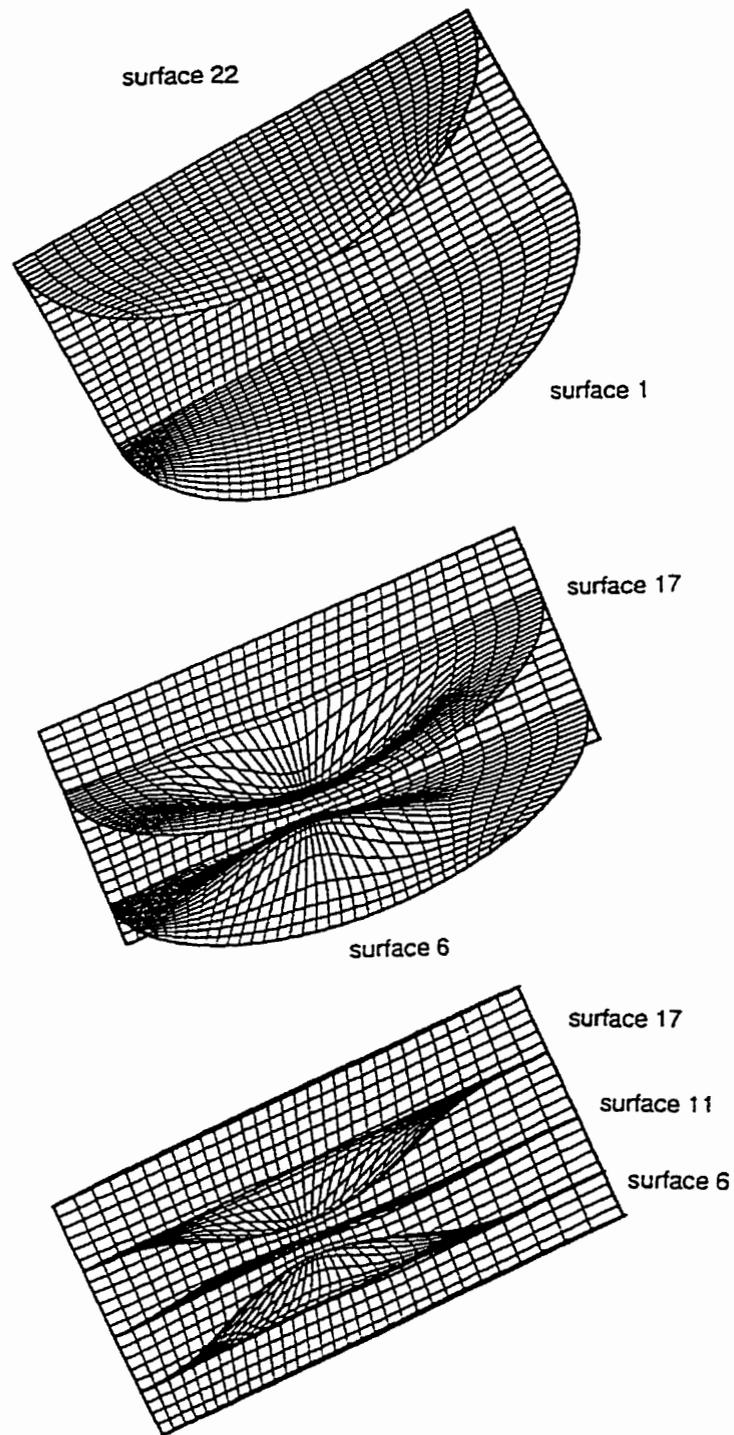
Figure C.5:   A three-dimensional adaptive grid

C.4. Closure

In this appendix the techniques of elliptic grid generation and two adaptive grid generations are detailed. The grid point distribution used in solving a fluid flow problem with reaction has a substantial influence on the quality of the solution. An adaptive grid which adjusts to solution changes provides the best results when the number of grid points available for use during the calculation is fixed. The initial grid distribution is generated by using an elliptic grid generation system. Adaptive grid generation based on the gradient variation of physical parameters is then provided by Anderson's method and a grid speed approach For completeness a brief discussion of moving boundary grids is presented.

Appendix D

Equations in Curvilinear Coordinate System with Axisymmetric Frame

In chapter 3 the equations based on an axisymmetric coordinate system are established. Suppose the axisymmetric coordinate system is in a computational domain frame with uniformly spaced grids with unit length cells. Then the governing and turbulence equations under the transformation from the axisymmetric physical domain to the axisymmetric computational domain can be expressed as follows:

$$\frac{\partial Q}{\partial \tau} + \frac{1}{r}\frac{\partial E}{\partial \xi} + \frac{1}{r}\frac{\partial F}{\partial \eta} = \frac{1}{r}\frac{\partial R}{\partial \xi} + \frac{1}{r}\frac{\partial S}{\partial \eta} + \frac{W}{J} \qquad (D.1)$$

$$Q = \frac{\rho}{J} \begin{bmatrix} 1 \\ u_z \\ u_r \\ E \\ Y_k \\ k \\ \varepsilon \end{bmatrix} \tag{D.2}$$

$$E = \frac{r}{J} \begin{bmatrix} \rho U_t \\ \rho u_z U_t + p\xi_z \\ \rho u_r U_t + p\xi_r \\ \rho E U_t + pU_n \\ \rho Y_k U_t \\ \rho k U_t \\ \rho \varepsilon U_t \end{bmatrix} \tag{D.3}$$

$$F = \frac{r}{J} \begin{bmatrix} \rho V_t \\ \rho u_z V_t + p\eta_z \\ \rho u_r V_t + p\eta_r \\ \rho E V_t + pV_n \\ \rho Y_k V_t \\ \rho k V_t \\ \rho \varepsilon V_t \end{bmatrix} \tag{D.4}$$

$$R = \frac{r}{J} \begin{bmatrix} 0 \\ \tau_{zz}\xi_z + \tau_{rz}\xi_r \\ \tau_{rz}\xi_z + \tau_{rr}\xi_r \\ u_z(\tau_{zz}\xi_z + \tau_{rz}\xi_r) + u_r(\tau_{rz}\xi_z + \tau_{rr}\xi_r) + \dfrac{c_p\mu_{eff}}{\sigma_t}[(\xi_z^2 + \xi_r^2)T_\xi + (\xi_z\eta_z + \xi_r\eta_r)T_\eta] \\ \dfrac{\mu_{eff}}{S_c}[(\xi_z^2 + \xi_r^2)\dfrac{\partial Y_k}{\partial \xi} + (\xi_z\eta_z + \xi_r\eta_r)\dfrac{\partial Y_k}{\partial \eta}] \\ \dfrac{\mu_{eff}}{\sigma_k}[(\xi_z^2 + \xi_r^2)k_\xi + (\xi_z\eta_z + \xi_r\eta_r)k_\eta] \\ \dfrac{\mu_{eff}}{\sigma_\varepsilon}[(\xi_z^2 + \xi_r^2)\varepsilon_\xi + (\xi_z\eta_z + \xi_r\eta_r)\varepsilon_\eta] \end{bmatrix}$$

$$S = \frac{r}{J} \begin{bmatrix} 0 \\ \tau_{zz}\eta_z + \tau_{rz}\eta_r \\ \tau_{rz}\eta_z + \tau_{rr}\eta_r \\ u_z(\tau_{zz}\eta_z + \tau_{rz}\eta_r) + u_r(\tau_{rz}\eta_z + \tau_{rr}\eta_r) + \dfrac{c_p\mu_{eff}}{\sigma_t}[(\xi_z\eta_z + \xi_r\eta_r)T_\xi + (\eta_z^2 + \eta_r^2)T_{\eta1}] \\ \dfrac{\mu_{eff}}{S_c}[(\xi_z\eta_z + \xi_r\eta_r)\dfrac{\partial Y_k}{\partial \xi} + (\eta_z^2 + \eta_r^2)\dfrac{\partial Y_k}{\partial \eta}] \\ \dfrac{\mu_{eff}}{\sigma_k}[(\xi_z\eta_z + \xi_r\eta_r)k_\xi + (\eta_z^2 + \eta_r^2)k_\eta] \\ \dfrac{\mu_{eff}}{\sigma_\varepsilon}[(\xi_z\eta_z + \xi_r\eta_r)\varepsilon_\xi + (\eta_z^2 + \eta_r^2)\varepsilon_\eta] \end{bmatrix}$$

$$W = \frac{1}{r}\begin{bmatrix} 0 \\[4pt] 0 \\[4pt] -\lambda(\nabla\cdot v) - 2\mu_{\mathit{eff}}\dfrac{u_r}{r} + p \\[6pt] r\sum h_k w_k \\[6pt] r\rho w_k \\[6pt] r\mu_{\mathit{eff}}\left[2\left(\dfrac{\partial u_z}{\partial z}\right)^2 + 2\left(\dfrac{\partial u_r}{\partial r}\right)^2 + 2\left(\dfrac{u_r}{r}\right)^2 + \left(\dfrac{\partial u_z}{\partial r} + \dfrac{\partial u_r}{\partial z}\right)^2\right] - \dfrac{2}{3}r\nabla\cdot v(\mu_{\mathit{eff}}\nabla\cdot v + \rho k) - r\rho\varepsilon \\[10pt] \dfrac{C_1 r\mu_{\mathit{eff}}\varepsilon}{k}\left[2\left(\dfrac{\partial u_z}{\partial z}\right)^2 + 2\left(\dfrac{\partial u_r}{\partial r}\right)^2 + 2\left(\dfrac{u_r}{r}\right)^2 + \left(\dfrac{\partial u_z}{\partial r} + \dfrac{\partial u_r}{\partial z}\right)^2\right] - \dfrac{2}{3}\dfrac{r\varepsilon}{k}\nabla\cdot v(C_1' \mu_{\mathit{eff}}\nabla\cdot v \\[10pt] + C_1'' \rho k) - C_2 r\rho\dfrac{\varepsilon^2}{k} + C_3 r\rho\varepsilon\nabla\cdot v + C_4\dfrac{r\rho\varepsilon}{\mu}\dfrac{\partial\mu}{\partial t} \end{bmatrix}$$

$$\tau_{zz} \equiv \lambda(\nabla\cdot v) + 2\mu_{\mathit{eff}}\frac{\partial u_z}{\partial z}$$

$$\tau_{rr} \equiv \lambda(\nabla\cdot v) + 2\mu_{\mathit{eff}}\frac{\partial u_r}{\partial r}$$

$$\tau_{rz} \equiv \mu_{\mathit{eff}}\left(\frac{\partial u_r}{\partial z} + \frac{\partial u_z}{\partial r}\right)$$

$$\nabla\cdot v \equiv \frac{1}{r}\left[\frac{\partial}{\partial z}(ru_z) + \frac{\partial}{\partial r}(ru_r)\right]$$

$$\lambda \equiv -\frac{2}{3}\mu_{\mathit{eff}}$$

The two-dimensional transformation can easily be deduced from the above axisymmetric transformation by setting the variable $r = 1$ and changing from the (r, z) frame to the (x, y) frame.

Appendix E

Numerical Method Uncertainties

E.1 Overview

This appendix addresses the uncertainties associated with the numerical method employed in this work. Error estimation schemes are discussed. Attention is paid to time step selection, grid size selection, and truncation error propagation in order to reduce the risk of non-physical solutions. A brief outline of the error checks performed in this work are discussed last.

E.2 Uncertainties in Numerical Method

An unavoidable question that must be asked of all CFD predictions is how accurate are the results? Put another way, how much confidence is there that the results accurately

reflect the physical situation being modelled. For complicated problems this answer is not easy to obtain.

There are a large number of factors which affect CFD accuracy. These factors may originate in the physical model or in the numerical method. The physical model includes the conservation equations, any equation of state, a turbulence model, and a combustion model. It also includes geometry and boundary condition specifications. Factors affecting the numerical method include the choice of discretization scheme, grid size and distribution, time step selection, convergence tolerances, and computer accuracy. This appendix focuses on accuracy considerations resulting from the numerical methods used.

When a set of conservation equations, which describe a physical phenomenon, are discretized into a set of non-linear algebraic equations, discretization errors (or truncation errors) result. Discretization errors are a function of discretization scheme, grid size, and time step (for a transient problem). A forth contributor to errors can result when seeking an implicit solution to a set of algebraic equations. A linearization scheme must be selected to form an iterative basis for the solution of the non-linear algebraic equations. In this research the Newton-Raphson iterative scheme is utilized [Chen and Pletcher, 1991, Karki and Patankar, 1989]. Note that when the solution variation between iterations in a linear system is exactly zero then there are no errors introduced in the linearization operation. If, however, the variation between iterations is not exactly zero a linearization error results.

Linearization errors are generally introduced by using some specified tolerance for minimizing the system residual in the solution of a large linear system when speed

and memory considerations necessitate the use of an iterative solver, such as a multigrid solver [Hutchinson and Raithby, 1986], the CGSTAB solver [Van der Vorst, 1992], etc. These solvers only minimize the residual vector not the error vector. Though the infinite norm (defined in Section E.2.1) of the residual vector satisfies a specified tolerance, the error vector may not satisfy this same tolerance. The reason is that the conditional number of the coefficient matrix may enlarge the infinite norm of residual vector.

The next section describes the condition number for a linear system. The condition number reflects the sensitivity of the linear system to an initial error. Section E.2.3 then extends the idea of a condition number for a linearized system derived from a non-linear system; this naturally leads to a discussion of grid and time step considerations as discussed in subsequent sections.

E.2.1 Condition Number for A Linear System

Consider the large linear system of equations represented by

$$A\,x = b \tag{E.1}$$

where the residual vector of the ith iteration, r^i, is defined as

$$r^i = b - A x^i \tag{E.2}$$

where A is coefficient matrix, x exact solution vector, b right hand side vector, and x^i guess vector of the ith iteration. The infinite norms are then defined as

$$\|x\| \equiv \max_i (|x_i|), \ and \ \|A\| \equiv \max_{1 \le i \le n} \sum_{j=1}^{n} |a_{ij}|, \tag{E.3}$$

Therefore Equation (E.2) can be expressed in terms of the error vector, e^i ,

$$A (x - x') \equiv A e^i = r^i \tag{E.4}$$

which yields for the error vector

$$e^i = A^{-1} r^i \tag{E.5}$$

where $e^i = x - x^i$ is the defined error vector. If we define the initial error vector and initial residual vector as

$$e^0 \equiv x - x^0, \tag{E.6}$$

and

$$r^0 \equiv A e^0, \tag{E.7}$$

respectively, the following inequalities can be obtained

$$\|e^i\| = \|A^{-1} r^i\| \le \|A^{-1}\| \|r^i\|, \tag{E.8}$$

and

$$\left\| r^0 \right\| \leq \|A\| \left\| e^0 \right\|.$$ (E.9)

Dividing Equation (E.8) by Equation (E.9) finally yields the following result for the condition number:

$$\frac{\left\| e^i \right\|}{\left\| e^0 \right\|} \leq \|A\| \left\| A^{-1} \right\| \frac{\left\| r^i \right\|}{\left\| r^0 \right\|} \equiv cond(A) \frac{\left\| r^i \right\|}{\left\| r^0 \right\|}$$ (E.10)

or

$$cond(A) = \|A\| \left\| A^{-1} \right\|.$$ (E.11)

where *cond(A)* is the condition number of matrix A.

From linear algebra the *cond(A)* is proportional to $\sqrt{\lambda_{max}(A^T A) / \lambda_{min}(A A^T)}$ where $\lambda_{max}(A^T A)$ is the maximum eigenvalue of matrix $(A^T A)$ and $\lambda_{min}(A A^T)$ is the minimum eigenvalue of matrix $(A A^T)$ [Jiang, 1978]. The *cond(A)* is a magnifying factor and represents the sensitivity of this linear system to a residual vector. A large condition number lowers the accuracy of the solution to the given linear system.

Reducing the condition number for a linear system increases solution accuracy. Numerical schemes to reduce the condition number include the Upwind Differencing

Scheme (UDS) [Patankar, 1980], the Mass-Weighted Discretization Scheme (MWS) [Hutchinson, 1996], etc. The physical problem can also guide condition number reduction approaches such as local grid refinement or adaptive grid refinement in sensitive regions around shock waves and contact surfaces. Multiple time stepping is another good approach. For example, a smaller time step (relative to an acceptable time step for the fluid flow alone) can be implemented to capture the smaller characteristic time of reaction zone kinetics. This smaller time step reduces the ratio of the largest to smallest eigenvalues between the fluid flow dominated and reaction dominated zones.

E.2.2 Convergence Considerations for A Non-Linear System

Section E.2.1 details the convergence characteristics of linear systems. The work presented in this thesis, however, involves a non-linear system, hence, the convergence characteristics of non-linear systems are described next. The analysis of a non-linear system is much more difficult than that of a linear system. This research implemented the Newton-Raphson method due to its fast convergence speed (in the non-linear iteration cycle) [Chen and Pletcher, 1991, Karki and Patankar, 1989]. The penalty for fast convergence is a stricter requirement for a good initial guess.

The convergence theory for the Newton-Raphson iterative method is now summarized [Wang, 1983]. Consider the n-dimensional sphere, of radius r defined by

$$S_r(x^*) \equiv \left\{ x \mid \|x - x^*\| < r \right\}$$

(E.12)

where x is a n-dimensional vector, and x^* is a converged solution at the centre point of this sphere. If for any x^1 and x^2 n-dimensional vectors

$$x^1, x^2 \in S_r(x^*) \tag{E.13}$$

the following expression holds

$$\left\| \phi(x^1) - \phi(x^2) \right\| \leq C \left\| x^1 - x^2 \right\| \tag{E.14}$$

where $0 \leq C < 1$ and $\phi(x)$ is the Newton-Raphson iterative method operator, then, for any initial n-dimensional vector guess $x^0 \in S_r(x^*)$, the x^i produced by the Newton-Raphson iterative method $x^i = \phi(x^{i-1})$ $\{i = 1, 2, 3, ...\}$ is also within this n-dimensional sphere $S_r(x^*)$. Subsequently the following expression also holds

$$\left\| x^i - x^* \right\| \leq C^i \left\| x^0 - x^* \right\|. \tag{E.15}$$

Therefore, the Newton-Raphson iterative method converges and is at least linear convergent [Wang, 1983]. This theory tells us that if we can find a n-dimensional convergence sphere with radius r that satisfies expression (E.14), it would be trivial to select an initial guess n-dimensional vector. It is, however, impossible to *a priori* find this convergence sphere for most real problems. However, by reducing the integral time step an initial guess vector is necessarily closer to the converged solution.

Now the important question is that, if the Newton-Raphson iterative method yields a converged solution, does this solution match the physical solution? To match a physical solution we need to consider several factors. Obtaining a converged solution with the Newton-Raphson iterative method is one necessary condition. For a transient problem the Newton-Raphson converged solution simply matches the algebraic equation solution for a given time step and grid size. Therefore, both time step and grid size associated errors are discussed in more detail in section E.4 and E.5, respectively.

E.3   Error Estimations

There are many error estimation schemes in computational fluid dynamics. None of them can, however, resolve all errors in the solution of a complicated problem. This section describes two error estimation methods. One reflects the error propagation, specifically for a hyperbolic system (used in this research), while another one reflects solution sensitivity to grid density and distribution. This research did not implemented either method because of time limitations, but such work should be pursued in future research.

In order for hyperbolic problems (directly related to this research) to achieve high resolution of localized flow structures, especially across discontinuities like shocks, use of locally refined adaptive computational grids is one of the most attractive strategies. The generation of such grids should be guided by error estimates which enable the adaptive algorithm to be applied efficiently [Zhang, 1996].

One dynamic method to solve a set of error equations is in error estimation method [Zhang, 1996]. The two-dimensional conservation laws for mass, momentum,

energy, turbulent kinetic energy, turbulent dissipation rate, and species transport for a chemically reacting gas of N-species can be written conveniently in the following vector form

$$\frac{\partial Q}{\partial \tau} + \frac{\partial E}{\partial \xi} + \frac{\partial F}{\partial \eta} = H \tag{E.16}$$

where Q is transient vector, E, F involve convection and diffusion flux vectors, and H is a source vector.

Based on the error estimation analysis discussed by Zhang [1996], the error equations can be written in quasi-linear form as follows

$$\frac{\partial T\varepsilon}{\partial \tau} + \frac{\partial A\varepsilon}{\partial \xi} + \frac{\partial B\varepsilon}{\partial \eta} + D\varepsilon = \Phi \tag{E.17}$$

where $T = Q_x, A = E_x, B = F_x, D = -H_x$, and Φ is an extra source term. The error estimation method that actually solves Equation (E.17) using a specific discretization scheme is very expensive, but it does reveal error propagation characteristics in the computation field and tell us where grid refinements are necessary.

Another error estimation method evaluates the error by using a grid convergence index (GCI) [Roache, 1994]. The GCI is artificially defined based on a fine grid and a coarse grid, as well as the order of the discretization scheme. An important property is that it shows the solution sensitivity to grid density and distribution. A detailed implementation is shown in Section E.5.

This research implemented the Chen and Pletcher's numerical method due to its fast convergence speed. The corresponding detailed discretization scheme and error analysis are shown in the reference [Chen and Pletcher, 1991].

E.4 Time Stepping Analysis

This section discusses time step selection, system stiffness, and their relationship. It also explains why a variable time step is used in this research.

In order to understand some of the basic properties of a density based formulation, the eigenvalues of an inviscid flux vector for a perfect, inviscid, and non-reacting gas are determined. Eigenvalues represent the various time-scales existing in a system of equations. Large differences in the eigenvalue magnitudes indicates that the physical phenomena described by the equations occur at greatly differing rates. Numerically, knowledge of the eigenvalues is useful in estimating the convergence properties and stiffness of a set of equations. The eigenvalues of interest (one-dimensional case) are

$$\lambda_1 = u, \ \lambda_{2,3} = u \pm a \tag{E.18}$$

where u is the flow velocity and a is the speed of sound. The stiffness problem for this density based system can be seen in the fact that the ratio of largest to smallest eigenvalues goes to infinity as Mach number goes to zero. Physically, Equation (E.18) represents the differing time-scales between the acoustic and convective phenomena exhibited by the flow field. The convective time-scale is represented by λ_1 while the other two eigenvalues are associated with acoustic behavior. The ratio of largest to

smallest eigenvalues is a measure of the stiffness of a system of differential equations. For the density based equations under consideration, this ratio diverges continuously as *1/M* as the Mach number, *M*, approaches zero. Even at Mach number not so close to zero (for instance Mach number equals 0.01), the stiffness is quite high. For numerical reasons, the implication of a large stiffness ratio is twofold. First, a relatively large eigenvalue compared to the remaining eigenvalues of a system sharply curtails the allowable time step due to the stability relationship

$$CFL = \frac{\lambda_{max} \Delta t}{\Delta x}$$
(E.19)

where λ_{max} is maximum eigenvalue, Δt is time step, Δx is grid size, and *CFL* is the Courant-Friedrichs-Lewy number. For a fixed *CFL*, the time step is inversely proportional to the maximum eigenvalue. As a result, a time step can be unsuitably small for the remaining processes of the system. Second, the convergence ability of a scheme is strongly linked to the smallest eigenvalue of a system. Since this smallest eigenvalue represents the most slowly evolving physical process of a system of equations, convergence is dependent on either numerical damping or the natural propagation (or convection) of errors. Both processes of damping and convection are inhibited when they progress based on the much smaller time step determined by the fastest, largest eigenvalue, physical phenomena. It should be noted that, in addition to when u goes to zero, the stiffness ratio also goes to infinity as the Mach number goes to unity. This is because at $M = 1$ the $u - a$ eigenvalue for the density based scheme goes to zero, causing the ratio to be unbounded. Numerically, this apparent stiffness at Ma = 1 has no

noticeable effect on scheme convergence. Most likely this is due to the fact that the sonic point is usually a very small region, and that any numerical errors that may exist would be quickly convected away due to the large flow velocity. When reactions occur the largest eigenvalue increases. Therefore, for a fixed *CFL*, the allowable time step in the presence of reactions must be reduced to ensure stability. When computing reacting flows it is very effective to overcome local stiffness by using a multiple time step or local refined time step approach.

In this numerical study of methane injection and autoignition system stiffness arises from both compression wave (shock wave) propagation and reactions. Future work should consider using adaptive gridding in both the compression wave and reaction regions, and a smaller local time step in the reaction region in order to reduce the impact of system stiffness.

E.5   A Grid Independent Test

Appendix A.1 presents test results for lid driven cavity flow at three different Mach numbers. The purpose of these tests is to investigate system stiffness in low Mach number flow. This section shows the grid convergence or grid sensitivity for the current solver. The lid driven cavity flow problem is used because of its benchmark comparison value.

The discretization errors, defined as the difference between the exact solution of the discretized equations on a given grid and the exact solution of the governing differential equations, do not reveal a system's grid sensitivity. Errors depend both on

the discretization scheme and on the grid used. The order of the truncation error associated with the discretization scheme is often falsely interpreted as a measure of accuracy [Demirdzic, 1992] (one often finds statements in the literature like '... second-order accurate'). In fact, the order only states at which rate the error is reduced when the grid is refined enough, but it gives no information about the absolute magnitude of the errors on a given grid. When evaluating the truncation error for a numerical method the lowest order term of Taylor series is always used as a measure of the error. This error does not necessarily reflect the "real truncation error" which is a summation of this lowest order term and all higher order terms for a given grid size. Convergence errors, defined the difference between the exact and the approximate solutions of the discretized equations left over after stopping the iterations, can be estimated by evaluating solution differences on consecutive refined grids. Convergence errors can also reveal the error sensitivity of the system to grid size and grid distribution.

Results from test cases are provided on a sequence of grids, e.g., from 10 x 10 to 100 x 100, with Reynolds numbers 100 and 1000. Other physical parameters are the same as in Appendix A.1. The linear iteration tolerance is set such that the maximum residual must decrease six orders of magnitude while the non-linear iteration tolerance forces the maximum errors over a particular time period to decrease five orders of magnitude. Time integrals halt when the maximum error is accurate to five significant digits. Figures E.1 and E.2 show centerline profiles for both the u- and v-velocity components respectively. The maximum u error verses the square root of grid number at a Reynolds number 100 is presented in Figure E.3. The result shows that different grid
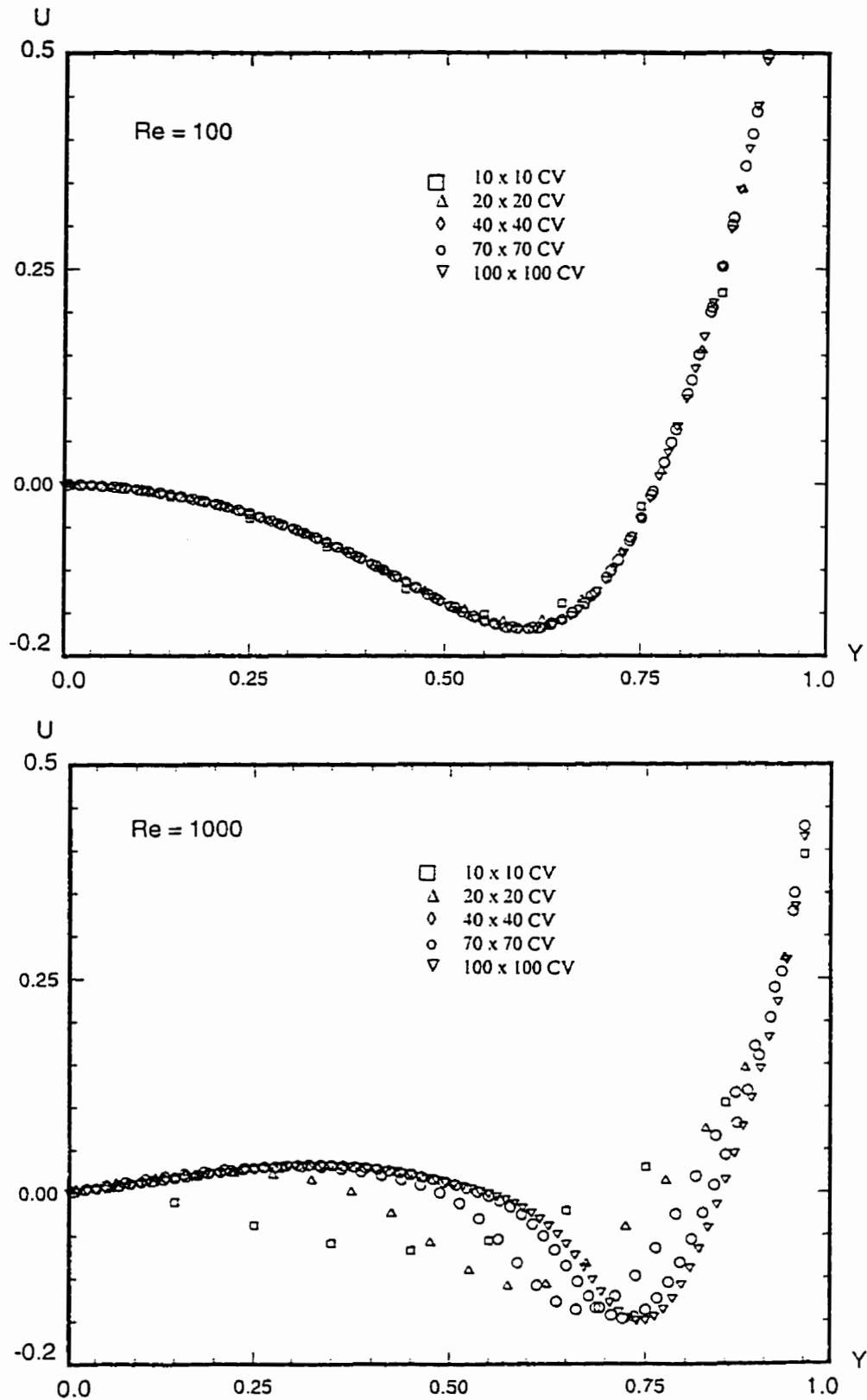
Figure E.1: Variation of the centreline velocity u
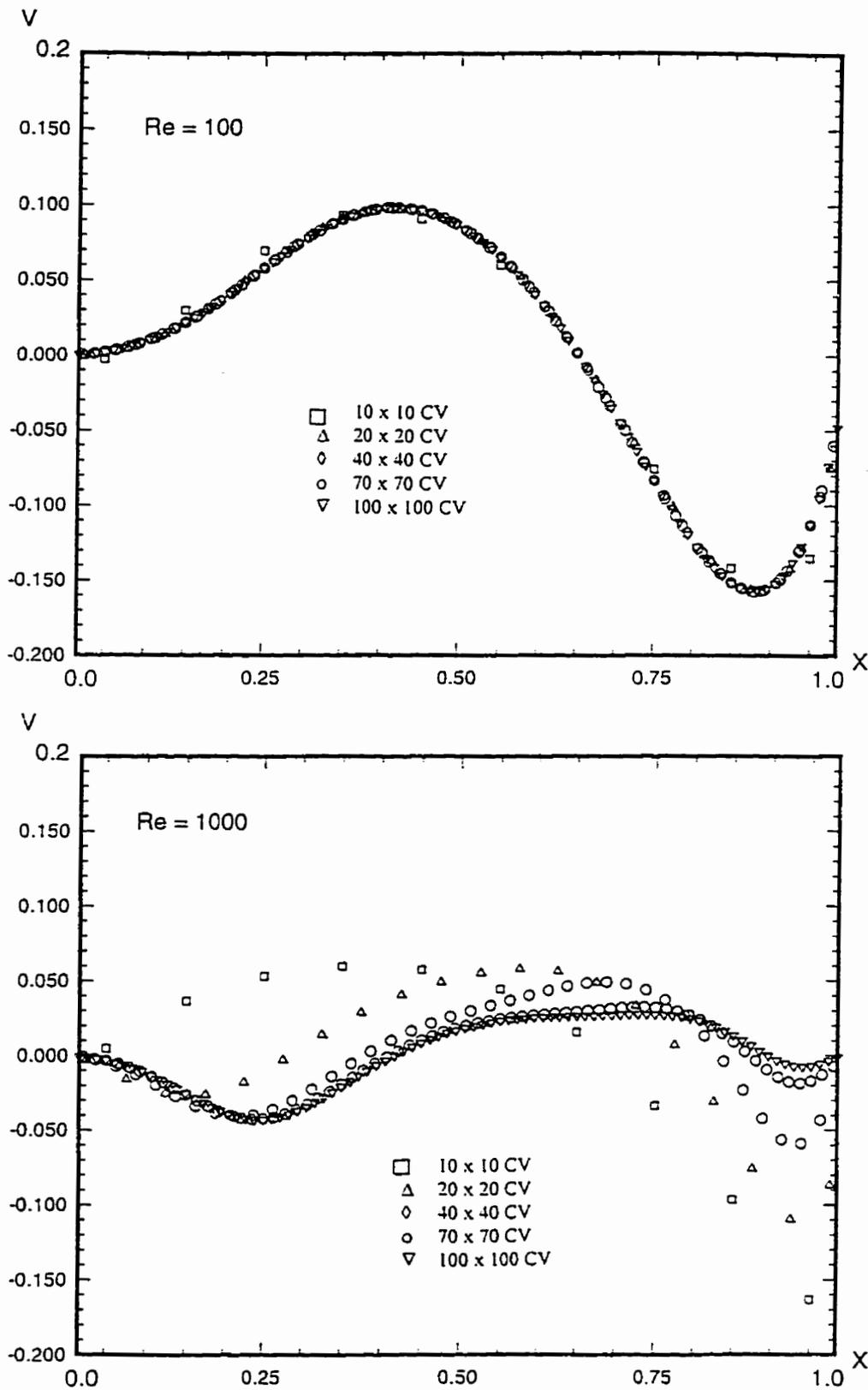
Figure E.2: Variation of the centreline velocity v
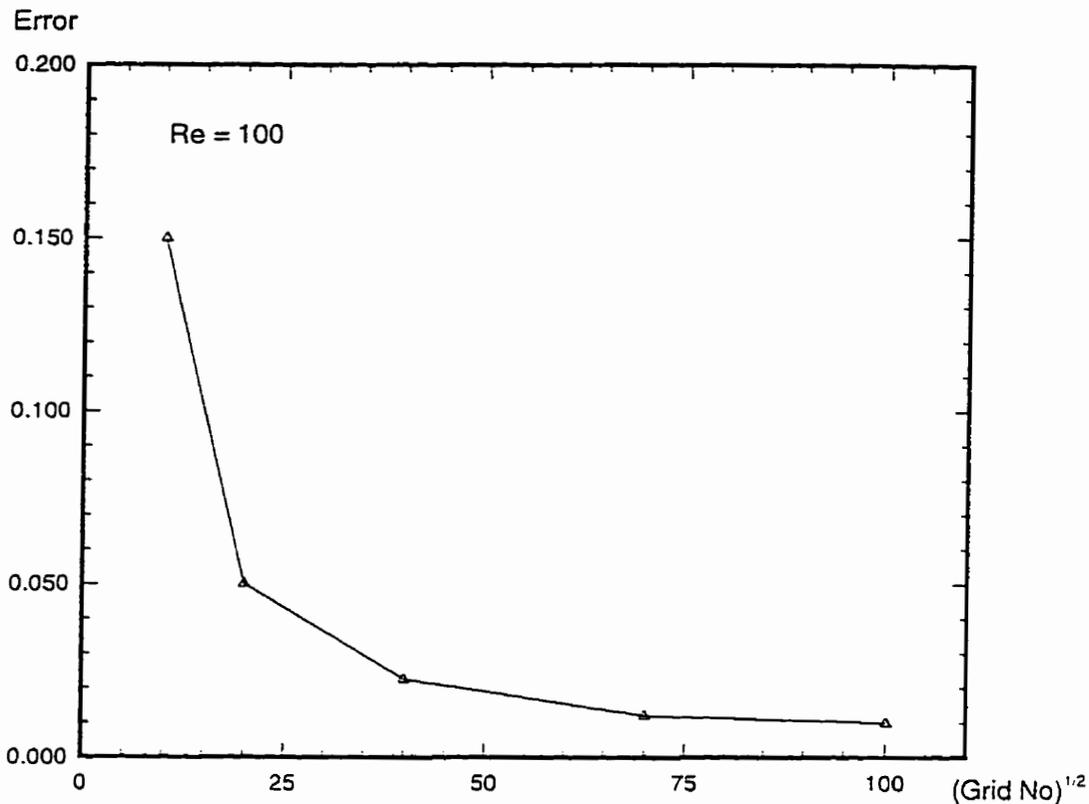
Error

Figure E.3: u-velocity error on centreline vs. square root of grid number

numbers are required to reach same accuracy for both cases (Reynolds numbers 100 and 1000). The results with Reynolds number 1000 are similar with Demirdzic's results.

E.6 Uncertainties in Methane Injection and Autoignition Results

This thesis has presented research into methane injection and autoignition more reflective of real diesel engine operation than other studies, though still, many real physical phenomena have been simplified. The uncertainties in the methane injection and autoignition results come from the following physical model and numerical errors.

The physical model uncertainties include (1) turbulence model and initial turbulence intensity, (2) combustion model, (3) injector geometry, (4) heat transfer at the boundary, as well as (5) radiation heat transfer. The quantitative evaluation of these physical model uncertainties is very difficult. Qualitative analysis of these factors is discussed in Chapter 3.

The numerical method used in this research is mainly based on the work of Chen and Pletcher [1991]. Code verification detailed in Appendix A includes a non-orthogonal grid test case (lid-driven cavity flow), a supersonic flow around a blunt body, a low speed gas jet computed on a non-uniform grid, and a steady state turbulence gas jet. The axisymmetric cylinder/injector configuration used in the methane injection and autoignition modelling presents a large aspect ratio, that is, a ratio of cylinder diameter to injector orifice diameter of 50 and a ratio of cylinder length to injector orifice length of 35. A non-uniform grid size that varies smoothly is used in order to reduce the error resulting from a sharp grid size change (see Figure 6.1). As a quantitative check the number of grid points is approximately doubled (Case 8 in Table 6.1). Case 8 profiles match the coarser, corresponding, Case 5 profiles well. The maximum difference between Case 5 and Case 8 velocities occurs on the centerline and is about 6%.

Integral time step is dependent on *CFL* number. Theoretically, a fully implicit discretization scheme on a set of linear partial differential equations usually presents unconditional stability. This theoretical result, however, does not extend to a set of non-linear partial differential equations. In addition, the integral time step is directly related to integration error in transient problems (especially for the first-order in time integration scheme). The *CFL* number (based on a summation of maximum sound speed and

maximum velocity) in this work when modelling methane injection and autoignition can be reach 100 (corresponding to an integral time step of about 10^{-5} second) without instability. Considering integration accuracy in this transient problem a maximum integral time step of 10^{-6} second is selected. It is desirable to employ a variable integral time stepping approach due to system stiffness from reaction as discussed in Section E.4. When ignition occurs the initial time step cannot yield a convergent solution, consequently the time step is halved and halved again as necessary.

Two iteration tolerances are used, a linear iteration residual tolerance and a non-linear iteration (Newton-Raphson iteration) error tolerance. Both tolerances are implemented in order to limit the maximum relative norms of the linear iteration residual, or the non-linear iteration error vectors. Neither tolerance is directly related to integral time step because of limiting the relative norms. The difference between maximum and average norms of a vector $\bar{r}$ is as follows [Jiang, 1978]

$$\|\bar{r}\|_{max} = C \|\bar{r}\|_{average} \qquad (E.20)$$

where C is a constant. Therefore, limiting a maximum norm is equivalent to limiting an average norm. Note that here we limit a relative norm, not a absolute norm. The absolute norm is directly related to the integral time step. An absolute norm decrease is associated with a reduction of in integral time step. The linear iteration tolerance forces the maximum relative residual norm to decrease six orders of magnitude while the non-linear iteration (Newton-Raphson iteration) tolerance forces the maximum relative error norm to five orders of magnitude.

The following four recommendations for future work would increase confidence in numerical accuracy, and increase computational efficiency:

(1)   use local grid refinement or an adaptive grid technique in regions containing steep gradients,

(2)   apply multiple time stepping to improve efficiency, that is, use a small time step in reaction regions and a large time step in fluid flow dominated regions,

(3)   implement the grid convergence index (GCI) to approximately evaluate solution sensitivity to grid density and grid distribution, and

(4)   expand on the number of time step and grid refinement tests.